Ricardo R. Ambriz
David Jaramillo
Gabriel Plascencia
Moussa Nait Abdelaziz *Editors*

Proceedings of the 17th International Conference on New Trends in Fatigue and Fracture

Springer

Proceedings of the 17th International Conference on New Trends in Fatigue and Fracture

Ricardo R. Ambriz · David Jaramillo
Gabriel Plascencia · Moussa Nait Abdelaziz
Editors

Proceedings of the 17th International Conference on New Trends in Fatigue and Fracture

Springer

Editors
Ricardo R. Ambriz
CIITEC-Instituto Politécnico Nacional
Mexico City
Mexico

David Jaramillo
CIITEC-Instituto Politécnico Nacional
Mexico City
Mexico

Gabriel Plascencia
CIITEC-Instituto Politécnico Nacional
Mexico City
Mexico

Moussa Nait Abdelaziz
Polytech' Lille
Université des Sciences et
Technologies de Lille
Villeneuve-d'Ascq
France

ISBN 978-3-319-70364-0 ISBN 978-3-319-70365-7 (eBook)
https://doi.org/10.1007/978-3-319-70365-7

Library of Congress Control Number: 2017959154

Printed on acid-free paper

This Springer imprint is published by Springer Nature
The registered company is Springer International Publishing AG
The registered company address is: Gewerbestrasse 11, 6330 Cham, Switzerland

Contents

Theoretical and Experimental Analysis of the Energy Dissipation at Fatigue Crack Tip Under Cyclic Loading with Constant Stress Intensity Factor

O. Plekhov, A. Vshivkov and A. Iziumova

Introduction

Fatigue crack propagation in metals is one the important problems of fracture mechanics. During pretty wide range of crack rates the kinetics of a crack growth can be described by correlation with a value of current stress intensity factor (Paris's law). This correlation is the result of the approximation of many experimental data and doesn't explain the physical nature of this process. Many authors proposed other correlations of the fatigue crack rate and different mechanical-structural parameters. For instance the J-integral, the work of plastic deformation, the size of the zone of a plastic deformation, the amount of dissipated energy were used as a parameter determining the crack propagation rate [1, 2].

The infrared thermography has been considered as a most effective method for estimating of the power of the heat sources in the process of mechanical testing. The main problem of application of this technique to the study of heat dissipation is caused by the uncertainty of solution of inverse problem. The principal solution of the problem of determination of energy dissipation under deformation can be obtained by the development of the additional system for direct monitoring of a heat flow. Such system based on the Seebeck effect was developed in ICMM UB RAS [3]. The system allows one to carry out quantitative measurements of a heat flow from the deformed sample within an area given by the dimensions of the used Peltier element.

The previous study of the authors was focused on crack growth problems under constant stress amplitude [3]. The experiments with constant stress intensity factor for the first time were reported in [4]. It has been shown that heat dissipation measured by contact heat flux sensor decreases during the crack propagation with the constant stress intensity factor.

O. Plekhov (✉) · A. Vshivkov · A. Iziumova
Institute of Continuous Media Mechanics UB RAS, 614014 Perm, Russia
e-mail: poa@icmm.ru

R. R. Ambriz et al. (eds.), *Proceedings of the 17th International Conference on New Trends in Fatigue and Fracture*, https://doi.org/10.1007/978-3-319-70365-7_1

To propose a theoretical explanation of this effect we derived an equation describing the evolution of plastic work at the crack tip. Following by the idea [5] we divided the plastic work and, as a consequence, heat dissipation at crack tip into two parts corresponding to reversible (cyclic) and monotonic plastic zones. Analysis of this approximation has shown the independence of heat dissipation in cyclic plastic zone from the crack advance. The dissipation in monotonic plastic zone is a function of both crack rate and characteristic diameter of the yield surface and gives well know correlation between fatigue crack rate and dissipated energy [3].

To confirm the proposed approximation we compare it with the results of fatigue crack propagation test in flat samples made from stainless steel AISE 304. The obtained results are in a qualitative agreement with the experimental data.

Experimental Setup

A series of samples made from stainless steel AISE 304 were tested. The detailed description of mechanical properties, geometry of the samples and test conditions are presented in [3, 4]. The samples were subjected to cyclic loading of 20 Hz with the constant stress intensity factor and loading ratio R = −1.

To analyze the dissipated energy at the crack tip a contact heat flux sensor was designed and constructed. The detailed description of the sensor is presented in [3]. The proposed sensor is based on the Seebeck effect, which is the reverse of the Peltier effect. The Peltier effect is a thermoelectric phenomenon, in which the passage of electric current through conducting medium leads to the generation or absorption of heat at the point of contact of two dissimilar conductors. The quantity of heat and its sign depend on the type of materials in contact, the direction and the strength of the electric current. A thermal contact between the sample and the sensor is provided by the introduction of the thermal paste. These sensors were calibrated using a device reproducing the sample under study with a controlled heat flux.

The experimental program includes four tests with the constant stress intensity factor. The constant stress intensity factors are equal of 15, 17.5, 20, 22.5. The crack rates were 2.0076, 6.6391e−08 m/cycle, 1.0245, 1.7177e−07 m/cycle, correspondingly. Each experiment includes first part with constant stress amplitude to initiate the fatigue crack with the length of 1 mm and the second part with the constant stress intensity factor which was kept up to the 8 mm crack length.

It is important to note that similar experimental program was realized in ICMM UB RAS. The detailed description of mechanical properties, geometry of the samples and test conditions are presented in [3]. The similar steel (Russian analog) with different sample geometries was tested with the loading ratio R = 0. The stress intensity factors were equal to 25 and 30 MPa $m^{1/2}$ (for crack rates of 1.4, 1.65e−07 m/cycle, correspondingly). The results of the both experimental programs are.

Results of Fatigue Experiments

The typical results of the test are presented in Fig. 1.

The test includes stress amplitude part up to 2200-th second. We can observe the stable accelerated crack propagation from 500-th to 2200-th second of the test accompanying by the increase of the heat dissipation. Form 2200-th second the stress intensity factors was kept constant. It leads to the decrease of the stress amplitude (Fig. 1a) and heat dissipation and nearly uniform crack propagation (Fig. 1b).

Theoretical Analysis of the Heat Dissipation

Following the idea proposed in [5], we can start from a relation between elastic and real deformation at the crack tip:

$$\varepsilon_{\mathrm{ij}}^{ef} = (G/G_s)^{\frac{1}{2}}\varepsilon_{ij}^{el}, \tag{1}$$

where G—the shear modulus, G_s—secant shear modulus.

Equation (1) was originally proposed by [6] as a result of photo elastic experiment data treatment. Using the Ramberg-Osgood relation $\gamma = \tau/G + A(\tau/\tau_0)^n$, we can write a following estimation for octahedral stress and link it with an elastic solution

$$\tau_{oct} = \tau_{oct}^{el}\left(3 + 2(1+v)B\xi^{n-1}\right)^{\frac{1}{2}} \Big/ 3\left(1 + B\xi^{n-1}\right), \tag{2}$$

where A, τ_0, n—material constants, $B = GA/\tau_0(\tau_e/\tau_0)^n, \xi = \tau_{oct}/\tau_e, \tau_e$—elastic limit.

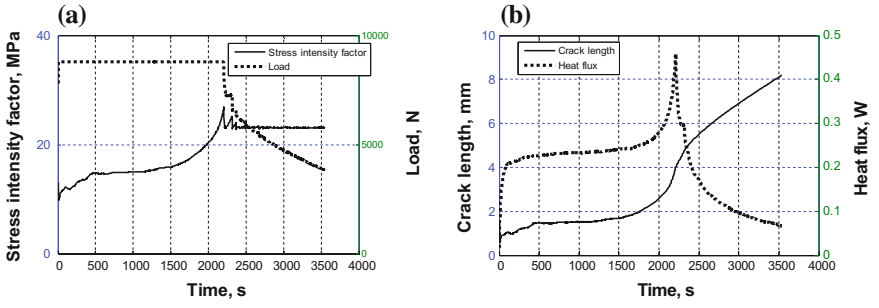

Fig. 1 The stress intensity factor and applied load (**a**), heat dissipation and crack length (**b**) histories during the whole test (The experiments were carried out at Bundeswehr University Munich)

To analyze plastic deformation at the crack tip under cyclic loading we need to divide energy dissipation in cyclic and monotonic plastic zones at the crack tip $U_p^{tot} = U_p^{cyc} + U_p^{mon}$.

The energy of representative volume at cyclic zone can be estimated as

$$U_p^{cyc} = 3/2\tau_{ec}\gamma_{pc}, \tag{3}$$

where τ_{ec}—characteristic size of the yield surface, γ_{pc}—amplitude of plastic deformation under an assumption of the validity of Ramberg-Osgood relationship, $\tau_{oct,c}$—stress change in the representative volume.

The full energy of cyclic plastic zone can be calculated as a double integral over the region (S) bounded on the outside of the monotonic plastic deformation zone and inside of the fracture zone

$$U_p^{cyc} = \int_S \int_0^{\pi} 3\tau_{ec}^2\left(G_S^{-1} - G^{-1}\right)\left(\tau_{oct,c}/\tau_{ec} - 1\right) r dr d\theta. \tag{4}$$

The simple approximation of cyclic-monotonic plastic zone boundary can be given by $r = r_{p,c}f_e$, *for* cyclic-fracture zone boundary—$r = r_{p,c}f_e\tau_{ec}/\tau_{fr}$.

The energy increment in cyclic plastic zone can be written as

$$dU_p^{cyc}\Big/dN = 3\tau_{ec}^2\left(G_S^{-1} - G^{-1}\right)\int_S \int_0^{\pi} d\tau_{oct,c}/d\tau_{oct}^{el} d\tau_{oct}^{el}/dN r dr d\theta \tag{5}$$

The direct calculation of Eq. (5) gives $dU_p^{cyc}\Big/dN = 0$. It means that dissipation in cyclic plastic zone doesn't depend on the crack advance and fully determined by the applied load.

The energy dissipation in monotonic plastic zone can be estimated as $U_p^{mon} = 3/2\tau_e\gamma_p$. The energy increment per one cycle can be written as

$$dU_p^{mon}\Big/dN = 3\tau_e\left(G_S^{-1} - G^{-1}\right)\int_{S_1} \int_0^{\pi} \tau_{oct} d\tau_{oct}/d\tau_{oct}^{el} d\tau_{oct}^{el}/dl dl/dN r dr d\theta \tag{6}$$

Solution of (6) for the case of $dr_p/dl \to 0$ presented in [5].

For the following analysis it is important that $dU_p^{tot}\Big/dN$ is a function of crack rate (dl/dN). Finally, Eqs. (5) and (6) allows us to propose the following approximation for energy of plastic deformation at the fatigue crack tip

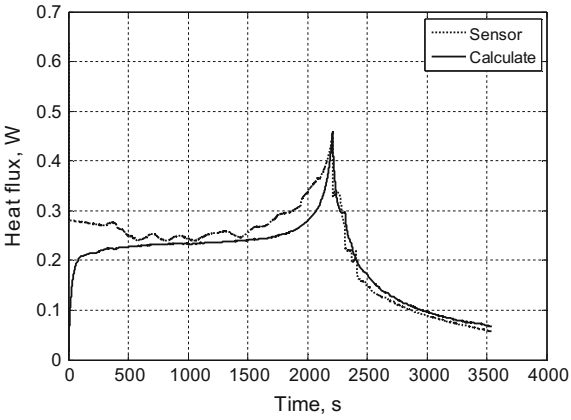

Fig. 2 Heat dissipation histories during the test carried out under constant stress amplitude (up to 2200-th second of the test) and constant stress intensity factor (remaining time) (Solid line— approximation (7), the dotted line—experimental results)

$$dU_p^{tot} \Big/ dN = W_1\left(A_\tau^2, r_p\right) + W_2\left(A_\tau^2, r_p\right) dl/dN = a_1 A_\tau^2 + a_2 A_\tau^2 dl/dN, \qquad (7)$$

where A_τ—applied stress amplitude which determines the diameter of yield surface.

The process of heat dissipation is determined by the plastic work. This relation could be complex due to the peculiarities of energy storage in material structure but taking into account the simplicity of Eq. (7) we will use the linear dependence of heat dissipation versus energy of plastic deformation for the first approximation of experimental results.

Figure 2 presents the comparison of approximation (7) and results of the contact heat flux sensor. Equation (7) gives a good qualitative description of peculiarities of heat dissipation in both regimes with the constant stress amplitude and constant stress intensity factor. For constant stress amplitude the plastic work and, as a consequence, energy dissipation at the crack tip is determined by crack rate as is shown [2] but for constant crack rate we can observe the regimes with the decrease of the heat dissipation caused by the decrease of the applied stress amplitude.

Conclusion

In this work the experimental and theoretical study of energy dissipated at fatigue crack tip in AISE 304 steel were carried out. The experiments include two regimes of crack propagations: constant stress amplitude and constant stress intensity factor. It has been experimentally shown that for constant stress amplitude we can observe the increase of the heat dissipation correlated with the fatigue crack tip. The crack propagation with the constant stress intensity factor is accompanied by the decrease of the heat dissipation. This effect was observed independently in two different experimental programs.

To propose one of the possible explanations for the observed results a theoretical analysis of plastic work at fatigue crack tip taking into account the evolution of both monotonic and cyclic plastic zones has been carried out. This analysis allows us to propose a simple approximation for the heat dissipation at fatigue crack tip. The theoretical results give a good qualitative description of peculiarities of the heat dissipation in both regimes with the constant stress amplitude and constant stress intensity factor. For the constant stress amplitude the plastic work and, as a consequence, energy dissipation at the crack tip is determined by the crack rate but for the constant crack rate regime the scenarios with a drop in the heat dissipation takes place.

Acknowledgements This work was supported by the Russian Science Foundation (Grant No. 17-11-01204).

References

1. Matvienko Yu.G., Morozov E.M., 2004. Calculation of the energy J-integral for bodies with notches and cracks // International Journal of Fracture 125, 249–261.
2. Izyumova A., Plekhov O., 2014. Calculation of the energy J-integral in plastic zone ahead of a crack tip by infrared scanning // FFEMS 37, 1330–1337.
3. Vshivkov A., Iziumova A., Bar U., Plekhov O., 2016. Experimental study of heat dissipation at the crack tip during fatigue crack propagation // Frattura ed Integrità Strutturale 35, 131–137.
4. Bär J., Determination of dissipated Energy in Fatigue Crack Propagation Experiments with Lock-In Thermography and Heat Flow Measurements // Procedia Structural Integrity, v. 2, 2016, 2105–2112.
5. Raju K. N. An energy balance criterion for crack growth under fatigue loading from considerations of energy of plastic deformation // International Journal of Fracture.
6. Dixon J.R., 1965. Stress and strain distributions around cracks in sheet materials having various work-hardening characteristics, Ministry of Technology, National Engineering Laboratory, Materials Group: East Kilbride, Glasgow, Scotland, 224–244.

A Study of Progressive Milling Technology on Surface Topography and Fatigue Properties of the High Strength Aluminum Alloy 7475-T7351

Miroslav Piska, Petra Ohnistova, Jana Hornikova and Charles Hervoches

Introduction

Machining process in aerospace industry is often characterized by high material removal up to 95%. Many of the primary and secondary aircraft structures such us spars and ribs have to be lightened by milling operations because of the strict weight reduction requirements and according the trend in design preferring the monolithic parts to the assembled parts. However, during machining process, the surface layer of the component is subjected to elastic-plastic deformation and heating, what result in different thickness of the machined walls, residual stresses, strain hardening, structural changes and surface topography changes which are having important impact on the fatigue properties, esp. in thin-walled parts [1–3].

It is well known that fatigue life and tensile strength are highly dependent on the final surface quality because the micro-cracks are usually initiated on the free surfaces where the stress concentrations are the highest [4], what can be observed in cyclic loading. Consequently, a set-up of some inappropriate cutting conditions may affect the surface quality and related fatigue properties of the machined components. In aircraft industry the need for optimal cutting conditions should be selected correctly with respect to the fatigue properties of the machined and exposed parts.

M. Piska (✉) · P. Ohnistova
Faculty of Mechanical Engineering, Institute of Manufacturing Technology, Brno University of Technology, 2 Technicka, 616 69 Brno, Czech Republic
e-mail: piska@fme.vutbr.cz

J. Hornikova
Central European Institute of Technology, Brno University of Technology, Purkyňova 123, 616 00, 616 69 Brno, Czech Republic

C. Hervoches
Nuclear Physics Institute, Czech Academy of Sciences Řež, 130, 25068 Řež Czech Republic

R. R. Ambriz et al. (eds.), *Proceedings of the 17th International Conference on New Trends in Fatigue and Fracture*, https://doi.org/10.1007/978-3-319-70365-7_2

Several studies have been already focused on the effect of cutting conditions on the surface quality and related fatigue life. For example, Sasahara [5] in his paper presents the effect of residual stresses and surface hardness on the fatigue life of the steel (0.45%C) resulting from different cutting conditions of turning. Suraratchaï [6] studied the influence of the surface integrity on the fatigue performance of an aeronautical aluminum alloy 7010-T74511 while using different cutting conditions of the face milling. Gómez [7] studied an influence of cutting conditions of the turning process on the fatigue performance of the aluminum alloy A92024-T351. Sunday [1] presented a study of the influence of machining parameters on the fatigue life of end milled aluminum alloy 2024. However, the effect of the cutting conditions of shoulder milling strategy on the surface quality and related fatigue life of thin walled components has not been fully examined in the previous studies, so this presents a contribution the problematic.

Theory of Milling

Chip Formation During Shoulder Milling

During shoulder milling operation, the cutting is accomplished by a peripheral flute of a cutter and the rotational axis of the cutter is always parallel to the machined surface. Chip formation is therefore performed by the peripheral cutter and is variable in time and over the position at the cutting edge. Chip cross section can be derived from the analysis of the helical conoid and can be determined for each flute (tooth) and its geometry. During shoulder milling operation, the motion of the tooth and associated variation of the chip cross section area at each point can be observed. Together with the time change the specific cutting forces, the total loading of the workpiece surface and related cutting performances vary [8].

Force Loading of the Shoulder Milling

Determination of the force loading during shoulder milling operations can be predicted theoretically and verified experimentally. All theoretical calculations are based on the specification of the chip cross section which corresponds to the analysis of a helical conoid and specific cutting forces [8]. Force loading of the milling cutter can be therefore defined as an indefinite integral with the hypergeometric function (1, 2) including a material constants c_0, mc and angle of engagement φ:

$$F_c = \int_{\varphi_1}^{\varphi_2} dF_c = c_o . \int_{\varphi_1}^{\varphi_2} \sin^{1-mc} \varphi \; . \; d\varphi. \tag{1}$$

The cutting force can be used for calculation of the specific cutting energy kc:

$$k_c = F_c / A_D = (c_o / (a_p . a_e)) . \int_{\varphi_1}^{\varphi_2} \sin^{1-mc} \varphi \; . \; d\varphi, \tag{2}$$

where A_D is the un-deformed chip cross-section, a_p and a_e the axial and radial depths of cut. Workpiece loading and its deflection, however, depends not only on cutting force F_c mentioned above but also on the force perpendicular to the cutting force that is acting in the radial direction to the cutting tool. This force is known as F_{cN} and its prediction is difficult because of its dependency on the macro and micro geometry of the tool, tribology of the interface tool-chip-workpiece and on the tool wear. Its magnitude and orientation vary significantly with the tool wear similarly as the orthogonal passive force F_p [8].

For these reasons, the experimental measurement of the instantaneous force loading corresponding to the maximal chip cross section is inevitable. Precise analyses of the force loading make the base for specific cutting energy calculations which are dominant for presence of residual stresses after machining.

Surface Quality After Machining

Machining process is determining for the final state of the workpiece surface [9]. Surface morphology after a machining operation contributes to the surface integrity which integrates several different aspects such as surface topography, surface microstructure, mechanical properties, residual stresses, corrosion resistance and life of a part [10].

Surface topography is defined by the 2D and 3D parameters [11]. The two dimensional parameters are further divided into many roughness amplitude parameters such as for example Rq, Rt, Rz, Rp and Rv, waviness parameters such as Wa, Wq, Wt and Wz and into the parameters defined by the Abbot-Firestone curve (specifying the percentage of the material of the profile elements at a defined height level relative to the evaluation length). Analysis of this curve is significant mainly for a prediction of initial wear, a wear evolution during operation or the ability to retain liquids in the operational use [12, 13].

In various publications, the average surface roughness Ra was used to evaluate the influence of surface topography on the fatigue life [14, 15]. However relatively large variance in fatigue results have been observed. With booming use of optical or other advanced measuring devices the other surface parameters are subjects of studies frequently.

Residual Stresses After Machining

The stresses imposed by the elastic-plastic deformation, heat treatment, strain hardening or even heat softening during mechanical processing of the raw material are commonly known as residual stresses [16]. These stresses vary in depth, magnitude and orientation and can have a very significant effect on the fatigue properties of the machined component. These stresses can be tensile or compressive and the stressed layers vary in depth according to the used cutting conditions, work material, tool macro and micro geometry and other conditions of the interface tool-chip [17]. Compressive residual stresses are usually beneficial at the free surface and they decrease with increasing depth. Compressive stresses generally improve fatigue performance of the machined component because in some case prevent fatigue crack nucleation or slow down its propagation. Further increase in the depth results frequently in the tensile residual stresses which accelerate the degradation and fracture damage [18, 19].

Experimental

Material of Workpiece

Aluminum alloy 7475-T7351 was selected as a workpiece material because of its real use in aerospace industry today especially for structural parts which are subjected to the cyclic loading during flight. The aluminum alloy 7475 is an alloy with the so-called controlled toughness, developed by the producer ALCOA, providing a combination of high strength, good fracture toughness and high resistance to the fatigue crack propagation—Tables 1 and 2. The alloy 7475 is a refinement of the alloy 7075 and its fracture toughness for plates are almost 40% greater than for the previous version 7075 at the same temperature. The prevalence in some properties is a result of the reduction of the Fe, Si and Mg contents and is as influenced by thermo-mechanical and heat treatments procedures. The material 7475 is recommended when a high fracture toughness of a part (typically the aircraft wings or wing spars) are considered. The application of T7351 heat treatment provides also optimal resistance to the stress corrosion cracking [20].

Cutting Tools, Machine

The SECO end-milling tool ∅ 16 × 55 × 115 JS513160D3C.0Z3-NXT (SMG N11, (Ti,Al)N coating) for the thin-wall machining was used. Tool micro-geometry was analyzed with Alicona Edge Master/ALICONA-IF G4. The cutting experiments

Table 1 Chemical composition of 7475-T7351 [20]

Element	Weight content (%)
Si	0.10 max.
Fe	0.12 max.
Cu	1.20–1.90
Mn	0.06 max.
Mg	1.90–2.60
Cr	0.18–0.25
Zn	5.20–6.20%
Ti	0.06 max.
Others, each	0.05 max.
Al	Balance

Table 2 Mechanical properties of 7475-T7351 [20]

Thickness of the sheet (mm)	25–38	50–63	75–89
Tensile strength (MPa)	490	476	448
Yield strength (MPa)	414	393	365
Elongation (%)	9	8	8

were carried out at the 5-axis milling center MCV 1210/Sinumerik 840D. Cutting experiments were performed for various cutting speeds and feeds—Fig. 1.

Force Loading Measurement

The force loading during milling was measured with the stationary KISTLER 9575B/SW and analysed with SW DynoWare. Mean values of the maximal instantaneous force loadings in X, Y and Z direction for determination of the resultant force F_{1M} and its decomposition to the force loadings F_c and F_{cN} and calculation of specific variables for up and down milling.

Surface Topography Measurement

A very complex measurement of the surface topography was performed on the rigid samples using high resolution optical device ALICONA-IF G4. A single measurement contained 30 million of data giving information about 2D and 3D parameters of the scanned surface of 5×5 mm^2. Surface topography was measured in two directions X and Y corresponding to the coordinate system of the measurement device ALICONA-IF G4. Axis X corresponded to the direction of the tool axis, direction Y is perpendicular to the previous and corresponds to the direction of the tool movement. Measured values were processed using of one-way analysis ANOVA.

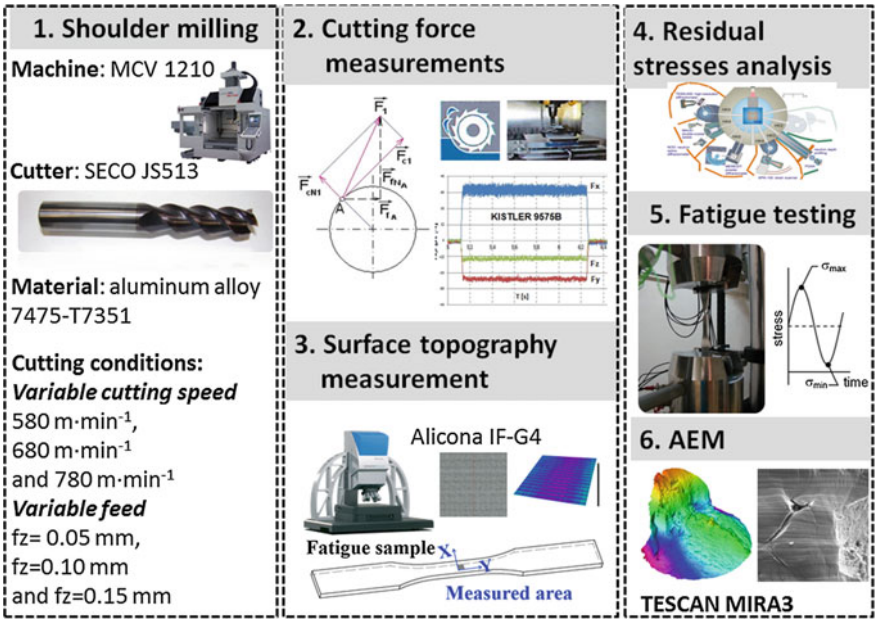

Fig. 1 Experimental set-up of the measurements

Fatigue Testing and Fracture Surface Analysis

First objective of the fatigue testing was to simulate tensile high cycle loading of the thin-walls separating pockets of the wing panels. Second objective was to examine the influence of the cutting conditions of the shoulder milling and corresponding surface quality on the fatigue life based on the S/N curve of un-notched

7475-T7351 plate from MMPDS (Metallic Materials Properties Development and Standardizations) the following specifications and parameters of the fatigue testing were used:

- an axial testing machine BISS,
- the flat un-notched fatigue specimen according to ASTM-E466 and EN 6072 with the minor adjustments of the clamping area of the sample,
- the fluctuating tensile cycle R = 0.1, f = 10 Hz.

In order to examine the influence of the cutting conditions, three series of the specimens according to the cutting conditions (fz = 0.05 mm, fz = 0.10 mm and fz = 0.15 mm), just corresponding with the surface quality were used for every stress level. The electron microscope Tescan MIRA 3 equipped with EDS probes was used to evaluate the source of the crack nucleation (SEM/AEM).

Residual Stresses

Residual stress analysis was performed at Neutron Physics Laboratory of CANAM infrastructure of Nuclear Physics Institute, Řež near Prague, Czech Republic according to the neutron diffraction method [21]. Two-axis diffractometer SPN-100 [22] placed at thermal neutron source (reactor LVR-15, which belongs to Research Centre Řež) was used for mapping of residual strains inside the material 7475-T7351. Principle of the measurement was based on the accurate evaluation of positions of a selected diffraction peak from small material volume defined by a set of input and output slits according to Hutchings [23]—Fig. 2. Positioning of flat specimens in dimensions 370 × 35 × 5 mm was ensured by the six-axis robotic arm allowing more flexible manipulation.

Results and Discussion

For both milling strategies (up and down milling) have been found, that an increase of feed speed resulted in a higher cutting force F_c and higher ratio F_c/F_{cN}. On the other hand, the increase of the cutting speed did not result in a significant growth of the force loading neither of the specific cutting energies (in the tested interval of cutting speeds). However, the down-milling milling strategy for all the experiments is analyzed more in detail here because of its superior results.

Surface topography measurement confirmed that the increase of the feed speed lead to an increase of roughness and waviness parameters. Increase of the feed by three times was followed by increases of the R_a from 0.31 to 0.80 µm (by 158%), R_v from 1.24 to 1.91 µm (by 54%) or W_t from 1.23 to 1.92 µm (by 56%). The effect of the cutting speed on the surface topography wasn't statistically

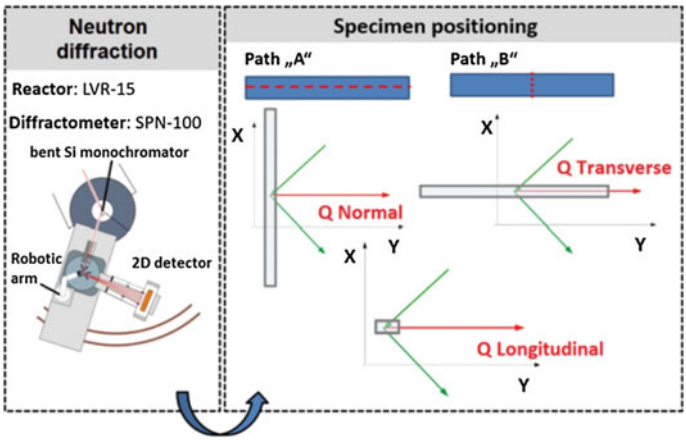

Fig. 2 A scheme of the residual stresses measurement by the thermal neutron diffraction

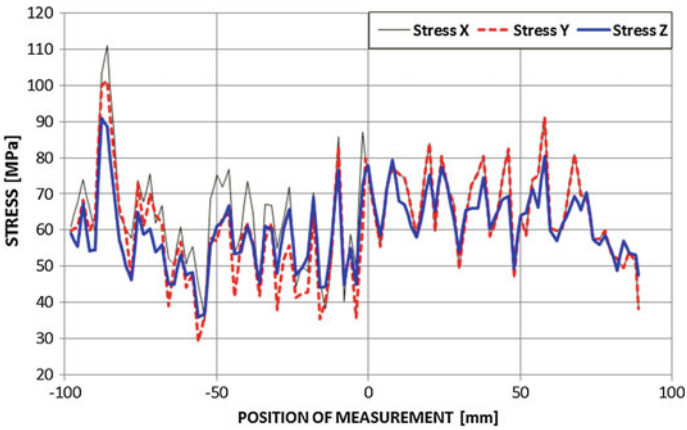

Fig. 3 Residual stresses along the longitudinal axe (Path "A") of a sample. Stress X: *Q Normal*, Stress Y: *Q Transverse*, Stress Z: *Q Longitudinal*

significant ($\alpha = 0.05$) in the tested interval of cutting speeds. The higher Rpk parameter values were observed with increase of the feed speed so more progressive wear of the workpiece surfaces can be expected while using higher feeds. The analysis of the orthogonal residual stresses showed relatively low values of for all tested conditions and measured samples—Fig. 3.

Results of the fatigue testing are presented in the S-N graph (see Fig. 4). The metallographic cross-sections proved that for the defined machining conditions of shoulder milling of aluminum alloy 7475-T7351, the thickness of layer affected by machining was approximately 1 μm and values of the roughness (Ra = 0.815 μm, Rt = 5.34 μm a Rv = 2.06 μm) showed not to be crucial to cause fatigue crack nucleation—Fig. 5.

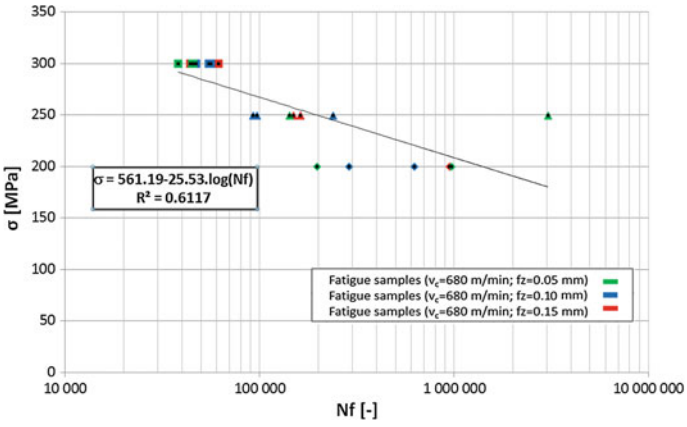

Fig. 4 S-N curve for un-notched machined sample made of aluminum alloy 7475-T7351

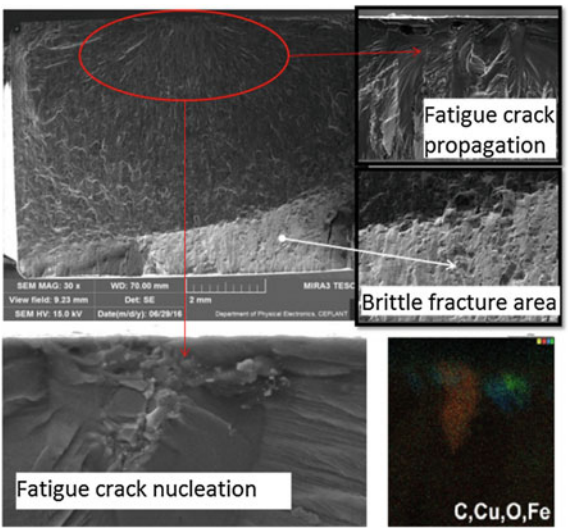

Fig. 5 Fatigue fracture surface analysis

Conclusions

The hard complex inclusions Fe-Cu-C-O were crucial for disturbing the material integrity and production of local stress risers and suppressed the role of surface roughness or selection of cutting conditions in the analyzed ranks. Neither the surface topography nor the imposed specific cutting energies were the key factors affecting the fatigue performance of the machined aluminum alloy 7475-T7351. Fatigue fracture analysis showed that the material inclusions dispersed in the adherent machined surfaces trigger the fatigue crack initiations and propagations. The next research is focused on the analysis of the mechanism in direct SEM tensile test observations and elimination of the material inhomogeneities.

Acknowledgements This research work was supported by the Brno University of Technology, Faculty of Mechanical Engineering, Specific research 2016, with the grant "Research of modern production technologies for specific applications", FSI-S-16-3717, and by the project CEITEC 2020, LQ1601, Ministry of Education, Youth and Sports of the Czech Republic, and the residual stress analysis was done in cooperation with CANAM infrastructure of Nuclear Physics Institute, Řež near Prague, Czech Republic, and was supported through MŠMT infrastructural projects LM2015056 and LM2015074.

References

1. SUNDAY J. Ojolo. Machining Variables Influence on the Fatigue Life of End-Milled Alumina Alloy. *International Journal of Materials Science and Applications*. 2014, 3(6), 391. ISSN 2327-2635.
2. PANDIAN, P., PRABHU, R., SAKTHIMURUGAN, K. Surface error compensation in HSM of thin wall structures. *International Journal of Engineering Science Invention.* 2013. vol. 2, no. 2, pp. 1–11.
3. DENKENA, B., SCHMIDT, C. Experimental investigation and simulation of machining thin-walled workpieces. *Production Engineering, Research and Development.* 2007, Vol. 1, no. 4, pp. 343–350.
4. SHAHZAD, Majid. Influence de la rugosité et des traitements d'anodisation sur la tenue en fatigue des alliages d'aluminium aéronautiques 2214 et 7050. Toulouse, 2011. Thesis. L'Université de Toulouse. Supervisor M. Farhad Rézaï-Aria.
5. SASAHARA, Hiroyuki. The effect on fatigue life of residual stress and surface hardness resulting from different cutting conditions of 0.45%C steel. *International Journal of Machine Tools and Manufacture*. 2005, **45**(2), 131–136. ISSN 08906955.
6. SURARATCHAÏ, Monchaï, Catherine MABRU a Rémy CHIERAGATTI. Influence de gammes d'usinage sur la tenue en fatigue d'un alliage léger aéronautique. In: 17ème Congrès Français de Mécanique. Toulouse, 2005.
7. GÓMEZ, A., SANZ, A., MARCOS, M. An Analysis of the Influence of Cutting Parameters on the Turning Process on the Fatigue Life of Aluminum Alloy UNS A92024-T351. *Advanced Materials Research*. 2012, **498**, 19–24.
8. FOREJT, M., PÍŠKA, M. Teorie obrábění, tváření a nástroje *(Theory of metal cutting and forming).* Brno. Akademické nakladatelství CERM s.r.o., 2006. ISBN 80-214-2374-9.
9. M'SAOUBI, R., *et al.* A review of surface integrity in machining and its impact on functional performance and life of machined products. *International Journal of Sustainable Manufacturing*, 2008, Vol. 1, Nos. 1/2, pp. 208–236.
10. DAVIM, J.P. Surface Integrity in Machining. London: Springer London, 2010. ISBN 978-1-84882-873-5.
11. JIANG, X. Jane, WHITEHOUSE David J., Technological shifts in surface metrology. *CIRP Annals - Manufacturing Technology.* 2012, 61(2), 815–836. ISSN 00078506..
12. RÎPĂ, Minodora, TOMESCU HAPENCIUC, Lorena.. TRIBOLOGICAL CHARACTERISATION OF SURFACE TOPOGRAPHY USING ABBOTT-FIRESTONE CURVE. Romania: University "Dunărea de Jos" of Galati, România, 2003. ISSN 1221-4590.
13. ABBOTT, E.J., FIRESTONNE, F.A. (1933), Specifying surface quality, Mech. Eng., 55, 569–572.
14. NOVOVIC, D., R.C. DEWES, D.K. ASPINWALL, W. VOICE a P. BOWEN. The effect of machined topography and integrity on fatigue life. *International Journal of Machine Tools and Manufacture.* 2004, **44(2–3)**, 125-134. ISSN 08906955.
15. SIEBEL, E. a M. GAIER. Influence of surface roughness on the fatigue strength of steels and non-ferrous alloys. Engineers Digest. 18(1957), 109–112.
16. ZAHAVI, Eliahu, TORBILO Vladimir. Fatigue design: life expectancy of machine parts. Boca Raton: CRC Press, 1996. ISBN 08-493-8970-4.

17. HEARN, E. J. Mechanics of materials: an introduction to the mechanics of elastic and plastic deformation of solids and structural materials. 3rd ed. Boston: Butterworth-Heinemann, 1997. ISBN 978-0-7506-3266-9.
18. THONAS, Watkins. Measurement and Analysis of Residual stress in ε-phase Iron Niitride Layers as a function of Depth. International Centre for Diffraction Data. 2000, 2(43), 31–38.
19. MANKAR, D. S. a P. M. KHODAKE. Residual stress produced after machining in mechanical components and its effects on fatigue life: A state of art *International Journal of Mechanical and Production Engineering Research and Development (IJMPERD)*. 2015, 5 (1), 1–10. ISSN 2249-6890.
20. ALLOY 7475 PLATE AND SHEET. Iowa: ALCOA. [cit. 2016-08-20]. Available from: https://www.arconic.com/mill_products/catalog/pdf/alloy7475techplatesheet.pdf.
21. G.A. WEBSTER, R.C. WIMPORY, Non-destructive measurement of residual stress by neutron diffraction, Journal of Materials Processing Technology, Volume 117, Issue 3, 2001, Pages 395–399, ISSN 0924-0136, http://dx.doi.org/10.1016/S0924-0136(01)00802-0.
22. HK4 strain scanner. Nuclear Physics Institute ASCR [online]. Available from: http://neutron.ujf.cas.cz/en/hk4/item/144-hk4-description.
23. HUTCHINGS, M.T., WITHERS, P.J., HOLDEN, T.M., LORENTZEN T., Boca Raton, FL: Taylor & Francis, 2005, p. 420. ISBN: 9780415310000.

Study and Design of a New Range of Composite Based Shock Absorbers for the Automotive Sector

J. Niez, M. Ben Amara, J. Capelle, V. Bouchart and P. Chevrier

Introduction

In the automotive sector, the absorption of the energy released during an impact is partly achieved by the plastic deformation of metallic systems [2]. However, with the tightening of laws on greenhouse gas emissions, the automotive sector seeks to reduce the mass of vehicles and thus to limit consumption and the production of harmful gases.

The new composite materials with mechanical properties similar to metals have the advantage of having better performances in terms of energy absorption and a lower density than those of current materials, while being recyclable [5]. For composites, energy absorption is in particular due to numerous phenomena of damage (rupture, delamination, etc.) and not to plastic deformation [3]. Mastering the breakdown of composite systems is therefore essential: the understanding of the real crush scenario enables to optimize the geometry and type of composite used to maximize the energy absorbed. Indeed, a large number of parameters related to the structure have an important influence on the quantity of final energy absorbed [8]: geometry, type of materials, orientation of the folds, etc. It is therefore essential to study and to correctly determine the values of these different parameters from the scientific literature but also from experimental tests.

At the scale of the ply, the rupture of the fibers, the matrix break and the fibers/matrix delamination are responsible for the ruin of the material [7]. This results in macroscopic two phenomena we can see during the crush of the absorber: a flare due to interlaminar delamination and a fragmentation of the composite in numerous debris. These ruptures coupled with the friction induced between the material and the support allow to absorb a greater or less amount of energy [1]. In order to

J. Niez (✉) · M. Ben Amara · J. Capelle · V. Bouchart · P. Chevrier
LEM3, ENIM, University of Lorraine, 1 route d'Ars Laquenexy,
CS 65820, 57078 Metz, France
e-mail: jeremy.niez@hotmail.fr

R. R. Ambriz et al. (eds.), *Proceedings of the 17th International Conference on New Trends in Fatigue and Fracture*, https://doi.org/10.1007/978-3-319-70365-7_3

maximize the number of breaks, different orientations of fibers, geometries and triggers (local overstressed areas) were chosen. First, it is important to note that since the 1990s, a large number of scientific studies have been carried out in order to exploit the capacity of composites to absorb a large amount of energy. However, these studies focus on thermosetting matrix composites [1]. For industrialization purposes, the use of thermoplastic matrix is preferred in this project. The majority of the studies also demonstrate a better energy absorption capacity for thermoplastic matrix composites than for thermosetting matrix composites [6].

It has therefore been decided to use a laminated composite of glass fibers and acrylic-based resin because of the interesting characteristics of its two constituents: high mechanical performance, processability, cost…

The use of triggers, to allow rupture in a specified area, will be tested, once the "basic" geometry have been determined. In the literature [4], the design of chamfer or a change of thickness on the system or the use of external triggers on the support side such as a conical guide is possible.

Materials

Two kinds of the glass/thermoplastic composite are studied: a unidirectional and a non-crimp fabric composite. Quasi-static (elongation rate of 10^{-3} s^{-1}) tensile tests have been carried out on a Zwick Z250 machine (Fig. 1) following the ISO 527-5 on 0°, 90° and 45° directions on 250 * 25 mm samples. Quasi-static compressive

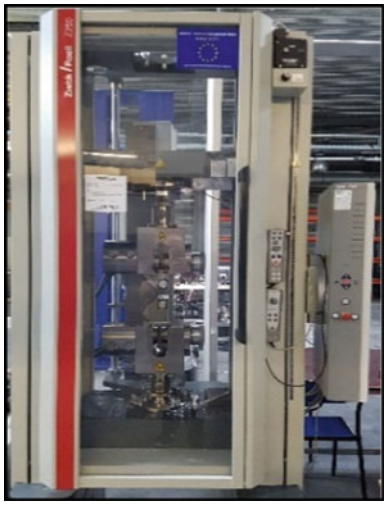

Fig. 1 Zwick Z250 test machine

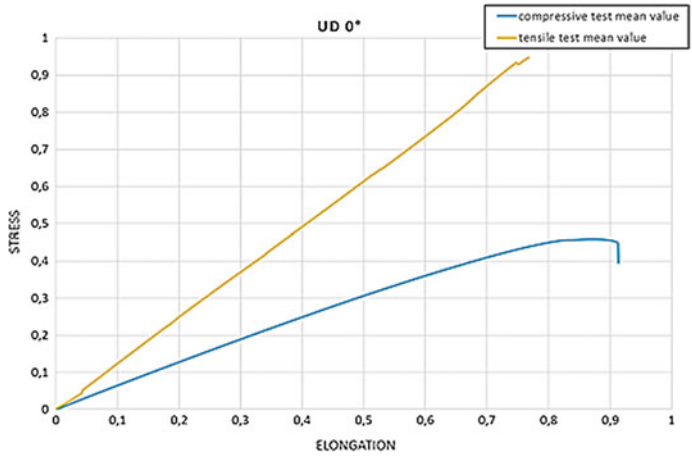

Fig. 2 Tensile and compressive test on UD 0° at 10^{-3} s^{-1} solicitation

tests have also been made according to the ASTM D3410/D3410M standard on the same three directions on 120 * 20 mm specimens. For these tests, unidirectional strain gauges have been used to measure the elastic deformation of the samples and so, to calculate the elastic compressive modulus on the three direction. Thanks to it, the mapping of the two versions of the composite has been established.

Besides the mechanical properties, the tensile and compressive tests also bring to light an interesting behavior of one of our glass reinforcements.

Under a compressive solicitation, with 0° oriented fibers, after a linear step, a sudden break is observed due to local bowings of the fibers (Fig. 2). On the contrary, ±45° non-crimp fabric allows the fibers and the matrix to deform: the fibers begin to move then the delamination between fibers and the matrix occurs; after that, ruptures in the matrix and fractures of the deformed fibers appeared. This behavior enables a greater deformation of the specimen under high stress level before global break.

Tensile tests actually show this interesting behavior of the [−45°/45°] non-crimp fabric in terms of energy absorption. Indeed, to optimize the amount of absorbed energy, the couple stress-strain has to be maximized. After a first linear phase, the non-crimp fabric version presents a second phase of pseudo-plastic behavior with an interesting stress level and an important strain grade (Fig. 3). The compression tests confirmed this behavior. Combination of multiple kinds of fractures allows the piece to absorb an important amount of energy.

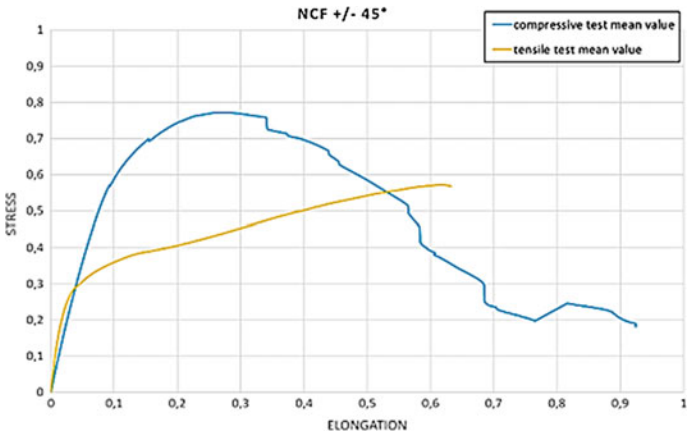

Fig. 3 Tensile and compressive test on NCF ±45° at 10^{-3} s^{-1} solicitation

Experimental Tests

Due to these results, a new phase of tests was made to compare NCF square section tubes and aluminum absorbers. On the Zwick Z250 machine, quasi-static compressive tests have been ruled on these structures to measure the amount of energy absorbed during the test and compare the behavior of the tubes. Dynamic solicitations (elongation rate of 10 s^{-1}) were also ruled on Zwick HTM 16020 machine (Fig. 4) to simulate realistic scenarios. To check the different phenomena of fracture during dynamic tests, a high-speed camera is used to take 30,000 pictures by second.

Fig. 4 Zwick Amsler HTM 16020 dynamic test machine

For quasi-static solicitation (Fig. 5), in terms of global behavior, a first initial peak is illustrated. The camera brings to light that this "peak" is corresponding to the initiation of the ruptures of the corners (fibers and matrix breaks) due to the swelling of the structure. The next phase corresponds to constant propagation of the fractures of the matrix, fiber ruptures and delamination between fiber and matrix. The last phase represents the increase of stress due to the compression of the resulting composite debris. These macro-fractures cause the early ruin of the specimen and so a low level of energy absorption.

With a dynamic solicitation, this 3-steps behavior is not clear (Fig. 6). Indeed, due the speed test, the material doesn't have time to deform and is forced to break several times; resulting in a larger number of small fractures (Fig. 7). However, the amount of absorbed energy is similar regardless of speed test.

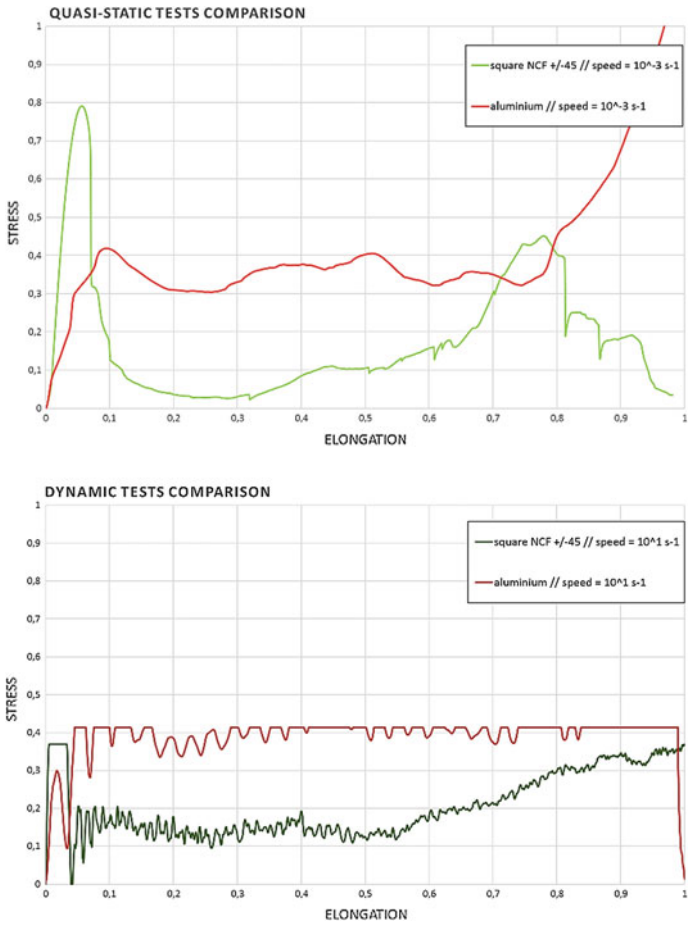

Fig. 5 Comparison of aluminum and NCF composite absorbers

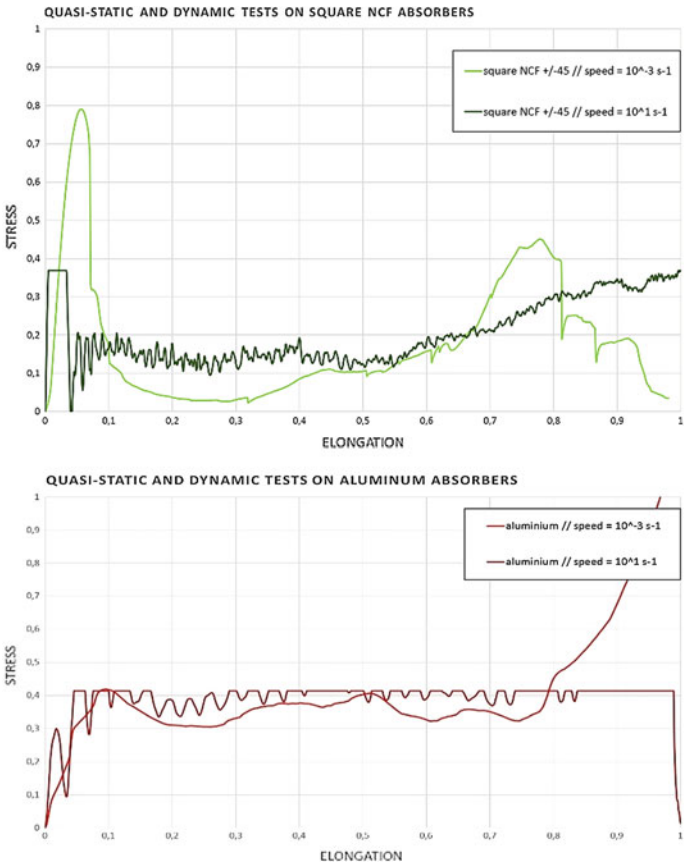

Fig. 6 Influence of speed of compressive tests on square section composites and aluminum tubes

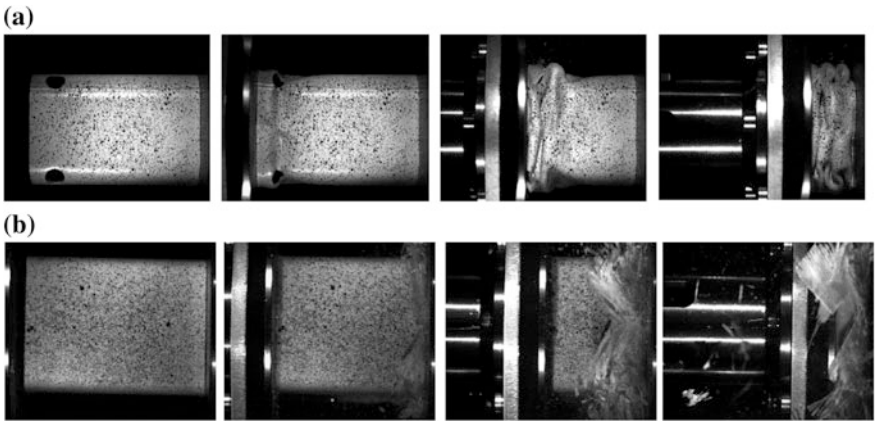

Fig. 7 Compressive test at 20 m s^{-1} on aluminum (**a**) and composite (**b**) specimen

In comparison of actual absorbers, the square system made of our NCF composite can absorb 25% less energy of the crash. As literature shows it, different triggers allow creating local over stressed areas and so bring best control of the start of fractures. The corners of the square sections act like triggers but they are not enough numerous to create a sufficient number of fractures.

Numerical Simulation

Thanks to the previous results, searching to maximize the fractures of the specimen, two geometries ("square-sinus" section called "proto 1" and "square-right angle" section called "proto 2") was developed through a numerical model on Abaqus. First, we check the precision of this model with the experimental results on square absorbers on dynamic solicitation (Fig. 8). The main observable difference is due to the limit of the sensor to record a high level of force during the initial peak during the experimental test.

Then, with the same model, we test the two geometries to see the influence of "corners" and so fractures on the absorption of energy. The behavior of the two "proto" absorbers is similar to the square absorber one, but the amount of energy is higher, that is to say about 15% more than aluminum absorber for the "proto 2" (Fig. 9).

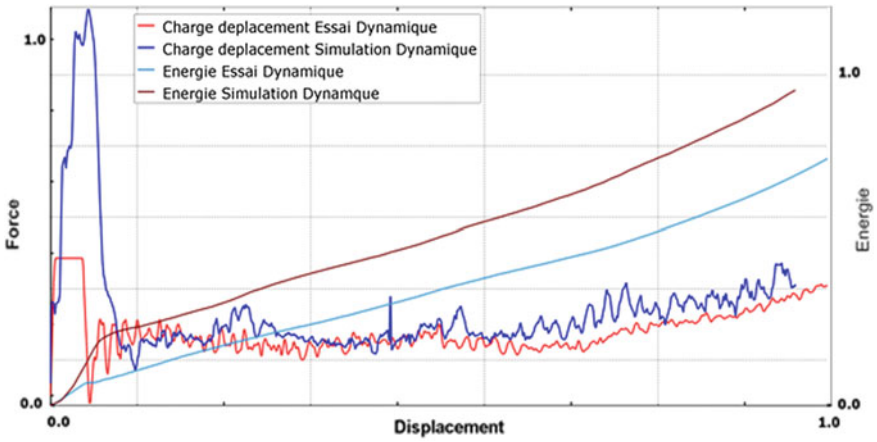

Fig. 8 Comparison of numerical model and experimental results

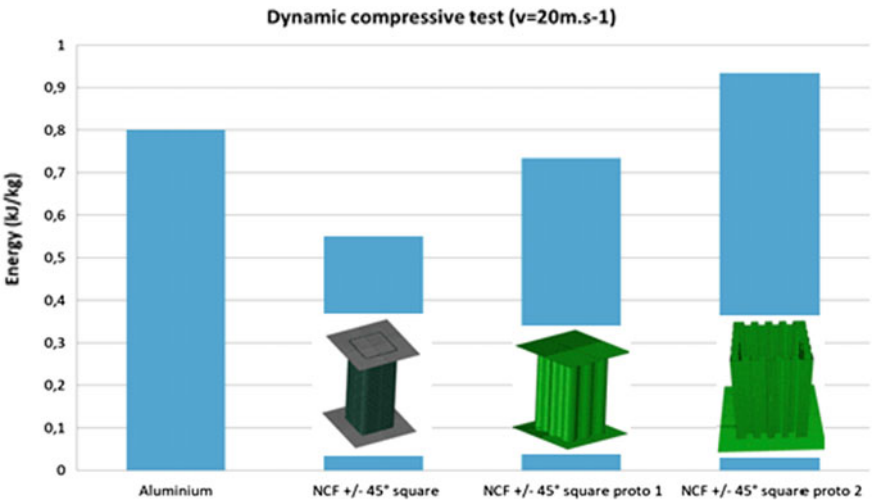

Fig. 9 Comparison of geometries

Discussions

As we have seen it above, the non-crimp fabric presents an interesting high level couple stress-elongation. Thanks to the number of different fractures and the level of elongation, the absorption of energy during compression of this material is really good. The geometry of the specimen has to enabling the full potential of this material. The "simple" square section brings macro-ruptures since the start of the tests and the specimen is rapidly ruined. New kinds of sections have been investigated numerically to allow a greater amount of energy absorption. Regarding these results, studies are still led to optimize the geometry with the possibility of the use of different kinds of triggers.

Acknowledgements The authors acknowledge the help of Project COMPAS funded by the European Union as part of the operational programme FEDER-FSE Lorraine et Massif des Vosges 2014–2020 in partnership with REHAU, Institut de Soudure Groupe and CINI for their support of this work.

References

1. **Abrate Serge.** Impact engineering of composite structures, Springer Science & Business Media, 2011. Vol. 526.
2. **Bonnet Bénédicte.** Comportement au choc de matériaux composites pour applications automobiles, Ph.D. dissertation/École Nationale Supérieure des Mines de Paris. 2005.

3. **Feraboli Paolo, Norris Chris and McLarty Doug.** Design and certification of a composite thin-walled structure for energy absorption, International journal of vehicle design. Inderscience Publishers, 2007. Vol. 44. pp. 247–267.
4. **Guillon Damien.** Etude des mécanismes dábsorption dnergie lors de lcrasement progressif de structures composites à base de fibre de carbone, Ph.D. dissertation. - 2008.
5. **Hamada H. [et al.].** Comparison of energy absorption of carbon/epoxy and carbon/PEEK composite tubes, Composites. 1992. Vol. 23. pp. 245–252.
6. **Hamada H., Ramakrishna S. and Satoh H.** Crushing mechanism of carbon fibre/PEEK composite tubes, Composites. 1995. Vol. 26. pp. 749–755.
7. **Haque A. and Ali M.** High strain rate responses and failure analysis in polymer matrix composites–an experimental and finite element study, Journal of composite materials. 2005. Vol. 39. pp. 423–450.
8. **Jacob George C. [et al.].** Energy absorption in polymer composites for automotive crashworthiness, Journal of composite materials. 2002. Vol. 36. pp. 813–850.

A New High-Cycle Fatigue Criterion Based on a Self-consistent Scheme for Hard Metals Under Non-proportional Loading

Kékéli Amouzou and Eric Charkaluk

Introduction

In the railway industry (axle, wheel, rail), the aeronautical industry (turbine blades, turbine disks), the petroleum industry (forge linings), the nuclear industry (pressurized water reactors) and the automotive industry (cylinder heads), the largest single cause of mechanical components failures is high-cycle fatigue (HCF). Initially, several empirical approach [1–4] taking as a starting point of the uniaxial HCF criteria, are elaborated to predict the fatigue limit. During the second half of the 20th century, Dang Van [5], thanks to Orowan's fatigue pioneering model, initiated the micro-macro fatigue criterion based on critical plane concept and the elastic shakedown theory. Empirical criteria and critical plane type criteria are integrated into solid fatigue designed tools (FemFat, Fe-Safe, MSC.Fatigue, nCode), widely used by fatigue design offices that offer solutions to several industries. Nevertheless, these criteria have mostly been elaborated in the case of proportional cyclic loads, and their use to design components under out-of-phase loading is generally unsatisfactory. In the latter case, the integral approach criteria of Papuga and Růžička [6], Liu-Zenner [7] and Papadopoulos [8, 9] gives better prediction. Among these integral criteria, only the Papadopoulos's criterion is based on micro-macro approach. This criterion is more optimal in terms of calculation time and the number of elementary tests to be carried out for the determination of its parameters. Furthermore, this criterion is reduced to a simple analytical formula when applied in the single frequency in phase or out-of-phase sinusoidal loading,

K. Amouzou (✉)
LML, CNRS UMR 8107, Laboratoire de Mécanique de Lille,
Polytech'Lille, Cité Scientifique 59650, Villeneuve d'Ascq, France
e-mail: kekeli.amazou@univ-lille1.fr

E. Charkaluk
LMS, CNRS UMR 7649, Laboratoire de Mécanique des Solides,
Ecole Polytechnique, Ecole Polytechnique, Route Saclay 91120, Palaiseau, France

R. R. Ambriz et al. (eds.), *Proceedings of the 17th International Conference on New Trends in Fatigue and Fracture*, https://doi.org/10.1007/978-3-319-70365-7_4

which avoids errors resulting from compute integrals in multiple dimensions. However, this criterion, like most of high-cycle fatigue criteria, does not taking into account the material anisotropy which has a very great influence on fatigue [10].

In this paper, we propose to introduce the elastic anisotropy of crystals in the Papadopoulos's integral approach [11] by using the self-consistent scheme of Bui [12]. This scheme is the extension of Kröner's scheme to anisotropic materials. The predictions of the new criterion are compared with the experimental data for hard steels which microstructure contains ferrite inclusions.

A Two-Scale Approach for Polycrystals Fatigue

The Papadopoulos's integral criterion is based on the Lin-Taylor scheme which makes it possible to link the macroscopic stress tensor $\underset{\sim}{\boldsymbol{\Sigma}}$, the elastic strain tensor $\underset{\sim}{\boldsymbol{E}}$ of the representative elementary Volume $\boldsymbol{V}$ surrounding a point $\mathbf{O}$ to the mesoscopic stress tensor $\underset{\sim}{\boldsymbol{\sigma}}$, strain tensor $\underset{\sim}{\boldsymbol{\varepsilon}}$, strain plastic tensor $\underset{\sim}{\boldsymbol{\varepsilon}}^{\boldsymbol{p}}$ of the grain or crystal (see Fig. 1). Let us consider further a cut of $\boldsymbol{V}$, that is a plane $\boldsymbol{\Delta}$ passing though the point $\mathbf{O}$. This plane is defined by its unit normal $\underset{\sim}{n}$. Let us consider these less resistant crystals of $\boldsymbol{V}$ are so oriented that one of their easy glide planes coincide with $\boldsymbol{\Delta}$. The easy glide directions $\underset{\sim}{m}$ of these slip planes are directions of $\boldsymbol{\Delta}$. Any $\underset{\sim}{m}$ direction will be located through the angle χ, formed between $\underset{\sim}{m}$ and an arbitrary, but fixed on $\boldsymbol{\Delta}$, axis ξ, see Fig. 2 (see Dang Van and Papadopoulos [11]):

$$n_x = \sin\theta\cos\varphi \quad n_y = \sin\theta\sin\varphi \quad n_z = \cos\theta \tag{1}$$

$$\begin{aligned} &m_x = -\sin\varphi\cos\chi - \cos\theta\cos\varphi\sin\chi \quad m_y = \cos\varphi\cos\chi - \cos\theta\cos\varphi\sin\chi \\ &m_z = \sin\theta\sin\chi \end{aligned} \tag{2}$$

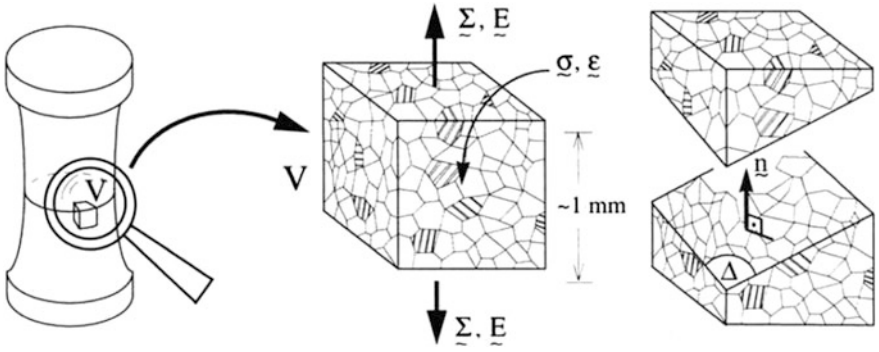

Fig. 1 Macroscopic and mesoscopic scales of material description [11]

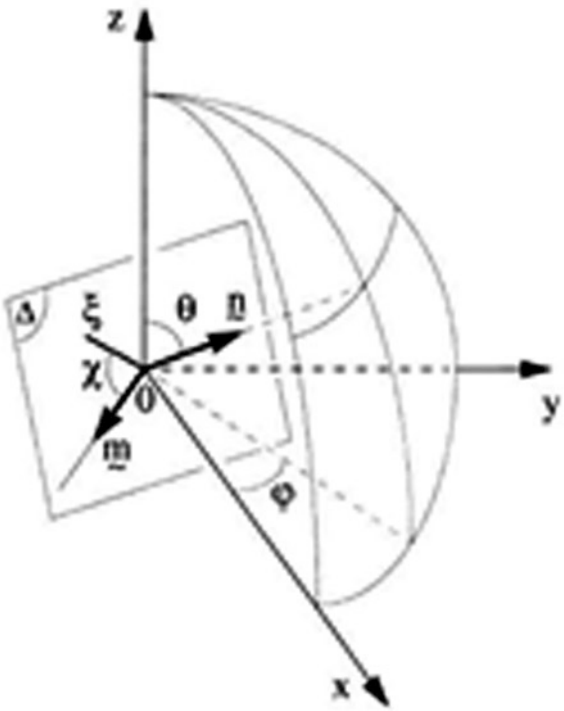

Fig. 2 Spherical coordinates (ϕ, θ) of n. Location of a glide direction m with the help of angle χ [11]

To extend this criterion to the case of anisotropic materials, we invoke Bui's self-consistent scheme [12]:

$$\underset{\sim}{\boldsymbol{\sigma}} = \underset{\sim}{\boldsymbol{A}} : \left[\underset{\sim}{\boldsymbol{\Sigma}} - 2\mu(1-\beta)\,\underset{\sim}{\boldsymbol{\varepsilon}}^{\boldsymbol{p}} \right] \tag{3}$$

where $\underset{\sim}{\boldsymbol{A}}$ the localization tensor is written:

$$\underset{\sim}{\boldsymbol{A}} = \left[\underset{\sim}{\boldsymbol{c}} : \left(\underset{\sim}{\boldsymbol{I}} + \underset{\sim}{\boldsymbol{P}} : (\underset{\sim}{\boldsymbol{c}} - \underset{\sim}{\boldsymbol{C}}) \right)^{-1} : (\underset{\sim}{\boldsymbol{C}})^{-1} \right] \tag{4}$$

With $\underset{\sim}{\boldsymbol{P}}$ the fourth order Hill tensor, under assumption of a spherical inclusion, is expressed as:

$$\underset{\sim}{\boldsymbol{P}} = f_1 \underset{\sim}{\boldsymbol{I}} - f_2 \underset{\sim}{\boldsymbol{J}} \tag{5}$$

with constants f_1, f_2 and the spherical $\underset{\sim}{\boldsymbol{J}}$ fourth order tensor, the deviator $\underset{\sim}{\boldsymbol{K}}$ fourth order tensor, the identity $\underset{\sim}{\boldsymbol{I}}$ fourth order symmetric identity tensor are written in the basis $\underset{\sim}{e_i} \otimes \underset{\sim}{e_j} \otimes \underset{\sim}{e_k} \otimes \underset{\sim}{e_l}$ (δ_{ij} is the Kronecker delta):

$$f_1 = \frac{3\lambda + 8\mu}{15\mu(\lambda + 2\mu)} \quad f_2 = \frac{3\lambda + 3\mu}{15\mu(\lambda + 2\mu)} \tag{6}$$

$$\underset{\sim}{\boldsymbol{J}} = \frac{1}{3}\delta_{ij}\delta_{kl}\underset{\sim}{e_i} \otimes \underset{\sim}{e_j} \otimes \underset{\sim}{e_k} \otimes \underset{\sim}{e_l} \quad \underset{\sim}{\boldsymbol{K}} = \underset{\sim}{\boldsymbol{I}} - \underset{\sim}{\boldsymbol{J}} \tag{7}$$

With $\underset{\sim}{\boldsymbol{c}}$ the elastic modulus of the inclusion is defined by three independent constants c_{11}, c_{12}, c_{44}:

$$\begin{aligned} \underset{\sim}{\boldsymbol{c}} = & \left[c_{12}\delta_{ij}\delta_{kl} + c_{44}(\delta_{ij}\delta_{jl} + \delta_{il}\delta_{jk})\right. \\ & \left. + (c_{11} - c_{12} - 2c_{44})\delta_{pi}\delta_{pj}\delta_{pk}\delta_{pl}\right]\underset{\sim}{e_i} \otimes \underset{\sim}{e_j} \otimes \underset{\sim}{e_k} \otimes \underset{\sim}{e_l} \end{aligned} \tag{8}$$

And $\underset{\sim}{\boldsymbol{C}}$ the macroscopic elastic modulus of $\boldsymbol{V}$ is defined as:

$$\underset{\sim}{\boldsymbol{C}} = 3k\underset{\sim}{\boldsymbol{J}} + 2\mu\underset{\sim}{\boldsymbol{K}} \tag{9}$$

With the k bulk, the μ shear and the λ Lamé's first modulus depend on the Young modulus E and the Poisson's ratio v of the material:

$$k = \frac{E}{3(1-2\nu)} \quad \mu = \frac{E}{2(1+\nu)} \quad \lambda = \frac{E\nu}{(1+\nu)(1-2\nu)} \tag{10}$$

Using this scheme, the integral criterion of Papadapoulos is extended to the anisotropic material by the following new criterion (Eqs. 11–21):

$$\sqrt{\langle K^2 \rangle} \leq \beta - \alpha_{ani}\Sigma_{H,ani} \tag{11}$$

where $\sqrt{\langle K^2 \rangle}$ the generalized anisotropic shear stress amplitude and $\Sigma_{H,ani}$ the quantity reflecting the effect of the hydrostatic stress amplitude $\Sigma_{H,a}$ and the mean value $\sqrt{\langle N_m^2 \rangle}$ of the normal stress $\underset{\sim}{N} = (\underset{\sim}{n} \cdot \underset{\sim}{\boldsymbol{\Sigma}} \cdot \underset{\sim}{n})\underset{\sim}{n}$ acting on $\boldsymbol{\Delta}$, are introduced as:

$$\sqrt{\langle K^2 \rangle} = \sqrt{5}\sqrt{\frac{1}{4\pi}\frac{1}{2\pi}\int_{\varphi=0}^{\varphi=2\pi}\int_{\theta=0}^{\theta=\pi}\int_{\chi=0}^{\chi=2\pi}(K(\varphi,\theta,\chi))^2 d\chi \sin\theta d\theta d\varphi} \tag{12}$$

$$\Sigma_{H,ani} = \zeta_1 \Sigma_{H,a} + \varpi \sqrt{\left| \frac{9\zeta_1}{10} \left[\frac{2}{\sqrt{3}} - \left(1 + \frac{f_{-1}}{5t_{-1}} \right) \left(\sin \varphi_{xx} + \sin \varphi_{yy} + \sin \varphi_{zz} \right) \right] \right| \sqrt{\langle N_m^2 \rangle}} \tag{13}$$

With $K(\phi, \theta, \chi)$ and $\sqrt{\langle N_m^2 \rangle}$ are given by:

$$\begin{aligned} K(\varphi, \theta, \chi) &= T_a(\varphi, \theta, \chi) \\ &+ \left(1 - \frac{\zeta_2}{\zeta_3} \right) \left(n_x m_x \Sigma_{xx,a} \sin \varphi_{xx} + n_y m_y \Sigma_{yy,a} \sin \varphi_{yy} + n_z m_z \Sigma_{zz,a} \sin \varphi_{zz} \right) \end{aligned} \tag{14}$$

$$\sqrt{\langle N_m^2 \rangle} = \sqrt{5} \sqrt{\frac{1}{4\pi} \int_{\varphi=0}^{\varphi=2\pi} \int_{\theta=0}^{\theta=2\pi} (N_m(\varphi, \theta))^2 \sin \theta d\theta d\varphi} \tag{15}$$

In the case of cyclic loading with period P, $T_a(\phi, \theta, \chi)$, $\Sigma_{H,a}$, and $N_m(\phi, \theta)$ are defined by:

$$T_a(\varphi, \theta, \chi) = \frac{1}{2} \left[\max_{t \in P} \left(\underset{\sim}{n} \cdot \underset{\sim}{\Sigma}(t) \cdot \underset{\sim}{m} \right) - \min_{t \in P} \left(\underset{\sim}{n} \cdot \underset{\sim}{\Sigma}(t) \cdot \underset{\sim}{m} \right) \right] \tag{16}$$

$$\Sigma_{H,a} = \frac{1}{2} \left[\max_{t \in P} \Sigma_H(t) - \min_{t \in P} \Sigma_H(t) \right] \tag{17}$$

$$N_m(\varphi, \theta) = \frac{1}{2} \left[\max_{t \in P} \left(\underset{\sim}{n} \cdot \underset{\sim}{\Sigma}(t) \cdot \underset{\sim}{n} \right) + \min_{t \in P} \left(\underset{\sim}{n} \cdot \underset{\sim}{\Sigma}(t) \cdot \underset{\sim}{n} \right) \right] \tag{18}$$

The anisotropic constants $\zeta_1, \zeta_2, \zeta_3$ are given by:

$$\zeta_1 = \frac{2c_{12} + c_{11}}{3kq_1} \quad \zeta_2 = \frac{c_{11} - c_{12}}{2\mu q_2} \quad \zeta_3 = \frac{c_{44}}{\mu q_3} \tag{19}$$

$$\begin{aligned} &q_1 = 1 + (f_1 - f_2)(2c_{12} + c_{11} - 3k) \quad q_2 = 1 + f_1(c_{11} - c_{12} - 2\nu) \\ &q_3 = 1 + 2f_1(c_{44} - \nu) \end{aligned} \tag{20}$$

To calculate the mean value of normal stress (Eq. 15), we choose to use L_2-norm. This choice requires using the sign symbol ϖ in the proposed criterion to take into account in the case of negative loads:

$$\varpi = \begin{cases} +1, & if\ \Sigma_{xx,m} + \Sigma_{xx,m} + \Sigma_{xx,m} \geq 0 \\ -1, & otherwise \end{cases} \tag{21}$$

The parameters β, α_{ani} are calculated by Eq. (22) using the fatigue limit in fully reversed torsion test t_{-1} and the fatigue limit in fully reversed bending (or fully reversed tension-compression) f_{-1} test:

$$\beta = t_{-1} \quad \alpha_{ani} = \frac{\left(3\frac{t_{-1}}{f_{-1}} - \sqrt{3}\right)}{\zeta_1} \tag{22}$$

Applications

The applications of the proposed HCF criterion Eq. (11) are performed in the bending–torsion ([13], Lempp data reported by Zenner et al. [13]) and biaxial–triaxial [14, 15] out-of-phase fatigue tests in the single frequency sinusoidal loading:

$$\Sigma_{ij}(t) = \Sigma_{ij,a} \sin\left(wt - \gamma_{ij}\right) + \Sigma_{ij,m} \quad i,j = 1,2,3 \tag{23}$$

where $w = \frac{2\pi}{P}$ is the frequency, P is the period, γ_{ij} is the phase difference, $\Sigma_{ij,a}$ is the amplitude and $\Sigma_{ij,m}$ is the mean value of Σ_{ij}.

By analogy to plasticity criterion, an equivalent stress can be introduced:

$$\Sigma_{eq} = \sqrt{\langle K^2 \rangle} + \alpha_{ani}\Sigma_{H,ani} \tag{24}$$

For the four fatigue tests, the error index I

$$I = \frac{\Sigma_{eq} - \beta}{\beta} \tag{25}$$

are calculated (see last column of Tables 1, 2, 3 and 4). If the fatigue index I below zero, the criterion predict safe domain or does not predict fracture. The relative error $|I|$ between the prediction of the proposed criterion and the fatigue test is the absolute value of I. For all simulations, the Poisson's ratio $\nu = 0.3$ and the elastic anisotropy coefficients $c_{11} = 230$ GPa, $c_{12} = 136$ GPa, $c_{44} = 117$ GPa are the same. These data are also summarized graphically in Fig. 3. In this figure, it can be observed that error $|I|$ is $\pm 10\%$, which shows that the proposed criterion is satisfactory.

In addition, attention was paid to the phase differ-ence of the shear stress on the proposed criterion by noting the values of Σ_{eq} in the case of Simbürger tests (Table 4). The Fig. 4 shows that Σ_{eq} does not change monotonically when γ_{xy}

Table 1 Zenner et al. [13] fatigue test data

Steel 34Cr4, E = 205 GPa, t_{-1} = 256 MPa, f_{-1} = 410 MPa								
	$\Sigma_{xx,a}$ (MPa)	$\Sigma_{xy,a}$ (MPa)	γ_{xy} (°)	$\Sigma_{xx,m}$ (MPa)	$\Sigma_{xy,m}$ (MPa)	$\sqrt{\langle K^2 \rangle}$ (MPa)	$\Sigma_{H,ani}$ (MPa)	I (%)
1	314	157	0	0	0	239.82	104.84	−0.55
2	315	158	60	0	0	240.91	104.17	−0.10
3	316	158	90	0	0	241.35	105.50	0.08
4	315	158	120	0	0	240.91	104.17	−0.10
5	224	224	90	0	0	258.65	74.07	5.15
6	380	95	90	0	0	239.08	125.67	0.37
7	316	158	0	0	158	241.35	187.34	4.68
8	314	157	60	0	157	239.82	186.16	4.02
9	315	158	90	0	158	240.91	187.01	4.50
10	279	140	0	279	0	217.94	218.96	−8.22
11	284	142	90	284	0	221.52	222.88	−6.70
12	355	89	0	0	178	223.45	210.73	−1.00
13	212	212	90	212	0	248.93	166.37	−0.99
14	129	258	90	0	0	268.53	42.66	7.27

Table 2 Lempp fatigue test data reported in Zenner et al. [13]

Steel 42CrMo4, E = 210 GPa, t_{-1} = 260 MPa, f_{-1} = 398 MPa								
	$\Sigma_{xx,a}$ (MPa)	$\Sigma_{xy,a}$ (MPa)	γ_{xy} (°)	$\Sigma_{xx,m}$ (MPa)	$\Sigma_{xy,m}$ (MPa)	$\sqrt{\langle K^2 \rangle}$ (MPa)	$\Sigma_{H,ani}$ (MPa)	I (%)
1	328	157	0	0	0	245.99	107.46	4.19
2	286	137	90	0	0	214.56	93.70	−9.13
3	233	224	0	0	0	261.29	76.33	7.30
4	213	205	90	0	0	239.06	69.78	−1.84
5	266	128	0	0	128	199.92	153.95	−9.38
6	283	136	90	0	136	212.58	163.70	−3.65
7	333	160	180	0	160	250.13	192.60	13.37
8	280	134	0	280	0	209.97	218.28	0.21
9	271	130	90	271	0	203.42	211.27	−2.93

Table 3 Mielke [14] fatigue test data

Steel 25CrMo4, E = 205 GPa, t_{-1} = 256 MPa, f_{-1} = 410 MPa										
	$\Sigma_{xx,a}$ (MPa)	$\Sigma_{xx,m}$ (MPa)	$\Sigma_{yy,a}$ (MPa)	$\Sigma_{yy,m}$ (MPa)	γ_{yy} (°)	$\Sigma_{xy,a}$ (MPa)	γ_{xy} (°)	$\sqrt{\langle K^2 \rangle}$ (MPa)	$\Sigma_{H,ani}$ (MPa)	I (%)
1	261	340	261	170	0	0	0	150.69	365.42	−7.62
2	275	340	275	170	60	0	0	201.64	221.98	4.40
3	240	340	240	170	90	0	0	203.20	185.00	2.43
4	196	340	196	170	180	0	0	196.00	194.27	−0.06
5	220	340	0	170	0	110	60	168.03	267.02	−7.09
6	233	340	0	170	0	117	90	178.28	271.32	−2.30
7	155	340	0	170	0	155	60	178.98	245.53	−3.84
8	159	340	0	170	0	159	90	183.60	246.85	−1.72

Table 4 Simbürger [15] fatigue test data

Steel CK45, E = 200 GPa, t_{-1} = 287 MPa, f_{-1} = 423 MPa									
	$\Sigma_{xx,a}$ (MPa)	$\Sigma_{xx,m}$ (MPa)	$\Sigma_{xy,a}$ (MPa)	$\Sigma_{xy,m}$ (MPa)	γ_{xy} (°)	$\sqrt{\langle K^2 \rangle}$ (MPa)	$\Sigma_{H,ani}$ (MPa)	Σ_{eq} (MPa)	I (%)
1	400	0	0	200	0	230.94	238.90	303.32	5.68
2	0	417	241	0	0	241.00	190.25	298.64	4.05
3	292	0	167	0	60	237.30	97.48	266.83	−7.03
4	304	0	174	0	90	247.15	101.48	277.89	−3.17
5	277	277	159	0	0	225.52	218.85	291.82	1.68
6	250	250	144	0	90	203.89	197.52	263.72	−8.10
7	285	0	163	163	0	231.61	181.01	286.45	−0.19
8	288	0	165	165	90	234.25	183.07	289.71	0.94

increases. It is deduced that the phase difference of the shear have no influence on the limiting fatigue endurance.

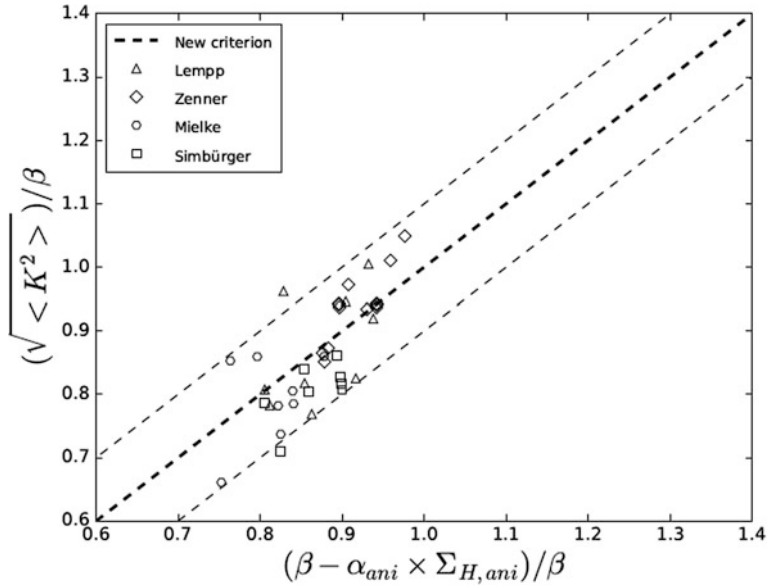

Fig. 3 Comparison of fatigue limits test data with the criterion prediction

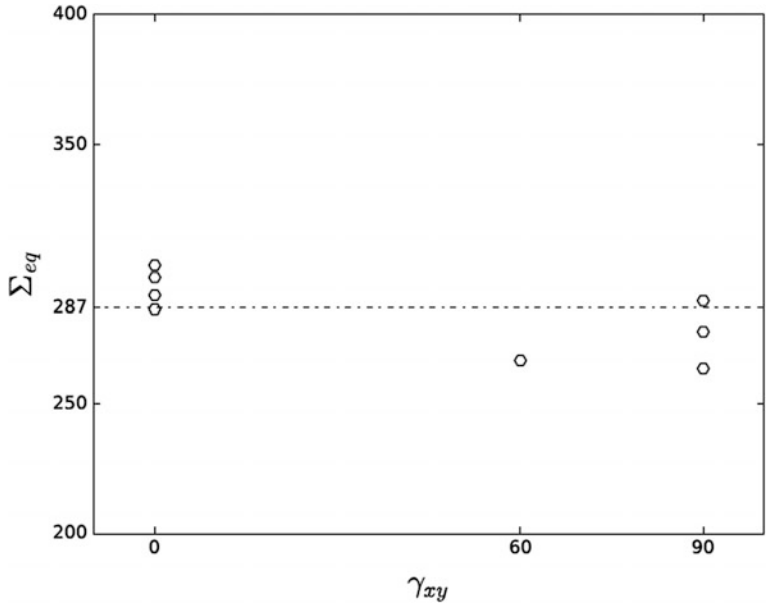

Fig. 4 Equivalent stress against phase difference for Simbürger test data

Conclusion

The extension of the HCF integral criterion of Papadopoulos to anisotropic materials has been proposed using the self-consistent scheme of Bui. The application of the new fatigue design criterion to hard steels under non-proportional loading is satisfactory. A first study of the effect of the phase difference of the shear stress on this criterion shows the no influence of this parameter on the limiting fatigue endurance, which is in good agreement with experimental observations. Other effects such as effects of frequency difference; mean normal stress, wave form and stress gradient will be studied later. The proposed criterion can be used to design rails, wheels, axles of highly anisotropic steels such as eutectoid R260 or R7T widely used in the railway industry.

Acknowledgements The authors gratefully acknowledge Ioannis Papadopoulos for very valuable advice on his fatigue integral criterion, Jan Papuga for fruitful discussion of the effect of normal stress. This work is part of the certification in virtual railway (CERVIFER) project and was supported by ADEME though the program "Véhicule du futur des investissements d'avenir".

References

1. Gough, H. J., Pollard, H. V. (1935). The Strength of Metals under combined Alternating Stresses. P. I. Mech. Eng., vol. 131, 3–103.
2. Stulen, F. B., Cummings, H. N. (1954). A failure Criterion for Multiaxial Fatigue Stresses. Proc. Am. Soc. Test. Mater., vol. 54, 822–835.
3. Crossland, B. (1956). Effect of Large Hydrostatic Pressures on the Torsional Fatigue Strength of an Alloy Steel. Proceedings of the International Conference on Fatigue of Metals, Institution of Mechanical Engineers, 138–149.
4. Sines, G. (1959). Behavior of Metals under Complex Static and Alternating Stresses. In Metal Fatigue, Sines G. and Waisman J.L. Editors, McGraw Hill, 145–169.
5. Dang Van, K. (1973). Sur la résistance à la fatigue des métaux. Thèse de Doctorat ès Sciences. Science et Techniques de l'Armement, vol. 47, 647–722.
6. Papuga, J., Růžička, M. (2008). Two new multiaxial criteria for high cycle fatigue computation. Int. J. Fatigue, vol. 30, pp. 58–66.
7. Liu, J., Zenner, H. (2003). Fatigue limit of ductile metals under multiaxial loading. In Carpinteri A, de Freitas M, Spagnoli A, editors. Biaxial/multiaxial fatigue and fracture, ESIS 31. Amsterdam: Elsevier, 63–147.
8. Papadopoulos, I. V. (1994). A new criterion of fatigue strength for out-of-phase bending and torsion of hard metals. Int. J. Fatigue, vol. 16, pp. 377–384.
9. Papadopoulos, I. V. (1995). A high-cycle fatigue criterion applied in biaxial and triaxial out-of-phase stress conditions. FFEMS, vol. 18, pp. 79–91.
10. Robert, C., Saintier, N., Palin-Luc, T., Morel, F. (2012). Micro-mechanical modelling of high cycle fatigue behaviour of metals under multiaxial loads. Mechanics of Materials, vol. 55, 112–129.
11. Dang Van, K., Papadopoulos, I. V. (1999). High-Cycle Metal Fatigue: from theory to appli cations. Springer-Verlag Wien GmbH, n 392, pp. 89–143.
12. Bui, H. D. (2006). Fracture Mechanics: Inverse Problems and Solutions. Solid mechanics & its applications, Springer, vol. 139.

13. Zenner, H. and Heidenreich, R. and Richter, I. Z. (1985). Dauerschwingfestigkeit bei nichtsynchroner mehrachsinger beanspruchung. Werkstofftech, vol. 16, 101–112.
14. Mielke, S. (1980). Festigkeitsverhalten metallischer Werkstoffe unter zweiachsiger schwingender Beanspruchung mit verschiedenen Spannungszeitverläufen. Disse., TH Aachen, Germany.
15. Simbürger, A. (1975). Festigkeitsverhalten zäher Werkstoffe bei einer mehrachsigen, phasenverschobenen Schwingbeanspruchung mit körperfesten und veränderlichen Hauptspannungsrichtungen. LBF, Bericht Nr. FB-121, Darmstad, Germany.

Characterization and Evaluation of a Railway Wheel Steel in the HCF and VHCF Regimes

Henrique Soares, Pedro Costa, Mário Vieira, Manuel Freitas and Luís Reis

Introduction

Fatigue studies are of the utmost importance for any system subjected to dynamic loadings. This type of failure is one of the most common and unpredictable and may happen in any range from low to very high number of cycles [1]. Therefore, acknowledging the material fatigue resistance provides a more reliable and secure mechanical system, structure or component. Several fatigue tests may be produced depending on the type of loading and on the number of cycles of interest. For the low cycle fatigue (LCF) and high cycle fatigue (HCF) regimes, conventional servo-hydraulic machines are usually used, where the rate of cycle application is not very high (below 50 Hz) but easily applicable and controllable. In the very high cycle fatigue (VHCF) regime, between 10E6 and 10E9 cycles, a conventional machine would take an unpractical time to achieve sample fracture. Therefore, an ultrasonic fatigue testing machine may be used, as the ones applied in [2–4].

In ultrasonic fatigue testing, a specimen is excited at its natural frequency in order to achieve high stresses on a certain high frequency setting. Mason was the first researcher to achieve a working system in 1950 [4], establishing the frequency standard of this fatigue testing method of 20 kHz. Since then, many researchers have worked in the development of new types of ultrasonic fatigue testing in the VHCF regime. Bathias is one of the most renown researchers of the field due to his high number of contributions, whereas many can be read on his book [5].

In this work, a railway wheel material is set under evaluation using both conventional and ultrasonic fatigue testing in order to evaluate its response on the two fatigue regimes. The HCF regime was studied using the servo-hydraulic machine with standardized specimens for the first one. For the VHCF regime, an ultrasonic

H. Soares · P. Costa · M. Vieira · M. Freitas · L. Reis (✉)
IDMEC, Instituto Superior Técnico, Universidade de Lisboa,
Av. Rovisco Pais, 1, 1049-001 Lisbon, Portugal
e-mail: luis.g.reis@tecnico.ulisboa.pt

R. R. Ambriz et al. (eds.), *Proceedings of the 17th International Conference on New Trends in Fatigue and Fracture*, https://doi.org/10.1007/978-3-319-70365-7_5

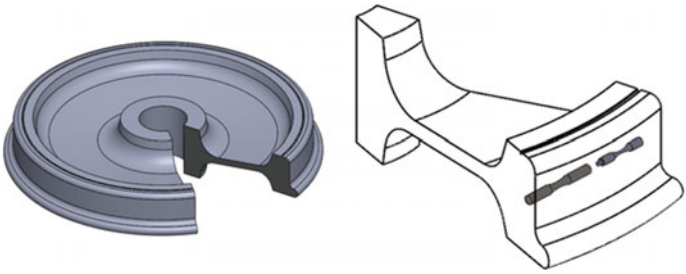

Fig. 1 Representation of the specimen's location on the railway wheel

fatigue machine with a specimen specifically designed to have a natural frequency of 20 kHz, for the second one. All the material specimens were machined from the railway wheel, as shown in Fig. 1.

Materials and Methods

The component in study is a worn-out railway wheel that was supposedly fabricated according to the EN_13262+A1-2009 standard. The material's Young Modulus and density were also evaluated. The machined that was used for conventional testing is an Instron 8874 equipped with a 25 kN load cell.

While loads are directly applied on a specimen in the conventional fatigue testing, the ultrasonic fatigue testing imposes a free vibration condition on the specimen. A piezoelectric transducer capable of inducing vibrations around 20 kHz is used. This transducer is connected to a booster, a horn and then to the material specimen, as it can be observed in Fig. 2. The booster and the horn are also projected to have a similar natural frequency at around 20 kHz, with their purpose being to amplify the displacement provided by the transducer. The specimen has a throat that promotes stress concentration and guarantees the achievement of relevant stresses using the low power ultrasonic transducer. This ultrasonic fatigue testing system used was created at Instituto Superior Técnico, at the IDMEC laboratories [6].

The control method also differs between both testing machines. While the servo-hydraulic controls the force or the displacement applied on the specimen, the ultrasonic testing controls the power induced on the piezoelectric transducer or the displacement on the free end of the specimen using a vibrometer, as showed in Fig. 2.

In order to define a specimen geometry with a natural frequency of 20 kHz, the differential equation for general three-dimensional isotropic elastic body is developed—Eq. (1), thus having:

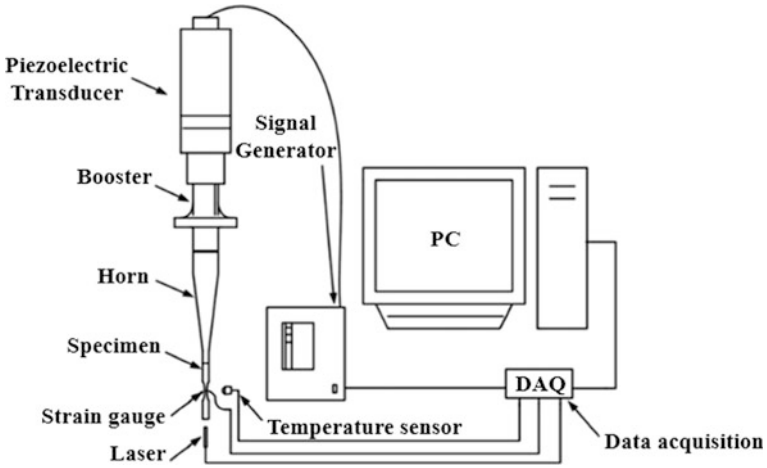

Fig. 2 Ultrasonic fatigue test scheme

Fig. 3 Ultrasonic specimen's dimensions

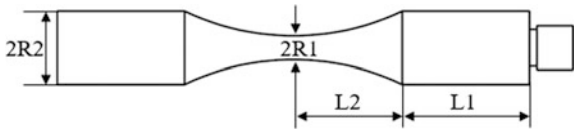

$$U''(x) + \frac{S'(x)}{S(x)} U'(x) + k^2 U(x) = 0 \tag{1}$$

where U(x) is the displacement at x, U′(x) is the speed at position x, U″(x) is the acceleration at position x, k is the wave vector, S is the cross-sectional area at position x and S′ is the rate of change of area at position x.

Considering a hyperbolic throat profile, and following the parameters according to Fig. 3, Eq. (1) results in:

$$\begin{cases} y(x) = R_2, \ L_2 < |x| < L \\ y(x) = R_1 \cosh(\alpha x), \ |x| < L_2 \end{cases} \tag{2}$$

where y is the diameter of specimen at position x and:

$$L = L_1 + L_2 \tag{3}$$

$$\alpha = \frac{1}{L_2} \operatorname{arccosh}\left(\frac{R_2}{R_1}\right) \tag{4}$$

Using the boundary conditions in Eq. (3), the specimen's resonance length is obtained through Eq. (5):

$$L_1 = \frac{1}{k}\arctan\left[\frac{1}{k}\left(\beta\coth(\beta L_2) - \alpha\tanh(\alpha L_2)\right)\right] \tag{5}$$

where:

$$\beta = \sqrt{\alpha^2 - k^2} \tag{6}$$

A hyperbolic profile is used to simplify the equation. The error between both profiles for the general size of the specimens is negligible, being around 1.8%, as Bathias shows in his book [5]. The chosen dimensions and the calculated terms are presented in Table 1.

After the analytical calculation of the specimen's geometry, a finite element analysis is conducted in order to check the resonance frequency, allowing also for geometry improvements. The specimen for the conventional fatigue test follows the standard ASTM E606 (2003) for axial fatigue tests. Figure 4 shows both specimens' final geometries and the correspondent dimensions.

In the conventional servo-hydraulic test, force control method was applied whilst, or the ultrasonic test, a displacement control method was used. In order to transform the force applied by the conventional machine to resulting stress, the Hook law was applied by measuring the smallest cross section radius of the specimen with a caliper. For the ultrasonic test, the highest stress was calculated through Eqs. (7) and (8):

$$\begin{cases} \varepsilon(x) = A_0\varphi(L_1, L_2)\frac{[\beta\cosh(\beta x)\cosh(\alpha x) - \alpha\sinh(\beta x)\sinh(\alpha x)]}{cosh^2(\alpha x)} \\ \sigma(x) = E_d A_0\varphi(L_1, L_2)\frac{[\beta\cosh(\beta x)\cosh(\alpha x) - \alpha\sinh(\beta x)\sinh(\alpha x)]}{cosh^2(\alpha x)} \end{cases}, \quad |x| \le L_2 \tag{7}$$

Being A_0 the measured displacement, E_d the dynamic modulus of elasticity and $\varphi(L_1, L_2)$:

Table 1 Chosen dimensions and calculated terms

R1 (mm)		R2 (mm)		L2 (mm)	
1.5		5.0		30.0	
α	β	w(rad/s)	c	k	L1 (mm)
124.921	122.461	125663.7	5094.47	24.97	15.15

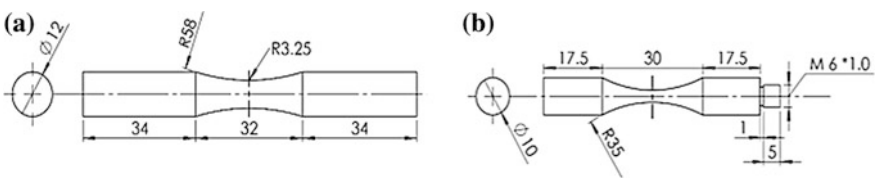

Fig. 4 **a** Conventional fatigue specimen. **b** Ultrasonic fatigue specimen

$$\varphi(L_1, L_2) = \frac{\cos(kL_1)\cosh(\alpha L_2)}{\sinh(\beta L_2)} \tag{8}$$

All the equations related to the ultrasonic axial test presented in this paper are explained in detail on the Bathias book [5].

Results and Discussion

The number of cycles necessary for fracture the specimen were registered for every tested specimen. With these results, an S-N curve was plotted, see Fig. 5. Figure 6 shows the fracture surface and the crack initiation site highlighted by an arrow and as an illustrative example of both tests, on the HCF and VHCF regimes. Figure 7 shows the materialography results in two different magnifications in order to evaluate the grain structure. Through the observation of the Fig. 7b, a ferrite-perlite structure was found.

Final Remarks

In this work, a material retrieved from a worn-out rail wheel was tested regarding its mechanical properties and fatigue behavior. An S-N fatigue curve was obtained for the material using two different methods: a conventional fatigue testing machine in HCF and another one with an ultrasonic testing machine in VHCF, both at the uniaxial stress state.

The fracture surfaces of the specimens obtained from both types of tests are considerably similar and, even using a microscope, the difference is not clear. In both specimens, crack initiation occurred on the surface of the specimen.

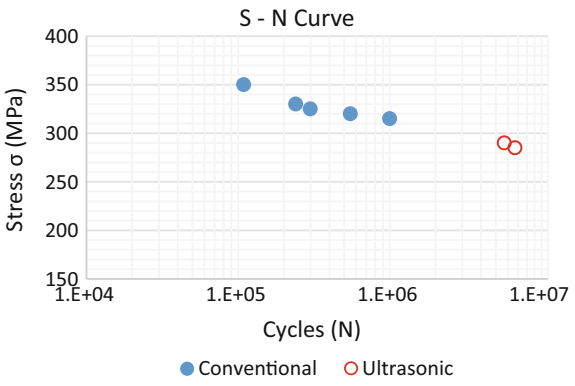

Fig. 5 S-N curve

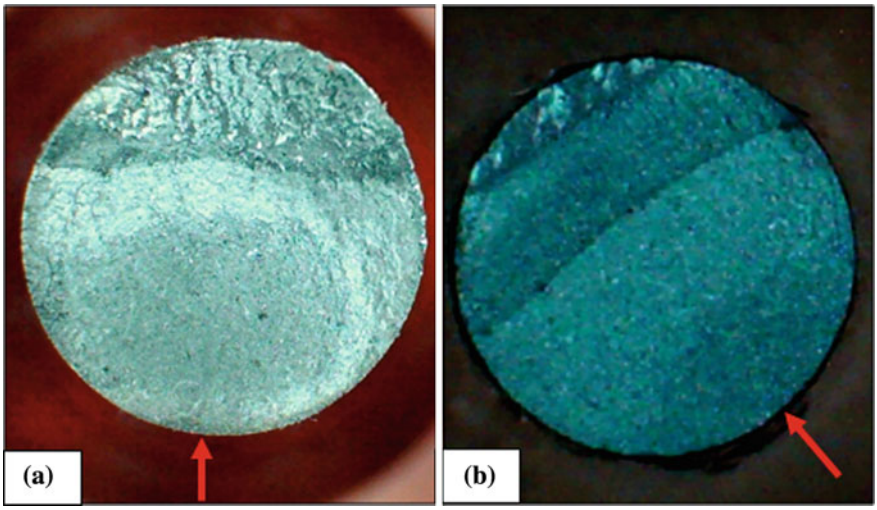

Fig. 6 Fracture surface and crack initiation site highlighted by an arrow: **a** conventional fatigue. **b** Ultrasonic fatigue

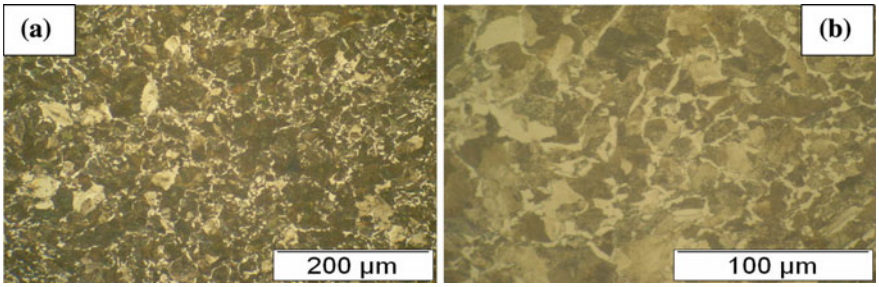

Fig. 7 Microscopy results. **a** 200x and **b** 500x

Further work is being carried out on fatigue characterization, namely on the production of a more detailed S-N uniaxial curve at both regimes, HCF and VHCF. The composition of the material will be assessed and a comparison will be made between the present material and the respective Standard. Moreover, fatigue tests regarding biaxial stress states will also be performed.

Acknowledgements This work was supported by FCT, through IDMEC, under LAETA, project UID/EMS/50022/2013. Financial support from Portuguese Fundação para a Ciência e Tecnologia (FCT) is acknowledged through Project PTDC/EMS-PRO/5760/2014.

References

1. Bathias, C. (1999). There is no infinite fatigue life in metallic materials. Fatigue Fract Engng Mater Struct, 22, 559–565.
2. Mayer, H. (2006). Ultrasonic torsion and tension-compression fatigue testing: Measuring principles and investigation on 2024–T351 aluminium alloy. International Journal of Fatigue, 28, 1446–1455.
3. Marines, I., Dominguez, G., Baudry, G., Vittori, J.-F., Rathery, S., Doucet, J.-P. & Bathias, C. (2003). Ultrasonic fatigue yesys on bearing steel AISI-SAE 52100 at frequency of 20 kHz and 30 kHz. International Journal of Fatigue, 28, 1037–1046.
4. Bathias, C. (2006). Piezoelectric fatigue testing machines and devices. International Journal of Fatigue, 28, 1438–1445.
5. Bathias, C., & Paris, P. C. (2005). Gigacycle Fatigue in Mechanical Practice (1st ed.). New York: Marcel Dekker.
6. Vieira, M., Reis, L., Freitas, M., Ribeiro, A. (2016) Strain measurements on specimens subjected to biaxial ultrasonic fatigue testing, Theoretical and Applied Fracture Mechanics 85, 2–8.

High-Temperature Low Cycle Fatigue Resistance of Inconel 713LC Coated with Novel Thermal Barrier Coating

Ivo Šulák, Karel Obrtlík, Ladislav Čelko, David Jech and Pavel Gejdoš

Introduction

Inconel 713LC was developed in the early 1950s and is still widely used in power generators especially because of favourable price in conjunction with satisfying properties such as high-temperature fatigue and creep resistance and surface stability. Incessant call for more efficient high-temperature facilities can be satisfied by an increase in operating temperature. The importance of surface protection against high-temperature and hostile environment thus increases rapidly. The substrate surface can be modified in several different ways. Diffusion coatings based on simple and modified aluminides are widely used and thoroughly investigated type of coatings with excellent corrosion and oxidation resistance [1–5]. However, these coatings do not fully meet industrial requirements. Thermal barrier coating (TBC) systems combine the corrosion and oxidation resistance with temperature insulation [6–9]. They comprise mainly a metallic CoNiCrAlY bond coat (BC) and a ceramic insulating top coat (TC) [10] mostly based on yttria-stabilized zirconia (YSZ). Even though YSZ TBC coatings are known for decades, only a little work has been done to investigate their impact on fatigue properties of substrate material [11–13]. Moreover, their effect on fatigue life is disputable. Effect of YSZ coating on low cycle fatigue of Inconel 713LC was studied by Obrtlík et al. [12]. The results showed the insignificant effect of the coating on the fatigue life in Coffin-Manson representation and the decrease of fatigue life in Basquin representation. Study of Kuba et al. [14] reported the beneficial effect of TBC coating on

I. Šulák (✉) · K. Obrtlík
Institute of Physics of Materials, Academy of Sciences of the Czech Republic, Žižkova 22, 616 62 Brno, Czech Republic
e-mail: sulak@ipm.cz

L. Čelko · D. Jech · P. Gejdoš
CEITEC—Central European Institute of Technology, Brno University of Technology, Purkyňova 123, 612 00 Brno, Czech Republic

R. R. Ambriz et al. (eds.), *Proceedings of the 17th International Conference on New Trends in Fatigue and Fracture*, https://doi.org/10.1007/978-3-319-70365-7_6

the fatigue life of Inconel 738LC. On the other hand, Ray et al. [11] showed the detrimental impact of TBC coating on C263 superalloy in the high stress amplitude domain and positive effect for low strain amplitudes. Recently, a promising family of eutectic oxide TBCs has stepped into the scope of interest [15–18]. Fatigue data on the eutectic TBC are, however, very rare. Obrtlík et al. [17] reported the fatigue behaviour of Inconel 713LC coated with $ZrO_2 + SiO_2 + Al_2O_3$ eutectic TC. Obtained results showed higher fatigue life in high strain amplitudes and negligible effect of TBC in lower strain amplitudes compared to uncoated Inconel 713LC.

This article is devoted to high-temperature low cycle fatigue resistance of Ni-based superalloy Inconel 713LC coated with complex thermal barrier coating system. The present results are a part of a more complex research program aiming to the development of modern and advanced TBC systems for aero and industrial applications. Fatigue behaviour of substrate material Inconel 713LC with and without TBC coatings has been studied [12, 17, 19–23].

Material Characterization

Nickel-based superalloy Inconel 713LC was supplied by PBS Velká Bíteš, a.s. in the form of button-end samples made by investment casting. The chemical composition of used melt in wt% is as follows: 11.98Cr–4.1Mo–0.06C–6.4Al–0.59Ti–1.82Nb–0.05Ta–0.06Zr–0.008B–bal. Ni. The substrate material is typical of a coarse dendritic structure with average grain size of 0.66 mm, set by linear intersection. Casting defects and shrinkage pores were present. Microstructure consists of γ matrix channels, γ' precipitates, $\gamma + \gamma'$ eutectics and carbides evenly distributed within interdendritic areas and at grain boundaries (Fig. 1a). Prior to the deposition of TBC coating, 10 specimens were grit blasted with alumina particles (Al_2O_3). Rough surface obtained by grit blasting provides higher mechanical bonding of TBC coating. It was proven that this process has the insignificant effect on the low cycle fatigue life at elevated temperature [20]. Figure 1b represents BSE image of TBC coating of the as-sprayed specimen. TBC system consists of CoNiCrAlY BC deposited by air plasma spraying and a ceramic TC sprayed with water stabilized plasma spraying. Insulating TC is a mixture of conventional YSZ (8% wt. Y_2O_3) and a eutectic nanocrystalline ceramic Eucor made of zirconia (ZrO_2), alumina (Al_2O_3) and silica (SiO_2)—in the ratio of 50/50 wt%. The average thickness of BC and TC found by image analysis system StreamMotion was 201 and 215 μm, respectively. Small pores and cracks are present in the TBC coating and it is believed to enhance its strain tolerance [9]. The porosity of the TC and BC is 4.3 and 0.6%, respectively. Microstructural investigations were accomplished by means of the scanning electron microscope (SEM—TESCAN Lyra3 XMU) equipped with the energy dispersive X-ray (EDX) spectroscopy analyser.

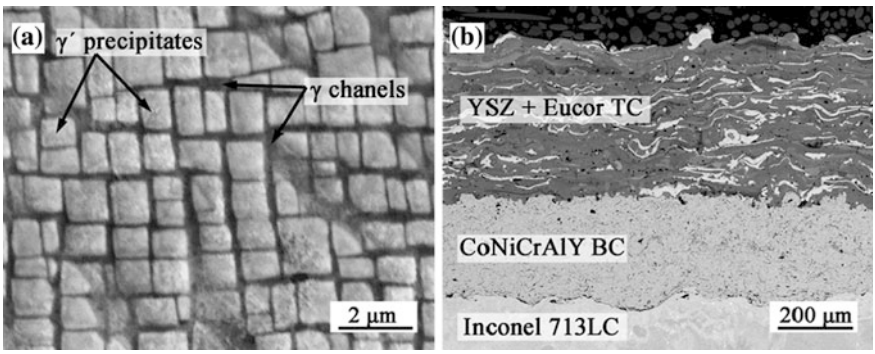

Fig. 1 **a** SEM micrograph of γ′ precipitates ($L1_2$) coherently embedded in the disordered γ matrix; **b** BSE image of YSZ + (ZrO_2 + Al_2O_3 + SiO_2) + CoNiCrAlY thermal barrier coating

Low Cycle Fatigue Tests Specification

Low cycle fatigue tests were performed on servo-hydraulic testing machine MTS 810 in fully reversed triangular wave form ($R_\varepsilon = -1$) under total strain control conditions with the constant strain rate of 2×10^{-3} s^{-1} at 900 °C in air. The tests were carried out on cylindrical specimens with the gauge length and diameter of 15 and 6 mm, respectively. We used 9 specimens in as-cast condition and 10 specimens sprayed with TBC coating. Heating was provided by three zone resistance furnace. The temperature was controlled by three thermocouples attached to an end of the gauge length and to both ends of the specimen. The temperature gradient within the gauge length of the specimen was ±1.5 °C. The total strain was controlled with sensitive extensometer with 12 mm long base. The extensometer equipped with 11.7 cm long ceramic tips was placed outside the furnace and air cooled to avoid the influence of high temperature. Details of high-temperature low cycle fatigue testing and tests evaluation could be found elsewhere [17].

Results and Discussion

Microstructure Stability

Polished cross sections of selected specimens representing the whole fatigue lifetime range were observed in order to reveal substrate and TBC degradation under high-temperature cyclic loading. Strengthening γ′ precipitates having an $L1_2$ crystallographic structure are coherently embedded in the disordered fcc γ matrix as shown in Fig. 1a. The application of a macroscopic external strain during high-temperature low cycle fatigue tests involves an anisotropic misfit relaxation led by dislocations motion. This process results in microstructural instability of γ′

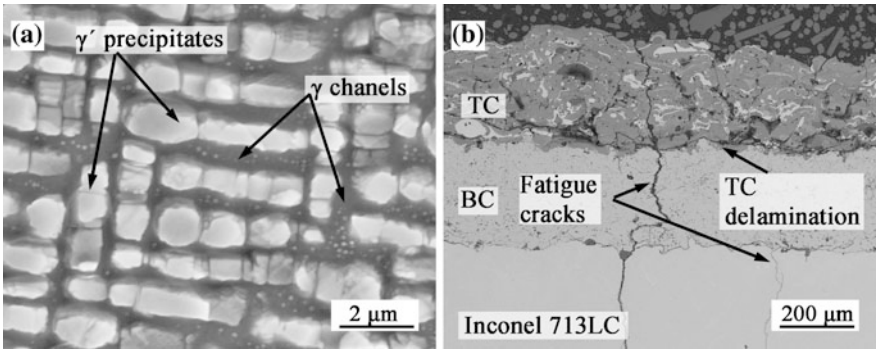

Fig. 2 Polished sections of a specimen fatigued to failure at 900 °C (ε_a = 0.40%, σ_a = 346 MPa) **a** Rafting of γ′ strengthening precipitates; **b** delamination and cracking of TBC coating

strengthening precipitates called rafting. SEM micrograph (Fig. 2a) of a metallographic section of specimen fatigue to failure with sprayed TBC coating shows well developing directional γ′ rafting. The similar degradation of microstructure was observed in all examined specimens. Cubic γ′ precipitates are effective obstacles that prevent movement of dislocations. Directional coarsening of γ′ precipitates decreases the ability to prevent dislocations movement. Dislocations mobility is higher and thus macroscopic mechanical properties are decreased. High-temperature degradation of TBC coating is mostly connected with increasing internal stresses that are attributed to the formation of thermally growth oxides (TGO) at the TC/BC interface [24, 25]. As a consequence of TGO formation delamination of the ceramic TC in the vicinity of TC/BC occurred as shown in Fig. 2b. Fatigue crack initiation from the TC surface occurred frequently. These cracks are mostly stopped at the TC/BC or BC/substrate interface and only some of them break through to the substrate material. Fatigue cracks grow perpendicular to the loading axis. As a general trend with an increase in strain amplitudes, the number of cracks increases as well as a diversity of crack initiation sites [26, 27]. The number of cracks per millimetre in coated Inconel 713LC is approximately 10 times higher compared to uncoated superalloy.

Cyclic Stress Response

The diagram of the stress amplitude versus the number of elapsed cycles shown in Fig. 3 depicts the stress response of coated and uncoated Inconel 713LC during cyclic loading at 900 °C. The cyclic hardening/softening curves vary with the strain amplitude, and they are similar in both the coated and the uncoated material. Low amplitude cycling results in the saturated stress response, while weak softening up

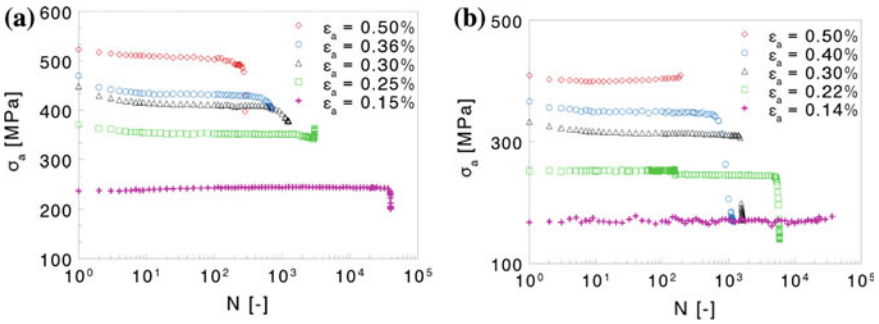

Fig. 3 Hardening/softening curves **a** uncoated and **b** TBC coated Inconel 713LC

to the end of the fatigue life is found in the high amplitude domain. Cyclic softening, the decrease in stress amplitude with the number of elapsed cycles, is connected with changes of γ' morphology.

Fatigue Life

Plastic strain amplitude ε_{ap} versus N_f is plotted in bilogarithmic representation in Fig. 4a. The values of ε_{ap} were established as the half-width of the hysteresis loop at half-life. Experimental data were fitted by the Coffin-Manson law:

$$\log 2N_f = \left(\frac{1}{c}\right)\log \varepsilon_{ap} - \left(\frac{1}{c}\right)\log \varepsilon'_f \tag{1}$$

with ε'_f being the fatigue ductility coefficient and c is the fatigue ductility exponent. The parameters were evaluated by regression analysis using least squares fitting. Values of ε'_f and c for uncoated (coated) Inconel 713LC are 0.294 ± 0.081 (0.178 ± 0.114) and -0.796 ± 0.033 (-0.709 ± 0.072), respectively. Data

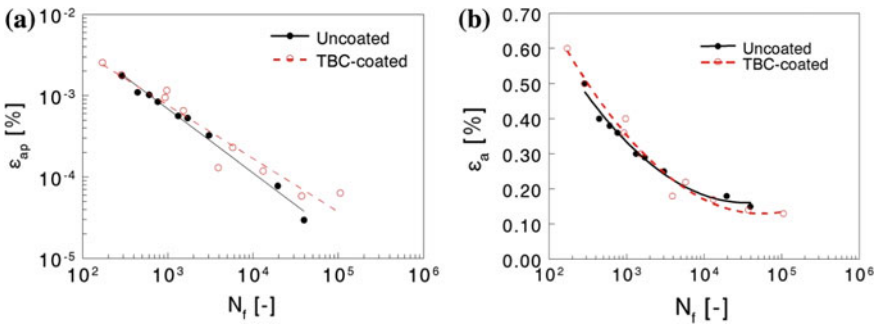

Fig. 4 **a** Coffin-Manson fatigue life curves; **b** Fatigue life curves in total strain representation

presented in Fig. 4a show a positive impact of complex TBC coating on fatigue life for low amplitudes and the curves meet each other at high amplitude domain. Increasing trend in fatigue life can be seen with the decrease in total strain amplitude. A higher number of cracks in the coated Inconel 713LC promotes a homogeneous distribution of plastic strain. The plastic strain is evenly distributed over the full gauge length and it is not only concentrated in highly localized areas. Therefore, the fatigue life of the coated superalloy can increase in this representation compared to the uncoated material [17, 27].

The diagram represented by the plot of ε_a versus N_f (Fig. 4b) is the basic fatigue life curve because ε_a was kept constant during high-temperature low cycle fatigue tests. The numbers of cycles to failure for both coated and uncoated Inconel 713LC are very close. The minor beneficial effect can be observed in high amplitudes and vice versa is valid for low amplitudes. The transient number of cycles is 3647.

Conclusions

High-temperature low cycle fatigue resistance of TBC coated and uncoated Inconel 713LC has been studied. The main conclusions can be drawn as follows:

(a) The application of a macroscopic external cyclic loading at 900 °C resulted in directional coarsening of γ' strengthening precipitates.
(b) Microstructural changes of substrate material are responsible for weak cyclic softening throughout the whole fatigue life.
(c) The complex TBC coating has a positive effect on fatigue life in the strain control test conditions. The Coffin-Manson curve shows the longer fatigue life. The total strain representation shows the transient number of cycles.

Acknowledgements The present research was financially supported by the grant No. 15-20991S of the Czech Science Foundation (GACR).

References

1. Kianicová M, Kafrík J, Trník J (2016) Degradation of Aluminide Coatings Deposited on Nickel Superalloys. Procedia Eng 136:346–352. doi:https://doi.org/10.1016/j.proeng.2016.01.221
2. Obrtlík K, Pospíšilová S, Juliš M, et al (2011) Low cycle fatigue behavior of cast superalloy Inconel 713LC with Al coating at 800 °C. Key Eng Mater 452–453:265–268. doi:www.scientific.net/KEM.452-453.265
3. Juliš M, Obrtlík K, Pospíšilová S, et al (2012) Influence of Al-Si diffusion coating on low cycle fatigue properties of cast superalloy Inconel 738LC at 800 °C. Key Eng Mater 488–489:307–310. doi:www.scientific.net/KEM.488-489.307
4. Obrtlík K, Pospíšilová S, Juliš M, et al (2012) Fatigue behavior of coated and uncoated cast Inconel 713LC at 800 °C. Int J Fatigue 41:101–106. doi:j.ijfatigue.2011.12.010

5. Slámečka K, Pokluda J, Kianicová M, et al (2013) Fatigue life of cast Inconel 713LC with/without protective diffusion coating under bending, torsion and their combination. Eng Fract Mech 110:459–467. doi:10.1016/j.engfracmech.2013.01.001
6. Padture NP, Gell M, Jordan EH (2002) Thermal Barrier Coatings for Gas-Turbine Engine Applications. Science 296:280. doi:https://doi.org/10.1126/science.1068609
7. Padture NP (2016) Advanced structural ceramics in aerospace propulsion. Nat Mater 15:804–809. doi:https://doi.org/10.1038/nmat4687
8. Ghasemi R, Vakilifard H (2017) Plasma-sprayed nanostructured YSZ thermal barrier coatings: Thermal insulation capability and adhesion strength. Ceram Int 43:8556–8563. doi:https://doi.org/10.1016/j.ceramint.2017.03.074
9. Liu JH, Liu YB, He X, Liu L (2016) Study on TBCs insulation characteristics of a turbine blade under serving conditions. Case Stud Therm Eng 8:250–259. doi:https://doi.org/10.1016/j.csite.2016.08.004
10. Bose S (2007) Chapter 7—Thermal Barrier Coatings (TBCs). In: High Temp. Coat. Butterworth-Heinemann, Burlington, pp 155–232
11. Ray AK, Dwarakadasa ES, Das DK, et al (2007) Fatigue behavior of a thermal barrier coated superalloy at 800 °C. Mater Sci Eng A 448:294–298. doi:https://doi.org/10.1016/j.msea.2006.10.035
12. Obrtlík K, Hutařová S, Čelko L, et al (2014) Effect of thermal barrier coating on low cycle fatigue behavior of cast Inconel 713LC at 900 °c. Adv Mater Res 891–892:848–853. doi:www.scientific.net/AMR.891-892.848
13. Chen ZB, Wang ZG, Zhu SJ (2011) Thermomechanical fatigue behavior of an air plasma sprayed thermal barrier coating system. Mater Sci Eng A 528:8396–8401. doi:https://doi.org/10.1016/j.msea.2011.08.031
14. Kuba S, Kojima Y, Suzuki H (2006) Effect of Thermal Barrier Coating Layer on HIP Treated IN738LC Fatigue Characteristic. Key Eng Mater 306–308:109–114. doi:www.scientific.net/KEM.306-308.109
15. Su H, Zhang J, Yu J, et al (2011) Rapid solidification and fracture behavior of ternary metastable eutectic Al2O3/YAG/YSZ in situ composite ceramic. Mater Sci Eng A 528:1967–1973. doi:https://doi.org/10.1016/j.msea.2010.11.046
16. Chráska T, Hostomský J, Klementová M, Dubský J (2009) Crystallization kinetics of amorphous alumina–zirconia–silica ceramics. J Eur Ceram Soc 29:3159–3165. doi:https://doi.org/10.1016/j.jeurceramsoc.2009.05.020
17. Obrtlík K, Čelko L, Chráska T, et al Effect of alumina-silica-zirconia eutectic ceramic thermal barrier coating on the low cycle fatigue behaviour of cast polycrystalline nickel-based superalloy at 900 °C. Surf Coat Technol. doi:https://doi.org/10.1016/j.surfcoat.2017.03.003
18. Ekström M, Thibblin A, Tjernberg A, et al (2015) Evaluation of internal thermal barrier coatings for exhaust manifolds. Surf Coat Technol 272:198–212. doi:https://doi.org/10.1016/j.surfcoat.2015.04.005
19. Petrenec M, Obrtlík K, Polák J (2005) Inhomogeneous dislocation structure in fatigued INCONEL 713 LC superalloy at room and elevated temperatures. Mater Sci Eng A 400–401:485–488. doi:https://doi.org/10.1016/j.msea.2005.01.058
20. Šulák I, Obrtlík K, Čelko L (2016) High Temperature Low Cycle Fatigue Characteristics of Grit Blasted Polycrystalline Ni-Base Superalloy. Key Eng Mater 665:73–76. doi:www.scientific.net/KEM.665.73
21. Šulák I, Obrtlík K, Čelko L (2016) Comparative Study of Microstructure and High Temperature Low Cycle Fatigue Behaviour of Nickel Base Superalloys Inconel 713LC and MAR-M247. Key Eng Mater 713:86–89. doi:www.scientific.net/KEM.713.86
22. Kunz L, Lukáš P, Konečná R (2010) High-cycle fatigue of Ni-base superalloy Inconel 713LC. Int J Fatigue 32:908–913. doi:https://doi.org/10.1016/j.ijfatigue.2009.02.042
23. Horník V, Šmíd M, Hutař P, et al (2017) Interaction of Creep and High Cycle Fatigue of IN 713LC Superalloy. Solid State Phenom 258:595–598. doi:www.scientific.net/SSP.258.595

24. Slámečka K, Čelko L, Skalka P, et al (2015) Bending fatigue failure of atmospheric-plasma-sprayed CoNiCrAlY + YSZ thermal barrier coatings. Int J Fatigue 70:186–195. doi:https://doi.org/10.1016/j.ijfatigue.2014.09.009
25. Hernandez MT, Karlsson AM, Bartsch M (2009) On TGO creep and the initiation of a class of fatigue cracks in thermal barrier coatings. Surf Coat Technol 203:3549–3558. doi:https://doi.org/10.1016/j.surfcoat.2009.05.018
26. Hutařová S, Obrtlík K, Juliš M, et al (2014) Degradation of TBC coating during low-cycle fatigue tests at high temperature. Key Eng Mater 592–593:461–464. doi:www.scientific.net/KEM.592-593.461
27. Šulák I, Obrtlík K, Čelko L, Gejdoš P (2017) Degradation of YSZ/EUCOR TBC Coating System during High Temperature Low Cycle Fatigue Tests. Solid State Phenom 258:420–423. doi:www.scientific.net/SSP.258.420

The Effect of Pearlite Banding on the Mechanical Anisotropy of Low Carbon Steel

M. Beltrán, J. L. González, D. I. Rivas, Felipe Hernández and Héctor Dorantes

Introduction

The API-5L pipe-line steel, used to hydrocarbon transportation, is usually regarded as an isotropic and homogeneous material. However, the steel shows directionality and orientation dependence on the mechanical properties. This anisotropic behavior can lead to an incorrect or overestimated results, in the assessments of mechanical integrity.

Generally, the mechanical behavior of the steel is related directly to its manufacturing processes and the resulting microstructural properties; such as inclusion content, microstructural heterogeneities and crystallographic texture [1]. In low carbon steel, with ferrite-pearlite microstructure, the pearlitic phase alignment is presented in banding form along the rolling direction, which represents microstructural anisotropy in the material [2]. Moreover, an oriented microstructure with elongated grains has been shown to cause variations in the tensile and impact properties according to the direction relative to the elongated structure [3]. This behavior is more pronounced in ductile fracture regime [4]. On the other hand, previous studies on pipeline steel suggest that crystallographic textures have an important function on toughness anisotropy; however, detailed discussions about the relationship between crystallographic textures and anisotropic fracture toughness are rare [5].

Nowadays, special attention has been paid to the fracture behavior, due to its importance in safety design of pipelines and pressure vessels [6]. However, the

M. Beltrán (✉) · J. L. González · D. I. Rivas · H. Dorantes
Instituto Politécnico Nacional, ESIQIE-IPN, GAID-IPN, UPALM Edif.7 Planta baja, Av. Instituto Politécnico Nacional s/n, 07738 Col. Lindavista, CDMX, Mexico
e-mail: mabz_2205@hotmail.com

F. Hernández
Instituto Politécnico Nacional, ESIME Unidad Azcapotzalco, Av. Las Granjas 682, Santa Catarina, 02250 Del. Azcapotzalco, Ciudad de México, CDMX, Mexico

R. R. Ambriz et al. (eds.), *Proceedings of the 17th International Conference on New Trends in Fatigue and Fracture*, https://doi.org/10.1007/978-3-319-70365-7_7

fracture analysis criteria considers the material as isotropic and homogenous. Hence, this consideration leave out the anisotropy in the fracture behavior of the steel and can compromise the safety of the component [7]. Therefore, it is necessary to understand the mechanical behavior of API-5L steel integrally and adequately describe it, in order to produce safe structures and pipelines of low cost and high efficiency.

The objective of this work is to determine the effect of the pearlite banding on the anisotropic mechanical behavior of two API-5L steels, as well as correlate the microstructural and crystallographic features to the variation in the mechanical properties between a low banded and a high banded steel.

Materials and Methods

Chemical Composition

The evaluated steels were named as S-A and S-B, which were extracted from two API X46 steel tubes. The nominal diameters were 24 in and a wall thickness of 0.875 and 1 in respectively. The experimental chemical composition obtained can be seen in Table 1.

Microstructural Analysis

The Microstructure was evaluated in the longitudinal direction by optical microscopy (OM) and by electron backscattered diffraction (EBSD) using Oxford HKL system incorporated on a field emission scanning electron microscope 7000F JEOL. The specimens were prepared according to the standard procedures contained in ASTM E-3 [8]. The data were interpreted by CHANNEL5 analysis software provided by Oxford Instruments HKL.

Tensile Tests

Tensile specimens were prepared as illustrated in Fig. 1, according to sheet type specimen contained in the ASTM E-8 [9] standard. The specimens were orientated

Table 1 Chemical composition table

Chemical composition of api-5 l steel (wt%)						
Element	Fe	C	Mn	P	S	Ti
S-A	98.0	0.117	1.05	0.019	0.019	0.001
S-B	98.1	0.175	1.27	0.044	0.018	0.002

API-5L X46 steel

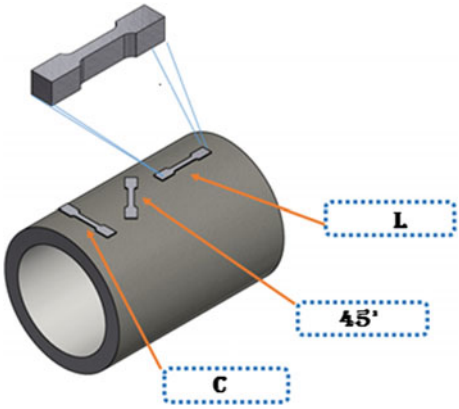

Fig. 1 Orientation of the tensile tests samples

in the longitudinal (L), 45° and circumferential (C) directions. The tests were conducted at ambient temperature and humidity, using crosshead speed of 5 mm min−1 using a 10t Shimadzu machine.

Charpy Impact Tests

Charpy impact tests were performed on V-notch specimens (CVN), with a 10 mm × 10 mm × 55 mm size each with a 2 mm-deep V-notch, according to ASTM E-23 [10]. Figure 2 shows the specified orientations of the specimens in the L, 45° and C directions. The tests were conducted in ambient temperature of 28 °C.

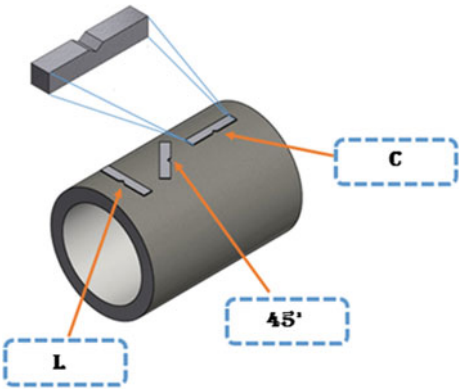

Fig. 2 Orientation of CVN impact tests specimens

Results and Discussion

Microstructure

Figure 3a, b shows an optical micrograph of the inclusions content of the API-5L X46 steel in the longitudinal, section. It can be seen the type and distribution of the inclusions, with the presence of non-metallic particles with spherical shape.

Figure 4 shows the microstructure of the API-5L X46 steel in the L section etched by 3% NITAL.

The microstructure is composed of ferrite grains and pearlite colonies which exhibited the characteristic banded microstructure of low carbon steels after rolling

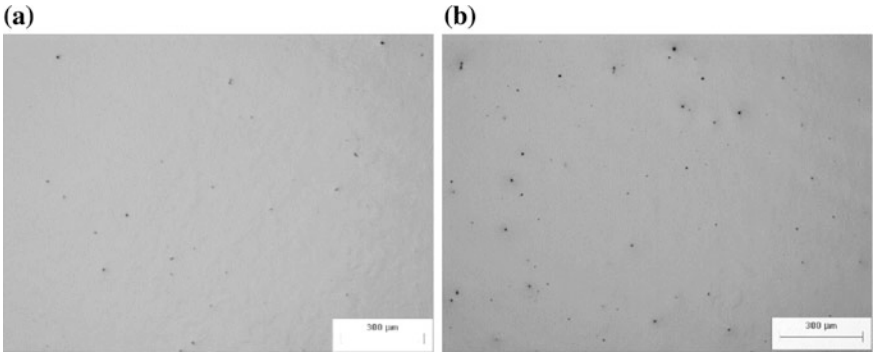

Fig. 3 Inclusions content in the longitudinal section of the API-5L X46 steel. **a** S-A, **b** S-B

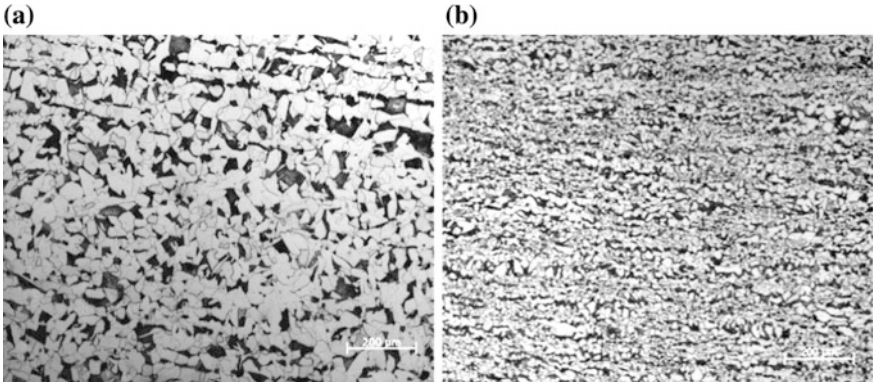

Fig. 4 Ferrite-pearlite microstructure of the TA and TB steels in the longitudinal section. **a** S-A, **b** S-B

Table 2 API-5L X46 microstructural characteristics of S-A and S-B samples

Sample	A_i	Ω_{12}	SB	Grain size G	% Inclusion	% Ferrite	% Pearlite
S-A	1.50	0.24	3.54	6.4	0.035	85.11	14.87
S-B	4.08	0.065	0.98	9.2	0.20	59.09	40.91

and recrystallization. Banding is associated with chemical segregation, particularly manganese, inherited from the solidification stage and spread into layers by the rolling deformation. Manganese is known to play a prominent role in the development of bands because transformation to allotriomorphic ferrite occurs first in Mn-depleted regions so that the residual austenite becomes enriched in carbon, to transform subsequently into pearlite depending on the rate of cooling experienced by the steel. The banding degree (A_i) and microstructure orientation grade (Ω_{12}) were calculated for the three sections according to the ASTM E-1268-99 standard [11]. Results indicate that longitudinal section has a low banding degree but, in comparison, in the transversal and normal sections there is a random and not-oriented distribution of the microstructure. The sample has an almost homogeneous grain size in all sections, just with a slight increase in the longitudinal section. The pearlite fraction content is larger in the longitudinal section than in transversal and normal sections. The quantitative analysis of the microstructural characteristics of the steel is presented in Table 2, this results were calculated for the three directions.

Texture Analysis

The texture analysis was realized by the CHANNEL5 software. Figure 5 shows the obtained results for the experimental measurements of the 45° ODF section for the API-5L X46 steel S-A and S-B. According to results, for both samples, it is observed an almost isotropic random texture typical of a hot rolled low carbon steel [12].

EBSD Analysis

The results of the EBSD analysis of the API-5L X46 steel, in the longitudinal section, are provided in Fig. 6 for the S-A and S-B samples. It can be seen the color coded orientation map along with the inverse pole figure from which a qualitative view of texture cam be made.

From the inverse pole figures, it can be seen that in both sections the sample orientation distribution do not favour the formation of preferential orientations of notable manner and that there is not an orientations clustering.

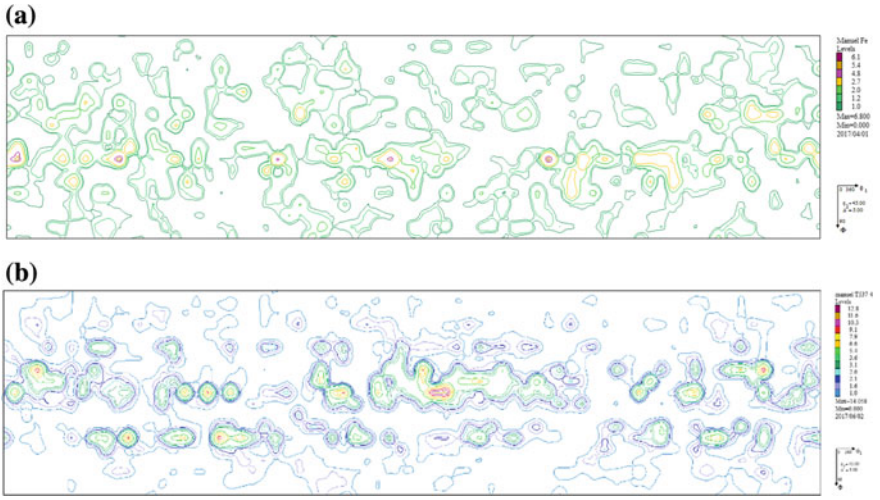

Fig. 5 The ODF 45° section for the API-5L X46 steel. **a** S-A, **b** S-B

Tensile Properties

Room-temperature tensile properties were obtained as listed in Table 3.

The both steels showed a yield strength (Ys) over 339 MPa (49 ksi), satisfying the strength requirements of API X46 grade pipeline steel. According to the tensile tests, the C direction has the higher yield and tensile strengths than the L direction, but lower elongation. On the other hand, he C direction does not show the yield point phenomenon, whereas the L direction do. Kim et al. [13] explained the yield behavior in terms of presence and amount of secondary phases contained in the acicular ferrite structure. They reported that the quasi-continuous yield behavior occurred with increasing volume fraction of the polygonal ferrite.

Charpy Impact Properties

Charpy impact tests results, of all the specimens in the longitudinal and circumferential orientations, are shown in Table 4. The CVN energy in the CL direction is lower than the LC direction. According to the CVN results, the fracture toughness values ($K_{IC–CV}$) were calculated in order to estimate the fracture resistance difference between the CL and LC directions, it could be seen a ($K_{IC–CV}$) difference larger than 10%.

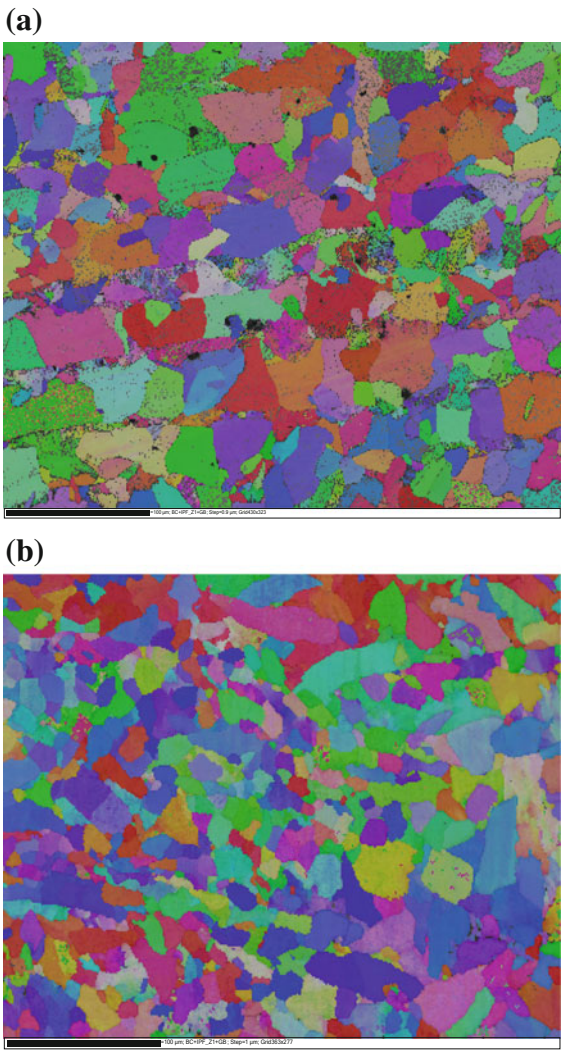

Fig. 6 Color coded map, longitudinal section of API-5L X46 steel. The results are presented relative to the normal direction (ND) and rolling direction (RD). **a** S-A, **b** S-B

Table 3 Tensile mechanical properties of API-5L X46 steel for S-A and S-B samples

Direction	Ys (MPa)	UTS (MPa)	% Elongation	UTS/ Ys
S-A				
L	339	504	35.3	1.48
45°	396	516	35.7	1.30
C	428	533	32.3	1.80
S-B				
L	354	534	37.9	1.50
45°	335	521	36.3	1.31
C	422	557	33.4	1.54

Table 4 CVN energy and ($K_{IC–CV}$) results in the L, 45° and C crack propagation directions within the API-5L X46 steel

Direction	Charpy impact energy (J)	
	S-A	S-B
L	299	113
45°	346	155
C	357	151

Conclusions

A low and a high banding degree steels, with API-5L grade X46 specification, were evaluated. It was observed that a higher degree of microstructural banding results in lower fracture toughness values. Although the two steels are X46 specification and met the tensile strength requirements, the fracture toughness variation between the less bare steel and the more bare steel is up to 50%. In contrast, the properties of uniaxial tension do not present significant variations, since the differences between steels are around 5%.

The steels presented anisotropy in their mechanical properties amongst directions. It was observed that both tensile and fracture toughness vary to approximately 30%. For both properties (tension and fracture toughness), the L direction has the lowest values. This behaviour was observed in the two studied steels. The yield stress varies between 10 and 25% amongst directions, while fracture toughness varies between 6 and 24%.

Acknowledgements The authors would like to acknowledge the National Polytechnic Institute (IPN), the National Council of Science and Technology (CONACYT) and the Analysis Integrity of Pipelines Group (GAID-IPN) for the support to carry out this research.

References

1. Joo M.S, Suh D.-W., and JBhadeshia H (2013). "Mechanical anisotropy in steels for pipelines". Iron and Steel Institute of Japan International Journal. Vol. 53, pp. 1305–1314.
2. Joo M.S., Suh D.-W., Bae J.H., and JBhadeshia H. (2012). Role of delamination and crystallography on anisotropy of Charpy toughness in API-X80 steel. Materials Science and Engineering A, Vol. 546, pp. 314–322.
3. Zong C., Zhu G., and Mao W (2013). Effect of crystallographic texture on the anisotropy of Charpy impact behaviour in pipeline steel". Materials Science and Engineering A. Vol. 563, pp. 1–7.
4. A. Ghosh, S. Sahoo, M. Ghosh, D. Chakrabarti (2014). Effect of microstructural parameters, microtexture and matrix strain on the Charpy impact properties of low carbon HSLA steel containing MnS inclusions. Materials science and engineering A. Vol 613, pp 37–47.
5. Xiao-Long Y., Xu Y., Xiao-Dong T. and Wu D (2015). Relationships among crystallographic texture, fracture behaviour and Charpy impact toughness in API X100 pipe-line steel. Materials Science and engineering A. Vol 641, pp. 96–106.

6. Jorge Luis González Velázquez (2013). Mecánica de fractura 2a edición. Limusa editorial. México.
7. Jorge Luis González Velázquez (2017). Fractografía y análisis de fallas. Author edition, Mexico.
8. ASTM (2011). Methods for preparation of metallographic specimens ASTM E-3. American Society of Testing Materials Standards Handbook. Philadelphia, USA, pp. 1–12.
9. ASTM (2013). Standard Test Methods for Tension Testing of Metallic Materials ASTM E-8. American Society of Testing Materials Standards Handbook. Philadelphia, USA, pp. 1–28.
10. ASTM (2012). Standard test methods for Charpy impact test of metallic materials ASTM E-23. American Society of Testing Materials Standards Handbook. Philadelphia, USA, pp 1–25.
11. ASTM (1999). Standard practice for assessing de degree of banding or orientation of microstructures ASTM E1268–99. American Society of Testing Materials Standards Handbook. Philadelphia, USA, pp. 1–29.
12. Engler O. and Randle V. Introduction to texture analysis, macrotexture, microtexture and orientation mapping 2nd edition.
13. Y. M. Kim, S. K. Kim, Y. J. Lim, N. J. Kim (2002). Effect of Microstructure on the Yield Ratio and Low Temperature Toughness of Linepipe Steels. Iron and Steel Institute of Japan. Vol. 42, pp. 1571–1577.

Analysis of Mechanical Behavior of the Underlying Soft Tissue to Ischial Tuberosities Using Finite Element Method

Diana Alicia Gayol-Mérida, Víctor Manuel Araujo-Monsalvo, José de Jesús Silva-Lomelí, Víctor Manuel Domínguez-Hernández, Marcos Martínez-Cruz, Elisa Martínez-Coría, Martín Luna-Méndez and Aylenid Alemán-Pérez

Introduction

Pressure injuries according to National Pressure Ulcer Advisory are defined as "a localized damage to the skin and/or underlying soft tissue usually over a bony prominence or related to a medical or other device. The injury can present as intact skin or an open ulcer and may be painful. The injury occurs as a result of intense and/or prolonged pressure or pressure in combination with shear. The tolerance of soft tissue for pressure and shear may also be affected by microclimate, nutrition, perfusion, co-morbidities and condition of the soft tissue" [1].

Patients with neurological problems that disrupt the sensitivity and mobility are prone to develop pressure injuries. In the world are estimated that 7.4 million people are suffering pressure injuries, excluding developing countries [2]. The subjects who suffer spinal cord injury due their sensitivity and mobility restrictions have tendency

D. A. Gayol-Mérida (✉)
Engineering Rehabilitation Laboratory, Instituto Nacional de Rehabilitación LGII, CDMX, Mexico
e-mail: dgayolmerida@gmail.com

V. M. Araujo-Monsalvo · V. M. Domínguez-Hernández
Biomechanics Laboratory, Instituto Nacional de Rehabilitación LGII, CDMX, Mexico

José de Jesús Silva-Lomelí · A. Alemán-Pérez
Unidad Profesional Interdisciplinaria y Tecnologías Avanzadas, IPN, CDMX, Mexico

M. Martínez-Cruz
Universidad Nacional Autónoma de México, CDMX, Mexico

E. Martínez-Coría · M. Luna-Méndez
Tomography Computed Department, Instituto Nacional de Rehabilitación LGII, CDMX, Mexico

R. R. Ambriz et al. (eds.), *Proceedings of the 17th International Conference on New Trends in Fatigue and Fracture*, https://doi.org/10.1007/978-3-319-70365-7_8

to develop pressure injuries. At Instituto Nacional de Rehabilitación Luis Guillermo Ibarra Ibarra (INRLGII) (CDMX, Mexico) was carried out a study about incidence of pressure injuries in subjects with spinal cord injury; the results are 61% of subjects with spinal cord injury had records of pressure injuries [3]. Pressure injuries are quality indicator of healthcare systems; every year, it is assigning resources for their treatment [4]. According to Sociedad Iberolatinoamerica Úlceras y Heridas (SILAUE) 95% of pressure injuries are prevented [5]. A strategy wide spread to prevent pressure injuries is to use support surfaces like wheelchair cushions or mattress; they are manufactured in several materials (gels, foam, filled with air or water), these surfaces redistributed the body weight in order to avoid high stresses in areas prone to develop pressure injuries like sacrum, heel and ischial tuberosities. In order to assess surfaces the interface pressure is measured between subject and their surface, these measurements do not guaranteed to avoid internal tissue damage. The internal high stresses can be precursor of Deep Tissue Injury (DTI), it is characterize by an intact or non-intact skin with an area of persistent non-blancheble deep reed or purple discoloration, but subcutaneous tissues are severely damage, and can be fatal due health complications (tissues infection, cellulitis, osteomyelitis or sepsis) [1]; according to Xio et al. [6], this injury is clinically challenging because the damage cannot be notice until it propagates to the skin surface. Gefen et al. [7] propose the use of computational models to simulate behavior of internal tissue loads in order to design support surfaces that reduce internal tissue stresses.

The present study approaches in behavior of stresses and strains generated in underlying soft tissue to ITs, applying FEM, in order to know the mechanical conditions that influence in development of pressure injuries.

Method

The CAD pelvis model was built from tomographic slices from a pelvis epoxy resin copy of a male subject cadaver, with 70 kg of weight and 1.70 m of high. 364 tomographic slices and 0.635 mm between of them were obtained. The images were in DICOM format (Digital Imaging and Communication in Medicine) so they can be processed in SolidWorks (Dassault Sistems, Vélizy-Villacoublay, France) and the keypoints were obtained.

The keypoints were imported to COMSOL Multiphysics Inc., Burlington, MA, USA Version 5.2 to obtain 3D model (Fig. 1). The soft tissue underlying ITs, was simulates by two blocks of 60 × 80 × 32 mm. The simulation conditions were: the tissues (bone and soft tissue) were assumed linear and isotropic: bone (E = 17E to 4MPa, $\upsilon = 0.38$) and soft tissue (E = 20 MPa, $\upsilon = 0.42$) [6, 8, 9]. The model was built with Solid92 elements (tetrahedrons of 10 nodes), the model contains 276,449 elements with 461,655 nodes (Figs. 1 and 2).

The condition load was 450 N, it is corresponding weight trunk of a man of 70 weight [10], and was applied in the sacrum´s base; the contact elements were between soft tissue blocks and ITs; the restriction was applied in the bottom of soft tissue blocks (Fig. 3).

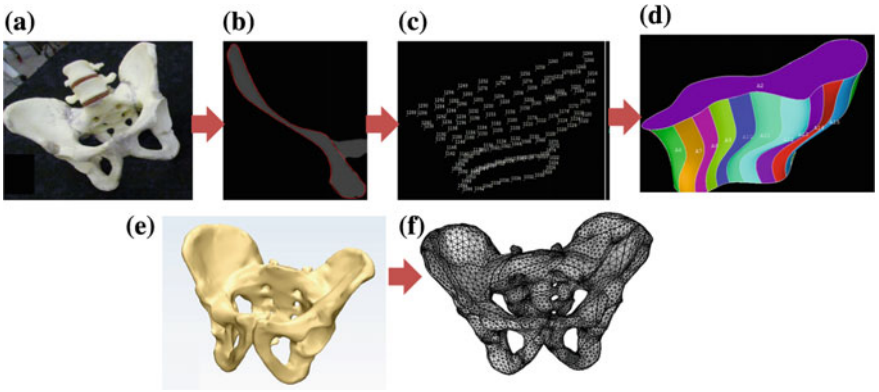

Fig. 1 Building 3D CAD pelvis model. **a** Epoxic Resine model. **b** Tomographic slice **c** Keypoints **d** Areas to build volumes **e** 3D CAD **f** Meshing model

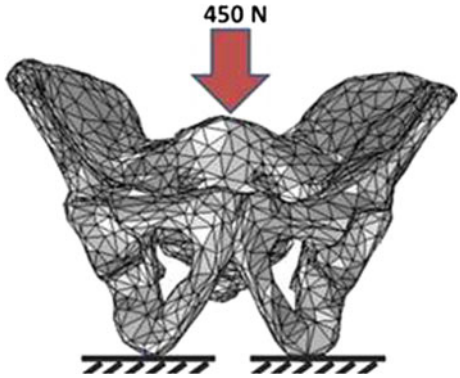

Fig. 2 Load applied in the sacrum's base

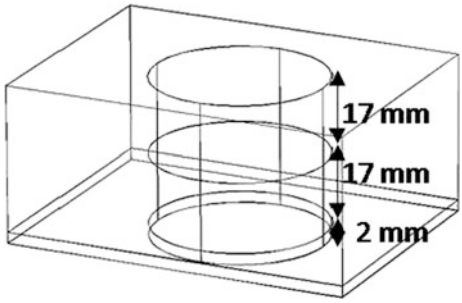

Fig. 3 Soft tissue block of 60 × 80 × 32 mm, the cylinder simulated a pressure injury

Every soft tissue block contained a cylinder of 20 mm of diameter and 36 mm of high (17 mm were soft tissue underlying ITs; 17 mm were soft tissue over skin layer; 2 mm were skin layer), these cylinders simulated pressure injury (Fig. 3). The cylinders were located underlying to ITs. The right cylinder was the health

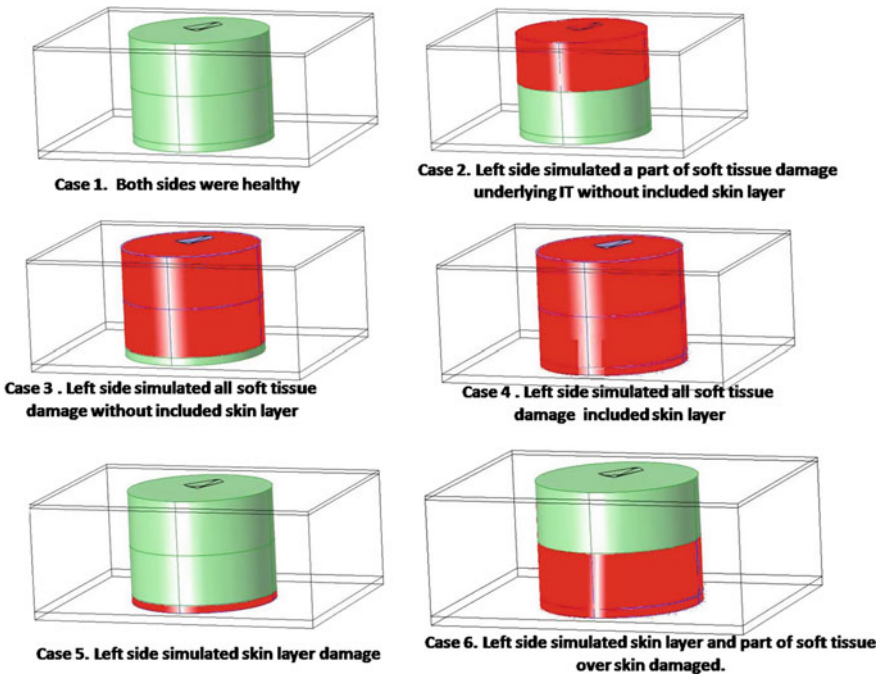

Fig. 4 Six cases of pressure injuries

side, and the left cylinder was the injured side. Six cases of injuries were simulated (Fig. 4):

Case 1: Both sides were healthy.
Case 2: Right side was healthy; left side simulated a part of soft tissue damaged underlying IT without included skin layer.
Case 3: Right side was healthy; left side simulated all soft tissue damaged without included skin layer.
Case 4: Right side was healthy; left side simulated all soft tissue damaged included skin layer.
Case 5: Right side was healthy; left side simulated skin layer damaged.
Case 6: Right side was healthy; left side simulated skin layer and part of soft tissue over skin damaged.

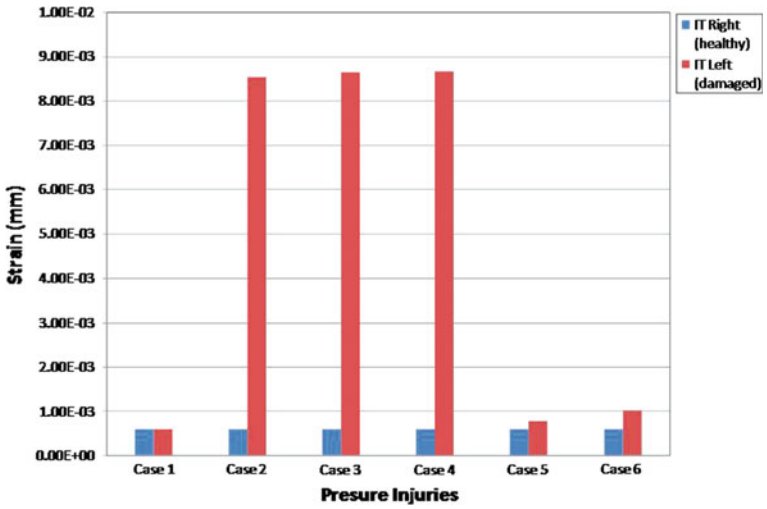

Fig. 5 Maximum strains

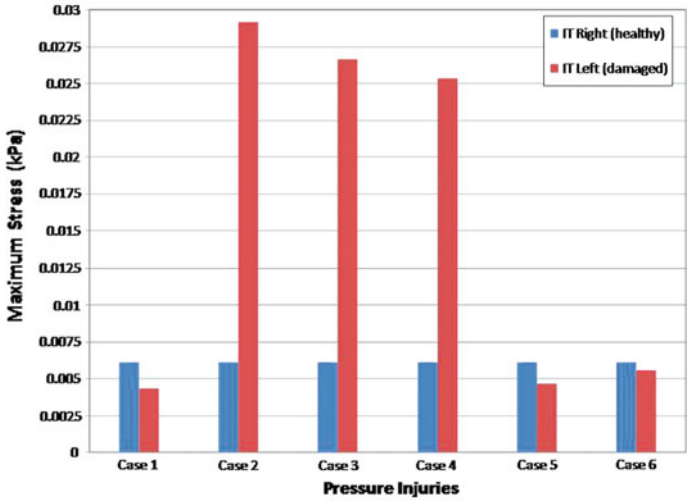

Fig. 6 Maximum von Mises stresses

Results

In Fig. 5 it is observed maximum strains for all cases. We put into the graph healthy side (Right) versus damage side (Left).

In Fig. 6 it is observed maximum von Mises stresses for all cases. We put into the graph healthy side (Right) versus damage side (Left).

The strains in Cases 2, 3 and 4 are increasing, until damage in tissue are increasing. In Cases 5 and 6, strains are less than Cases 2, 3 and 4, but they are higher than strains recorded in healthy side.

The stresses are higher in the cases that injured tissue is near to IT, this behavior is similar to strains behavior, but in Case 4 it is observed that stress decreases. In Cases 5 and 6, these injuries are similar to external pressure injuries, according to NPUAP Stage 1 or 2; the stresses are than healthy side (Right).

Discussion

The strains and stresses are higher when the injury is near to IT, this injury generates high stresses in early stage, and it could damages more quickly internal soft tissue, without it noticed by physician this is the case of DTIs. In Cases that injured tissue is closer to skin layer or it is skin layer, stresses are lower than healthy tissue, it could be influence in the Interface Pressure measurements; this result should be study further.

In other hand, the studies developed with physics models indicated that stress point in under IT; Gefen and Levine [11] reported maximum stresses between 5 and 11 times higher than external maximum stresses. In our FEM simulation the internal maximum stresses are 4.54–6.26 times higher than external maximum external stresses, this highlight is agree with Gefen and Levine [11] experiment.

The used of FEM in order to study the mechanical behavior in internal tissue can apply to design surface that to relieve internal stresses and strains.

References

1. NPUAP.org. National Pressure Ulcer Advisory Panel. 2016 [cited 2017 Jun 29]. Available from: www.npuap.org.
2. Sen C, Gordillo G, Roy S, Kirnser R, Lambert L, Hunt T, et al. Human Skin Wounds: A major and snowballing threat to Public Health and Economy. Wound Repair Regen. 2009; 7 (6):763–71.
3. Pérez-Zavala R, Rodríguez-Velazco E, Escobar-Rodríguez ÁD. Frecuencia de úlceras por presión en el paciente lesionado medular, su correlación con el nivel neurológico y escala de ASIA. Rev Mex Med Física y Rehabil. 2007; 19:16–23.
4. Bersgstrom N. Patients at risk for pressure ulcers and evidence-based care for pressure ulcer prevention. In: Bouter C, Bader DL, editors. Pressure Ulcer Researh Current and Future Perspective. Berlín: Spriger; 2005. p. 36–49.
5. SILAUHE. Declaracion De Río de Janeiro sobre la prevención de las úlceras por presión como derecho universal [cited 2017 Jun 29]. 2011. p. 1–4. Available from: http://silauhe.org/img/Declaracion/de/Rio-Espanol.pdf.
6. Xio DZ, Wu SY, Mak AF Accumulation of loading damage and unloading reperfusion injury-modeling of propagation of deep tissue ulcers. J. Biomech 2014; 47(7):1659–64.
7. Gefen A, Linder-Ganz E, Margulies SS. In vivo muscle stiffening under bone compression promotes deep pressure sores. J Biomech Eng. 2005; 127(3):512–24.

8. Lin F, Moran B, Bankard J, Hendrix R, Makhsous M. FEM model for evaluating buttock tissue response under sitting load. Conf Proc IEEE Eng. Med Biol Soc, 2014; 7:5088–91.
9. Majumder S, Roychowdhury A, Pal SA. Finite Element study of the behavior of human pelvis under impact through car door. Berichte der Bundesanstalt Fuer Strassenwesen. Unterreihe Fahrzeugtehcnin. 2005; 55: 196–203.
10. Matsuo J, Sugama J, Sanada H, Okuwa M, Nakatani T, Konya C, Sakamoto J. Development and validity of a new model for assessing pressure redistribution properties of suppor surfaces. J Tissue Viability. 2011; 20(2):55–66.
11. Gefen A and Levine J. The false premise in measuring bodu-support interface pressures for preventing serious pressure ulcers. J Med Eng Technol. 2007; 31(5):375–80.

Study of the Endurance Limit of AA7075 Aluminum Produced by High-Pressure Vacuum Die Casting Analyzed by Classical Whöler Curve

David Levasseur, Jimmy Simard, Francis Breton and Lotfi Toubal

Introduction

Casting 7075 with the high pressure vacuum die cast (HPVDC) process poses many difficulties due to the high die soldering tendency of the alloy. Further, the microstructure of the as cast parts contains many defects, some caused by the process itself, but others due to the solidification path of the alloy. The defects that are inherent to the HPVDC process are oxide film entrainment, and externally solidified particles. Porosity, which is known to plague high pressure die cast parts, is mitigated by the application of vacuum. However, shrinkage porosity and hot tearing tendency are inherent to the alloy solidification process. Defects in conventional high pressure die casting (without vacuum assistance) such as porosity, intermetallic particles and oxide films are well known fatigue crack initiation sites [1]. Porosity is among the most detrimental defect to fatigue life of part produced from all casting processes [2, 3]. Surface or sub-surface porosity act as local stress concentration and accelerates the crack initiation phase. It is often assumed that the crack initiation time can be ignored in castings because of the presence of porosity [4]. However, the surface of aluminum high pressure die casting parts is dense due to the high solidification rate at the mold interface and porosity is not the dominant initiation site of fatigue cracks in such parts. In A356 aluminum produced by conventional high pressure die casting the fatigue, crack was found to initiate from sub-surface eutectic microconstituent [5]. The presence of micro-pores (5 μm

D. Levasseur (✉) · J. Simard
Centre de Métallurgie du Québec, Trois-Rivières, Canada
e-mail: david.levasseur@cegeptr.qc.ca

F. Breton
Centre de Recherche et Développement Arvida, Joncquière, Canada

L. Toubal
Université du Québec à Trois-Rivières, Trois-Rivières, Canada

R. R. Ambriz et al. (eds.), *Proceedings of the 17th International Conference on New Trends in Fatigue and Fracture*, https://doi.org/10.1007/978-3-319-70365-7_9

average diameter) near the surface of conventional high pressure die casting aluminum parts, due to dissolved hydrogen in the melt, were found to initiate fatigue cracks [6]. The maximum pore size and the dendrite arm spacing (DAS) were reported as the most significant factors influencing the fatigue life of aluminum castings [7].

This study will focus on the fatigue behavior of HPVDC 7075 alloy in the T73 condition as well as the effect of grain refiner on the fatigue life and microstructure of the cast 7075.

Experimental

The HPVDC Process

The 7075 aluminum alloy used in this study had the chemical composition given in Table 1.

The alloy was melted in a 500 lbs clay-graphite crucible in an electric furnace that was also used for holding the melt at the process temperature during the trials. The molten alloy was degassed with a rotary degasser using argon and a reduced pressure test was performed to validate the hydrogen level lower than 0.07 ml/100 g.

The trials were carried on a Bühler Evolution 26D die casting machine (Bühler, Switzerland) using a prototype plate mold that is used mainly for alloy development. Figure 1 shows the part that was cast in this study.

The mold was evacuated with a vacuum unit (Castool, Canada), and thermoregulation is maintained by hot oil flowing through the mold. Grain refiner (GR) was added to the melt in the form of 5:1 TiB_2 master alloy rod. Two levels of GR were cast: 0 and 50 ppm. The HPVDC process was set into steady state operation by pouring 20 parts. Following the warm up casting, 20 parts were produced for each level of GR in the melt. The main process parameters were a gate velocity of 50 m/s, die temperature of 200 °C and melt temperature of 760 °C. Unusually high melt temperature was used to avoid formation of externally solidified particles in the shot sleeve due to the small shot weight and heavy shot sleeve section.

Table 1 Aural™2 composition determined by Optical Emission Spectrometry

Alloy	Si	Fe	Cu	Mn	Mg	Zn	Cr	Ti	Sr
Cast 7075	0.12	0.26	1.55	0.27	1.96	5.50	0.20	0.004	0.014
7075 spec	0.4	0.5	1.2–2.0	0.3	2.1–2.9	5.1–6.1	0.18–0.28	0.2	0.05

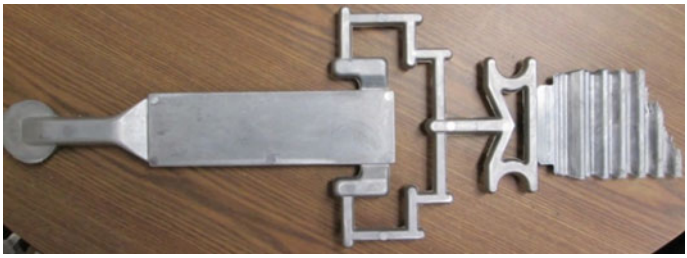

Fig. 1 Prototype plate 65 × 220 × 3 mm

Heat Treatments

The casting structure in the as cast condition is composed of aluminum alpha grains and solute rich interdendritic compound. This segregation of solute to interdendritic regions can be homogenized during the solution treatment due to the high diffusion rate experienced at the solution treatment temperature. Therefore, the solution treatment duration was determined based on the time needed to homogenize the parts. The solution treatment temperature for HPVDC parts is a critical parameter as it should be as high as possible to produce a supersaturated solid solution upon quenching; however, to avoid blistering, the solution treatment temperature and time are typically low. Solution temperatures of 450 and 480 °C were tested for 1–16 h. Blistering was difficult to avoid completely and in order to minimize it, the solution treatment temperature that was selected was 450 °C. The solution treatment time was set at 16 h to improve the homogeneity of the cast structure. The T73 artificial aging treatment for 7075 consisted in a two-step heat treatment: 8 h at 107 °C followed by 27 h at 163 °C.

Sample Extraction and Size

Tensile test bars were extracted from the castings based on the ASTM E8 standard geometry. Each casting yielded 2 tensile bars that were tested in the F and T73 conditions to evaluate the yield strength (YS), tensile strength (UTS) and elongation (EL) of HPVDC 7075 alloy. The tensile test were done on a Tinius Olsen Superl—120 press using displacement control to maintain a strain rate of 0.03 po/min from stress level of 50–430 MPa and a strain rate of 0.1 po/min from 430 MPa to failure. The tensile test results were averaged out of a sample size of three tensile bars.

The uniaxial tensile fatigue test samples were machined from the castings according to the geometry given in ASTM E466 standard. The fatigue specimen dimensions are given in Fig. 2.

$W = (6{,}50 \pm 0{,}05)\ mm$
$T = (2{,}95 \pm 0{,}1)\ mm$
$R = (60{,}0 \pm 0{,}1)\ mm$
$L = (16{,}0 \pm 0{,}1)\ mm$

Fig. 2 Uniaxial tensile fatigue specimen size

The uniaxial tension-tension fatigue tests were performed on a MTS machine equipped with MTS FlexTest 40 digital controller using load amplitude ranging from 3.2 kN (170 MPa) to 6.2 kN (329 MPa) and with R = 0.05.

Microstructure Observation

Samples for microstructure observation were cut from the grip section of tensile test bars using a SiC abrasive wheel with coolant. The samples were mounted in resin, ground and polished using appropriate procedures for metallography. The grains were revealed using immersion etching in 2 g NaOH, 5 g NaF and 93 ml water (2–3 min) and cross-polarized light microscopy. An image analysis software (Clemex, Canada) was used to measure the grain size in the center of the plate thickness. The grain size measurements were all taken at least 200 µm under the surface of the casting to avoid the very fine surface layer.

The fatigue crack initiation site was observed on the fracture surface of failed samples using a scanning electron microscope (Hitachi SU-3500).

Results and Discussion

Homogenisation and Microstructure Observation

The microstructure shown in Fig. 3 is the 7075 without GR both in the as cast (F) and heat-treated (T73) condition (450 °C, 16 h + aging).

In the F condition, the microstructure contains large solute enriched inter dendritic regions, however the amount and size of solute rich regions decreases after the 16 h solution treatment as can be seen in Fig. 2b. The EDS analysis (not shown in this paper) revealed that both in the F and T73 conditions, Cu, Zn, Mg, Si, Fe, Cr segregation was present in the interdendritic regions as compared to the primary phase.

To assess the extent of the homogenisation during solution treatment, electrical conductivity measurements were obtained from each solution treatment time as presented in Fig. 4.

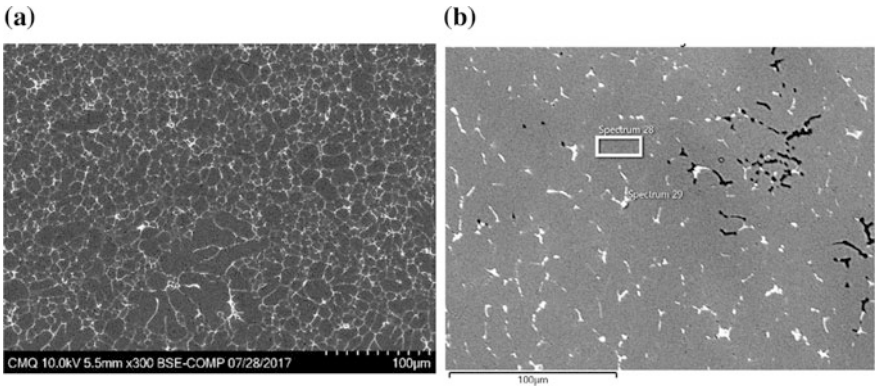

Fig. 3 **a** As cast microstructure observed in backscattered electron mode, **b** T73 microstructure using a solution treatment temperature of 450 °C for 16 h

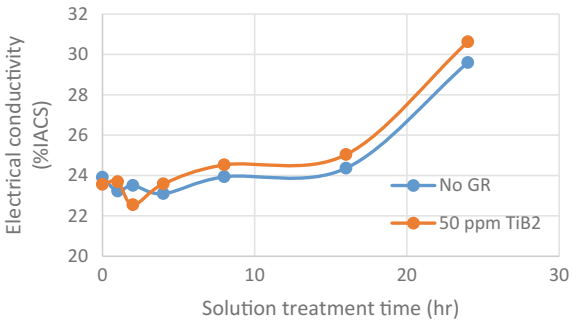

Fig. 4 Electrical conductivity evolution of the solution treated HPVDC 7075 at 450 °C

The conductivity measurements varied from 23.56 to 23.91%IACS in the as cast condition, 24.36–25.03 after 16 h and 29.6–31.46 after 24 h solution treatment at 450 °C. The conductivity of 7075 T73 and 7075 T6 was reported as 37.6%IACS and 32.0%IACS respectively and both were brought to 41–42%IACS after 1 h annealing at 315 °C. The observed increase in electrical conductivity is unusual for a solution treatment. Typically, the electrical conductivity is inversely proportional to the amount of solute trapped into solid solution. However, since the solute rich regions form a continuous network at grain boundaries in the as cast state, there is no path of least resistance. As the homogenization proceeds, the resistance decreases. The electrical conductivity was the highest after 24 h solution treatment, however the castings were distorted and blistering defects was worst than for the 16 h trials. Therefore this condition was excluded for the mechanical test.

The grain size was measured as a function of solution treatment time to assess grain growth. The measurements are reported in Fig. 5.

The grain size after up to 16 h solution treatment at 450 °C was between 13 and 15 µm. These values are within experimental error of the grain size after 1–8 h

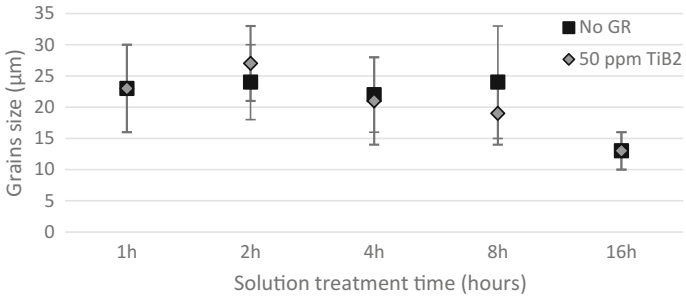

Fig. 5 Grain size measured for solution treatment duration between 1 and 16 h

solution treatment. The integration of 50 ppm TiB_2 in 7075 produced by HPVDC did not decrease the grain size. The rapid cooling in the die cavity is responsible for the fine grain size (<20 µm), and the addition of TiB_2 could not reduce it further. As such, the amount of nucleation sites added with 50 ppm TiB_2 was not substantially higher compared to the nucleation sites formed during the injection and solidification of HPVDC 7075.

Mechanical Properties

A tensile test map of the yield strength and elongation obtained in the F condition and the T73 condition for each solution treatment time is shown in Fig. 6. Note that only the results of tensile specimens without defects are presented. Since defect free samples were not obtained for the 2 and 4 h solution time for both GR level, neither for the 8 h solution treatment for the no GR alloy, they are not represented on Fig. 6.

The tensile properties obtained in the F condition was a YS of 206 MPa, a UTS of 255 MPa and elongation of 2%. The tensile properties of the alloy in the as cast

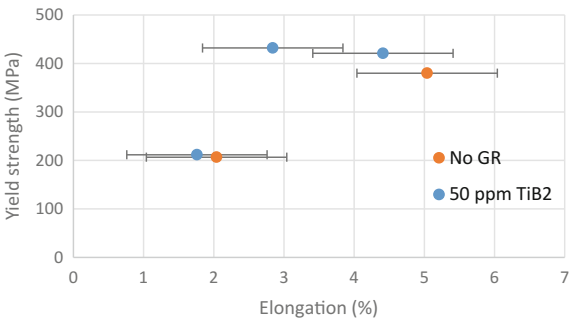

Fig. 6 Yield strength versus elongation map for HPVDC 7075 in the F and T73 condition

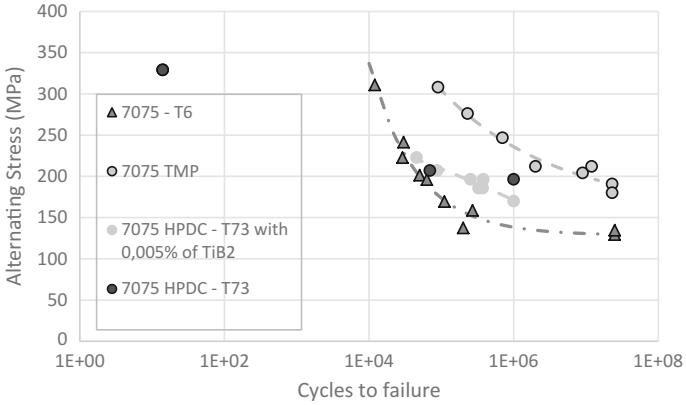

Fig. 7 Unnotched fatigue properties of the commerical Al–Zn-Mg-Cu alloy 7075 and unnotched fatigue properties of HPDC 7075. PS proof stress (MPa); TS tensile strength [8]

condition are superior to all common secondary HPDC alloys, and could be further improved by the T73 heat treatment.

The solution treatment duration did not have a strong influence on the YS or the elongation of the 7075 cast with 50 ppm TiB_2, however there was a difference in tensile properties between the grain refined and non grain refined alloys. The YS and EL results obtained in the T73 condition ranged from 380 MPa (No GR) to 432 MPa (50 ppm TiB_2) and 2.84% (50 ppm TiB_2) to 5.04% (No GR) respectively. More results are needed to assess statistically the effect of TiB_2 on the mechanical properties of HPVDC 7075.

The cycles to failure are presented in the form of Whöler curves in Fig. 7 along with reference data for wrought 7075-T6.

The samples tested had a fatigue life in line with the reference data, but lower than 7075 TMP (Thermomechanical processed). Analysis of the fracture surface was done to assess the failure mechanisms.

Fractography

The fracture surfaces of two samples tested with the same alternating load are compared in Fig. 8.

The crack initiation sites are identified with an arrow. The crack initiation site appears to be located in the center of the sample, where most casting defects are present in HPVDC. The backscattered electron image of the fracture initiation site in the sample with no GR reveals a slightly darker area (circled) which could be due to the presence of oxide film or segregation of heavier solute elements. Both samples presented the same defect and fracture initiation site away from the surface.

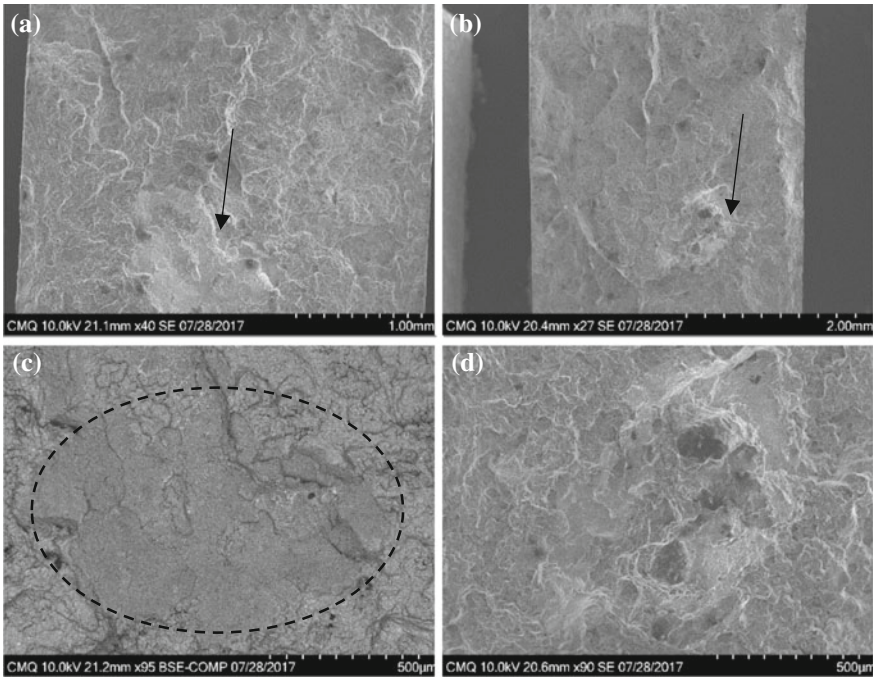

Fig. 8 **a** Fracture surface of a HPVDC 7075 alloy without GR in the T73 condition, **b** Microstructure of a fracture surface of a HPVDC 7075 alloy with 50 ppm TiB_2 in the T73 condition, **c** crack initiation site in **a**, **d** crack initiation site in **b**

It is known that the surface layer (the "skin") of HPVDC parts is denser and has better properties than the core of the casting. This is due to the very fast solidification of the aluminum that first contact the mold surface. Since the casting used in this study is thin (3 mm wall thickness), it has a strong contribution from the surface layer to the overall mechanical strength of the part. The fatigue life of a part is influenced by its surface condition (roughness, hardness, defects), and it could explain the fatigue life obtained that is comparable to wrought alloy.

Figure 9 show another sample that failed after 250 k cycles at a load of 207 MPa.

The fracture initiation site was located closer to the surface because of the presence of a blister as shown in Fig. 9b. Observation of the fracture surface of all samples revealed that the fracture propagation path preferentially followed shrinkage defects and interdendritic regions as suggested by Fig. 10.

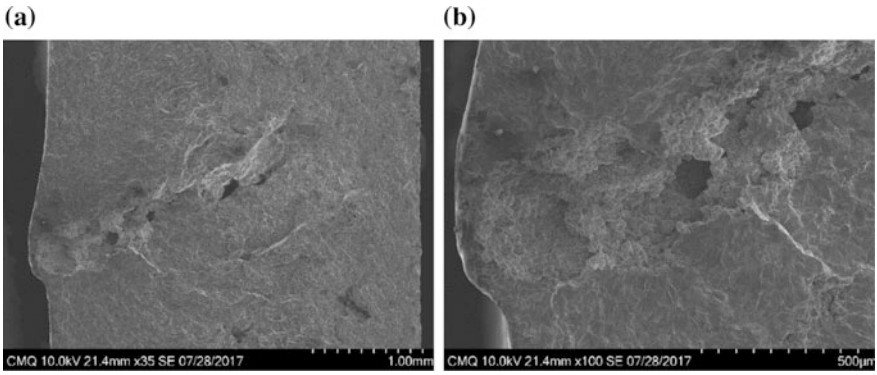

Fig. 9 **a** Fracture surface of HPVDC 7075 with 50 ppm TiB_2 showing a linear defect, **b** blister present under the surface that initiated the fatigue crack

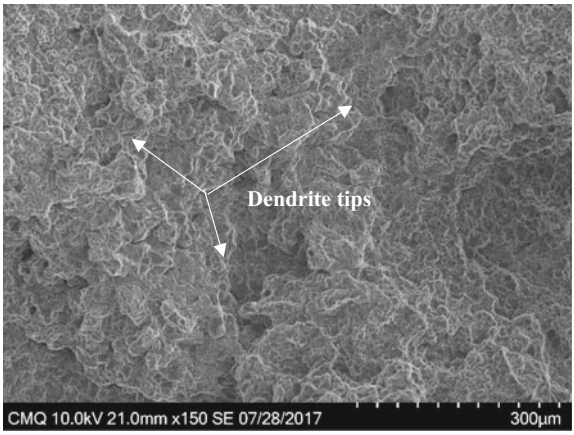

Fig. 10 Fracture surface of HPVDC 7075 showing the presence of many dendrite tips

Summary

The HPVDC process was used to produce 7075 prototype plates to assess the alloy mechanical properties and the effect of grain refiner on the fatigue life. The process was found to yield good parts but shrinkage and hot tearing defects inherent to the alloy could not be avoided. Moreover, the defects associated with the HPVDC process were found to be better crack initiation site compared to shrinkage porosity. The crack propagation was found to follow the interdendritic region and shrinkage defects. The addition of GR to the melt was not found to decrease grain size, but increased the tensile strength at the expanse of lower elongation. The GR did not have noticeable effect on the fatigue life or failure mechanism.

Acknowledgements The authors acknowledge the financial assistance of Natural Science and Engineering Research Council of Canada through the Industrial Research Collegial Chair program.

References

1. Wang QG., Apelian D., Griffith JR., Microstructural effects on the fatigue properties of aluminum castings, Proc. Materials Solutions 98, Rosemont IL, USA, Materials Park OH: ASM International, Member/Customer Service Center, 1998 p. 217–233
2. Toda H., Hidaka T., Kobayashi M., Uesugi K., Takeuchi A., Horikawa K., Acta Mater 2009; 57: 2277–2290
3. Ammar HR., Samuel AM., Samuel FH., Mater Sci Eng A, 2008, 473, 65–75
4. Wang QG., Jones PE., Metall Mater Trans B, 2007, 38, 615–621
5. Zhang B., Chen W., Poirier DR., Fatigue Fract Eng Mater Struct 2000, 23, 417–423
6. Toda H., Masuda S., Batres F., Kobayashi M., Aoyoma S., Onodera M., Furusawa R., Uesugi K., Takeuchi A., Suzuki Y., Acta Mater, 2011, 59, 4990–4998
7. Major JF., Porosity Control and Fatigue Behavior in A356-T61 Aluminum Alloy, AFS Transactions, 2002, 901–906
8. Howard E. Boyer, Atlas of fatigue curves, America Society for Metals, 1999, 518 p

Life Prediction of a Mono Contact Aluminum/Steel at Constant and Variable Amplitudes Loading in Fretting Fatigue Configuration

A. Belloula, A. Amrouche and M. Nait-Abdelaziz

Introduction

Fretting can be referred as a material damage caused by small oscillatory movements between the contacting bodies. Combined with cyclic fatigue loading, the so called fretting-fatigue loading can induce catastrophic damages, which critically reduce the endurance of assemblies or structures [1]. Due to the contact a local stress and strain concentrations are induced in the bodies and the stress state in the contact zone is multiaxial and consequently leads to a decrease of the fatigue resistance of materials compared to the uniaxial loading [2].

In addition, fretting fatigue experiments aim to represent industrial problems and most of them endure variable loadings. Being able to assess lifetime of structures, especially for variable loading applied for very high number of cycles, is essential as experimental validation is often too expensive.

Crack nucleation risk is usually investigated by applying multi-axial fatigue criterion. Predictions were improved by considering the severe stress gradients imposed by the contact loading, using non-local process volume stress averaging strategy [2–4] or equivalent critical distance [5]. Hence, that allows to compute the estimated life under fretting fatigue. Some researchers have used continuum damage mechanics (CDM) approach and lifetime up to crack initiation can be estimated using bulk material properties [6].

A. Belloula
Département Des Sciences et Technologies, AMC, Cherchell, Tipaza, Algérie

A. Amrouche (✉)
Université d'Artois, FSA, Béthune, Laboratoire de Génie Civil
et Géo-Environnement (LGCgE), EA 4515, 62400 Béthune, France
e-mail: abdelwaheb.amrouche@univ-artois.fr

M. Nait-Abdelaziz
Université Lille 1, Laboratoire de Mécanique de Lille, UMR CNRS
8107, 59650 Villeneuve d'Ascq, France

R. R. Ambriz et al. (eds.), *Proceedings of the 17th International Conference on New Trends in Fatigue and Fracture*, https://doi.org/10.1007/978-3-319-70365-7_10

Materials—Experiments—Simulation

The studied material is a 6082-T6 aluminum alloy (E = 70GPa, $\upsilon = 0.33$, $\sigma_{0.2\%} = 278$MPa); it exhibits an important scattering of the grains size varying from approximately 30–130 µm [2]. The fatigue response of this material is modeled with the Basquin law $1180(N)^{-0.139}$. The material was then tested under various fretting fatigue conditions, using a cylinder/plane contact configuration, with a cylinder of 12.7 mm radius, a normal force P = 1 kN being applied on the flat specimen. The cylinder was made of Z160CDV12 steel (E = 207 GPa, $\upsilon = 0.3$). The fretting fatigue test device is shown in Fig. 1a. It consists in two hydraulic actuators which allows controlling independently the normal force P and the applied fatigue stress (σ). The fretting actuator imposes a purely sinusoidal cyclic fatigue stress $\sigma(t)$ on the specimen, generating an cyclic tangential load Q(t) on the contact surface. During the test, normal force P and tangential force Q were recorded. As crack nucleation was to be investigated, the displacements were kept small enough to maintain partial slip conditions. All tests were performed at constant normal force P. The frequency was fixed at 20 Hz, high enough to investigate a long test condition and low enough to guarantee test control stability. The fretting stress ratio was R = 0.1. The crack initiation is assumed to occur when a certain limit of the amplitude variation of displacement has been reached, which leads to the detection of a crack of about 1 mm length. For more detailed information, readers are referred to reference [2].

Finite element analysis was carried out using Abaqus 6.9 software. A 2D plain strain model of the fretting fatigue test was generated (Fig. 1b). The dimensions and boundary conditions reproduce the experimental conditions. The model was meshed with CPE3-type linear triangular elements, except in the contact zone where CPE4R-type linear quadrilateral elements were used; this zone was also meshed more densely than the other regions (squares of 5 µm length).

Surface-to-surface discretization with small sliding was adopted for contact accommodation. The Lagrange multiplier was selected as the contact algorithm. The friction coefficient of the contact µ was determined experimentally using the variable loading technique described by Belloula et al. [2], µ = 0.5. Based upon test

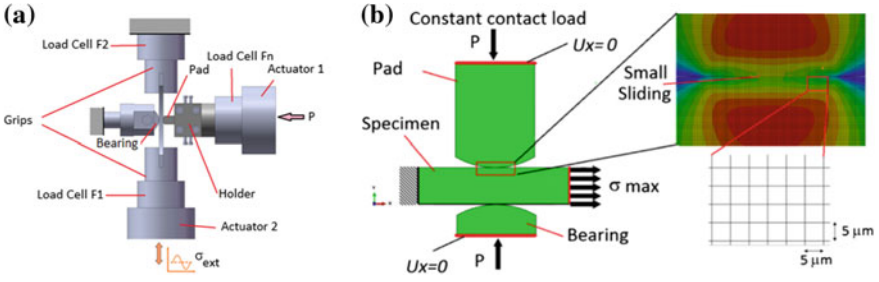

Fig. 1 Fretting fatigue test device, **a** Experimental **b** Simulation

results obtained by Borregois [7] on a 6082-T6 alloy, the Armstrong–Frederick's nonlinear kinematic hardening plastic model [8] was used to model the cyclic behavior of the material.

Multiaxial Criterion

Smith-Watson-Topper (SWT)

SWT parameter can be used to predict fretting fatigue crack initiation life. It is defined as the product of the normal strain amplitude, εa, and the maximum normal stress σ_{max}. The parameter proposed by Smith et al. [9] can be expressed as a function of number of cycles to initiation (N) as:

$$SWT = \sigma_{max} \cdot \frac{\Delta\varepsilon}{2} = \frac{\sigma_f^2}{E}(2N)^{2b} + \sigma_f \varepsilon_f (2N)^{b+c} \tag{1}$$

Cracking Energy Density (CED)

The cracking energy density (Wc) proposed by Mars [10] for the analysis of fatigue crack nucleation under multiaxial loading in the case of rubber materials, is expressed as follows:

$$\Delta CED = dW_c = \vec{\sigma} \cdot \vec{\varepsilon} = \left(\vec{r}^T \cdot \overline{\overline{\sigma}}\right)\left(d\overline{\overline{\varepsilon}} \cdot \vec{r}\right) = f(N) \tag{2}$$

where $\vec{r}$ is a unit vector that defines the normal to the virtual crack plane, $\vec{\sigma}$ is the stress tensor and $\vec{\varepsilon}$ is the strain tensor increment.

This parameter was used to estimate fatigue life when dealing with fretting fatigue [2].

Continuum Damage Model

Linear Miner's Rule

Failure of a component subjected to different fatigue loadings is supposed to occur if the cumulative damage sustained by the component equals or exceeds unity [11]. Cumulative damage is the sum of the damage fractions (D) due to each individual fatigue loading undergone by the component.

$$D = D_1 + D_2 + \cdots + D_{i-1} + D_i \tag{3}$$

where $D_i = \frac{n_i}{N}$ is the damage fraction due to an individual fatigue loading. The rupture occurs when D = 1.

The Non-linear Damage Stress Model (DSM)

The Damaged Stress Model (DSM) which was developed and detailed in [12] is regarded as having many advantages such as taking into account the loading history and the non-linear damage accumulation. This damage indicator is easily connected cycle by cycle to the (S-N) curve.

The expression of the DSM indicator gives the increase of damage D_i due to a given applied stress σ_i and is defined as follows:

$$D_i = \frac{\sigma_{ed} - \sigma_i}{\sigma_u - \sigma_i} \tag{4}$$

where σ_{ed} is the damage stress; σ_i is the applied stress and σ_u the ultimate stress. A detailed description of the damage stress model is given in [12].

Results—Discussions

The obtained values for the constant amplitude loading case are compared with the reference curve given by the high cycle fatigue under uniaxial tension (S-N curve). The results clearly show that the data obtained, when calculated on a material point on the contact surface, strongly deviate from the reference curve. To address this issue, it was suggested to average the mechanical quantities (stresses and strains) in a so-called process zone and then apply the fatigue criteria by using these quantities. The optimum value of the effective size was found of about 30 μm [2].

In the variable loading conditions, two blocks of different fretting fatigue loading were applied. The aim of this set of tests is to determine the influence of increasing (225–250 MPa) or decreasing (250–225 MPa) loading conditions on lifetime and to determinate the fretting fatigue lifetime under variable block loading.

For fretting fatigue loading, we introduce a modified damage stress model (MDSM), and defined as the ratio increment of parameter value $P_{\sigma_{ed}}$ due to stress damage over the difference between the parameters due to ultimate stress P_{σ_u} and the applied stress P_{σ_i}. The damage MDSM indicator is therefore defined as:

$$D_i = \frac{P_{\sigma_{ed}} - P_{\sigma_i}}{P_{\sigma_u} - P_{\sigma_i}} \tag{5}$$

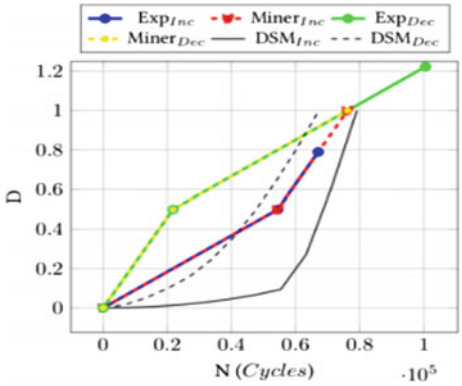

Fig. 2 Damage evolution as a function of number of cycles

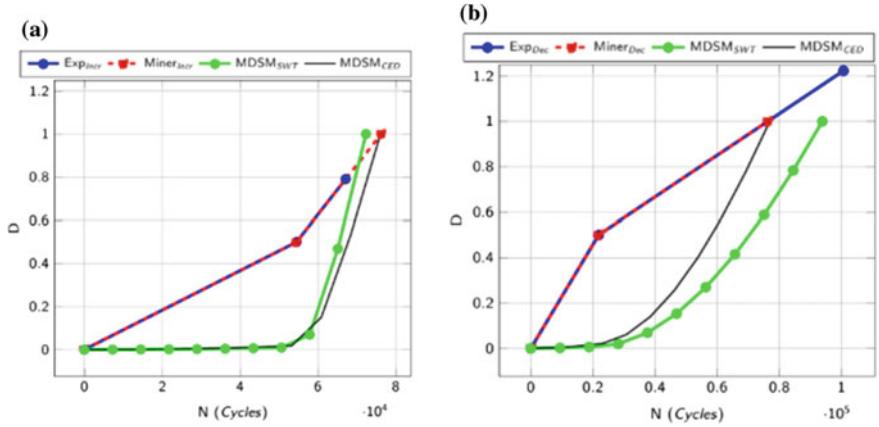

Fig. 3 Damage evolution as a function of number of cycles: **a** Increasing and **b** Decreasing

Figure 2 represents the fatigue damage evolution for two configurations; they show the evolution of the damage according to the number of cycles for damage stress model, Miner's model and the experimental results calculated by the sum of fractional damage (Miner law). The damage evolution given by Miner rules is linear; the curve is composed of straight portions associated to the elementary loads. The DSM model evolves in a nonlinear way. This model allows to take into account the loading history.

Figure 3 presents the evolution of the damage according to the number of cycles using the uniaxial fatigue curves obtained with SWT and CED parameters.

During the total lifetime of specimens and for different types of loading increasing (Fig. 3a) and decreasing (Fig. 3b), the evolution of the damage determined by the modified DSM model is below than that obtained by Miner rule's. This difference comes from the nonlinearity and the loading history accounted for in the DSM model.

Conclusion

The crack initiation of fretting fatigue was investigated both experimentally and numerically. A finite element analysis was used to obtain the stress and strain states at the zone of contact thus to predict crack initiation. The result shows the existence of a local influence on the initiation of the cracks due to the severe gradients present in the contact zone. Averaging stress and strain within a process zone and use these quantities to compute the multiaxial fatigue parameters allows to lessen this strong effect.

To predict the fretting fatigue lives, two multiaxial fatigue parameters, namely Smith-Watson-Topper "SWT", and Crack Energy Density "ΔCED" were coupled with damage laws. The first one is the linear law developed by Palmgren-Miner and the second one is a nonlinear Damage Stress Model (DSM). The estimates obtained with the modified (DSM) model are in good agreement with the experimentally measured ones and seem very promising to predict fatigue life under conditions of fretting fatigue.

References

1. D. Nowell, D.A. Hills, Crack initiation criteria in fretting fatigue, Wear, 136, 329–343, 1990.
2. A. Belloula, A. Amrouche, M. Nait-Abdelaziz, N. Benseddiq, Comparison of the cracking energy density and the Smith–Watson–Topper parameters in predicting fretting fatigue lifetime of a steel/aluminum alloy contact, Fatigue & Fracture of Engineering Materials & Structures, 37, 1355–1366, 2014.
3. C. Navarro, S. Muñoz, J. Domínguez, On the use of multiaxial fatigue criteria for fretting fatigue life assessment, International Journal of Fatigue, 30, 32–44, 2008.
4. Fouvry, S., Kapsa, P., Vincent, L., A multiaxial fatigue analysis of fretting contact taking into account the size effect, ASTM STP., 1367 (2000) 167–182.
5. J.A. Araújo, D. Nowell, The effect of rapidly varying contact stress fields on fretting fatigue, International Journal of Fatigue, 24, 763–775, 2002.
6. N.A. Bhatti and M. Abdel Wahab, A Review on fretting fatigue crack initiation criteria. International Journal of Fracture Fatigue and Wear, 4, 78–85, 2016.
7. Borrego, P. L., Abreu, M. L., Costa, M. J. and Ferreira, M. J. (2004) Analysis of low cycle fatigue in ALMg-Sialuminium alloys. Eng. Fail. Analysis 11, 715–725.
8. Armstrong, J. P. and Frederick, O. C. (1966) Berkeley Nuclear Laboratories, Tech. Rep. RD/B/N731.
9. N. Smith R., P. Watson, and H. Topper T. A stress-strain function for the fatigue of metals. Journal of Materials 4 (1970), pp. 767–778.
10. V. Mars W. Multiaxial Fatigue of Rubber. PhD thesis. University of Toledo, 2001.
11. A. Miner M. Cumulative damage in fatigue. Journal of Applied Mechanics. 12 (1945), 159–164.
12. G. Mesmacque et al. Sequential law in multiaxial fatigue a new damage indicator. International Journal of Fatigue 27.4 (2005), 461–467.

Influence of Microstructure on Fatigue Crack Formation and Growth in a Low-Carbon Steel

Donka Angelova, Rozina Yordanova and Svetla Yankova

Introduction

In the present work investigations of microstructurally-short fatigue crack propagation are done at tension-tension (**T-T**), rotating-bending (**RB**) and pure-bending (**PB**) loading conditions in clarifying relationship between the typical features of the studied microstructure and the specific behaviour of crack growth through it. The microstructural features can act as stress raisers or can cause shielding effect at the crack tip. The microstructural barriers can reduce the effective driving force for crack propagation and that is why short crack growth is so microstructurally sensitive; all the variations in the microstructure surrounding the crack tip are responsible for its specific growth behaviour [1, 2]. Three different groups of specimens are used: two groups of hour-glass specimens [3] and one group of flat specimens notched by Focused Ion Beam (FIB) technique [4, 5]. The obtained data are presented by combining microstructural photos, and plots "Crack length—Cycles", "Crack growth rate—Crack length", "Crack growth rate—Effective stress intensity factor range"; newly modified and new mathematical models of fatigue crack propagation are introduced.

Experimental Procedure: Material Specimens and Testing

A **ro**lled **l**ow-**c**arbon, **l**ow-**a**lloyed **s**teel, ROLCLAS, marked as 09Mn2 Steel (ac-cording to the Bulgarian Construction Steel Standard), used mostly for offshore applications and in shipbuilding, was subjected to **T-T**, **RB** and **PB** fatigue.

D. Angelova (✉) · R. Yordanova · S. Yankova
Faculty of Metallurgy and Materials Science, University of Chemical Technology and Metallurgy, St. Kliment Ohridski 8, Blvd, 1756 Sofia, Bulgaria
e-mail: donkaangelova@abv.bg

R. R. Ambriz et al. (eds.), *Proceedings of the 17th International Conference on New Trends in Fatigue and Fracture*, https://doi.org/10.1007/978-3-319-70365-7_11

Table 1 Chemical composition, mechanical and microstructural properties of ROLCLAS 09Mn2

Chemical composition									
C (%)	Si (%)	Mn (%)	Cr (%)	Ni (%)	P (%)	S (%)	Cu (%)	Al (%)	As (%)
0.09	0.28	1.63	0.05	0.04	0.017	0.026	0.13	0.12	0.014
Mechanical and microstructural properties									
Tensile strength σ_B (MPa)		Proof strength $\sigma_{0,2}$ (MPa)		Cross section contraction ψ (%)		Hardness HB (MPa)		Average grain size (μm)	
482		382		62.3		148		25.6	

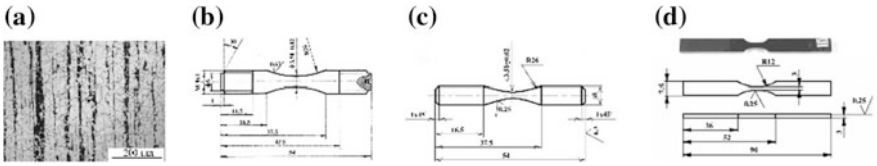

Fig. 1 Microstructure of cross section of ROLCLAS specimens (**a**); hour-glass fatigue specimens for tension-tension (**b**); and rotating-bending fatigue (**c**); notched flat fatigue specimen for rotating-bending fatigue (**d**); all dimensions are in mm

The chemical composition of ROLCLAS and its mechanical and microstructural characteristics are shown in Table 1. ROLCLAS was available in sheets of 8 mm thickness. Its microstructure revealed a sequence of long and uniform pearlite and ferrite bands, Fig. 1a. The bands are wider in the middle of the sheet but loose and thinner close to the surface.

Two groups of hour-glass specimens were under investigation: Group **A** for **T-T** fatigue, Fig. 1b; and Group **B** for **RB** fatigue, Fig. 1c. Shape and sizes of notched flat specimens for **PB** fatigue (Group **C**) are shown in Fig. 1d, [5]. These specimens have four micro-notches machined by FIB technique in different positions in the microstructure, Fig. 2a, b; the notch geometry is presented in Fig. 2c, d. Three of the notches are central; the forth one is an edge notch aligned with the top notch from the group of the central notches. The distance between notches is 200 μm.

The **T-T** tests were carried out on Amsler Fatigue Machine (Institute of Metals Science, Bulgarian Academy of Sciences) at the following loading conditions: applied stress range $\Delta\sigma$ = 396 MPa; stress ratio R = 0.1; frequency—190 Hz. The **RB** tests were conducted on a table model **Fat**igue **Ro**tating-**Be**nding **M**achine, FATROBEM-2004 (Fracture and Fatigue Laboratory, UCTM-Sofia [4]); the loading conditions were: $\Delta\sigma$ = 580 MPa and 620 MPa; R = −1; f = 11 Hz. The **PB**-tests were carried out on Schenk Fatigue Machine (Erich Schmid Institute of Materials Science, Austrian Academy of Sciences, Leoben) under constant stress control at: stress level 580 MPa, R = −1, f = 5 Hz [5]. The surface short-crack propagation on the hour-glass specimens was monitored by acetate-foil replica

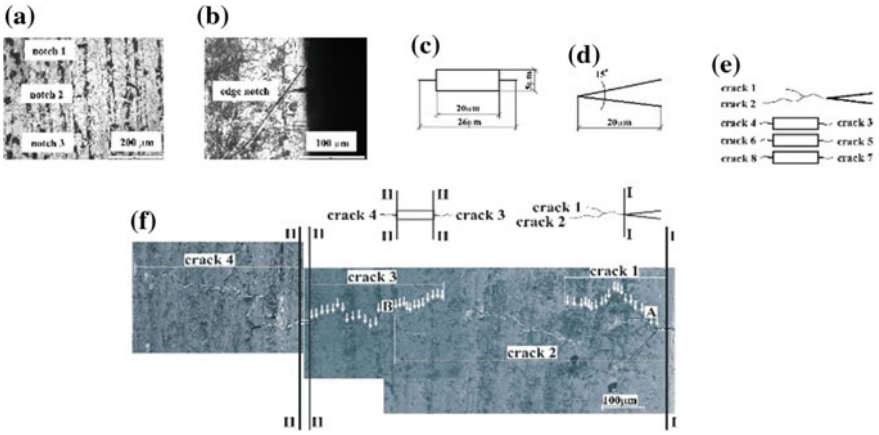

Fig. 2 FIB-machined micronotches in a specimen of Group **C**: central notches (**a**), edge notch (**b**); notch geometry (**c**), (**d**); cracks starting from notches at stress range 580 MPa (**e**); two parts of the fracturing crack according to the axis perpendicular to the top central notch (**f**)—*right part* with cracks 1, 2 (started from the edge notch aligned with the top central notch) and crack 3 (started from the top central notch), and *left part* with crack 4 (started from the top central notch); crack bifurcation at point **A** and crack merging at **B**

technique during a fixed interval of fatigue cycles, and observed on the replicas by an optical micro scope used as well for measuring of surface crack lengths. The short fatigue-crack experiments with notched flat specimens included test interruptions at every 1000 cycles for (in situ) examination of specimen surface with optical and SEM-microscopy. The crack lengths were measured by using an image analyzer [5].

Results and Discussion

Data obtained from the conducted fatigue experiments with specimens from Groups **A, B, C**—the crack lengths a, at the corresponding numbers of cycles N are plotted as:

- *functions* "Crack length, a—Number of cycles, N", $\{\boldsymbol{a}-\boldsymbol{N}\}$, in log-log scale, shown in Fig. 3a;
- *functions* "Number of cycles, N—Crack length, a", $\{\boldsymbol{N}-\boldsymbol{a}\}$, in semi-log scale, N in log scale and a in ordinary scale; they are presented in Figs. 3b, 4, 5, and 6;
- *functions* "Crack growth rate da/dN—Crack length a", $\{\boldsymbol{da/dN}-\boldsymbol{a}\}$, in semi-log scale, ($N$ in log scale and a in ordinary scale, Figs. 4, 6, and 7) represented by a Parabolic-Linear Model, **PLM**, proposed and described in detail in [6, 7] and newly modified in [8, 9]; **PLM** consists of three sections—two parabolas and a linear part—and is applied to the data of all presentations $\{\boldsymbol{da/dN}-\boldsymbol{a}\}$, Figs. 4 and 7; the three sections of **PLM** are located in the following $\boldsymbol{a}$-intervals $[0, d_1]$,

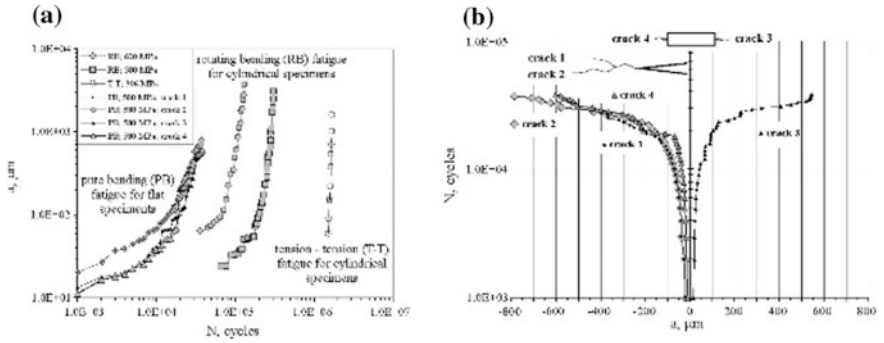

Fig. 3 Plots **{*a*−*N*}** for cracks from Groups **A, B, C—T-T, RB, PB—(a)**; **{N−a}** for cracks 1, 2, 3, 4 from Group **C** specimen—**PB**—(**b**); **{N−a}** Plot from (**b**) uses a coordinate system with *N*-axis located in the middle of the central notches specifying *left* and *right* cracks propagation

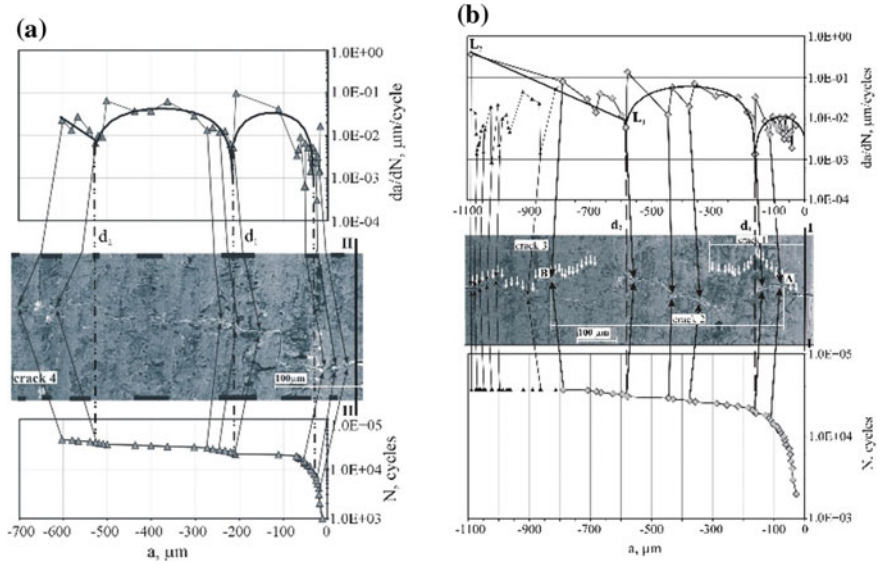

Fig. 4 Group **C**: Microstructural paths of **a** crack 4 (which is the *left part* of the two-parts notch-specimen fracturing crack, Fig. 2f) and **b** part of crack 1, crack 2 and part of crack 3 (which together form the *combined right part* from the 2-parts notch-specimen fracturing crack, Fig. 2f) with their corresponding growth rates in ***{da/dN−a}*** terms, propagation in {*N*−*a*} terms, and **PLM** applied to all data of ***{da/dN−a}*** Plot; here a part of crack 1 reaches the bifurcation point **A**, and a part of crack 3 reaches the merging of cracks 2 and 3 at point **B**

$[d_1, d_2]$, $[d_2, a]$) where d_1, d_2 are known as microstructural barriers connecting with microstructural influence on crack propagation;

– *functions* "Crack growth rate *da/dN*—Effective stress intensity factor range $\Delta K_{eff} = f(\Delta\sigma)a^{1/2}$", ***{da/dN−ΔK$_{eff}$}***, in semi-log scale (*N* in log scale and *a* and

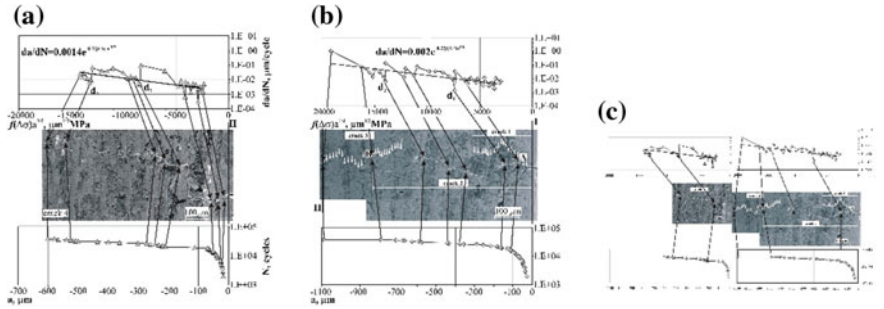

Fig. 5 Group **C**: Microstructural paths of crack 4 (**a**); the combined crack consisting of part of crack 1, crack 2 and part of crack 3 (**b**); and the whole fracturing crack of the notched specimen (**c**); microstructure is presented with crack corresponding growth rates in $\{da/dN-\Delta K_{eff}\}$ terms, propagation in $\{N-a\}$ terms, and **LM** applied to all data of $\{da/dN-\Delta K_{eff}\}$ Plot

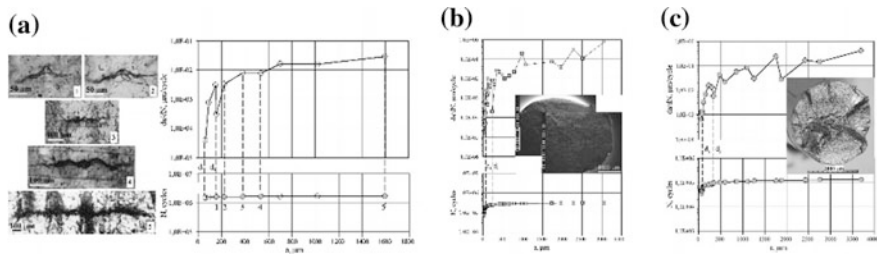

Fig. 6 Combined plots $\{da/dN-a$ **&** $N-a\}$ in semi-log scale for Group **A** (**a**); and Group **B** at $\Delta\sigma$ = 580 MPa (**b**) and $\Delta\sigma$ = 620 MPa (**c**); d_1 and d_2 are the microstructural barriers in **PLM** [8, 9]

ΔK_{eff} in ordinary one) represented by a new Linear Model, **LM**, Fig. 5; ΔK_{eff} is calculated in the same way as ΔK describing data from long fatigue-crack tests, f—the geometry factor in ΔK, $\Delta\sigma$—the applied stress range.

Propagation of the observed short cracks through the microstructure is presented in Figs. 2e, f, 4, 5, and 6.

The first analysis begins with a notched specimen from Group **C**. This specimen shows appearance of 8 cracks started from the notches, Fig. 2e, f [5]. Our main interest is focused on **cracks 1, 2, 3, 4** which fracture the specimen, Figs. 2f, 3, 4, and 5. The longest crack is crack 2, which originates from crack 1 as its branch at N = 15,000. At this moment **crack 1** has a length of 107,73 μm and higher da/dN than the others, Fig. 3b, but later on it becomes a non-propagating crack and stops at N = 27,000 with final length of 367,36 μm. After a bifurcation at point **A,** Fig. 2f, **crack 2** grows faster and more differently than the other cracks during the rest of fatigue lifetime, Fig. 3b; it causes the specimen failure, merging with cracks 3 (point **B**) and 4 which start from the top central notch. (In the beginning of its propagation crack 2 starts with permanently increasing da/dN, when the other

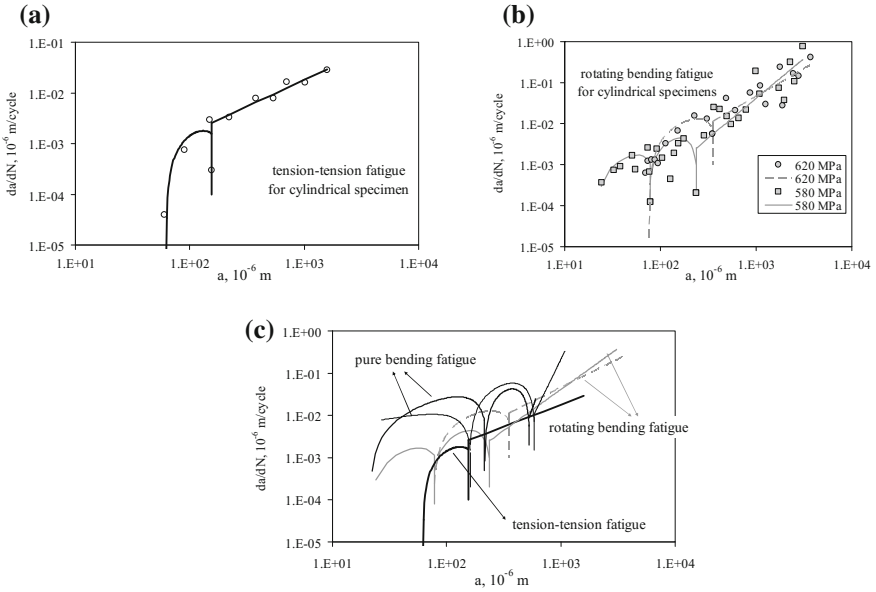

Fig. 7 Description of fatigue data by **PLM** [8, 9] for all **Groups** of specimens

cracks show mostly decreasing *da/dN* due to an intensifying crack closure effect. In detail as it is described in [5] the micronotch surfaces do not contact during the loading, hence in the beginning the propagating crack is open during the complete load amplitude, even at R = −1; with the growth of crack length, new-generated fracture surfaces come to an effective contact and crack closure load increases.) The central top notch is machined in the ferrite band, so that its right side is very close to the next pearlite band, Fig. 2a, f. Thus the **crack 3** starts its growing through the pearlite band at the very early loading cycles without significant retardation. On the other side of the top central notch, **crack 4** begins its growing into the ferrite band; in the beginning its growth is slower than that of crack 3. Afterwards both cracks continue to grow faster and faster through the microstructure having higher *da/dN* than those of the other central-notches cracks, Fig. 2e. It can be clearly seen in Figs. 4 and 5 that short fatigue crack growth data exhibit considerable fluctuations and scattering, and alternating decreases and increases in crack propagation rates. This effect is caused by the interactions between the crack tip and associated microstructural obstacles, and crack geometry. Such a behavior and data can be described by both the models: the newly modified **PLM** shown in Figs. 4 and 7, and the new **LM** which is applied only to the notch specimen and can be seen in Fig. 5; the adequacy of **PLM** is proved in [8, 9]. The equations of lines from **LM** are shown in Fig. 5; the lines include all fatigue data, but the corresponding correlation coefficients are low (in the range [0.48–0.58]). So, in this case of

preliminary notched specimen, the microstructure influence is very strong, dominating notch effects, which means that only **PLM** is suitable for describing the propagation of all the cracks initiated from the notches.

According to the microstructure influence on crack propagation, the most interesting data are obtained at **PB** fatigue where the fracturing crack consists of *left* & *right* parts, Fig. 2. These data show higher *da/dN* (dominated by the interaction with ferrite and pearlite grain boundaries and interfaces, ferrite grains, pearlite colonies and non-metal inclusions) and shorter fatigue life in comparison with the specimens subjected to **RB** fatigue. In general *da/dN* at **PB** fatigue decrease in the vicinity of (i) interface between ferrite and pearlite bands when a crack propagates into the ferrite or pearlite colony, (ii) ferrite-ferrite or pearlite-pearlite grain boundary, (iii) obstacles, where a crack changes its propagation direction or bifurcates. In this case, the observed rows of longitudinal nonmetal inclusions (MnS) increase *da/dN* serving as crack paths. The registered **T-T** data represent the lowest *da/dN*, due to much lesser loading than that applied at **RB** and **PB** fatigue.

Some of the minimums of *da/dN* in Figs. 4 and 5 are connected by arrows with the corresponding elements of the microstructure which slow down cracks propagation. The same elements are connected by other arrows with the corresponding crack lengths from the newly inserted Plots ***{N−a}***, built in semi logarithmic scale to correspond to real crack growth through the microstructure. In Fig. 4 there are examples of a perpendicular dash line to the *a*-axis, which connects a minimum of *da/dN* from ***{da/dN−a}*** Plot with the corresponding crack length from ***{N−a}*** Plot. The dash line is a *resulting line* which fixes the projection (on the *a*-axis) of the crack-length increase (between two successive interruptions of the cycles); usually crack propagates at an angle to the *a*-axis. Only in the case when a crack increase is perpendicular to the *a*-axis the *resulting dash line* coincides completely with the two arrows, Fig. 4.

Analyzing all fractured specimens [Groups **A** and **B** (Fig. 6)], [Group **C** (Figs. 4 and 5)], two important things have to be marked: **(1)** All *da/dN* minimums from ***{da/dN−a}*** Plot, connected by *resulting lines* (dash lines) with the corresponding crack lengths from ***{N−a}*** Plot show change in direction of propagating crack presented in ***{N−a}*** Plot. So when there are not direct observations of a crack propagation through the microstructure, the combined plots "Crack growth rate *da/dN*—Crack length *a*" & "Number of cycles, *N*—Crack length, *a*", ***{da/dN−a & N −a}***, can give some information about presence of obstacles or specific elements in the microstructure, Fig. 4 [8, 9]. This is of the special interest for the interval [crack initiation, d_1], Figs. 4, 5 and 6, as in this interval the influence of microstructure on crack propagation is the most pronounced one; the interval [d_1, d_2] (see Figs. 4, 5, and 6) is interesting too, as in this interval cracks change their mode from shear to tensile. In this sense Fig. 4 includes only one deep minimum which coincides with d_1; all the previous minimums do not influence significantly crack 2 propagation, as they belong to the primary growth of crack 1, from which crack 2 branches. In the interval [crack initiation, d_1], crack 1 develops from the edge notch and is not so

sensitive to the microstructure influence; **(2)** When cycle intervals (N_m and N_{m+1}) corresponding to two successive crack lengths (a_m and a_{m+1}) are almost equal and ($a_{m+1} - a_m$) is significantly bigger in comparison with the other crack length intervals, it means that there is probably a big real change in crack propagation direction—nearly at 90°, Fig. 4 [8, 9].

Conclusions

Three groups of specimens made of low-carbon steel with ferrite and pearlite microstructure are subjected to **T-T**, **RB** and **PB** fatigue. The obtained data at **PB** fatigue show higher crack growth rates (dominated by the interaction with ferrite and pearlite grain boundaries and interfaces, ferrite grains, pearlite colonies and non-metal inclusions) and shorter fatigue life in comparison with the specimens subjected to **RB** fatigue. The registered **T-T** fatigue data present the lowest crack growth rates, due to much lesser loading than that applied at **RB** and **PB** fatigue.

The newly inserted Plots "Number of cycles, *N*—Crack length, *a*" in semi logarithmic scale are a basis for using combined presentations *"Crack growth rate da/dN—Crack length a" & Microstructure & "Number of cycles, N—Crack length, a"* for more successful analyzing of microstructural crack paths together with fatigue characteristics; also for getting some useful information even without detailed microstructural observations.

The applied modified **PLM** can describe and predict more adequately microstructurally short crack behaviour under conditions of **T-T**, **RB** and **PB** fatigue (even in notch specimens) than the newly introduced **LM**; the model of parabolic-linear functions allows comparison between fatigue characteristics at different kind of loading.

Acknowledgements Our work is valuably supported by the Company ALCOMET AD—Leading Bulgarian manufacturer of aluminum rolled and extruded products, and the University of Chemical Technology and Metallurgy-Sofia, Bulgaria.

References

1. Suresh, S., 1998. Fatigue of Materials. Cambridge Univ. Press, Cambridge, UK
2. Dowling, N., 2006. Mechanical Behavior of Materials. Engineering Metods for Deformation, Fracture, and Fatigue. 3th edition, Prentice Hall
3. Angelova, D., Yordanova, R., 2009. Bending Fatigue in a Low-Carbon Steel, in the Book "Fracture Mechanics of Materials and Structural Integrity", 4th International Conference, 23–27 June 2009, Lviv, Ukraine, 309–314
4. Davidkov, A., 2007. On factors influencing fatigue in 09Mn2 steel, PhD Thesis, University of Chemical Technology and Metallurgy–Sofia
5. Davidkov, A., Pippan, R., 2006. Studies on short fatigue crack propagation through a ferrite-pearlite microstructure, 9-th International Fatigue Congress, Atlanta, Georgia, USA

6. Yordanova, R., 2003. Modeling of fracture process in a low-carbon 09Mn2 steel on the bases of short fatigue crack growth experiments. Comparative analyses on the fatigue behaviour of other steels, PhD Thesis, University of Chemical Technology and Metallurgy–Sofia
7. Angelova, D., Davidkov, A., 2005. In: Proceedings of Second International Conference Deformation, Processing and Structure of Materials, Belgrade, Serbia and Montenegro, 179–184
8. Angelova, D., Yordanova, R., Yankova, S., 2015. Fatigue crack paths in a low-carbon steel. Modelling of fatigue behaviour, 5th Int. Conference on Crack Paths CP 2015, Ferrara, Italy
9. Donka Angelova, Rozina Yordanova, Svetla Yankova, 2016. Fatigue crack development in a low-carbon steel. Microstructure influence. Modelling, Procedia Structural Integrity, Volume 2, pp. 2726–2733

Determination of the Region of Stabilization of Low-Cycle Fatigue HSLE Steel from Test Data

Bojana Aleksić, Vujadin Aleksić, Abubakr Hemer, Ljubica Milović and Aleksandar Grbović

Introduction

The most important role in fracture of the materials of machine parts and structures has various types of fatigue. The fatigue life of reliable components of engineering elements, such as bearings, which are exposed to variable load over the life of exploitation, can be estimated by the analysis of the behaviour that includes processing of the data on loading, geometry and the material selected for manufacture of the bearings, both by simulation and experimentally [1–5].

Steel, NN-70, selected in this study to investigate the experimental behaviour affected by fatigue loading, among other things, is used in shipbuilding and for manufacture of pressure vessels as well. The experiment was conducted using smooth round specimens made of steel NN-70 as parent material (PM). When selecting stabilized hysteresis as a representative of all of stabilized hysteresis for one strain level, and for the further processing of low-cycle fatigue test results, the recommendations of standards [6, 7] have been used as well as the methodology

B. Aleksić (✉)
Innovation Centre of Faculty of Technology and Metallurgy,
Karnigijeva 4, 11120 Belgrade, Serbia
e-mail: baleksic@tmf.bg.ac.rs

V. Aleksić
Institute for Testing Materials—IMS Institute, Bulevar vojvode Mišića 43,
11000 Belgrade, Serbia

A. Hemer · L. Milović
Faculty of Technology and Metallurgy, University of Belgrade,
Karnigijeva 4, 11120 Belgrade, Serbia

A. Grbović
Faculty of Mechanical Enginnering, University of Belgrade,
Kraljice Marije 16, 11120 Belgrade, Serbia

R. R. Ambriz et al. (eds.), *Proceedings of the 17th International Conference on New Trends in Fatigue and Fracture*, https://doi.org/10.1007/978-3-319-70365-7_12

based on which linearity of the stabilization regions of low-cycle fatigue was numerically determined [8].

Background and Characteristics of Steel NN-70

Parent material (PM) used to make the test specimens was a plate of the dimensions (45 × 205 × 353) mm made of low-alloy high-strength steel NN-70 with properties shown in Tables 1 and 2.

Steel NN-70 is the Yugoslav version of American steel HY-100 and is intended for manufacture of ship structures, submarines and pressure vessels by welding, where the required toughness is extremely important. The technology of manufacture and thermomechanical processing (TMCP steels [10]) of the steel called Nionikral-70 is the result of joint research work of the metallurgists of Military Technical Institute in Žarkovo (VTI) and the steelworks "Jesenice" from Jesenice [11], in the early 90s of the last century. It was made in the electric furnace, cast in brams, subsequently rolled into slabs and finally the sheets of various thicknesses. Due to some of its characteristics, it is classified among the fine-grained steels. The process of hardening is the combination of classical improvement (quenching and tempering) with grain refinement in accordance with selected chemical composition, by micro-alloying and appropriate deposition [12]. In determining the limit values of carbon and other alloying elements for the analysis, bearing in mind the purpose of the steel, care was taken to meet the requirements for the combination of characteristics such as strength, ductility, resistance to crack initiation and propagation, the stability of these properties at low temperatures, good resistance to fatigue and stress corrosion, and good workability and weldability [12]. Steel NN-70 is intended to be shaped by welding, so that after it was successfully mastered, its suitability for welding was also subjected to assessment [11].

Table 1 Chemical composition of NIONIKRAL 70, %wt [8]

C	Si	Mn	P	S	Cr
0.106	0.209	0.220	0.005	0.0172	1.2575
Ni	Mo	V	Al	As	Sn
2.361	0.305	0.052	0.007	0.017	0.014
Cu	Ti	Nb	Ca	B	Pb
0.246	0.002	0.007	0.0003	0	0.0009
W	Sb	Ta	Co	N	–
0.0109	0.007	0.0009	0.0189	0.0096	–

Table 2 Mechanical properties of NIONIKRAL 70 [8]

Property	PM
Ultimate tensile strength, MPa	855, rounded value
Yield strength, MPa	815, rounded value
Elastic modulus, GPa	221.4, dynamic, LCF
Impact toughness, J	97, rounded value, 20 °C
E initiation, J	40, rounded value, 20 °C
E propagation, J	57, rounded value, 20 °C
HV30, plate of PM	257, mean value, plate of PM
HV10, stick for LCF specimen [9]	257, mean value, specimen of LCF

Testing of Steel NN-70 at Low-Cycle Fatigue

From the necessity to assess the low-cycle fatigue life, and in order to determine the fatigue characteristics of the material, the test of resistance of the parent material (PM) of steel NN-70 to low-cycle fatigue was carried out. Preparation of the test of resistance of steel NN-70 to low-cycle fatigue consisted of making smooth cylindrical specimens, Fig. 1 item 1, and tool for placing the specimens in the tearing-machine jaw, Fig. 1 items 2 and 3, and check of the target static tensile properties of steel NN-70, Table 2.

The procedure for determination of the low-cycle fatigue characteristics and geometry of cylindrical smooth specimen as well, Fig. 1 item 1, is defined by the ISO 12106:2003(E) [6] and ASTM E 606-04^{e} [7] standards.

Fatigue test was conducted on a universal MTS system (Material Testing System—Universal hydraulic dynamic tearing machine of 500 kN) for the material testing, schematically presented by photos in Fig. 2.

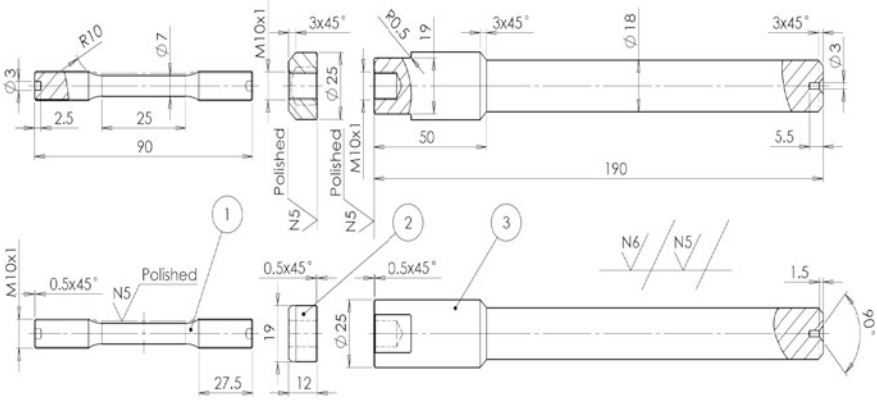

Fig. 1 Specimen and specimen holder for testing LCF of steel NN-70 [8]. Item 1, LCF specimen, NN-70, D = 7 mm; item 2, Jam nut, 42CrMo4; item 3, Grip holder, 42CrMo4.

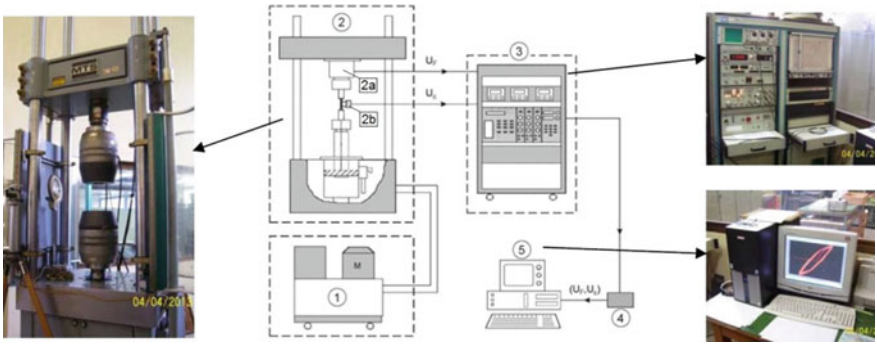

Fig. 2 MTS universal system for the material testing, 1—Hydraulic aggregate, 2—Pulsating device, 2a—MTS force-feeding device, 2b—MTS extensometer, 3—Control system, 4—A/D convertor, 5—PC

Used MTS force-feeding device, Fig. 2 item 2a, with linear characteristics $F[kN] = F[V] \cdot 10$, and MTS extensometer with measuring length of $L_0 = 25$ mm, Fig. 2 item 2b with linear characteristics $\varepsilon[\%] = \varepsilon[V] \cdot 0.2$, are graphically presented in Fig. 2.

Low-cycle fatigue tests were performed on a series of smooth specimens made of steel NN-70, with semi-amplitudes of controlled and fully reversible strains, $\Delta\varepsilon/2 = 0.35, 0.45, 0.50, 0.60, 0.70$ and 0.80 ($\Delta\varepsilon/2 = \text{const}$, $R_\varepsilon = \varepsilon_{min}/\varepsilon_{max} = -1$).

Numerical Determination of the Region of Stabilization

Most of the materials, at low-cycle fatigue and at a certain level regulated strain, achieve a so-called stabilized condition. It is a condition when the height of the hysteresis loop expressed through a range of force of loading or stress slightly changes, Fig. 3 item 9.

The most common methods for determination of the number of cycles to crack initiation, N_f, are defined by the standards [6, 7]. New methods [8] for determination of the beginning and end of the crack initiation and establishment of linearity of stabilization regions are based on experimental data, by arbitrary selection of three cycles on the basis of which we can establish linearity that we maintain by filtering the data in the programme EXCEL, toward the beginning and end of the test. The results of established linearity in the areas of stabilization for steel NN-70 are shown in Table 3.

In this way we determine the initial, N_{bs}, and final, N_{es}, cycle of stabilization, i.e. the beginning and end of the crack initiation, Fig. 4a. Stabilized hysteresis, N_{s1}, Fig. 4b, is located in the middle of the region 9, Fig. 3, and is determined by the formula, $N_{s1} = N_{bs} + (N_{es} - N_{bs})/2$. This method of determination of the stabilized hysteresis, N_{s1}, is called "Method of the middle stabilization (ms)" [8]. In a similar

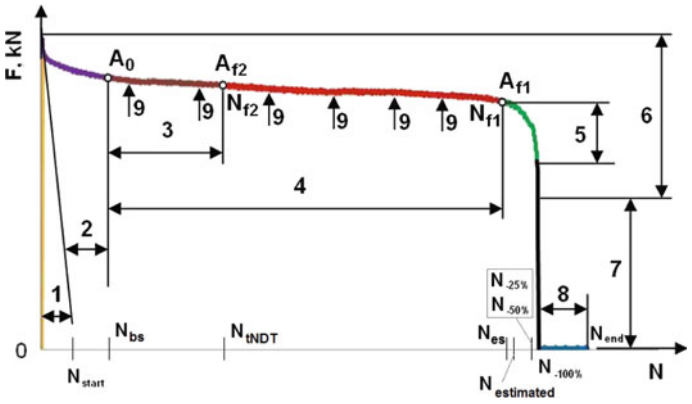

Fig. 3 Regions of low-cycle fatigue. 1—Adjustment of tearing machine, 2—Adaptation of tearing machine, tools and specimen, 3—Crack formation up to threshold of NDT, 4—**Stabilized state**, 5—Force drop of 25 % (ISO 12106:2003(E)) [6], 6—Force drop of 50 % (ASTM E 606-04) [7], 7—Force drop to F = 0, 8—Stoppage of tearing machine, 9—Height of hysteresis loop, N_{start}—Test start up, **F=max**, N_{bs}—Beginning of stabilization, A_0, mm, N_{tNDT}—threshold of the NDT, A_{f2}, mm, N_{es}—End of stabilization, A_{f1}, mm, $N_{estimated}$—force-drop assessment of an operator, N_{end}—Test termination, A_0—initial cross-section of the specimen (css), A_{f1}—css at the end of stabilization, A_{f2}—css at the threshold of the NDT

way, we can establish a cycle of appearance of a crack of 1 mm^2 surface area [13], which can be identified by the NDT methods, which is called the "threshold NDT method (tNDT)" [8], and then the cycle of stabilized hysteresis, N_{s2}, Fig. 4b, which is located in the middle of the region 3, Fig. 3, so that $N_{s2} = N_{bs} + (N_{tNDT} - N_{bs})/2$. This procedure was applied to other specimens as well, i.e. other strain levels, $\Delta\varepsilon/2 = 0.35$, 0.45, 0.50, 0.60, 0.70 and 0.80.

The accuracy of determination of the exponents and coefficients of cyclic stress-strain curve (**CSSC**) and basic curve of low-cycle fatigue (**BCLCF**) depends on accuracy of determination of linearity of stabilization region (for **7 samples**, determination coefficient, $\mathbf{R^2 = 0.85–0.98}$, Table 3) and for chosen method for determination of the stabilization curve it ranges as follows: for CSSC (for ms method for determination of $\mathbf{n'}$ and $\mathbf{K'}$ it is $\mathbf{R^2 = 0.66}$, and for tNDT method it is $\mathbf{R^2 = 0.62}$, Table 4, while for BCLCF (for ms method for determination **b** and $\boldsymbol{\sigma_f'}$ it is $\mathbf{R^2 = 0.77}$, and tNDT it is $\mathbf{R^2 = 0.78}$, Table 4) (for ms method for determination of **c** and $\boldsymbol{\varepsilon_f'}$ $\mathbf{R^2 = 0.72}$ **and for tNDT method** $\mathbf{R^2 = 0.68}$, Table 4).

After processing of registered data from all stabilized hysteresis of interest obtained using the methodology described, the curves of low-cycle fatigue for steel NN-70 are defined [14]:

Table 3 Data on the area of stabilization and characteristic cycles of LCF for PM of steel NN-70

Specimen	Δε/2%	Stabilization regions		Characteristic cycle of stabilization					
		y = F, kN; x = N	R^2	N_{bs}	$Nt_{NDT} = N_{f2}$	[b]N_{s2}	$N_{es} = N_{f1}$	[a]N_{s1}	
PM-01	0.35	y = −0.002x + 26.77	0.98	385	668	527	948	667	
PM-10	0.45	y = −0.001x + 29.01	0.95	210	535	373	1354	782	Figure 4
PM-03	0.50	y = −0.002x + 28.57	0.97	256	575	416	1271	764	
PM-06	0.60	y = −0.005x + 29.65	0.94	127	261	194	415	271	
PM-07	0.60	y = −0.006x + 29.84	0.90	97	210	154	293	195	
PM-05	0.70	y = −0.006x + 29.04	0.91	135	272	204	333	234	
PM-08	0.80	y = −0.013x + 30.47	0.85	82	142	112	165	124	

[a]Ns1 = Nbs + (Nes − Nbs)/2
[b]Ns2 = Nbs + (NtNDT − Nbs)/2

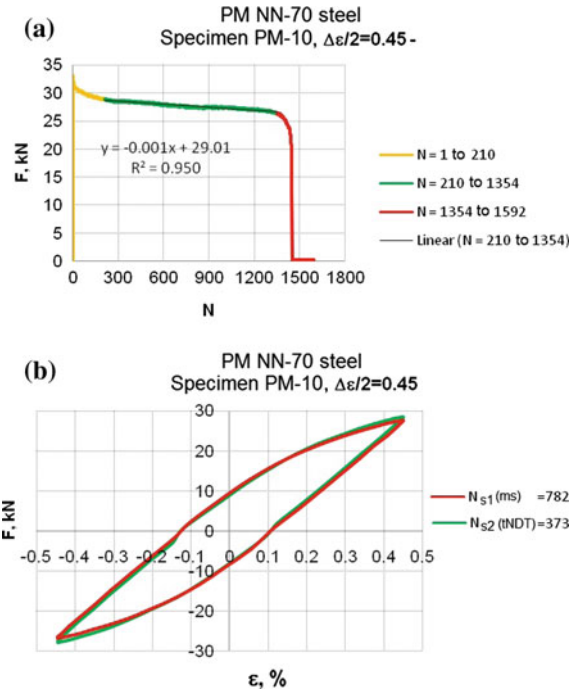

Fig. 4 **a** The region of stabilization, N = 210 to 1354 and **b** stabilized hysteresis in cycles Ns1 = Ns(ms) = 782 and Ns2 = Ns(tNDT) = 373

Cyclic stress-strain curves,

$$\frac{\Delta\varepsilon}{2} = \frac{\Delta\sigma}{2E} + \left(\frac{\Delta\sigma}{2K'}\right)^{\frac{1}{n'}}:$$

$$\text{for } \underline{\mathbf{N_{s1}}}: \frac{\Delta\varepsilon}{2} = \frac{1}{221378}\cdot\frac{\Delta\sigma}{2} + \left(\frac{1}{946.2}\cdot\frac{\Delta\sigma}{2}\right)^{\frac{1}{0.047}}, \tag{1}$$

$$\text{for } \underline{\mathbf{N_{s2}}}: \frac{\Delta\varepsilon}{2} = \frac{1}{221378}\cdot\frac{\Delta\sigma}{2} + \left(\frac{1}{887.2}\cdot\frac{\Delta\sigma}{2}\right)^{\frac{1}{0.032}}$$

and

Basic curves of low-cycle fatigue,

$$\frac{\Delta\varepsilon}{2} = \frac{\sigma'_f}{E}N_f^b + \varepsilon'_f N_f^c:$$

$$\text{for } \underline{\mathbf{N_{s1}}}: \frac{\Delta\varepsilon}{2} = 0.005105\cdot N_f^{-0.061} + 0.0612\cdot N_f^{-0.564}, \tag{2}$$

$$\text{for } \underline{\mathbf{N_{s2}}}: \frac{\Delta\varepsilon}{2} = 0.005117\cdot N_f^{-0.065} + 0.0881\cdot N_f^{-0.695}$$

Table 4 Coefficient of determination (R^2) in processing of the data from LCF tests of PM of NN-70

		CSSC			BCLCF					
Specimen	Δε/2%	n′	K′	R^2	b	σ_f'	R^2	c	ε_f'	R^2
		1 2	1 2	1 2	1 2	1 2	1 2	1 2	1 2	1 2
PM-01	0.35	0.047 0.032	946.2 887.2	0.66 0.62	−0.061 −0.065	1130.1 1132.7	0.77 0.78	−0.564 −0.695	0.0612 0.0881	0.72 0.68
PM-10	0.45									
PM-03	0.50									
PM-06	0.60									
PM-07	0.60									
PM-05	0.70									
PM-08	0.80									

1 Method of the middle stabilization (ms), $N_{s1} = N_{bs} + (N_{es} - N_{bs})/2$

2 Threshold NDT method (tNDT), $N_{s2} = N_{bs} + (N_{tNDT} - N_{bs})/2$

Processing and Presentation of Test Results

As a result of low-cycle fatigue test on one specimen (one amplitude level of strain) there is a record in the program EXCEL which, using the tools available in EXCEL, can be further processed according to our requirements [8]. Before processing of the results it is possible to roughly determine the cycle in which there is a significant drop of force, $N_{estimated}$. To determine the indicators of low-cycle fatigue of the material presented by cyclic stress-strain curve (CSSC) and basic curve of low-cycle fatigue (BCLCF), the following analyses of the results of low-cycle fatigue tests were made:

1. For each amplitude level of strain (each specimen), by filtering the data, extreme values of the load forces and number of cycles were paired, and thus we eliminated the excess data. Both positive and negative values of the load forces were filtered.
2. The diagrams of extreme values of the load forces and number of cycles (F-N curves) were drawn for each amplitude level of strain.
3. The diagrams of determination of the areas of stabilization, Fig. 4a, were drawn (positive part of the F-N curves, the area of stabilization, was determined by linearization of the data on maximum tensile forces of load in low-cycle fatigue tests for each amplitude level of strain, Table 3). The areas of low-cycle fatigue and characteristic hysteresis were defined after the following:
    a. Determination of maximum force and starting cycle N_{start},
    b. Determination of the cycle of start of stabilization, N_{ss}, end of stabilization, N_{es}, threshold of NDT, N_{tNDT} and area of stabilization,
5. The characteristic data of stabilized hysteresis curves, Fig. 4b, for each amplitude level of strain were defined:
    a. Extreme values of load force F_{smax} and F_{smin} were read.
    b. The spots of intersection of the hysteresis curve and positive part of strain axis were established in EXCEL (coefficients of the straight line, m and b [8] were determined). This can be done graphically [4], too, in some of the programmes for precision drawing. $\Delta\varepsilon_p/2$, $\Delta\varepsilon_e/2$, $A_0 = D^2 \cdot \pi/4$ (3), $F_{mean} = (\,|\,F_{smak}\,|\,+\,|\,F_{smin}\,|\,)/2$ (4) i $\Delta\sigma/2 = F_{mean}/A_0 \cdot 1000$ (5) values were calculated.
6. The data on all amplitude levels of strain were classified, cyclic stress-strain curves and basic curves of low-cycle fatigue were constructed [8, 15] and cyclic versus monotonous stress-strain curves compared, Figs. 5 and 6:
    a. The exponents and coefficients were determined using linearized step function, n' and K'.
    b. The exponents and coefficients were determined using linearized elastic component, b and σ'_f. The exponents and coefficients of linearized plastic component, c and ε'_f, were determined.

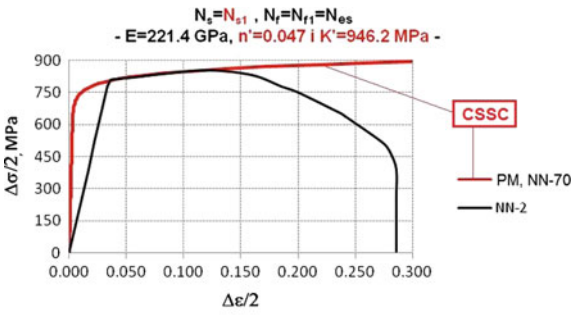

(a) $N_f = N_{fl}$ (End of stabilization [8])

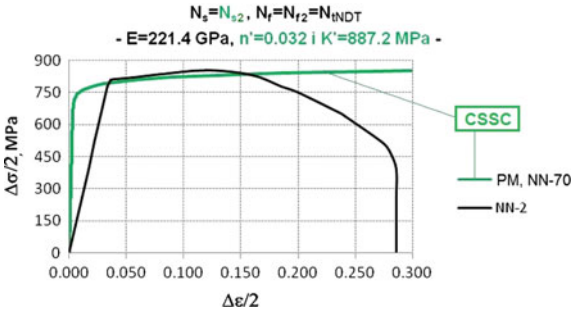

(b) $N_f = N_{f2}$ (threshold of NDT [8])

Fig. 5 Comparison of cyclic (CSSC) and monotonous stress-strain curve of PM of NN-70 steel

7. The data on cyclically stress-strain curves, Fig. 5a, b, and basic curves of low-cycle fatigue, Fig. 6a, b, were classified for the group of selected stabilized hysteresis, N_{s1} and N_{s2}, in order to construct them [8], and finally,
8. Transition life, N_{fT}, was determined for a group of selected stabilized hysteresis, N_{s1} and N_{s2}, Fig. 6a, b and Table 5 [8].

Conclusions

The theoretical, experimental and numerical research of the behaviour of low-alloy high-strength steels exposed to loading induced by low-cycle fatigue that are described in this paper are very complex research task. Extensive theoretical studies have required synthesis of knowledge in multiple engineering fields and disciplines, and numerical and experimental studies are an important part of this work. One of the goals of the research imposed itself during the processing of the results of experimental investigations, and is expressed through improvement of the methodology and methods of processing of the test results in order to establish a

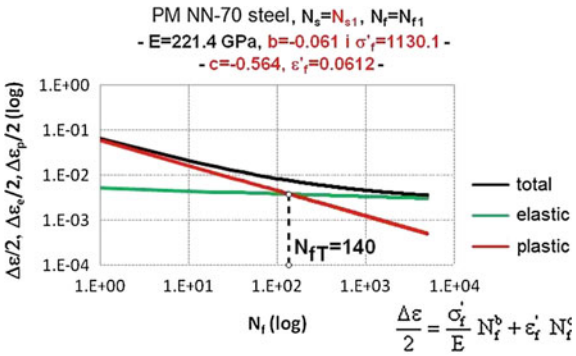

(a) $N_f = N_{f1}$ (End of stabilization [8])

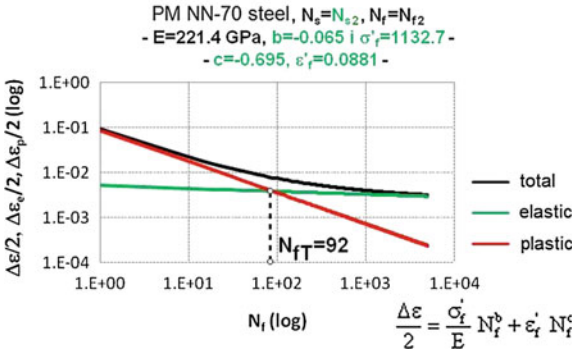

(b) $N_f = N_{f2}$ (threshold of NDT [8])

Fig. 6 Basic curve of low-cycle fatigue of PM of NN-70 steel

Table 5 Transition life of PM of steel NN-70

PM, NN-70	E, MPa	221378	Elastic part		Plastic part		
	N_f	N_s	b	σ'_f	c	ε'_f	N_{fT}
$N_{s1} = N_{ps} + (N_{ks} - N_{ps})/2$	$N_{ks} = N_{f1}$	N_{s1}	−0.061	1130.1	−0.564	0.0612	**140**
$N_{s2} = N_{ps} + (N_{pNDT} - N_{ps})/2$	$N_{pNDT} = N_{f2}$	N_{s2}	−0.065	1132.7	−0.695	0.0881	**92**
Transition life			$N_{fT} = \left(\frac{\varepsilon'_f \cdot E}{\sigma'_f}\right)^{\frac{1}{b-c}}$ (6)				

N_{fT} is transition life of PM of steel NN-70, and we calculated it for two different methods

universal methodology for assessment of the behaviour of materials affected by low-cycle load. The results of experimental investigation have given us important information about the understanding of fatigue behaviour of HSLA steel, NN-70, and the newly applied methods and recommendations of standards as well have enabled the precise determination of characteristic stabilized hysteresis for each strain level. From certain characteristic stabilized hysteresis, based on defined

criteria, the data necessary for determination of the equations of characteristic curves of low-cycle fatigue have been collected, which show the difference between the values of exponents and coefficients defined by presented methodology depending on the method applied for the determination of stabilized hysteresis.

The results obtained represent practical contribution to estimation of the behaviour of low-alloy high-strength steel NN-70 exposed to the effects of low-cycle fatigue.

Acknowledgements This work is a contribution to the Ministry of Education and Science of the Republic of Serbia funded Project TR 35011.

References

1. Ferjaoui A, Yue T, Abdel Wahab M and Hojjati-Talemi R, 2015, *International Journal of Fatigue* 73, 66–76.
2. Kumar D, Biswas R, Poh LH and Abdel Wahab M, 2017, *Tribology International* 109, 124–132.
3. Bhatti NA and Abdel Wahab M, 2017, *Tribology International* 109, 552–562.
4. Resende Pereira KdF, Bordas S, Tomar S, Trobec R, Depolli M, Kosec G and Abdel Wahab M, 2016, *Materials* 9 639; https://doi.org/10.3390/ma9080639.
5. Hojjati Talemi R and Abdel Wahab M, 2013, *Tribology International* 60, 176–186.
6. ISO 12106:2003(E): Metallic materials-fatigue testing-axial-strain-controlled method, Geneva: ISO 2003, Switzerland.
7. ASTM E606-04, Standard practice for strain-controlled fatigue testing, ASTM International, West Conshohocken, Pennsylvania, USA.
8. Aleksić V., 2016, *Low-cycle fatigue of high-strength low-alloy steels*, The draft version of the doctoral dissertation reported on the Serbian, University of Belgrade, Faculty of Technology and Metallurgy, Belgrade.
9. Bulatović S., 2014, *Elastic-plastic behaviour of welded Joint of high-strength low-alloy in conditions of low-cycle fatigue*, Doctoral dissertation on the Serbian, University of Belgrade, Faculty of Mechanical Engineering, Belgrade.
10. Radović N., Drobnjak Đ., 2001, *Development of steels for fabrication on welded constructions with improved safety*, Welding and Welded Structures, vol. 46, No. 3, p. 81–92.
11. Grabulov V., 1986, A contribution to the assessment of chemical composition and plate thickness influence on crack initiation in welded joints made of Nionikral 70 steel, Master thesis on the Serbian, University of Belgrade, Faculty of Technology and Metallurgy, Belgrade.
12. Radović A., Marković D., 1984, *The conquest of shipbuilding steel of high-strength - NIONIKRAL-70*, The report in Serbian, Military Technical Institute, Belgrade.
13. Janković D. M., Malociklusni zamor, Univerzitet u Beogradu, Mašinski fakultet, Beograd, 2001.
14. Aleksić V., Aleksić B., Milović Lj.: *Methodology for determining the region of stabilization of low-cycle fatigue*, Book of Abstracts, 16th International Conference on New Trends in Fatigue and Fracture (NT2F16), May 24–27, 2016, Dubrovnik, Croatia, p. 189–190.
15. Aleksić V., Milović Lj., Aleksić B., Abubkr M. Hemer: *Indicators of HSLA steel behaviour under low-cycle fatigue loading*, 21st European Conference on Fracture, ECF21, 20–24 June 2016, Catania, Italy, Procedia Structural Integrity 2 (2016) 3313–3321.

Study of a Stud Bolt Wrench Failure Due to an Inadequate Heat Treatment

Sandra L. Rodriguez-Reyna, Francisco G. Perez-Gutierrez, J. Luis Hernández-Rivera, Jorge Zaragoza-Siqueiros and Christian J. Garcia-Lopez

Introduction

Forensic engineering (FE) relates engineering and scientific facts to re-build the events sequence that leaded a mechanical component to failure. Its objective is to propose modifications to fabrication or operation procedures and standards to avoid future failures [1]. FE is supported by several disciplines such as: chemical metallurgy, materials science and engineering, mechanics, manufacturing processes, design, and finite element method, among many others. Nowadays, the reasons for a mechanical component to fail are well known and these could be: wrong material selection, wrong design, wrong fabrication and/or treatment, material imperfections, wrong assembly, wrong operation conditions.

FE has had progress during the last decades, which has allowed a perfect understanding of the most common causes that produce material failures. However it is still not possible to accurately predict how a component will fail, when it is subjected to mechanical and/or thermal stress, different strain rates and any other mechanism that modifies its internal structure. Even the most sophisticated simulation testing cannot adequately duplicate the varied factors and the many unanticipated events that may lead to failure [2]. The objective of this work is to provide a better understanding of the events that leaded the stud bolt wrench to fracture, so that necessary actions are taken to avoid the same problem in the future.

S. L. Rodriguez-Reyna (✉) · F. G. Perez-Gutierrez · J. L. Hernández-Rivera · J. Zaragoza-Siqueiros · Christian J.Garcia-Lopez
Facultad de Ingeniería, Universidad Autónoma de San Luis Potosí,
Av. Dr. Manuel Nava No. 8, Zona Universitaria, 78290
San Luis Potosí, S.L.P., Mexico
e-mail: sandyreyna@uaslp.mx

R. R. Ambriz et al. (eds.), *Proceedings of the 17th International Conference on New Trends in Fatigue and Fracture*, https://doi.org/10.1007/978-3-319-70365-7_13

Materials and Methods

The first step was to perform a historical study of the part to know the fabrication process and operation conditions while failure occurred. The company which produces this assembly was the source of such information. Once this information was collected, a chemical analysis was carried out to figure out the type of steel used to make the part. Later, in order to figure out the most probable region for failure, metallographic, tensile strength and hardness tests were carried out.

A stud bolt wrench is an "L" shape tool used to easily apply a torque and remove or tighten the stud bolts from a vehicle's wheel. It was made of two components: the lever and the wrench connector (Fig. 1). To perform the assembly, the wrench connector was heated to expand the material, which allowed easy coupling between the lever and the connector. Later, when the connector cooled down, it was positioned between both lever's stoppers. Finally, the complete assembly was subjected to a normalizing heat treatment. During the tests to validate the production, the wrenches were subjected to a torque of approximately 180 Nm. The failure that was analyzed in this work occurred during these tests in several pieces in the lever-wrench connector as it is shown in Fig. 2.

The pieces that failed showed a fracture in the same region, just next to the hole where the lever was inserted. Two groups from different production batches were analyzed in order to make comparison between their properties. Three samples were tested on each group. All the wrenches in the first group showed the mentioned fracture while the second group did not show any failure.

For a microstructural analysis, test pieces from batches with and without failure were cut, polished, attacked with 3% Nital and prepared for metallographic analysis according to the ASTM E3-01 standard [3]; observations were done using an Axiotech Zeiss optical microscope equipped with an Axio Cam at 500x and 1000x magnification. In addition, 3 samples 0.5″ in diameter and 2″ long were cut from samples with and without failure according to the ASTM E-08 standard [4] in order to carry out tensile tests and determine the yield stress and ultimate tensile strength (UTS). A head velocity of 0.5 mm/min was used. Such tests were carried out using

Fig. 1 Stud bolt wrench assembly

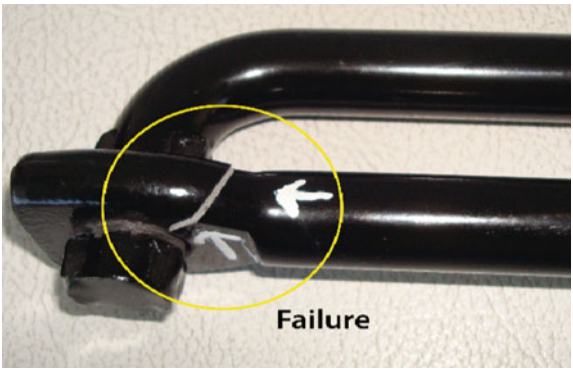

Fig. 2 Photograph which shows the region on which the failure occurred

a 10 kN AG-1 SHIMADZU universal testing machine. Rockwell C hardness tests were carried out using a Zwick ZU250 hardness tester equipped with a diamond indenter and a 1500 kN load.

Results

Chemical Composition

Table 1 shows the chemical analysis for the samples with and without failure. It can be observed that there was no significant difference between samples. The greatest difference was the magnesium content, which was not critical for the purposes of this study. Based on these results, it was suggested that it can be a medium carbon steel with silicon and copper content lower than 1.65 and 0.60%, respectively. Due to the fact that the total content of alloying elements was less than 5%, it was a low-alloy steel.

Table 1 Chemical composition of the test pieces (wt%)

	C	Mn	S	P	Si	Cu	Ni	Mo	Al
Without failure	0.45	0.6	0.06	0.02	0.26	0.48	0.025	0.005	0.002
With failure	0.46	0.67	0.06	0.02	0.27	0.46	0.025	0.003	0.002

Mechanical Properties

During the machining of the test pieces for tensile tests, some pieces from the batch with failure showed difficulties with the tools and the final roughness, which can indicate that the machinability was poor. Such initial observation allowed suspecting that there could be hardness gradients along the part. Figure 3 shows the results obtained from the tensile tests for pieces with and without failure. It can be observed that, for the part that failed, the UTS (760 MPa) and yield stress (600 MPa) are higher compared with the samples that did not (590 and 400 MPa, respectively). In contrast, the elongation of the first is slightly lower compared to that of the second. Based on these mechanical properties values and the chemical composition analysis, the material seems to be a 1045 steel.

Figure 4 shows pictures of the entire length of the part where hardness measurements were obtained. Figure 5 shows the comparison of the results for parts that failed and parts that did not fail. The piece that did not fail showed relatively uniform hardness values distribution between 20 and 28 HRC along the entire connector, while the piece that failed showed discontinuous hardness values ranging from 20 and 60 HRC, being the higher values in the region next to failure zone while the lower hardness values were found near the opposite side. Such observation provided reasons to believe that this was the region where the fracture was originated.

It is clear from Fig. 5 that after indentation 4, hardness values for the sample with failure are higher than those for the piece without failure by a factor of three. Since both samples had the same global chemical composition, such a significant difference in hardness values can be explained if the microstructure in both pieces is examined in detail.

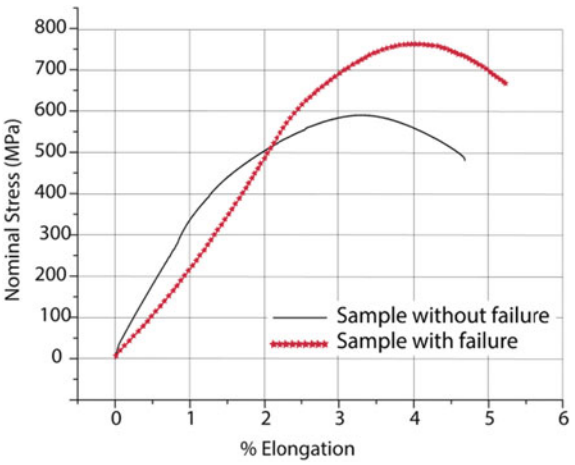

Fig. 3 Stress-strain curves obtained during tensile tests for test pieces with and without failure

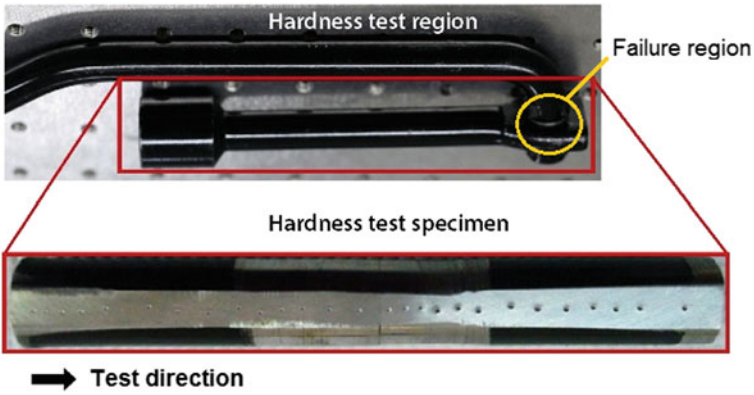

Fig. 4 Regions where hardness was measured

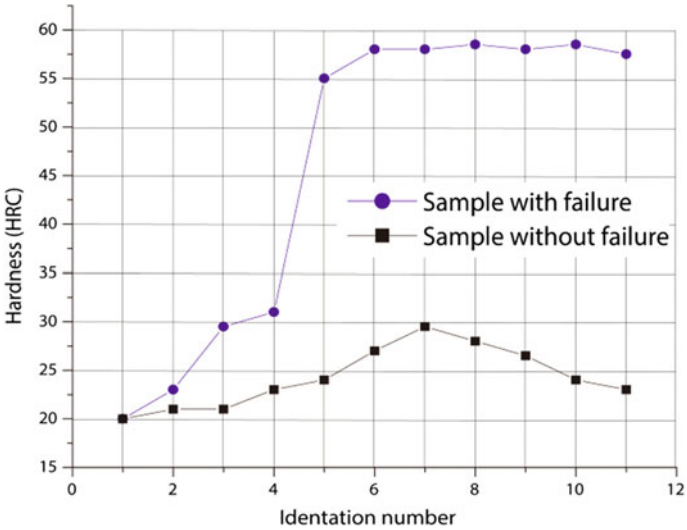

Fig. 5 Hardness profile obtained in samples with (squares) and without (circles) failure

Metallographic Tests

Figure 6 shows SEM images obtained from the surface of the fracture. It was found that there was very little evidence of plastic deformation, i.e. there was no material yielding, which means that the connector experienced brittle fracture. The appearance of Fig. 6b supports this fact since there were very few areas with dimples which are characteristic of a ductile fracture. In contrast, it can be seen that most of the fracture surface contains characteristics of intergranular fracture (flat brightly surfaces). The fracture began next to the hole (bottom part) and propagated

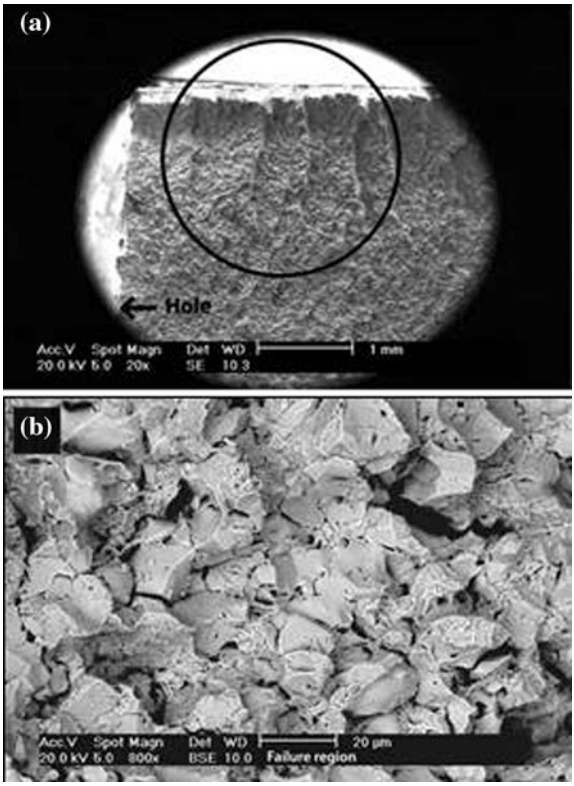

Fig. 6 SEM micrographs that show the details of the piece with failure

rapidly towards the exterior of the component (top part). In fact, Fig. 6a shows a set of radial lines, which are called "Chevron lines" [5]. These lines are also the result of the intersection and connection of cracks that propagated in different zones. In other research about failure analysis of open end wrenches, the fractographic inspection of the failure surfaces indicated brittle overload. A chevron pattern was present on the fracture surface, which indicated that the fracture initiated at the edge of wrench face [6], in a similar way to this research study. On the other hand, Nasrazadani [7] have observed the disadvantage of applying a deficient heat treatment when a wrench socket fails during service. In this case, the observed failure was of ductile nature in low carbon steel produced by powder metallurgy.

Figure 7 shows the microstructure of the sample that did not fail. Figure 7a shows the microstructure of a hipoeutectic steel (C content lower than 0.77%), which shows primary ferrite α (white regions) and perlite (dark regions). This type of microstructure was formed when the steel was cooled and the austenite was transformed into pearlite through an eutectic reaction [8]. Figure 7b shows the same microstructure at a higher magnification. The temperature required for austenite formation onset is 770 °C, being ferrite (α) formed around the austenite phase during cooling.

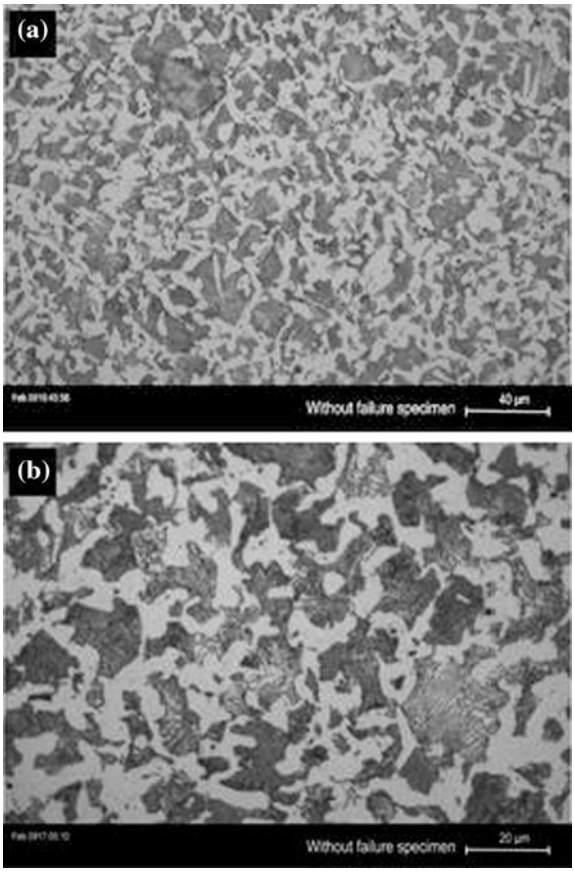

Fig. 7 Microstructure of the sample without failure

The lever rule was used to determine the amount of each phase present in the steel that did not fail. Using a temperature below the eutectic reaction, it was found that the weight fraction of pearlite was approximately 57 and 43% for the primary phase α if it is considered that this is a 1045 steel. This structure makes the steel resistant due to dispersion-hardened pearlite, even though it is still ductile due to the presence of primary ferrite. According to the literature [9], for steel with 0.45% carbon content, the yield and the ultimate tensile strength must be 400 and 600 MPa, respectively, with a perlite and ferrite microstructure. These data are very similar to those obtained experimentally (yield strength = 400 MPa y UTS = 590 MPa) for this investigation.

Figure 8 shows the microstructure of the sample that failed, where laths of martensite can be observed. This phase forms during a transformation in the solid state without diffusion, opposite to the pearlite, whose transformation does depend on diffusion. Martensite is very hard and brittle phase, which forms when the steel is cooled rapidly from the stable austenite region. The presence of this phase may explain the fracture observed and the mechanical properties values. Grange et al.

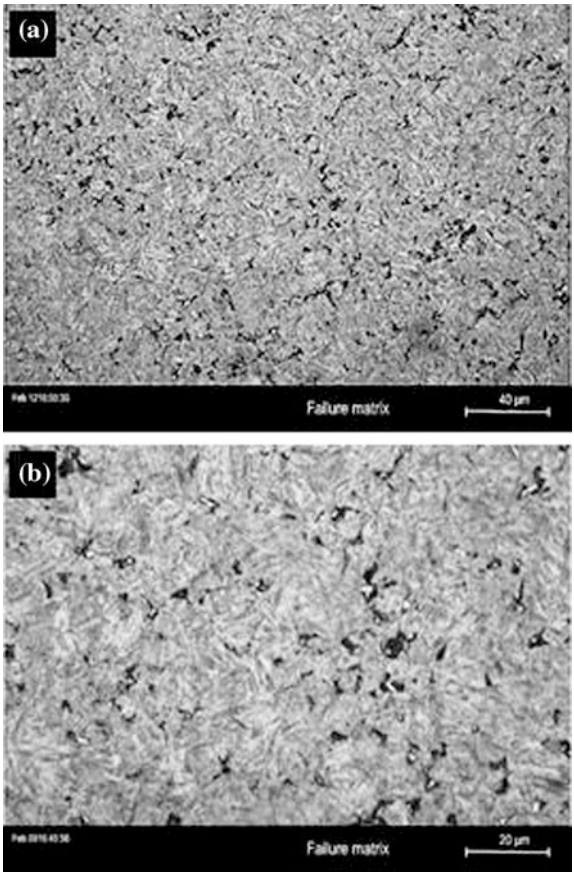

Fig. 8 Microstructure of the sample with failure

have established that when martensite forms in low alloy steel with 0.45% carbon content, it exhibits an approximated hardness value of 61 HRC [10], which agrees with the experimental values measured in this study.

Conclusions

Hardness profiles obtained along the parts tested showed a difference up to a factor of three between samples with and without failure, which means that the samples had different microstructures, given that both had the same chemical composition.

Tensile tests results support the argument that the samples had different microstructures since the components that failed exhibit a yield strength of 600 MPa and an UTS of 760 MPa while the sample without failure displayed yield strength of 400 MPa and an UTS of 590 MPa.

Martensite was found in the region of the part where the torque was applied. The type of failure found was a brittle intergranular fracture, which was confirmed with Chevron marks. Therefore, it is concluded that the part failed because it was subjected to an incorrectly applied heat treatment.

Acknowledgements The authors would like to thank the support CVU-105494 from the National Council for Science and Technology (CONACyT) in Mexico.

References

1. S. Brown. Forensic engineering: Reduction of risk and improving technology (for all things great and small). Engineering Failure Analysis. 14 (2007) 1019–37.
2. S.K. Bhaumik. A View on the General Practice in Engineering Failure Analysis. J Fail. Anal. and Preven. 9 (2009) 185–92.
3. ASTM, Standar E3-11, Standard Practice for Preparation of Metallographic Specimens, ASTM International, West Conshohocken, PA., 2003.
4. H. Kuhn, D. Medlin, ASM Handbook, Volume 08 - Mechanical Testing and Evaluation, ASM International.
5. K. Mills, J.R. Davis, ASM Handbook, Volume 12 - Fractography, ASM International.
6. H. Iwand, J. Wagner. Failure Analysis of Open End Wrenches Containing Forging Defects. J Fail. Anal. and Preven. 10 (2010) 520–4.
7. S. Nasrazadani, P. White. Failure Analysis of a Fractured Wrench Socket. J Fail. Anal. and Preven. 13 (2013) 673–7.
8. G.F. Vander Voort, A. International, A.I.H. Committee. Metallography and microstructures. ASM International, 2004.
9. J.D. Verhoeven. Fundamentals of physical metallurgy. Wiley, 1975.
10. R.A. Grange, C.R. Hribal, L.F. Porter. Hardness of tempered martensite in carbon and low-alloy steels. MTA. 8 (1977) 1775–85.

Multiaxial Fatigue of Rubbers: Comparative Study Between Predictive Tools

G. Ayoub, M. Naït Abdelaziz and F. Zaïri

Introduction

Rubbers exhibit large strains and highly non-linear but quasi-reversible mechanical behavior [1, 2]. Among the multitude of criteria developed in the literature the maximum principal stretch $\lambda_{\max}$ [3, 4], the maximum principal Cauchy stress $\sigma_{\max}$ [5, 6] and the strain energy density (SED) W[7, 8] are the most reported.

Based on critical plane approaches, the cracking energy density (CED) and the configurational mechanics are more sophisticated criteria that were introduced to account for the damage mechanisms which could not be captured by the other criteria. The cracking energy density (CED) W_c initially proposed by Mars [9] and modified by Zine et al. [10] is defined as follows:

$$dW_c = \frac{1}{\mathbf{R}_\theta^T \mathbf{C}^{-1} \mathbf{R}_\theta} \mathbf{R}_\theta^T \mathbf{S} d\mathbf{E} (\mathbf{F}^T \mathbf{F})^{-1} \mathbf{R}_\theta = \frac{\mathbf{R}_\theta^T \mathbf{S} d\mathbf{E} \mathbf{C}^{-1} \mathbf{R}_\theta}{\mathbf{R}_\theta^T \mathbf{C}^{-1} \mathbf{R}_\theta} \tag{1}$$

With $\mathbf{R}_\theta = (\cos\theta, \sin\theta, 0)$ is the unit vector in the un-deformed configuration (θ is the crack orientation angle), $\mathbf{S}, \mathbf{E}, \mathbf{F}$ and $\mathbf{C}$ are the second Piola-Kirchoff stress tensor, the Green Lagrange strain tensor, the deformation gradient and the right Cauchy-Green strain tensor, respectively. The criterion stipulates that cracks nucleate in the plane where the CED is maximum.

Verron and Andriyana [11] based on the configurational mechanics proposed an alternative criterion. In their approach, Eshelby tensor is considered to be the

G. Ayoub
Industrial and Manufacturing Systems Engineering,
University of Michigan Dearborn, Dearborn, MI, USA

M. Naït Abdelaziz (✉) · F. Zaïri
Laboratoire de Mécanique de Lille (LML), Université Lille 1
Sciences et Technologies, UMR CNRS 8107, 59650 Villeneuve d'Ascq, France
e-mail: moussa.nait_abdelaziz@polytecj-lille.fr

R. R. Ambriz et al. (eds.), *Proceedings of the 17th International Conference on New Trends in Fatigue and Fracture*, https://doi.org/10.1007/978-3-319-70365-7_14

predictor for crack nucleation and is then defined as $\mathbf{b} = W\mathbf{I} - \mathbf{CS}$. It can be considered as a potential energy which must be minimized. Therefore the criterion is written as follows:

$$b^* = \left|\min\left[(b_i)_{i=1,2,3}, 0\right]\right| \tag{2}$$

More recently, the cracking equivalent stress (CES) was proposed, the criterion combining the continuum damage mechanics (CDM) and the cracking energy density (CED) [12, 13]. The criterion is developed to account for multiaxial loadings by using a generalized incompressible Ogden strain energy density of nth order. The developed multiaxial stress fatigue predictor is defined by the following equation:

$$S_{eq} = \frac{1}{\left(\cos^2\theta + B^{-2}\sin^2\theta\right)}\left(\frac{S_1^2\lambda_1\cos^2\theta}{\partial S_1/\partial\lambda_1} + \frac{S_2^2 B\lambda_1\sin^2\theta}{\partial S_2/\partial\lambda_2} + \frac{-S_3 S_2 B^3\lambda_1^4\sin^2\theta}{\partial S_3/\partial\lambda_3}\right) \tag{3}$$

where $B = \lambda_2/\lambda_1$ is the biaxiality ratio defined as the ratio between the second and first principal stretches and, S_1, S_2 and S_3 are the principal components of the second Piola-Kirchhoff stress tensor $\mathbf{S}$. The fatigue criterion is considered to be equal to the difference between the CES and a threshold value. The threshold is noted S_{th}, accounts for the loading limit below which there is no crack initiation due to fatigue, this further.

The aforementioned criteria requires a cumulative damage law to be able to predict the fatigue life of variable loading conditions, e.g. a Miner or modified Miner models are used. Ayoub et al. [12, 13] proposed a combined criterion and a cumulative model. The predictive capabilities of three cumulative models are examined in this work.

Materials—Experiments

In order to assess the capability of these above mentioned multiaxial criteria, experimental tests combining tension and torsion loading paths were performed on a carbon-filled styrene-butadiene rubber (SBR). The SBR cylindrical hourglass-shaped specimens, present curvature radii equal to 2 and 42 mm and respectively denoted called AE2 and AE42 in the following [12].

The specimens were subjected to tension, torsion or combined tension-torsion loadings achieved under displacement or angle control, both in constant and variable amplitudes. All tests were performed at ambient temperature under frequencies ranging from 3 up to 5 Hz. The amplitudes were selected in order to cover a wide range of fatigue lives. Fatigue life is defined as the number of cycles for which the first crack or group of cracks of 1 mm length occurs. The finite element (FE) MSC.

Marc code was used to calculate the required mechanical quantities. Figure 1 shows the meshed specimen. A second order Ogden strain energy density is used:

$$W = \sum_{i=1}^{2} \frac{\mu_i}{\alpha_i} \left(\lambda_1^{\alpha_i} + \lambda_2^{\alpha_i} + \lambda_3^{\alpha_i} - 3 \right) \tag{4}$$

In this equation, μ_I and α_i are the parameters to be identified via monotonic tests and λ_i are the principal stretches (the Eigen values of the strain gradient tensor). The same material constants than those identified by Ayoub et al. [12] have been used in this work.

Results-Discussion

The capability of the different criteria to predict the fatigue life under multiaxial loading was assessed using the experimental data we have collected. A more extended and detailed analysis can be found in [13]. In a second step, we will examine how damage laws can capture the effects of two blocks loadings.

Fatigue Criteria

The evolution of the fatigue life as a function of the selected parameters is shown in Fig. 1. It is clearly highlighted that the CES parameter given by Eq. 3 allows capturing the multiaxial loading effect since the data are aligned along a straight line

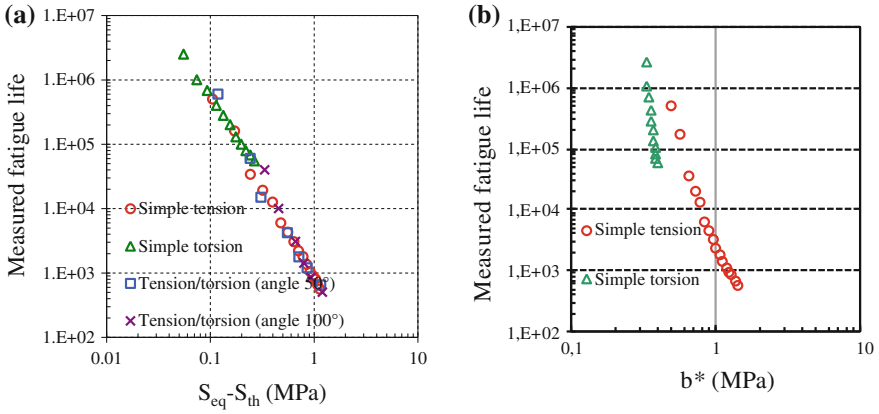

Fig. 1 Fatigue life as a function of the fatigue parameter: **a** cracking equivalent stress, **b** configurational stress

in logarithmic coordinates. In contrast, the configurational stress is not able to unify the experimental data corresponding to tension and torsion tests.

Damages Rules

Under regular operation conditions, structures are subjected to random and/or multilevel loadings, therefore, an estimation of the damage is generally required to estimate the fatigue life under such loading conditions. The Miner linear damage rule, mostly used in multilevel ladings, is based upon a damage parameter defined as follows:

$$D = \frac{N}{N_f} \tag{5}$$

where D is the current damage (evolving from 0 to 1), N is the actual number of cycles and N_f is the fatigue life for a given deformation level. According to the Miner law, the damage can be written in the following form:

$$D = \sum_{i=1}^{n} D_i = \sum_{i=1}^{n} \frac{N_i}{N_{fi}} = 1 \tag{6}$$

in which i is the current deformation level, n is the number of deformation levels. Generally, this linear rule is sufficient to get quite satisfactory estimates for rubbers.

The continuum damage mechanics framework [8, 12, 13] allows simultaneously defining the fatigue life criterion and estimating the damage level. Indeed, the damage variable D_i can be estimated step by step and for a given amplitude loading, it can be written as follows:

$$D_i = 1 - \left[(1 - D_{i-1})^{1+a} - (1+a) \left(\frac{S_{eq}}{A} \right)^a N_i \right]^{\frac{1}{1+a}} \tag{7}$$

where a and A are damage parameters to be identified using fatigue data obtained under tension loading. For n blocks, the fatigue life $N_f = N_n$ can be extracted from the following general equation:

$$\int_{D_0=0}^{D_f=1} (1 - D)^a dD = \sum_{i=0}^{n-1} \int_{N_i}^{N_{i+1}} \left(\frac{S_{eq(i+1)}}{A} \right)^a dN \tag{8}$$

Figure 2 shows a comparison between the experimental fatigue life and the estimates given by the Miner linear rule (Fig. 2a) and the continuum damage mechanics (Fig. 2b).

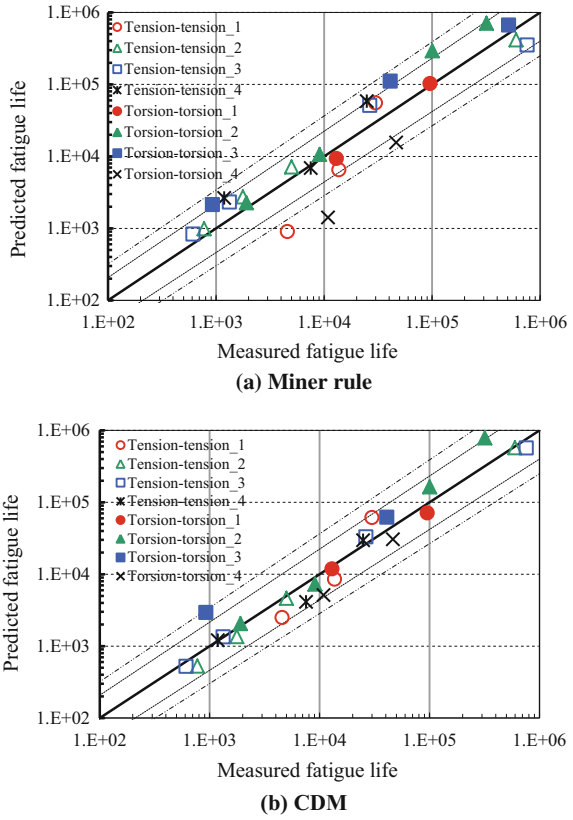

Fig. 2 Estimated fatigue life versus experimental data

It is clearly highlighted that CDM based model gives less scattered results than the linear rule, perhaps because the Miner law does not discriminate low-high and high-low loadings.

Conclusion

In this work, we have shown that the CDM based model derived from the cracking energy density parameter allows getting satisfactory results in terms of multiaxial fatigue life estimates. When dealing with variable loadings, the CES parameter can be combined with the Miner rule but, since this parameter was developed in the framework of CDM, a direct evaluation of the damage can be derived. We have shown that, taking this approach, a good agreement between experimental data and estimates was pointed out.

References

1. W.V. Mars, A. Fatemi, Factors that affect the fatigue life of rubber: a literature survey, Rubber Chem. Technol. 77 (2004) 391–412.
2. G. Ayoub, F. Zaïri, M. Naït-Abdelaziz, J.M. Gloaguen, Modeling the low-cycle fatigue behavior of visco-hyperelastic elastomeric materials using a new network alteration theory: Application to styrene-butadiene rubber, J. Mech. Phys. Solids 59 (2011) 473–495.
3. S.M. Cadwell, R.A. Merrill, C.M. Sloman, F.L. Yost, Dynamic fatigue life of rubber, Ind. Eng. Chem. 12 (1940) 19–23.
4. B.J. Roberts, J.B. Benzies, The relationship between uniaxial and equibiaxial fatigue in gum and carbon black filled vulcanizates, In: Proceedings of Rubbercon' 77 2. (1977) 1–13.
5. N. André, G. Cailletaud, R. Piques, Haigh diagram for fatigue crack initiation prediction of natural rubber components, Kaut. Gummi Kunst. 52 (1999) 120–123.
6. F. Abraham, T. Alshuth, S. Jerrams, The effect of minimum stress and stress amplitude on the fatigue life of non strain crystallising elastomers, Mater. Des. 26 (2005) 239–245.
7. A.N. Gent, P.B. Lindley, A.G. Thomas, Cut growth and fatigue of rubbers. I. The relationship between cut growth and fatigue, J. Appl. Polym. Sci. 8 (1964) 455–466.
8. G. Ayoub, M. Naït-Abdelaziz, F. Zaïri, J.M. Gloaguen, Multiaxial fatigue life prediction of rubber-like materials using the continuum damage mechanics approach, Proc. Eng. 2 (2010) 985–993.
9. W.V. Mars, Cracking energy density as a predictor of fatigue life under multiaxial conditions, Rubber Chem. Technol. 75 (2002) 1–17.
10. A. Zine, N. Benseddiq, M. Naït Abdelaziz, N. Aït Hocine, D. Bouami, Prediction of rubber fatigue life under multiaxial loading, Fatigue Fract. Eng. Mater. Struct. 29 (2006) 267–78.
11. E. Verron, A. Andriyana, Definition of a new predictor for multiaxial fatigue crack nucleation in rubber, J. Mech. Phys. Solids 56 (2008) 417–443.
12. G. Ayoub, M. Naït-Abdelaziz, F. Zaïri, J.M. Gloaguen, P. Charrier, Fatigue life prediction of rubber-like materials under multiaxial loading using a continuum damage mechanics approach: effects of two-blocks loading and R ratio, Mech. Mater. 52 (2012) 87–102.
13. G. Ayoub, M. Naït-Abdelaziz, F. Zaïri, Multiaxial fatigue life predictors for rubbers: Application of recent developments to a carbon-filled SBR, International Journal of Fatigue, 66, 2014, Pages 168–176.

Laboratory Study of Fatigue in Water Conveying HDPE and PVC Pipes Subject to Extreme Hydraulic Transient Pressures

René Autrique Ruiz and Eduardo Antonio Rodal Canales

Introduction

In previous papers [1, 2] the authors have proposed, for extruded pipes of high density polyethylene pipes (HDPE pipes), used in the transportation and distribution of potable water, S-N curves that can be representative of HDPE materials (PPI 3608 and PPI 4710 resins). In these curves, the applied loads or stresses, relative to its nominal or design values, are represented versus the number of times that the material resists the applied loads or the applied stresses. In these graphs, we can distinguish a crack initiation curve, a failure or rupture curve, and a crack development region between the curves (Fig. 1).

The first experimental curve [1], which was obtained from a very long test (10^6 cycles) and two other short tests (10^0 and 10^3 cycles), was equivalent to the S-N fatigue curves obtained for typically elastic materials [3], such as steel and other metals. Further experiments [2], in which the pipe samples, altered with triangular grooves of different depths machined in its external surface were brought to failure through the application of repeated cycles of hydraulic transient overpressures, are shown in Fig. 2.

R. A. Ruiz (✉)
Policonductos, Cracovia 54, C.P. 01000 San Ángel, Ciudad de México, Mexico
e-mail: rautrique@prodigy.net.mx

E. A. R. Canales
Instituto de Ingeniería, UNAM, Ciudad Universitaria, C.P. 04510 Coyoacán
Ciudad de México, Mexico

R. R. Ambriz et al. (eds.), *Proceedings of the 17th International Conference on New Trends in Fatigue and Fracture*, https://doi.org/10.1007/978-3-319-70365-7_15

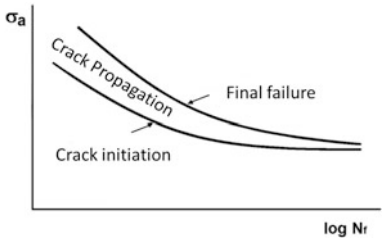

Fig. 1 S–N curves, Ref. [3]

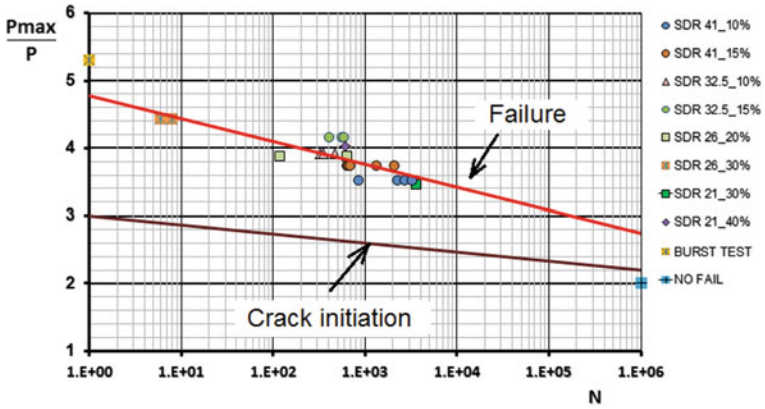

Fig. 2 S–N curves for HDPE PPI 4710 [2]

Viscoelasticity

High density polyethylene (HDPE) and PVC are viscoelastic materials. These materials respond to the application of loads with an instantaneous elastic deformation, followed by a slow and continuous deformation, known as viscous flow or creep. When the load disappears, there is an instantaneous recovery of the elastic deformation, and an inverse viscous flow recovering gradually the viscous deformation (Fig. 3a [4]).

According to the Boltzmann superposition principle [4], if two loads or stresses are superposed, its corresponding deformations are equally superposed (Fig. 3b).

In our fatigue studies, the pipe samples are subject to an initial internal pressure that gives rise to an elastic deformation and to the viscous flow mentioned above. The application of cyclic overpressures caused by waterhammer will produce a new deformation curve, above the viscous flow curve. The deformations due to these transient loading and unloading cycles will be located between these two curves (Fig. 3c).

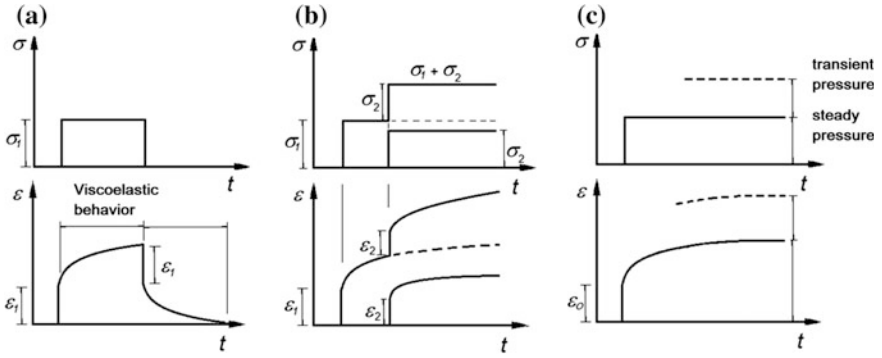

Fig. 3 **a** and **b** Viscoelastic material deformations under stresses and superposed stresses [4]. **c** Deformations under transient overpressures

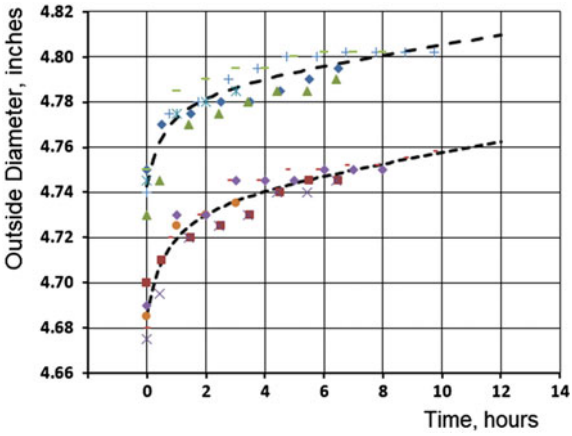

Fig. 4 Outside diameters measured during steady and transient flow

The theoretical curves shown in Fig. 3c were obtained experimentally in an HDPE pipe sample and are shown in Fig. 4. The lower curve corresponds to the measured outside pipe diameter and its growth due to the viscous flow or creep caused by the permanent internal pressure. The upper curve corresponds to the instantaneous deformation caused by the application of the transient pressures shown in Fig. 5. The constant separation between the curves shows that the deformation and recovery are purely elastic.

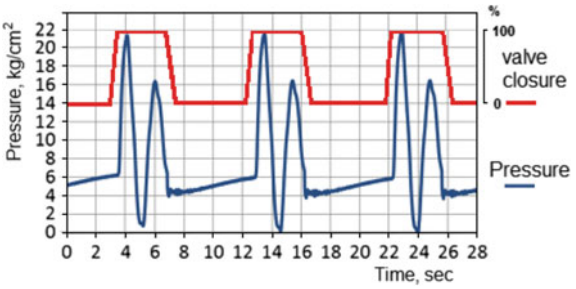

Fig. 5 Transient pressures and opening and closing cycle of the valve

Glass Transition Temperatures

Polymers, or plastics, go through different types of mechanical behavior, depending on its temperature and specifically, as solids, on its glass transition temperature, Tg, which is a transition temperature below which a plastic behaves as a glass, and above which it behaves as a rubber. This characteristic behavior is shown in Fig. 6, where the Young modulus E is plotted versus the dimensionless absolute temperature T/Tg [5]. It can be seen that the modulus of elasticity, and correspondingly the design stress for internal pressure, are reduced drastically when the material goes from the glassy to the rubbery state.

Glass transition temperature for PVC is 90 °C, and −90 °C for HDPE. Figure 7 shows the E-T and S-T curves for PVC and HDPE, showing that, for the typical ambient temperatures, 0–40 °C, PVC is clearly in the glass plateau, and HDPE is clearly in the rubber plateau, behaving accordingly. The Young modulus E and the design stresses S are shown in its real values, as they are used for the design of pipes that convey water under pressure.

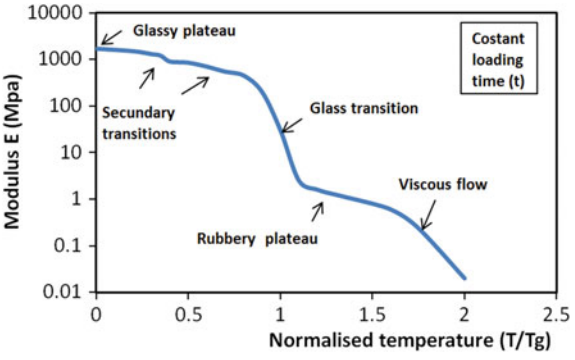

Fig. 6 Young modulus, linear polymer [5]

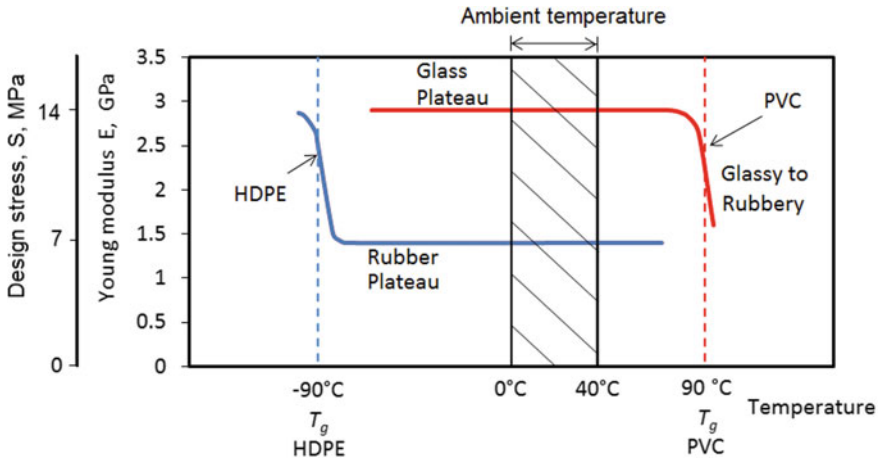

Fig. 7 Glass transition temperatures, PVC and HDPE

Experimental Installation

The experiments were conducted in the city of San Luis Potosí, in a model consisting of a 277 m long steel pipe, diameter of 100 mm and thickness of 1.5 mm, D/t ratio of 67, with two hydropneumatic tanks in the extremes, acting as constant head and as pressure wave reflecting bodies (Fig. 8). Pressure wave celerity is 1120 m/s. In both ends of the steel pipe, upstream and downstream, 6–12 m of HDPE or PVC test pipes can be installed, and subject to extreme transient pressures, made possible by the high wave celerity of the steel pipe. Butterfly valves are installed at the upstream and downstream ends, with 0.2 s closure time. The valve has also a mechanical counter, which accumulates the number of valve cycles. This experimental installation is located in San Luis Potosí, Mexico, and was built under the technical advice of the Institute of Engineering of the Universidad Nacional Autónoma de México (UNAM), in the frame of an industry–university collaboration. The installation is available for research projects of universities and institutes.

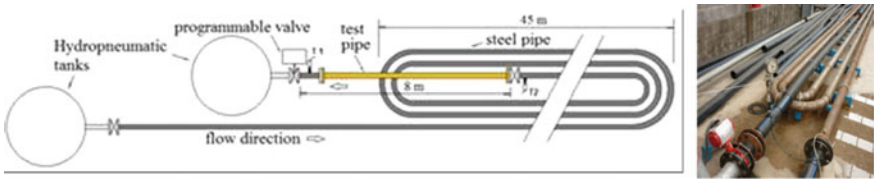

Fig. 8 Experimental set up

Experimental Results

The aim of the experiments reported in this paper is to obtain S-N curves for PVC and compare them with those obtained for HDPE in a previous paper [2]. Several PVC pipe samples, 6 m long, were subject to cycles of extreme transient pressures, which were higher than the internal design pressures of the pipes P (calculated as $P = 2S/(SDR - 1)$, where S is the design stress and SDR is the D/t ratio) and higher than the maximum pressures allowed by the codes during waterhammer events. For HDPE, the pipes are allowed pressures as high as 1.5 times its design pressure for recurring events, and 2 times its design pressure for occasional events [6]. The HDPE pipe final design thickness will be therefore the same as that calculated for steady state conditions. For PVC, the pipes must be calculated for the specific transient pressures that can occur during their lifetime [8], meaning that the pipe final design thickness will be generally greater than that calculated for steady state conditions.

The extreme pressure cycles, shown in Fig. 11, were continued until the failure of the pipe. Different pipe samples were tested, for different values of the D/t ratio, also known as Standard Dimensional Ratio (SDR). For HDPE, SDR's 41, 32.5, 26 and 21 had been tested [2]. For PVC, SDR's 51, 41, and 32.5, were tested. A "sanitary" grade (SDR 51) was also tested. Outside diameter of the PVC pipes is 100 mm. The pipe samples were prepared with triangular grooves, machined in its external surface, 30 mm long, parallel to the pipe axis, with depths from 10 to 40% of the nominal thickness, with an angle of 60°, similar to those cut in the round bar samples used in the standard fatigue tests (Fig. 9), with the aim of provoking the development of cracks in those weakened pipe sections (Fig. 10).

The same type of experiments made with HDPE pipe samples [2] were repeated with PVC pipe samples. Initial pressures were between 0.7 and 1.7 times (1.3–1.9 times for HDPE) the design pressures of the pipes, and the average water hammer

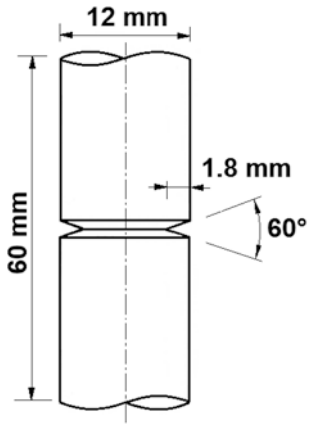

Fig. 9 Typical test specimen

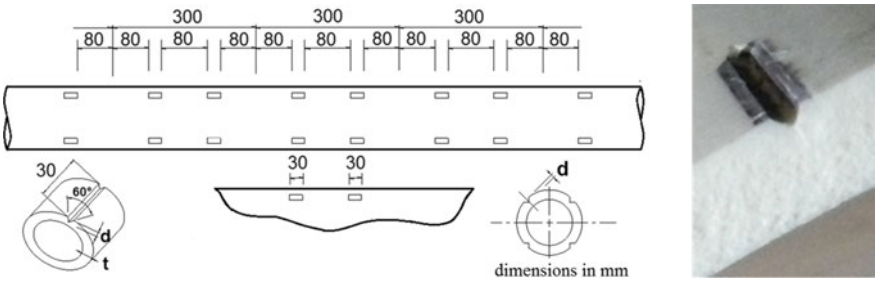

Fig. 10 Groove detail and pattern in pipe test samples

overpressures were between 2.1 and 2.7 times (3.5–4.4 times for HDPE) the design pressures of the pipes. The typical load cycles to which the pipes were subjected are shown in Fig. 11. Peak frequency is 0.3 Hz.

A total of 11 experiments were made, in which all pipe samples were brought to failure. In all cases, the failures occurred with a big burst and started in one of the grooves made with the purpose of provoking the failure. Contrarily to the case of HDPE pipes, where the failures were localized, fixed in length, and stable, that is, without propagation during the experiment, as shown in Photos 1–3 [2], the PVC pipe failures propagated very rapidly from the initial groove failure, destroying completely the pipe, as shown in Photos 4–9.

The results of the 11 experiments are shown in Fig. 12, in which the logarithmically adjusted curves for HDPE and PVC are compared. The normalized maximum pressure applied, P_{max}/P, was calculated with the average overpressures in each cycle and the design pressure of each pipe sample, according to its real average thickness and SDR. In Fig. 12, three points in the PVC curve were added for N values of 10^4, 10^5 and 10^6, from Ref. [7], which summarizes a number of conventional fatigue studies made with large numbers of load cycles, and which correspond very well with our smaller load cycles experiments with real pipes.

In addition, virgin PVC pipe samples, not previously subject to internal pressure, were also tested under the quick burst test (ASTM D 1599 99R05), in which the pipe samples are sealed with blind flanges and subject, inside a water tank, to an increasing internal pressure, until the moment in which the pipe fails, recording the maximum pressure reached. The average of these maximum pressures, normalized, is also plotted in Fig. 12, as was for HDPE.

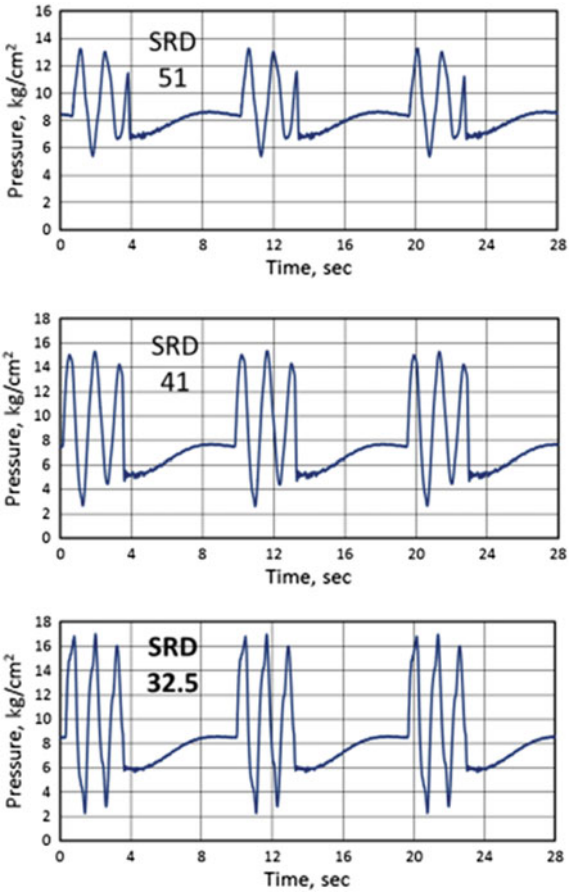

Fig. 11 Typical load cycles, PVC pipes, for different SDR's

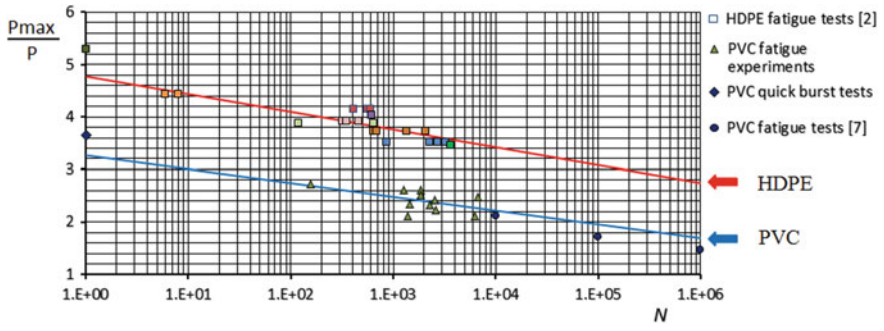

Fig. 12 Experimental results and S-N fatigue curves (logarithmic adjustment)

Photo 1. HDPE SDR 41

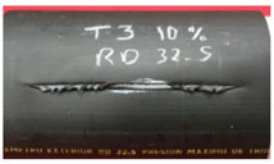

Photo 2. HDPE SDR 32.5

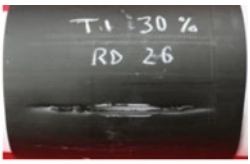

Photo 3. HDPE SDR 26

Photo 4. PVC pipe failure

Photo 5. PVC pipe failure

Photo 6. PVC pipe failure

Photo 7. PVC pipe failure

Photo 8. PVC pipe failure

Photo 9. PVC pipe failure

Conclusions

Curves S–N for HDPE pipes and PVC pipes were presented, resulting from experiments in which test pipes were subject to extreme transient pressures and where the transient cycles were maintained until the failure of the pipes.

The experiments confirmed that failures in pipes are caused by small cracks that appear in its weak sections, and develop gradually, under cyclic loads or transient overpressures, until the moment in which the failure happens.

It was shown that, contrarily to HDPE pipes, which have a very high resistance to fatigue and high pressures and whose failures are localized and do not propagate, PVC pipes do not have a high resistance to high pressures, and that its failures are brittle and propagate very rapidly, destroying completely the pipes.

The difference in the behavior of the two materials can be explained considering their respective glass transition temperatures, which show that for the normal ambient temperatures PVC behaves as a glass and HDPE behaves as a rubber.

References

1. Autrique R., Rodal E. (2012). "Fatiga en tuberías de polietileno sometidas a presiones extremas producidas por golpe de ariete" *Memorias*, XXV Congreso Latinoamericano de Hidráulica, San José, Costa Rica (in Spanish).
2. Autrique R., Rodal E. (2014). "Estudio en laboratorio de fatiga en tuberías de polietileno sometidas a presiones transitorias extremas" *Memorias*, XXVI Congreso Latinoamericano de Hidráulica, Santiago, Chile (in Spanish).
3. Suresh, S. (1998). *Fatigue of materials*. Cambridge University Press, 2nd Ed, Cambridge, U.K.
4. Findley W, Lai J, Onaran K. (1976). *Creep and relaxation of nonlinear viscoelastic materials (with an introduction to linear viscoelasticity).* Dover, New York, U.S.A.
5. Ashby, M., Jones, D. (1986). *Engineering Materials 2. An introduction to microstructures, processing and design.* ISMST, Vol 39, Pergamon, U.K.
6. Plastic Pipe Institute (2009). *Handbook of polyethylene pipe*. PPI, 2nd Ed, Irving, Texas, U.S.A.
7. Joseph, S.H. (1984). "Fatigue failure and service lifetimes in uPVC pressure pipes", *Plastic and rubber processing and applications*, Vol 4, No 4, pp 325–330, Plastics and Rubber Institute, England.
8. American Water Works Association (2010). *PVC Pipe Design and Installation. Manual of Water Supply Practices, M 23*, 2nd Ed, AWWA, Denver, Colorado, U.S.A.

Probabilistic Assessment of Nuclear Piping Integrity by Considering Environmental Fatigue and Stress Corrosion Cracking

Seung Hyun Kim, Md Nasimul Goni and Yoon-Suk Chang

Introduction

Most of the operating nuclear power plants (NPPs) were designed with original permission period of 40 years but extension of their lives has been considered world widely. To achieve this goal, structural integrity against aging mechanisms such as fatigue, thermal aging, primary water SCC (Stress Corrosion Cracking) and boric acid corrosion etc. should be assured. Among them the fatigue has been known as very important aging mechanisms defining component lives and, particularly, environmental effects were controversy since 1990s [1]. On the other hand, probabilistic assessment codes have been developed for determining failure probabilities of structural components. PINTIN (Piping Integrity Inner flaws) was developed due to limitations of other codes [2].

In this paper, the effects of the aging mechanism and evaluation method were confirmed by applying PINTIN to a typical reactor coolant system. Piping failure probabilities with small and big leak probabilities are assessed in the typical reactor coolant system. Subsequently, sensitivity analyses were also performed to find out parameters significantly affecting to the integrity of piping.

S. H. Kim · M. N. Goni · Y.-S. Chang (✉)
Department of Nuclear Engineering, Kyung Hee University, 1732 Deogyeong-daero, 17104 Giheung-gu, Yongin-si, Gyeonggi-do, Republic of Korea
e-mail: yschang@khu.ac.kr

R. R. Ambriz et al. (eds.), *Proceedings of the 17th International Conference on New Trends in Fatigue and Fracture*, https://doi.org/10.1007/978-3-319-70365-7_16

Evaluation Methods

Fatigue Crack Initiation and Growth

Since we know that the values of F_{en} can be obtained from the Argonne National Laboratory fatigue life model, where N_{air} defined as the ratio of life in air at room temperature and N_{water} is in water at service temperature. The fatigue life, N, of SS is represented by Eq. (1) [3].

$$\ln[N_i(x)] = 6.449 - 1.808\ln(\varepsilon_a - 0.151) \tag{1}$$

The environmental fatigue correction factor is Eq. (2) as follow:

$$F_{en} = \exp(0.702 - 0.101S^*T^*O^*\dot{\varepsilon}^*) \tag{2}$$

Environment has significant effect on crack growth period. In water environment, it reduces the fatigue life and increases the fatigue growth rate. The fatigue crack growth rate, da/dN, of the SS is characterized in terms of the range of the applied stress intensity factor, ΔK. This characterization is generally in the form of Eq. (3) [4],

$$\frac{da}{dN} = C_0 \Delta K^n \tag{3}$$

where n and C_0 are parameters dependent on the material and environmental conditions, n is slope of the log (da/dN) versus log (ΔK) curve, n is 2.25 and C_0 is parameter which accounts for the effect of a number of variables on crack growth rate. The fatigue crack growth rate of the material is affected by R ratio ($K_{\text{min}}/K_{\text{max}}$) and environmental conditions. These variables are accounted for in C_0 as defined below in Eq. (4) [4]:

$$C_0 = CS_TS_RS_{ENV} \tag{4}$$

where constant, C is 9.10×10^{-6} mm/cycle for SS. ΔK_{th} is defined as 1.10 MPa $\text{m}^{0.5}$. Besides, S_{T} is the parameter defining the effect of temperature on crack growth rate.

SCC Initiation and Growth

Garud developed an SCC initiation model for application to an engineering evaluation of SCC initiation in primary water conditions. In this model, the duration of SCC initiation is a function of stress, temperature, environmental factors and material strength. The Garud's SCC initiation model was used for PINITN as follows [5]:

$$t_{\mathrm{i}} = a_{\mathrm{n}}\lambda_{\mathrm{e}}\mathrm{In}(A)\left[\mathrm{In}\left(\frac{A-Z}{S_u/S_{\mathrm{y}}-Z}\right)/\ln\left(\frac{A-Z}{1-Z}\right)\right] \tag{5}$$

where t_{i} is time, a_{n} is normalized resistance factor, λ_{e} is material environment factor including the Arrhenius temperature dependence, A and Z are material constant. S_{u} and S_{y} are ultimate tensile strength and tensile yield strength respectively.

Now, for the SCC growth model of PINITN, below equation was used for the evaluation of SCC growth [6]:

$$\frac{da}{dt} = \exp\left[-\frac{Q_{\mathrm{CGR}}}{R}\left(\frac{1}{T}-\frac{1}{T_{\mathrm{ref}}}\right)\right]\alpha_1(K-K_{\mathrm{th}})^{\beta_1} \tag{6}$$

where da/dt is crack growth rate at temperature T, Q_{CGR} is thermal activation energy for crack growth, R is the universal gas constant, T is coolant temperature, T_{ref} is room temperature, α_1 is crack growth amplitude, K is stress intensity factor, K_{th} is crack tip stress intensity factor threshold and β_1 is exponent.

Monte Carlo Simulation

The Monte Carlo simulation technique shown in the figure is adopted to predict the leak probability of the nuclear plant piping. First, the initial crack size or crack size during growth is defined as coordinates in the sample space. The next step is to determine the crack size using a stratified sampling scheme and calculate the probability (P_{m}) that the crack is in the cell [5].

$$P(t_F \le t) \sim \sum\nolimits_{m=1}^{M} \frac{N_F(t)}{N_m} P_m \tag{7}$$

where M is total number cells, N_m is number of samples from m-th cell, P_m is probability of an initial defect having coordinates within the boundaries of m-th cell (Fig. 1).

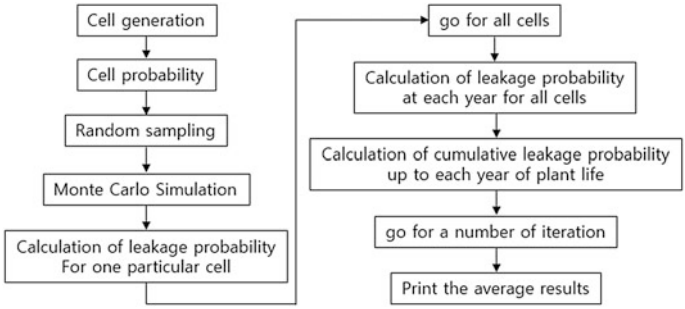

Fig. 1 Flow chart of Monte Carlo simulation for PINTIN [2]

Analysis of Piping Integrity

Analysis Condition

Leak probabilities were calculated by PINTIN the aging mechanisms (fatigue, SCC, fatigue + SCC). An analysis target is hot leg of the reactor coolant system, pipe diameter and thickness are 878.84 and 71.12 mm. Input conditions were summarized by Table 1 for calculation of small and big leak probabilities. In order to evaluate the effect of each parameter, heat-up/cool-down frequency, the oxygen concentration and coolant temperature were evaluated by complex aging mechanisms (fatigue and SCC). The small and big leak probabilities were calculated by increasing the heat-up/cool-down frequency, oxygen concentration and coolant temperature. Figure 2 shows the user friendly input window of the PINTIN.

Table 1 Conditions for PFM analysis

Fatigue crack growth properties	Fatigue constant, C	9.14×10^{-12}
	Fatigue exponent, n	4.0
	Heat-up/Cool-down frequency	**5/year**
		7/year
		9/year
Water chemistry and conditions that affect SCC	Oxygen concentration	**0.05 ppm**
		0.07 ppm
		0.09 ppm
	Duration of plant heat-up	5 h
	Coolant conductivity	0.2 μs/cm
Operating conditions	Operation pressure	15.51 MPa
	Plant life time	40 years
	Coolant temperature	**319.39 °C**
		344.39 °C
		369.39 °C

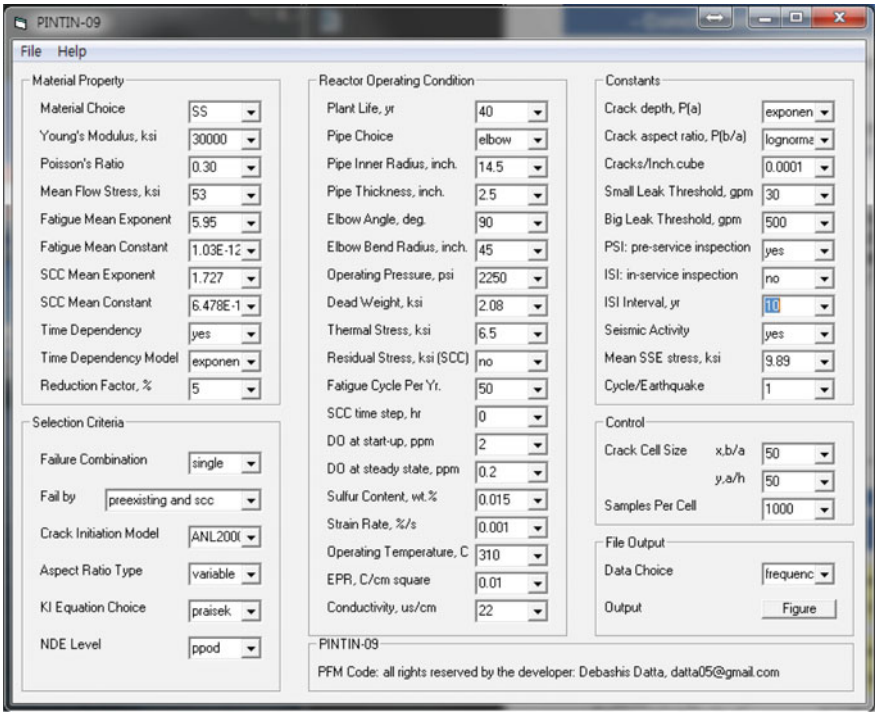

Fig. 2 Main window of PINTIN [2]

Analysis Results

Figure 3 shows the small and large leak probability due to aging mechanisms of the hot leg. The maximum difference of leak probability between fatigue and SCC occurred about 17%. In the case of complex aging mechanism (fatigue and SCC), when the life of nuclear power plant was 40 years, the leak probability was increased by 2 times, approximately.

Figure 4 shows leak probabilities when heat-up/cool-down frequency in the hot leg are 5, 7 and 9 per year. The oxygen concentration was 0.05 ppm and the coolant temperature was 319.39 °C, respectively. When heat-up/cool-down frequency was increased from 5 to 9 per year, the leak probability was increased up to 10^4 times. The difference in the leakage probability according to heat-up/cool-down frequency was constantly increased.

Figure 5 shows the leak probability according to the change of oxygen concentration. The heat-up/cool-down frequency was 5/year, and the coolant temperature was 319.39 °C, respectively. As the oxygen concentration was increased from 0.05 to 0.09 ppm by 0.02 ppm, the leak probability was increased up to 10^4 times,

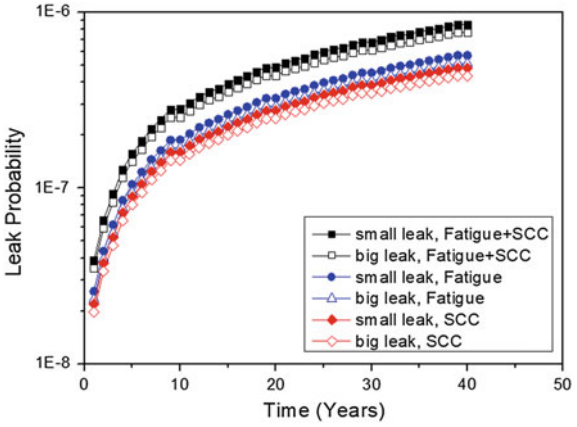

Fig. 3 Effect of aging mechanism on the leak probabilities

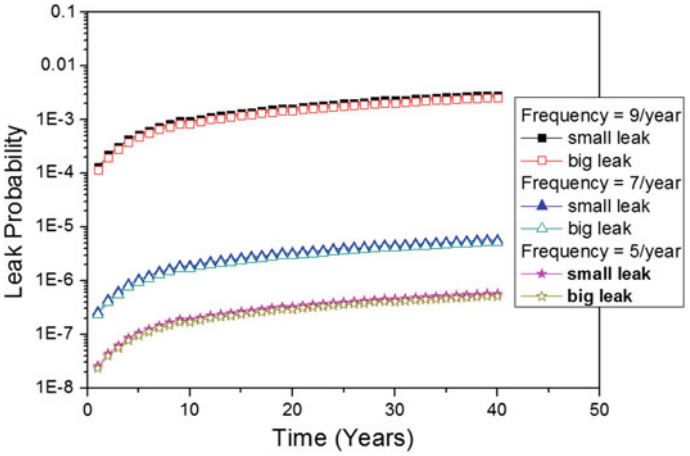

Fig. 4 Effect of heat-up/cool-down frequency on the leak probabilities

and the leak probability trend of the hot leg was similar to that of the heat-up/cool-down frequency.

Figure 6 shows the leak probability according to the change of coolant temperature. The heat-up/cool-down frequency was 5/year, and the oxygen concentration was 0.05 ppm, respectively. As the coolant temperature was increased from 319.39 to 369.39 °C by 25 °C, the leak probability was increased up to 10^5 times.

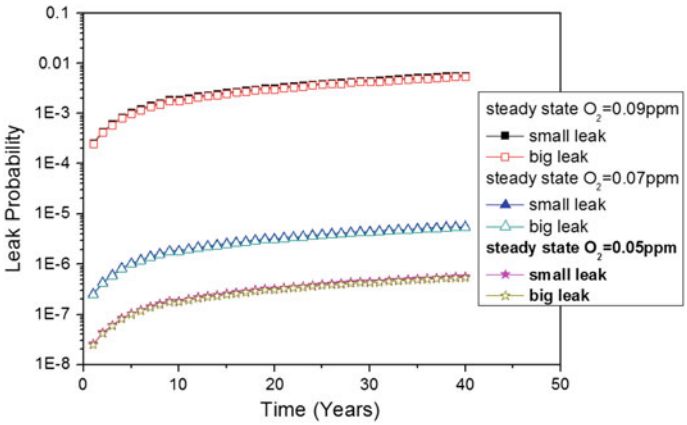

Fig. 5 Effect of steady state oxygen concentration on the leak probabilities

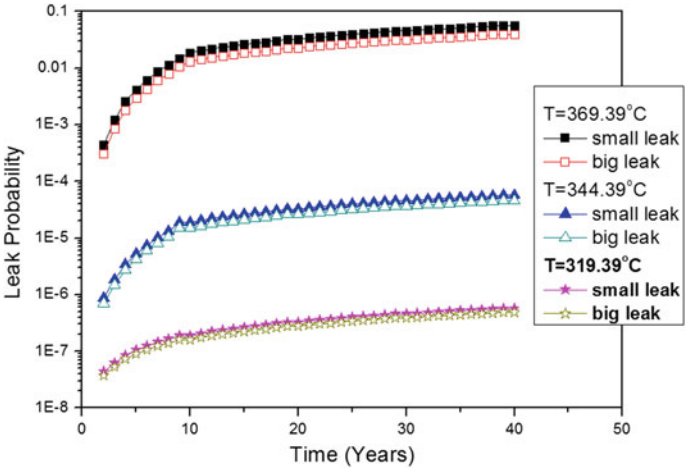

Fig. 6 Effect of coolant temperature on the leak probabilities

Conclusions

In this study, small and big leak probabilities according to the aging mechanisms in the hot leg were calculated, and effects of key parameters on fatigue and SCC were evaluated through sensitivity analyses.

(1) Dominant factors influence on the leak probability were fatigue and coolant temperature from degradation mechanisms and analysis parameters standpoints.
(2) When heat-up/cool-down frequency and oxygen concentration increased 40 and 80%, the leak probabilities increased 10 and 10^4 times approximately.

Acknowledgements This work was supported by the Nuclear Safety Research Program through the Korea Foundation Of Nuclear Safety (KOFONS) and "Human Resources Program in Energy Technology" of the Korea Institute of Energy Technology Evaluation and Planning (KETEP), granted financial resource from the Nuclear Safety and Security Commission (NSSC), Republic of Korea (No. 1403003) and Ministry of Trade, Industry & Energy, Republic of Korea. (No. 20151520101080)

References

1. NRC, "Guidance for Performance-Based Regulation", NUREG/BR-0303, 2002.
2. D. Datta, "Development of an Advanced PFM Code for the Integrity Evaluation of Nuclear Piping System under Combined Aging Mechanisms", Ph.D. thesis, KAIST, 2010.
3. U.S.NRC, "Effect of LWR Coolant Environments on the Fatigue Life", NUREG/CR-6909 Rev.1, 2014.
4. ASME Code Case N-792-1, "Fatigue Evaluation Including Environmental Effects", ASME, 2012.
5. NRC, "Theoretica1 and User's Manual for pc PRAISE, A Probabilistic Fracture Mechanics Computer Code for Piping Reliability Analysis, NUREG/CR-5864,1992.
6. ASME Code Case N-809, "Reference Fatigue Crack Growth Rate Curves for Austenitic Stainless Steels in Pressurized Water Reactor Environment", ASME, 2012.

The Inspections, Standards and Repairing Methods for Pipeline with Composite: A Review and Case Study

M. Hadj Meliani, O. Bouledroua, Z. Azari, A. Sorour, N. Merah and G. Pluvinage

Introduction

An accident free pipeline operation is the dream of every player in oil and gas industry, but corrosion by nature is a contending issue in this regard. Corrosion has been around for all recorded history and causes the degradation of the mechanical properties of pipeline system due to chemical reaction with the operational fluid and environment.

The paper initially inspects some points of view on the burst pressure standards calculation on pipeline with external corrosion defect. A real test will be presented, and a comparison on the two methods to repair the pipeline will be focus on the second part. A FEM simulation should be a good tool to estimate the safety factor on both parts. For the first part, an inspection is given for a real pipe exhibiting a surface corrosion defect. Details are given in Section "Clock Spring Pipe Repairing". The data collected by the intelligent pig are regrouped with the critical pressure establish by different codes ASME B31G [1], DNV RP F-101 [2], PCORRC [3], SHELL 92 [4], RSTRENG [5], Barlow's equation [6], Modified B31G code [7], the Netto et al. method [8], the Choi's method [9] and the average shear stress criterion method [10]. Effect of corrosion length and depth are studied. Additionally, in Section 3.2, a Finite Element Method, FEM has been used to compute the different Stress at defect tip and semi-elliptical defects were considered: diagonally, horizontally and vertically. The interest of the paper is to give

M. Hadj Meliani (✉) · O. Bouledroua · N. Merah
LPTPM, Hassiba BenBouali University of Chlef, 02000 Chlef, Algeria
e-mail: m.hadjmeliani@univhb.chlef.dz

M. Hadj Meliani · Z. Azari · N. Merah · G. Pluvinage
LaBPS-ENIMI, Paul Verlaine University of Metz, Ile de Saulcy, 57045 Metz, France

A. Sorour · N. Merah
Center of Research Excellence in Corrosion (CoRE-C), King Fahd University of Petroleum & Minerals, P.O.Box 5040, 31261 Dhahran, Saudi Arabia

R. R. Ambriz et al. (eds.), *Proceedings of the 17th International Conference on New Trends in Fatigue and Fracture*, https://doi.org/10.1007/978-3-319-70365-7_17

some critical about the more conservatives result given by the different standards in the literature. A proposal method to repair pipeline after inspection were presented in detail in Section "History of the Pipe, Inspection of Defects and Experimental Burst Test". Two methods, ISO/TS 24817 and ASME PCC-2, are supposed to be the able to given the more safety.

History of the Pipe, Inspection of Defects and Experimental Burst Test

In the aim to anticipate the operational regime maintaining on the GG1 gas pipeline under optimal safety conditions, analysis on a highly corroded tube are conducted by the DRC and the MNI project at the Boukeroues base on 20 April 2011. To study the behavior of API 5L X60 steel, corrosion lords of the bursting test and thus checking the safety of the standards requested. This test was limited to tubes referenced No. 12510 taken from PK 266.895 of the pipeline GG1. The test was carried out in two stages, firstly checking the extent of corrosion against the results of the intelligent tool and then testing the burst and analyzing preliminary data.

An example of a risk-based inspection planning method is given for a subsea oil export pipeline installed in 1981. Table 1 shows general information about the target pipeline, with inspection results of the corrosion defect in 2011. By an internal pipeline inspection using the Magnetic Flux Leakage (MFL) intelligent pig tool, collected corrosion zones can be measured with the locate, size and assess anomalies along the full length. The data collected were downloaded and processed for evaluation of the entire length of the pipeline, details of a subsea pipeline, such as segments and corrosion locations, as shown in Fig. 1.

Measurements of the instances and penetration depth of corrosion on the inner side of operating pipelines were collected. A total of 67 measurements were available for the present study, categorized as depth, width and length, Fig. 2.

All defects reported were evaluated in according to the different standards. This approach used the axial length, the circumferential extension as well as the depth

Table 1 General information about the target pipeline

Type of pipeline	Crude oil pipeline, operating
Diameter (mm)	42 in.
Wall thickness (mm)	11.91–12.7
Length (km)	437
Material grade	API 5L X 60
Max. allowable operating pressure (MAOP) (MPa)	69 bars
Max. actual pressure (Design)	73 bars
Date pipeline was commissioned (year)	1981
Report date	20.04.2011

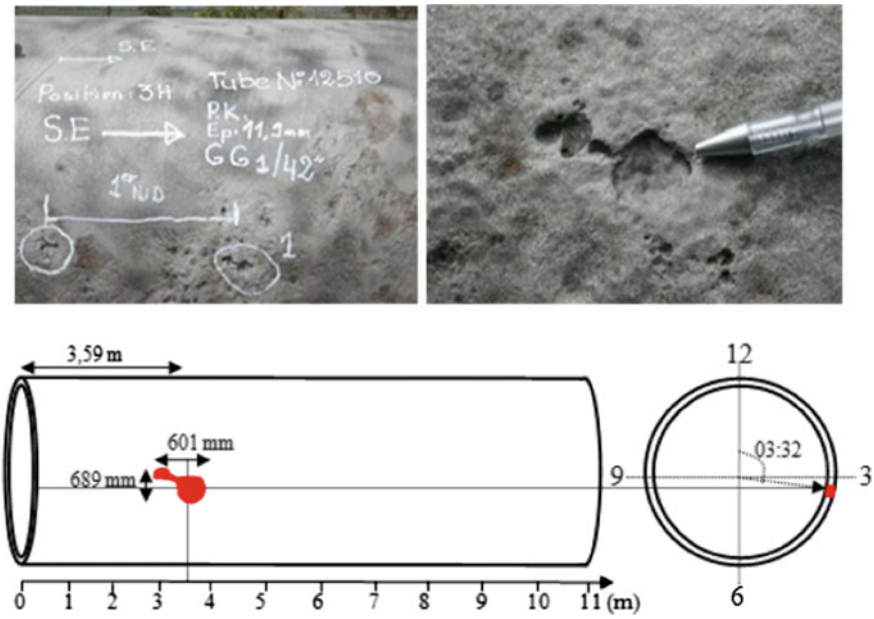

Fig. 1 Information on weld location and segment of a subsea pipeline

Fig. 2 Schematic view of gas pipeline corrosion

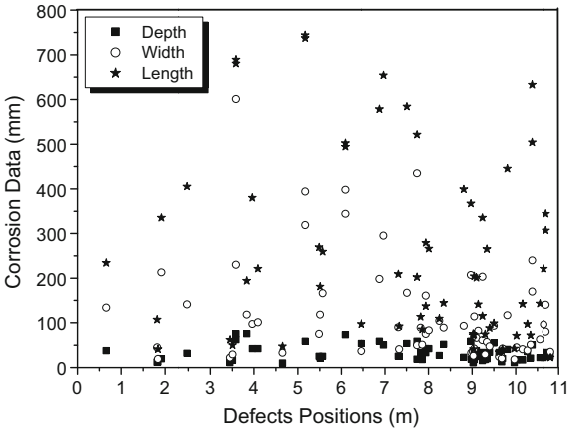

for the determination of the new safety pressure. Example of burst test are prepared from the tube No. 12510 with a pressure according to Fig. 3. In the API 5L X60 with design and operational burst pressures of 73 and 69 bars, respectively, the pressure recorded was 95 bars with a defect of 75.6% of depth, Fig. 4. The result has highlighted the more conservative of the current standards used. And the recommendation that further testing be conducted to a database required for optimal integrity management.

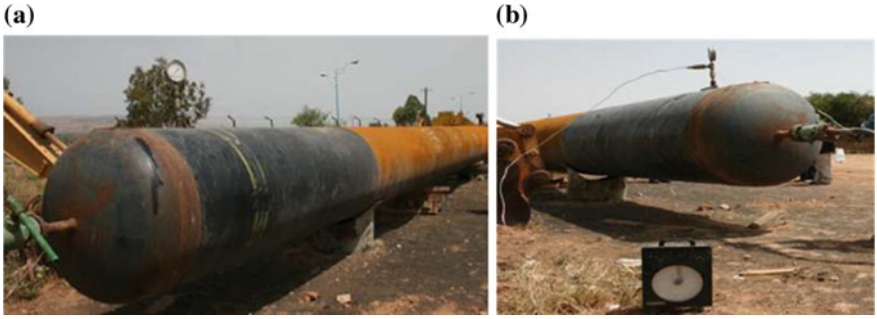

Fig. 3 Preparation of tube No. 12510 from GG1 for the bursting test (**a**) and the pressure recording (**b**)

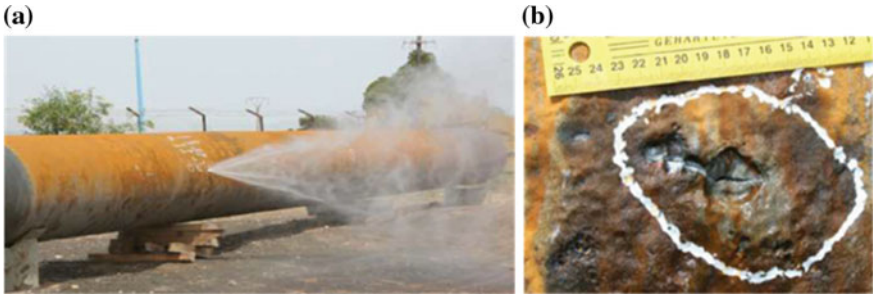

Fig. 4 Resistance of all the corrosion nest (**a**) and state of scratcher (**b**) at 95 bars of pressure

For regions of external corrosion where the deepest penetration is less than 80% of the wall thickness, an ASME B31G or RSTRENG evaluation of acceptable defect length (L) can be conducted. The acceptable circumferential extent (c) of the collected defects are evaluated in Fig. 5, with the standards API RP 579, where (t) is the nominal pipe wall thickness, (d) is the maximum defect depth, and (D) is the nominal pipe diameter. Pipe that is not severely corroded enough to fail either of the criteria for acceptable defect length and the criterion for acceptable defect circumferential extent requires no repair except recoating and backfilling.

Clock Spring Pipe Repairing

In this part a numerical study of the pipe repair using with the Clock Spring method is presented. This method of reparation is using in Algeria. A composite sleeve manufactured from E-glass fibers and polyester resin is used. The fibers are oriented in order to run around the hoop direction of the pipe and to maximize the strength in this direction. The sleeve is colored in yellow in the picture, Fig. 6. A methacrylate

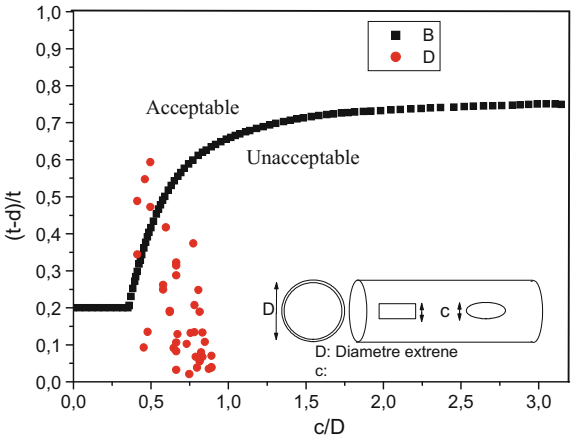

Fig. 5 Acceptance criterion for circumferential extent of metal-loss defect

Fig. 6 Clock Spring® sleeve being applied to a damaged, steel pipe

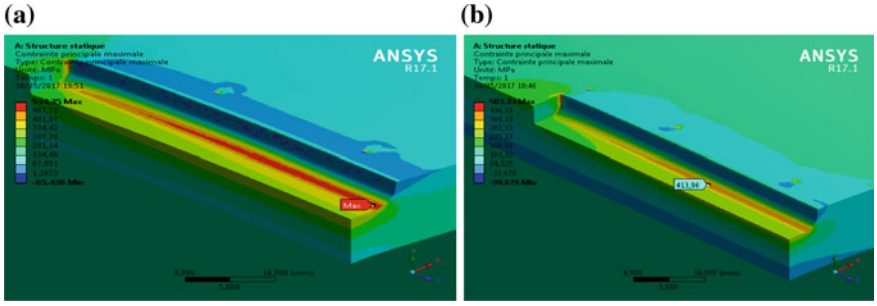

Fig. 7 Stress distribution at the inside repaired defect **a** Two Sleeve, **b** Eight sleeves

adhesive is used to secure the repair. The adhesive is colored blue in the picture, Fig. 6. The model of repaired pipe is presented and the effect of sleeve number on the stress value has been studied. The maximum stresses is localized at the defect tip and presented in Fig. 7. We note that the sleeve number has an effect on the

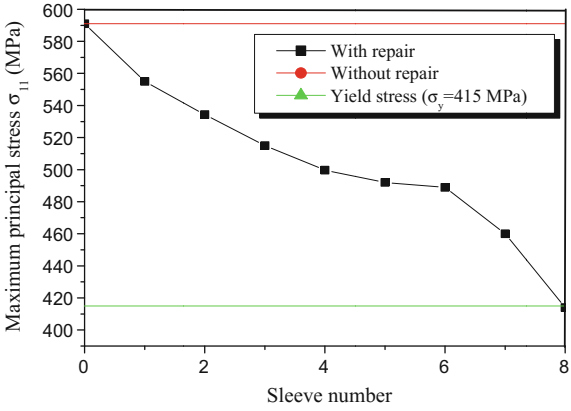

Fig. 8 Maximum principal stress evolution with sleeve number

maximum stress value. Figure 8 presents the maximum principal stress evolution with sleeve number. This result indicates that after Clock Spring repair, the maximum principal stress decreases, with sleeve number. This maximum principal stress has a value 413 MPa for 8 sleeves close to yield stress (σ_y = 415 MPa), this stress diminution is about 34%.

Failure Assessment Diagram

The failure assessment diagram (FAD) methodology replaces the three fracture mechanic parameters relationship (fracture toughness, defect size and loading) by a two parameters, one in order to have a plane representation where non dimensional crack driving force k_r and non-dimensional applied stress L_r are the coordinates. The non-dimensional crack driving force k_r is defined as the ratio of applied stress intensity factor, K_{app}, to the fracture toughness of material, K_{Ic}.

$$k_r = \frac{K_{app}}{K_{Ic}} \tag{1}$$

An improvement was made by introducing the J integral or crack opening displacement as:

$$k_r = \sqrt{\frac{J_{app}}{J_{mat}}} \quad or \quad k_r = \sqrt{\frac{\delta_{app}}{\delta_{mat}}} \tag{2}$$

where, J_{app}, δ_{app} are the applied J integral and crack opening displacement and J_{mat} and δ_c are fracture toughness in terms of critical value of J integral or critical crack opening displacement of the material. Non dimensional stress L_r is described as the ratio of the gross stress σ_g over flow stress (chosen as yield stress σ_Y, ultimate stress, σ_U or classical flow stress $\sigma_0 = (\sigma_y + \sigma_{ul})/2$

$$L_r = \frac{\sigma_g}{\sigma_0} \tag{3}$$

The FAD exhibits a failure curve as the critical non-dimensional crack driving force $k_{r,c}$ versus the critical non-dimensional stress or loading parameter $L_{r,c}$. This curve $k_{r,c} = f(L_{r,c})$ is obtained from fracture toughness data measured from specimens tested under high levels of stress triaxiality (deep crack associated with bending). Such conditions ensure conservative conditions. Local stress distribution ahead of the crack tip is assumed to be plane strain with high constraint. However, for real structures, defect tip constraint is reduced by small thickness, blunt defect or tensile loading and real fracture toughness increases. The failure assessment curve $k_{r,c} = f(L_{r,c})$ delineates a fracture design curve according to the available codes, e.g SINTAP [9], R6 [10] and RCC-MR [11]. The failure curve for the basic level of the SINTAP procedure is given by Eq. (4). The fracture toughness, yield strength and ultimate strength of the material are required for this level.

$$k_{r,c} = \frac{1}{\sqrt{1 + L_{r,c}^2/2}} . \left[0.3 + 0.7\exp\left(-\mu . L_{r,c}^6\right)\right] \quad \text{for} \quad 0 \le L_r \le 1 \tag{4}$$

$$k_{r,c} = f\ (L_r = 1).L_r^{(N-1/2N)} \quad \text{for} \quad 1 \le L_r \le L_{r,max} \tag{5}$$

and $L_{r,max} = 0.5.\left[\sigma_y + \sigma_{ul}/\sigma_{ul}\right]$
with

$$\mu = min\left\{\left(0.001E/\sigma_y\right); 0.6\right\} \quad N = 0.3.\left(1 - \left(\sigma_y/\sigma_{ul}\right)\right)$$

The assessment point of a component can be highlighted by a point of coordinates k_r^* and L_r^*. If this point is inside of the boundary lines of the diagram which is limited by the failure assessment curve; the structure is safe Fig. 9. If not, failure occurs, and the assessment point is situated outside of the interpolation curve.

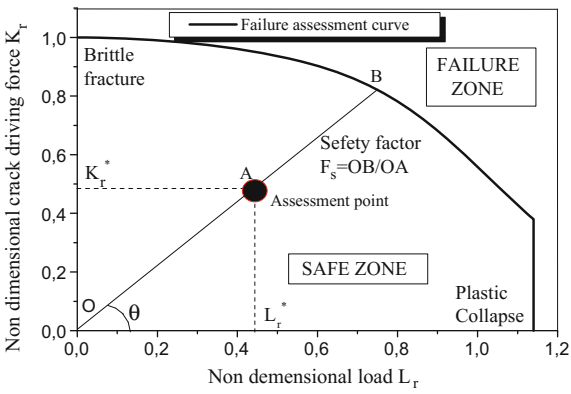

Fig. 9 Typical failure assessment diagram (FAD) indicating the safe and failure zones and assessment point and safety factor

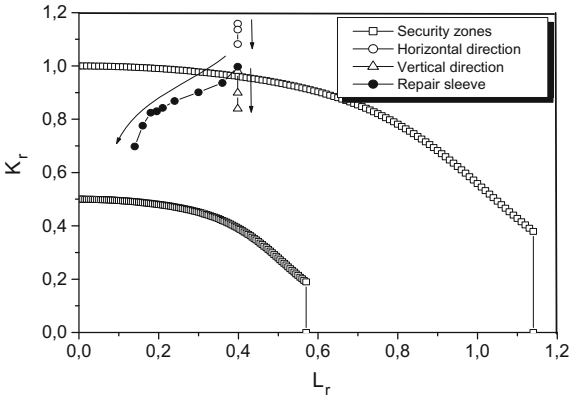

Fig. 10 FAD for corrosion defects with and without repairing. Influence of sleeve number

Table 2 Influence of sleeve number on SF on API X60 pipe steel with 7 bars in the pressure

Sleeve number	Without	1	2	3	4	5	6	7	8
Safety factor	0.96	1.03	1.08	1.13	1.17	1.19	1.20	1.27	1.41

In case of corrosion defect, non-dimensional defect driving force is obtained by Volumetric Method [12]. Assessment points have been determined for the following conditions: (i) the pipe made of API 5L X60 steel with the following dimensions: 600 mm diameter, 12.7 mm wall thickness with a pressure service conditions 70 bars for a gas pipe, Two aligned defects in the circumferential direction with $d/t = 30\%$, $W = 10$ mm and $L = 100$ mm, separation distance dl mm and two aligned defects in the circumferential direction with $d/t = 30\%$, $W = 10$ mm and $L = 100$ mm, separation distance dc mm. In other hand two aligned defects in the circumferential direction with $d/t = 30\%$, $W = 10$ mm and $L = 100$ mm, separation distance dl mm with repairing (number of sleeves 1–8) are used. The different assessment points are seen in Fig. 10. Table 2 gives the safety factors versus the number of sleeves. One notes that the defect lead to failure under service pressure and the pipe is safe after repairing. The safety factor increases with number of sleeves. However, with eight sleeves the safety factor is far from the value of 2 which ensures security.

Discussion

In this study, the expected numerical results confirm the strong influence of geometry and position of defects on the service life of high pressure pipes. Single base corrosion defects (length, width and depth) geometry affects markedly the local stress and strain distributions, playing a critical role in the failure pressure prediction of pipelines. Corrosion defect depth values are more "restrictive" than the length ones. The obtained results will permit establish a comparative analysis in order to discuss the interaction of two defects in both longitudinal and circumferential directions with a service pressure. Based on the opening stress, as a dominant stress and responsible on the probable failure of pipe, critical distances are given in the two senses, given the started points to consider separate or colony defects. It is essential information taking into account in the engineering application to use the standards to repair probable failure pipe. Corrosion defect affects the safety of pipe under service pressure. Repairing using Clock Spring sleeves increases the safety factor determined by Failure Assessment Diagram. However, before repairing it is necessary to ensure that the assessment point is in the security domain i.e. the safety factor is greater than 2. This gives an indication of the limit of this repair technic.

Conclusion

An accident free pipeline operation is the dream of every player in oil and gas industry, but corrosion by nature is a contending issue in this regard. Corrosion has been around for all recorded history and causes the degradation of the mechanical properties of pipeline system due to chemical reaction with the operational fluid and environment. Therefore, pipeline companies need to determine critical distance between defects for making decisions about repairing the defects or leaving them for further service. Finite element analysis (FEA) can improve the corrosion, integrity assessment process and also evaluate the effect of defect geometries on the operating pressure. It is a good tool, to optimize the experimental tests in the aim to provide the assessment techniques in order to investigate the repairing methods and their capabilities. In the same way, the monitoring techniques via ameliorating can be enhanced by the testing methods or making more input data by establishing the required grid.

References

1. ASME B31G. 2012. Manual for Determining the Remaining Strength of Corroded pipelines. Supplement to the ASME B31 Code for Pressure Piping.
2. Canadian Standard Association. 2015. Oil and gas pipeline systems. CSA standard Z662-15, Mississauga, Ontario, Canada.

3. DNV-RP-F101. 2015. Corroded Pipelines. Det Norske Veritas, Norway.
4. Bipul Chandra, B.C. Mondal. 'Burst Pressure Assessment for Pipelines With Multiple Corrosion Defects', Resilient Infrastructure, June 1–4, 2016.
5. Kiefner, J.F. and Vieth, P.H., "Evaluating pipe Conclusion: PC program speeds new criterion for evaluating corroded pipe", Oil & Gas Journal, Vol. 88, No. 34, pp. 91–93, August 20 (1990).
6. Pipeline Operator Forum Document: "Specifications and requirements for intelligent pig inspection of pipelines", Version 3.2, January (2005).
7. ANSYS, Inc.; 2017.
8. Andrade, E.Q. d., Benjamin, A.C., Machado Jr., P.R.S., Pereira, L.C., Jacob, B.P., Carneiro, E.G., Guerreiro, J.N.C., Silva, R.C.C. and Noronha Jr., D.B. 2006. Finite element modeling of the failure behavior of pipelines containing interacting corrosion defects. Proceedings of OMAE2006 25th International Conference on Offshore Mechanics and Arctic Engineering Hamburg, Germany.
9. SINTAP: Structural Integrity Assessment Procedure, Final Report E-U project BE95-1462 Brite Euram Programme Brussels, (1999).
10. Harrisson R.P, Milne I and Loosmore K "assessment of the integrity of structures containing defects". Central Electricity Generating Board Report R/H R6 Revision 1, Leatherhead, Surrey, UK, (1977).
11. RCC-MRx 2015 - EN Design and Construction Rules for mechanical components of nuclear installations: high-temperature, research and fusion reactors, AFCEN, Paris (2015).
12. Pluvinage G. "Fracture and Fatigue emanating from stress concentrators" Kluwer Academic Publishers, Dordrecht, Netherlands, (2003).

Effect of Microstructure on Tension, Charpy and DWTT Properties on Two API X70 Plates

Fernando Guzmán, Moisés Hinojosa and Eduardo Frias

Introduction

The current demand of petroleum and natural gas is increasing, as shown in Fig. 1, which includes the consumption of these products from 1985 to the present and the expected demand up to 2035, the most efficient way to transport these products is by welded pipeline, this means that the demand for pipeline will continue increasing in the next years. An important part of the manufacturing process is the reception of raw material, which must meet API (American Petroleum Institute [1]) standards. In this study, we compared two API X70 PSL2 steels from different suppliers, looking to understand the effect of chemical composition and microstructure in the tension, CVN and DWTT test.

The microstructure of these steels varies according with the TMCP parameters used by the supplier, as discussed in the work by Byoungchul et al. [2], where the TMCP parameters were manipulated in twelve different ways for three different chemical compositions in a API X70 steel, manipulating parameters such as the rolling temperatures and cooling rates. A variety of ferrites with small percentages of martensites and bainites were obtained giving different mechanical properties under tension, Charpy impact and DWTT. A phenomenon called inverse fracture was observed in DWTT, denoted by a cleavage morphology in the fracture surface on the side opposite to the notch, this phenomenon was explained in terms of high strain rate generated by the impact of the pendulum hitting the sample. This phenomenon occurs more in microstructures with higher density of polygonal ferrite (PF) and a lesser amount of acicular ferrite (AF). In a similar work,

F. Guzmán (✉) · M. Hinojosa
UANL, FIME, San Nicolás de los Garza, Nuevo León, Mexico
e-mail: yoshua_003@hotmail.com

E. Frias
Tubacero, Monterrey, Nuevo León, Mexico

R. R. Ambriz et al. (eds.), *Proceedings of the 17th International Conference on New Trends in Fatigue and Fracture*, https://doi.org/10.1007/978-3-319-70365-7_18

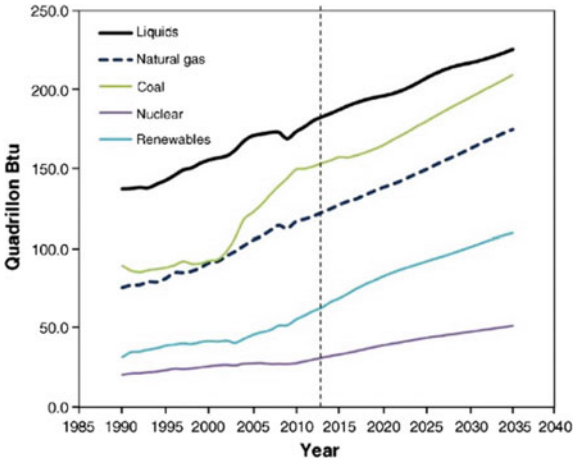

Fig. 1 Prediction of consumption of petroleum and natural gas up to 2035 [10]

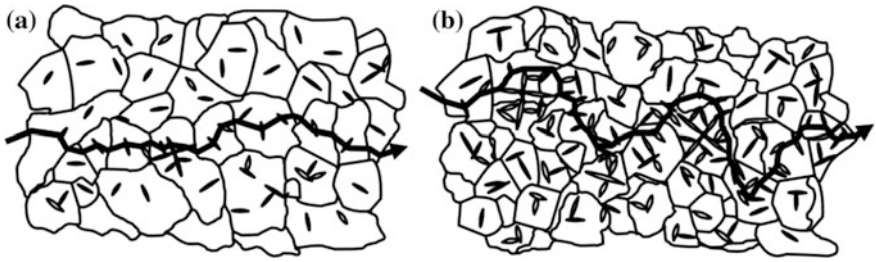

Fig. 2 Fracture mechanism in acicular ferrite proposed by Yong Tian et al. 2015 [4]

Byoungchul et al. [3] manipulated TMCP parameters focusing on Charpy impact tests and confirmed that the best toughness was associated to microstructures with high AF percentage whereas the lower toughness corresponds to large PF. In a recent study, Tian Yong et al. [4] studied the mechanism of ductile and brittle fracture in X70 and X80 steels processed by UFC (Ultra-Fast Cooling), different microstructures and thus different mechanical properties were obtained, noting that the microstructure of both steels was composed of polygonal and acicular ferrites, some bainite and some martensite islands, with more polygonal ferrite in the X70 and more acicular ferrite in the X80 steel. The model shown in Fig. 2 was proposed for the propagation of a crack in a polygonal or acicular ferrite matrix where we can see that in the polygonal ferrite the crack propagates in a transgranular manner on the BCC structure <100> cleavage planes [5, 6], whereas the crack propagation is chaotic in acicular ferrite and does not follow the cleavage planes.

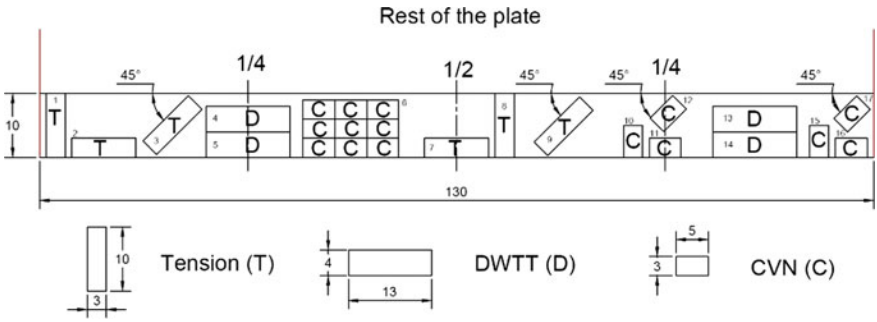

Fig. 3 Sketch of location and direction of the samples taken from the plate (all in inches)

Experimental Procedure

Specimens taken from one end of the plate were prepared to perform tension, Charpy (CVN) and DWT tests, specimens to analyze the microstructure were also obtained. In Fig. 3 we can see the sketch of the position and direction in which the specimens were taken also assigned a number for subsequent location, taking samples of transverse tension in the center of the plate, transverse CVN in a quarter and also transverse DWTT in other quarter of the plate, these positions defined by the API 5L 45 ed. [1], being these samples for accreditation process of material, the other longitudinal samples and 45° were taken for the purpose of analyzing the material behavior at different positions, as well taking samples as the possible in center and the most extreme possible of the plate, to see the effect of plate cooling in the process on the microstructure and later in the mechanical properties, in Fig. 3 section 6 you can see a cluster of CVN samples were collected for testing CVN at different temperatures from 10 to −70 °C and observing its mechanical behavior and toughness.

Results

Starting with the chemical composition of the two steels indicated in Table 1 which was extracted from quality certificates provider by the supplier we can see a significant difference in Cr, which tells us that is the supplier 1 steel should have higher percentage of ferritic phases since chromium is a ferrite phase stabilizer [7], the other relevant elements such as C, Mn, Ni, and the sum of Nb + V + Ti show no significant differences.

Table 1 Chemical composition of the steel according to the quality certificates

	Supplier 1	Supplier 2
C	0.056	0.060
Mn	1.690	1.710
P	0.007	0.015
S	0.001	0.003
Si	0.280	0.220
Al	0.033	0.040
Cu	0.010	0.020
Cr	0.240	0.020
Ni	0.010	0.020
Mo	0.010	–
Ti	0.008	0.015
Nb	0.043	0.034
V	0.001	–

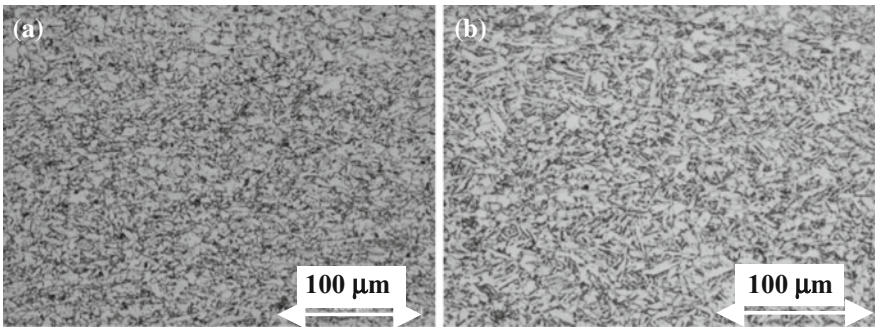

Fig. 4 Microstructure of Supplier 1 (**a**) and Supplier 2 (**b**)

Microstructure

The metallographic preparation of the pieces consisted of polishing with sandpaper from 320 grid to 1200 grid following the ASTM E-3 [8] standard, mirror finish was obtained using a cotton cloth and 1 µm alumina: The specimens were etched with 3% Nital during 10–15 s obtaining the microstructures shown in Fig. 4 where we it can be seen that in the steel 1 (a) there is a mixture of quasi polygonal and acicular ferrite along with some bainite, in the steel 2 (b) there is a greater quantity of quasipolygonal ferrite, bainite, a lesser quantity of acicular ferrite and second phase particles, which are presumably carbides that could serve as cracks initiators.

Charpy Impact CVN

Charpy impact tests were conducted under ASTM E23 [8] and API 5L 45 ed. [1] standards with a V-notch in 1/1 sample size, tests were performed in the raw material at a temperature of −10 °C according with the API method, in addition, a transition curve was made from −70 to 10 °C. Figure 5a shows the results of the CVN test at −10 °C, where a homogeneous behavior for supplier 1 steel is observed regardless of the test direction, the behavior of the steel from supplier 2 is very heterogeneous. In Fig. 5b we can see strong differences in the ductile to brittle transition, with the toughness of the steel from supplier 2 beginning to fall at −30 °C and exhibiting heterogeneity whereas that from supplier 1 hold its properties down to −60 °C with a homogeneous behavior.

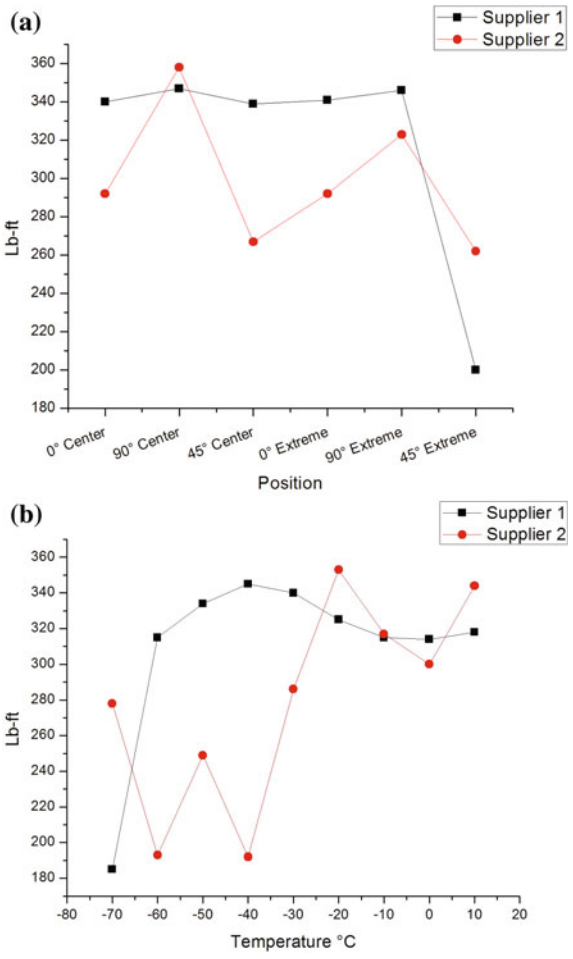

Fig. 5 **a** CVN at −10 °C. **b** CVN at different temperatures

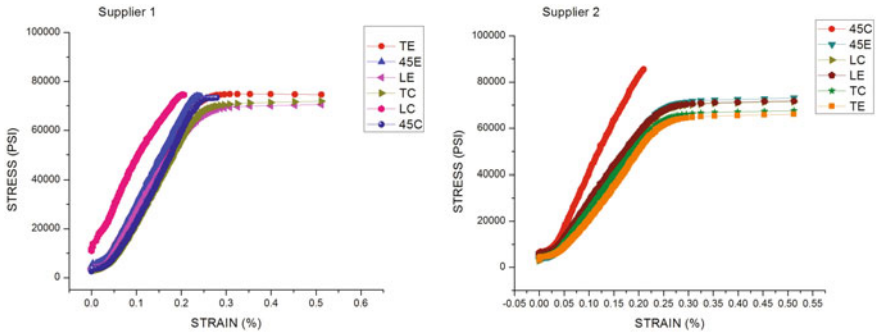

Fig. 6 Comparative longitudinal, transverse and diagonal directions for both steels

Tension

Tension tests were carried out according to ASTM E8 [9] and API 5L 45 ed. [1] standards in specimens cut along the longitudinal, transverse and diagonal direction in the locations indicated in Fig. 3, at the center and one end of the plate. We can see a fairly constant behavior in the steels regardless of their direction or location in Fig. 6, with a similar strain to fracture in the two steels, reaching greater level of stress for Supplier 2 steel, but this one continues having an heterogeneous behavior in comparison with Supplier 1 steel, both steels meet the requirements imposed by the API 5L 45 ed. [1] confirming its cataloging as API X70 steel.

DWTT

The DWTT was performed under the API 5L 45 ed. [1] standard, at a temperature of 0 °C. The main purpose of this test is to determine the ductile or brittle character of the fracture surface generated by the tearing of the specimen, in some reports it may present inverse fracture [2]. In our case a completely ductile fracture surface was observed as no specimen was completely broken, concluding that this material behaves quite well in this test and these conditions.

Discussion

Microstructure

As stated before, supplier 1 steel has a higher content of Cr, which is a ferrite stabilizer [6], although its percentage is not very high, we could see an effect on the

microstructure. Obviously, these materials did not have the same TMCP parameters, nevertheless a higher percentage of ferrite was observed in the microstructures of Supplier 1 steel, whereas in Supplier 2 steel we observed bainite and second phase particles which may be carbides or retained austenite, this phase favored by the percentages of Mn in both steels as this element is known as an austenitic stabilizer [6], promoting the formation of phases such as retained austenite and bainite. The microstructures did not exhibit evidence of the rolling direction except for slight texture which had some effect on the tension tests.

Charpy Impact CVN

In the CVN tests at −10 °C we can observe variation in the supplier 2 steel for the different directions and locations, this is maybe due to the presence of second phase particles which may nucleate crack that later propagate in different ways depending on the material texture. The lower values toughness in this material compared to that of supplier 1 may be due to the difference in the microstructure, which exhibits more quasi polygonal ferrite in supplier 2 along with the nucleating second phase particles which favor the nucleation of cracks that can propagate over the cleavage planes in the quasi polygonal ferrite, moreover the homogeneous behavior in Supplier 1 is associated to the fact that it not has a preferential texture, the high toughness values are explained by the lower percentage of polygonal ferrite in the microstructure and by the absence of second phase particles.

The CVN tests at the different temperatures confirms the already discussed effect of microstructure, with higher toughness values for supplier 1 steel down to temperature of −60 °C, whereas supplier 1 steel hold it only down to −30 °C structures.

Tension

The tension test clearly reveals difference in these two steels, as it can be seen in Fig. 6. Steel from supplier 1 exhibit higher strength than that from supplier 2 steel, this behavior can be explained by the presence of second phase particles, such as carbides, or retained austenite, as these serve as anchors to the dislocation motion in the case of carbides, and in the case of retained austenite it transform to martensite with the deformation thus hardening the material. And interesting result is that both steels have a similar deformation percentages although supplier 2 steel has second phase particles, comparing results we observed that these particles do not influence significantly the tension test result but their effect is strongly evident in the Charpy impact tests.

Conclusions

Both steels meet the requirements imposed by the API 5L 45 standard [1], Supplier 1 steel having better performance in CVN testing as standard and at different temperatures. Both steels behaved as expected in tension test, with better properties for supplier 2 steel. In DWTT both steels showed a 100% ductile character, although they have differences in the microstructure and in the chromium content. We conclude that the supplier 1 steel is the best because it has better toughness and good ductility which is desirable in these steels as they can work in different temperatures including sub-zero environments.

A higher quantity of acicular ferrite was observed in the steel from supplier 1, whereas higher densities of quasi polygonal ferrite, bainite and second phase particles were present in supplier 2 steel. Thus supplier 1 steel had a better performance at low temperatures by reducing brittle crack propagation by the high density of acicular ferrite and low percent of quasi polygonal ferrite

References

1. API 5L 45 ed. July 1, 2013.
2. Effect of microstructure on Inverse Fracture Occurring during Drop-Weight Tear Testing of High-Toughness X70 Pipeline Steels, Byoungchul Hwang et al. Metallurgical and Material Transaction A, vol. 36A, 2005.
3. Effective Grain Size and Charpy Impact Properties of High-Toughness X70 Pipeline Steels, Byoungchul Hwang et al. Metallurgical and Material Transaction A, vol. 36A, 2005.
4. Effect of Ultra-Fast Cooling on Microstructure and Mechanical Properties of Pipeline Steels, Yong Tian, et al. Journal of Material Engineering and Performance, vol. 24(9), 2015.
5. Role of delamination and Crystallography on Anisotropy of Charpy Toughness in API X80 steel, M. S. Joo, et al. Material Science and Engineering A 546, 314–322, 2012.
6. Steels: Microstructure and Properties, H. K. D. H. Bhadeshia and R. W. K. Honeycombe, Elsevier, 2006.
7. ASTM E 3, Standard Practice for Preparation of Metallographic Specimens.
8. ASTM E 23, Standard Test Method for Notched Bar Impact Testing of Metallic Material.
9. ASTM E 8, Standard Test Method for Tension Testing of Metallic Materials.
10. Oil and Gas Pipeline, Integrity and Safety Handbook, R. Winston Revie, Wiley, 2015.

Fatigue Analysis in a Bellow Expansion Joint Installed a Heat Exchanger

I. Villagómez, J. L. González, J. J. Trujillo and D. Rivas

Introduction

The expansion joints are employed in piping system to absorb different thermal expansion while containing the system pressure. They are successfully utilized in refineries, chemical plants, fossil and nuclear systems, heating and cooling systems, and cryogenic plants [1].

Any pipe connecting two points is subject to numerous types of loads which result on stresses on the pipe (Fig. 1).

Some of the causes of these stresses are:

- Internal or external pressure at working temperature
- Weight of the pipe itself and the parts supported
- Movement imposed on the pipe sections by external restraints
- Thermal expansion

The stress on the piping wall is related to the force or movement exerted on it by external resistance and the flexibility of the pipe itself.

When either the value of the stresses or that of the external forces or movements exceeds the maximum allowable ones, the flexibility of the pipe must be increased artificially. This can be done by altering the layout of the pipe or by inserting high flexibility sections. This is precisely the function of expansion joints [1].

In this work, the failure analysis of a bellows expansion joint installed in a heat exchanger is a U-shaped corrugated type gasket made of Alloy ASTM B127 grade 400. The design pressure of the joint expansion is $13.50\,\mathrm{kg/cm^2}\,(192\,\mathrm{psi})$ and the design temperature is $110\,^{\circ}\mathrm{C}\,(230\,\mathrm{F}^{\circ})$ [2].

I. Villagómez · J. L. González · J. J. Trujillo (✉) · D. Rivas
Instituto Politécnico Nacional, ESIQIE-IPN, GAID-IPN, UPALM Edif. 7 Planta baja, Av. Instituto Politécnico Nacional s/n, Cp. 07738 Col. Lindavista, Mexico
e-mail: jjtrujillotadeo@hotmail.com

R. R. Ambriz et al. (eds.), *Proceedings of the 17th International Conference on New Trends in Fatigue and Fracture*, https://doi.org/10.1007/978-3-319-70365-7_19

Fig. 1 Refinery expansion joint

Methodology of Failure Analysis

The failure analysis was performed with the methodology developed by the GAID-IPN by Dr. Jorge Luis González Velázquez, which is in accordance with the ASTM E 2332-04 standard [3].

Visual Exam

Figure 2 shows the 8″ diameter bellow expansion joint in the condition that was received, for its study in the Laboratories of Engineering in Metallurgy and Materials of the National Polytechnic Institute. The expansion joint is a U-shaped corrugated linear bellows and was welded to two sections of carbon steel tube by fillet welding on the edge of the overlapping sleeve of the joint over the outer diameter of the pipe. It should be noted that the junction of the expansion joint and the pipe exhibits a variation in the wall thickness. The expansion joint presented three fasteners welded to the tube body.

Figure 3 shows a circumferential fracture of approximately 190 mm in length, located on the fusion line of the weld expansion joint with the tube. The fracture is simple with no branching or secondary cracks and its path follows the contour of the weld bead line but one end of the crack deflects at an oblique angle towards the center of the expansion joint. No plastic deformation associated with the fracture was observed. The body of the expansion joint has a metallic appearance, with a gloss and a polished finish, although rust residues and some dents and light scrapes are observed.

Fig. 2 Expansion joint in the condition as it was received for study in the Laboratories of the DIMM-IPN

Fig. 3 Fracture in 8″ diameter bellow expansion joint

Chemical Analysis

The chemical composition of the expansion joint manufacturing material and that of the bellows pipe sections were determined by X-ray fluorescence spectrometry. The experimental chemical composition obtained can be seen in Table 1.

Hardness Test

The hardness testing of the bellows fabrication material was performed by micro-indentation on the Vickers (HV) scale, testing was performed in accordance with ASTM E384 [4]. Rockwell B hardness tests were performed on the pipe

Table 1 Chemical composition table of expansion joint and pipe

Specimen	C	Si	Mn	S	P	Cu	Cr	Ni	Mo	V	Fe
Expansion joint	U	U	1.06	U	U	30.28	0.53	65	0.14	U	2.5
ASTM B 127 400	NS	NS	2.0max	NS	NS	28–34	NS		NS	NS	2.5max
Pipe	0.128	0.281	1.07	0.032	0.011	0.067	0.036	0.041	0.028	0.036	Bal
ASTM A 106 grade B	0.30max	0.10min	0.29–1.06	0.035max	0.035max	0.4max	0.4max	0.4max	0.15max	0.08max	Bal

U: Undetermined; NS: Not Specified; Bal: Balance

Table 2 Hardness values table of expansion joint and pipe

Specimen	Scale	Average Value	Minimum Value	Maximum Value	UTS (ksi)
Expansion joint	Vickers	223	218	232	107
Pipe	Rockwell B	82	81	83	77

welded to the bellows, tests were performed in accordance with ASTM E-18 [5]. Table 2 shows the test result, including the equivalent value of tensile strength.

Microstructure

Figure 4 shows the bellows microstructure formed by equiaxial grains with annealing twinning. The microstructural condition corresponds to a condition of sheet worked in cold and annealed. In the case of the pipe, a microstructure of ferrite matrix with lamellar pearlite colonies is observed; the microstructural condition corresponds to a normalized heat treatment.

Macroscopic Examination for Failure Analysis

In Fig. 5, the cross-section of the sample of the failure zone is observed where the fracture is adjacent to the weld bead and has a straight path. In addition, the welding is of the fillet type and does not present macroscopic defects like fusion faults, porosity, undermined or entrapped slags.

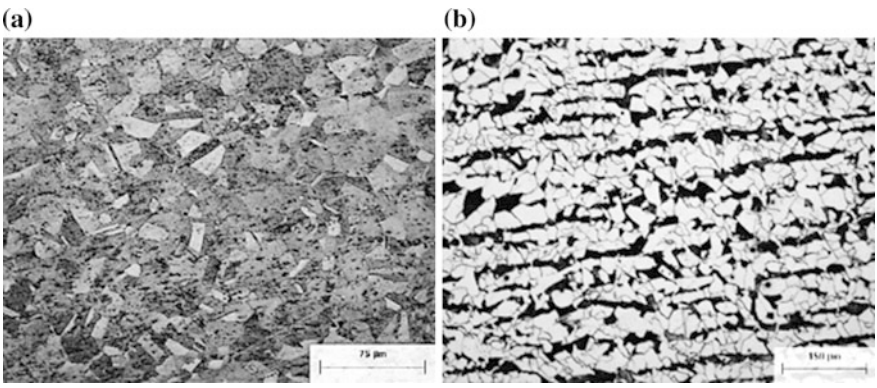

Fig. 4 Microstructure **a** Bellow expansion joint, **b** Pipe

Fig. 5 Cross section of the fracture zone (The arrow points to the line of the fracture)

Microscopic Examination for Failure Analysis

The scanning electron microscopy, shows the presence of thin lines in the form of grooves, parallel to the crack propagation front, that are identified as microscopic striations, typical of fatigue fractures. Also, the surface is free of deposits of corrosion products and no evidence of selective attack, melting of material, or heat or mechanical damage is observed. This is shown in Fig. 6.

Results and Discussion

(1) The chemical composition and microstructure of both the expansion joint and the pipe match its material specification. (ASTM B127—Expansion joint/A106-C-Pipe) [2, 6].
(2) The failure mode of the bellows-type expansion joint was identified by the fractographic examination as a fatigue fracture.

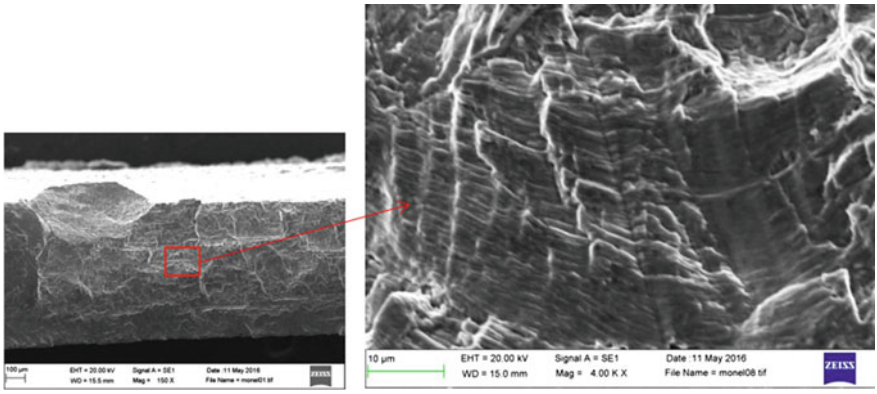

Fig. 6 Microscopic striations, typical of fatigue fractures (Expansion joint section)

(3) A conservative estimate of the magnitude of stress concentration for a 1 mm thick tube, attached to an 18.4 mm thick tube and subjected to axial stress is 1.5 times. That is, the stresses in the expansion joint increase by 50% in the welded joint.
(4) Now, it is known that the number of fatigue failure cycles of the Monel 400 alloys obeys a power law represented by the following equation:

$$N_f = 1.35 \times 10^6 \sigma^{-0.111}$$

$$\sigma_{DP} = 19.2\ ksi \longrightarrow \boldsymbol{N_f = 972,475\ cycles}$$

$$\sigma_{SC} = 1.5(19.2\ ksi) = 28.8\ ksi \longrightarrow \boldsymbol{N_f = 2,912\ cycles}$$

(5) Improper installation of the expansion joint caused a concentration of stress in the system. It is recommended according to manufacturers, connect it with flanges or nipples.

Acknowledgements The authors would like to acknowledge the National Polytechnic Institute (IPN), the National Council of Science and Technology (CONACYT) and the Analysis Integrity of Pipelines Group (GAID-IPN) for the support to carry out this research.

References

1. PACIFIC HOSEFLEX. Expansion Joint. Recovery from https://www.hoseflex.com/wp-content/uploads/2014/07/Expansion-Joints.pdf2.
2. ASTM B127-05(2014) “Standard Specification for Nickel-Copper Alloy (UNS N04400) Plate, Sheet, and Strip”.
3. ASTM E2332-04 “Standard Practice for Investigation and Analysis of Physical Component Failures (Withdrawn 2004)”.
4. ASTM E384 “Standard Test Method for Knoop and Vickers Hardness of Material”. 5. ASTM B127-05(2014) “Standard Specification for Nickel-Copper Alloy (UNS N04400) Plate, Sheet, and Strip”.
5. ASTM E18-17 “Standard Test Methods for Rockwell Hardness of Metallic Materials”.
6. ASTM A106/A106 M-15 “Standard Specification for Seamless Carbon Steel Pipe for High-Temperature Service”.

Failure Analysis of Stress Corrosion Cracking of a Ball Valve in Service

I. Mortera, J. L. González, A. Casarrubias and D. Rivas

Introduction

The ball valves are used to let or not pass a fluid (ON-OFF). Otherwise, if left partially open, the fluid and the pressure thereof will wear parts of the valve. According to the latter and depending on the operating conditions (fluid-pressure-temperature), the interior of the valve will fail, resulting in undesirable leaks [1].

When the flow in the valve is horizontal, the rod must be in horizontal position with the pressure from the right. The two adjusting screws of the gasket must be gently tightened in the direction of the watch with an Allen wrench and turn each screw to the same tightening torque [2].

The failed component, analyzed in this work, was installed in a 3 in nominal diameter pipeline. The valve was installed in 2013 and was operating at 29 kg/cm^2; the service temperature was 23 °C. The line transported condensate and liquids, with 0.44% Vol. H_2S and 0.58% Vol. of CO_2.

The objective of this work is to perform a failure analysis of the ball valve, to know the failure mechanism.

I. Mortera · J. L. González · A. Casarrubias (✉) · D. Rivas
Instituto Politécnico Nacional, ESIQIE-IPN, GAID-IPN, UPALM Edif. 7 Planta baja, Av. Instituto Politécnico Nacional s/n, 07738 Col. Lindavista, CDMX, Mexico
e-mail: david.casarrubiasalvarez@gmail.com

R. R. Ambriz et al. (eds.), *Proceedings of the 17th International Conference on New Trends in Fatigue and Fracture*, https://doi.org/10.1007/978-3-319-70365-7_20

Materials and Methods

Failure analysis was performed using a methodology developed specifically for GAID-IPN by Dr. Jorge Luis González Velázquez, which is in accordance with the standard ASTM E 2332-04 "Standard Practice for Investigation and Analysis of Physical Component Failures" [3].

Visual Inspection

During visual inspection of the valve, it was noted that the bonnet seat seal was broken and a metal material adhered. The main feature observed in the failed valve was the fracture of the four screws holding the bonnet with the valve body. Also, it was observed that the fracture zone presents a strongly adhered oxide layer that precludes a detailed observation of the characteristics of the fracture.

Chemical Analysis

The contents of carbon (C), sulfur (S), silicon (Si), manganese (Mn), chromium (Cr), molybdenum (Mo) and phosphorous (P) were determined, for the screws, by spectrophotometry by the atomic absorption technique.

Hardness Test

In order to carry out the hardness test, the "J" bolt (see Fig. 1) was selected. This test was based on ASTM E-18 [4], using the Rockwell C scale and following the guidelines described here. The test conditions were: 120° Diamond Tip Indentor, a preload of 10 Kgf and a total load of 150 Kgf.

Metallographic Study

A metallographic sample was prepared from the cross section of bolt "I" (see Fig. 1), by thinning and polishing until the mirror finish for microscopic observation. To reveal the microstructure of the steel, the sample was etched with the reagent "Nital 3", and it was observed in the metallographic microscope with the "clear field" technique.

Fig. 1 Disassembling the bonnet, the elements named G, H, I and J, correspond to the failed screws

Fracture Surfaces

To examine the fracture zone of the screws, the screws were cut, cleaned and observed by a stereoscopic microscope.

Results and Discussion

Visual Inspection

In reviewing the seal, it was observed that the polymeric material of manufacture is in good condition and the metallic material appears to be a type of filler for leakage control by the method known as caulking. Figure 2 shows the seal and a piece of the metal caulking material.

Fig. 2 Fractured bonnet seat seal and caulk leak seal material

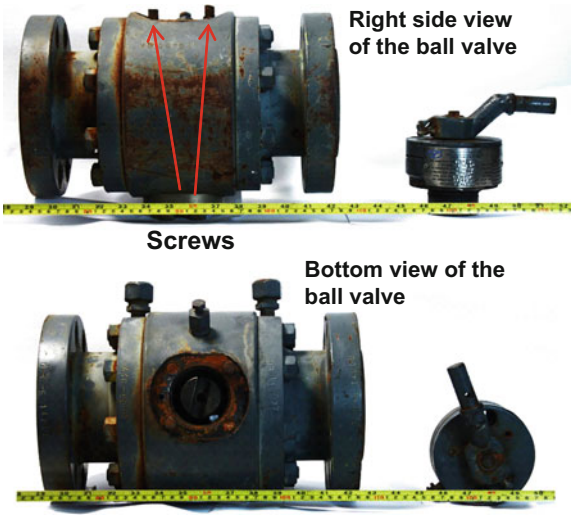

Fig. 3 Condition as received from ball valve DN 80 mm NPS 3″ in GAID-IPN laboratories

Figure 3 shows the fracture surface of the bolts on the body side and bonnet side of the valve, in the condition as they were found at the time of the present failure analysis.

It can be seen that two of the screws have a brittle and flat fracture, while the other two screws exhibit a ductile fracture type cup and cone.

Chemical Analysis

The results of the chemical analysis are presented in Table 1, as well as the specified values of the ASTM A-193 [5].

Hardness Test

The hardness tests results are shown in Table 2, together with the specified value for steel ASTM A 193 [5].

Table 1 Results of chemical analysis in% weight of steel

Element	C	Mn	P	S	Si	Cr	Mo
Screw	0.304	0.752	0.016	0.01	0.262	1.042	0.203
ASTM A 193 B7, B7M	0.37–0.49	0.650–1.10	0.035 max	0.04 max	0.15–1.20	0.75–1.20	0.15–0.25

Table 2 Rockwell hardness values on C scale

No. of indentations	Middle value	Minimum value	Maximum value	Uncertainty	HB approximate
10	40	39	41	±2.13	381
ASTM A 193 B7, B7M	Max 35 HRC, 321 HB				

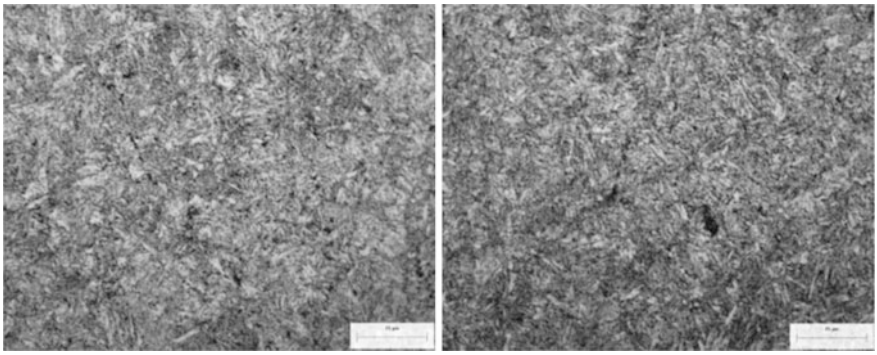

Fig. 5 Steel microstructure of the "I" bolt, consisting of a welded martensite matrix. Metallographic microscope "clear field", 1000X cross section

Metallographic Study

Figure 5 shows the microstructure of the steel, which corresponds to a matrix of annealed martensite.

Fracture Surfaces

The images of Fig. 6 show that the screws I and J exhibit brittle fracture. The images of Fig. 7 show the screws G and H, which present ductile fracture, with area reduction of 8.6% and presence of cutting lip.

Conclusions

1. The failure mechanism, observed on the screws of the NPS ball valve, was identified as stress corrosion cracking, and it was generated as a consequence of a leak in the seal of the valve cap seat.

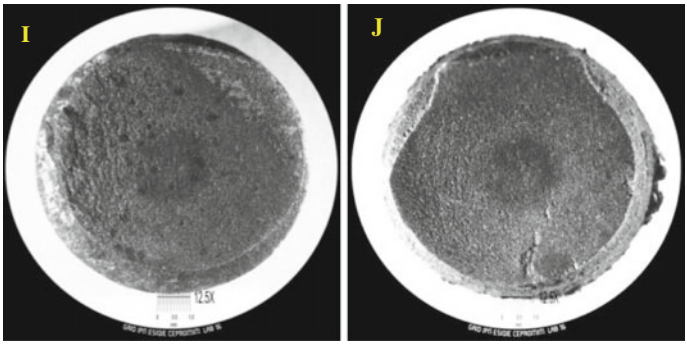

Fig. 6 Surface of fracture screws I and J, showing a brittle, flat and smooth fracture

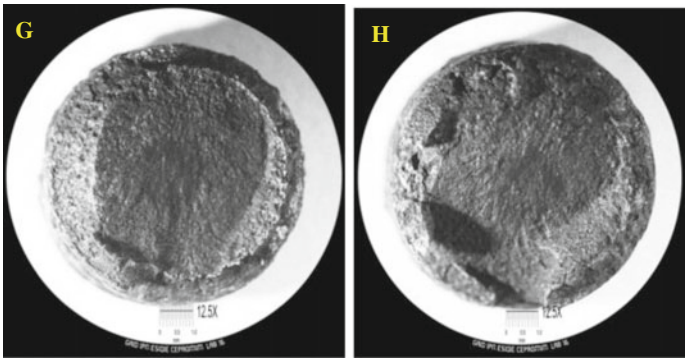

Fig. 7 Fracture surface of the screws G and H, showing a fracture with ductile fracture characteristics

2. It is inferred that the presence of caulking material in the valve seat, is due to an attempt to control a leak caused by the rupture of the O Ring seal of the cap seat. However, it was not possible to seal the leak completely; hence, the working fluid continued in contact with the cap screws, allowing the SCC to be developed.
3. The SCC occurs gradually and is not detectable to the naked eye. Therefore, the cracking propagated until cause a brittle fractures in the screws J and I. Subsequently, as a result of the failure of these screws, the other two end up failing by overload.

Acknowledgements The authors would like to acknowledge the National Polytechnic Institute (IPN), the National Council of Science and Technology (CONACYT) and the Analysis Integrity of Pipelines Group (GAID-IPN) for the support to carry out this research.

References

1. SCFluids Valves and meters recovery from: http://www.valvulasymedidores.com/valvulas_de_bola.html.
2. CAMERON operating and maintenance manual for ball valves recovery from: https://cameron.slb.com/∼/media/543a778cd31046f9b2a9b57daed7db35.ashx.
3. ASTM E 2332-04 “Standard Practice for Investigation and Analysis of Physical Component Failures”.
4. ASTM E 18 “Standard Test Methods for Rockwell Hardness of Metallic Materials”.
5. ASTM A 193 “Standard Specification for Alloy-Steel and Stainless Steel Bolting Materials for High-Temperature Service”.

Assessment of Danger Due to Cracks in Structural Elements of Different Shapes and Geometry

Orest Bilyy

Introduction

This is known that a problem of man-caused and environmental safety of the critical objects of industrial infrastructure becomes more and more important and actual for many industrial countries as well as for the whole world [1].

Technical diagnostics and exploitation experience of critical structures and technological equipment showed that in such objects the number of so-called "non-traditional" damaging increases. These types of damages are not predicted by the current instructions or codes and they occur because of long-term exploitation or as a result of different deviations from the standard mode of the equipment operating regimes [2]. Such damages have mainly a corrosion-mechanical nature and exist at the sites of higher stress concentration caused by specific features of design or manufacturing technology of the structural component [3].

Such fracture, in physical sense, is a multistage localised process of initiation and propagation of crack-like defects (sharp-tipped stress concentrators) to a critical size. Here the physicochemical factors of the interaction between stressed metal and operating environment play a determinant role: they principally change the kinetics of material damaging and as result significantly accelerate its fracture [4].

Samples of typical damages and defects in elements of long-term operation structures in different branches of industry are: heat-and-power; pipeline transport; chemical industry; mechanical engineering [2].

O. Bilyy (✉)
Centre for Corrosion Research, Autonomous University of Campeche,
Av.Agustín Melgar s/n Cal. Buenavista, P.C. 24039 Campeche, CAM, Mexico
e-mail: orebilyy@uacam.mx

R. R. Ambriz et al. (eds.), *Proceedings of the 17th International Conference on New Trends in Fatigue and Fracture*, https://doi.org/10.1007/978-3-319-70365-7_21

Material and Procedures

In the paper [5] an analysis of the ratios for determining oft the stress intensity factor (SIF) for specific structural elements—hollow cylinders under the internal pressure has been carried out. With their help it is convenient to model pipeline systems of the oil and gas industry, which are mainly loaded under the influence of internal pressure. However, this analysis does not provide always a clear answer for the rapid analysis of various piping systems in the presence of defects of differences shapes and geometries. Also it is given an answer with a somewhat delayed effect when the structural element in particular the pipeline is on the verge of fracture on the evaluation of the durability of specific structural elements. In this work are used the analytical relations for SIF K_I and the speed of his change dK_I/da at the peak of the crack size a in the investigated pipeline systems (here a—the depth of the crack-like defect) to apply a certain procedure for express analysis of damaging pipelines systems.

This analytical framework is serviced to assess the rate of change in the SIF K_I depending on the different sizes of damaged pipelines according to the presented models in the proposed index of "resistance of the structural element of the crack growth" [5]. The basis of this analysis is the dependence of the characteristic depth of the defect on a particular parameter of the pipe sizes characterized by the ratio R/t.

To implement this approach are considered four typical cases—hollow cylinder under internal pressure with axial crack on internal surface; hollow cylinder under internal pressure with axial crack on external surface; hollow cylinder under internal pressure with semielliptical crack on external surface; hollow cylinder under internal pressure with off-set embedded elliptical crack, of which models are presented in Figs. 1, 2, 3 and 4.

These models are chosen for the analysis of existing crack-like defects of pipeline systems.

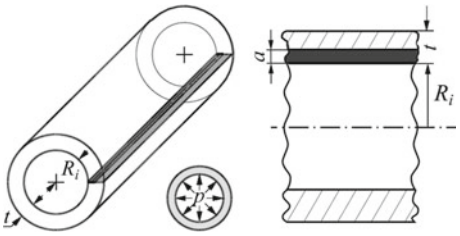

Case I

Fig. 1 Hollow cylinder under internal pressure with axial crack on internal surface: a – **depth of crack**; R_i – **internal radio of** cylinder; t – **wall thickness of** cylinder; p – **internal pressure**

Analytical Relationships

For Case I (Fig. 1), SIF is calculated by the formulas [6]

$$K_{\mathrm{I}} = 2p\frac{R_a^2}{R_a^2 - R_i^2}F\sqrt{\pi a} \tag{1}$$

who

$$F = F_2 + \left(\frac{t}{R_i} - X_2\right)\left(\frac{F_1 - F_2}{X_1 - X_2}\right); \quad R_a = R_i + a.$$

For

$$\frac{R_i}{t} > 0,\ 1: \quad F_1 = 1.1202 + 0.44395\left(\frac{a}{t}\right) + 2.7289\left(\frac{a}{t}\right)^2 + 2.5313\left(\frac{a}{t}\right)^3;$$

$$F_2 = 1.11432 + 1.54228\left(\frac{a}{t}\right) + 1.5241\left(\frac{a}{t}\right)^2 + 5.480\left(\frac{a}{t}\right)^3; \quad X_1 = 0.2; \quad X_2 = 0.1.$$

For Case II (Fig. 2), SIF is calculated [7] as in (1), except

$$R_a = R_i + t - a.$$

For Case III (Fig. 3), SIF is calculated by the formulas [8]:

$$K_{\mathrm{I}a} = F\sigma\sqrt{\pi a}0.97\left(\frac{R_a^2 + R_i^2}{R_a^2 - R_i^2} - 1 + 0.5\sqrt{\frac{a}{t}}\right)\frac{t}{R_i}1.07 \tag{2}$$

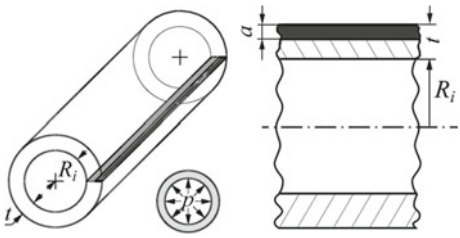

Case II

Fig. 2 Hollow cylinder under internal pressure with axial crack on external surface: a – **depth of crack**; R_i – **internal radio of** cylinder; t – **wall thickness of** cylinder; p – **internal pressure**

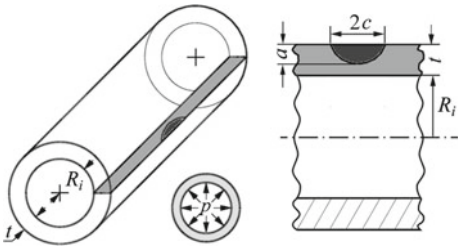

Case III

Fig. 3 Hollow cylinder under internal pressure with semielliptical crack on external surface: a – **depth of crack**; $2c$ – **width of crack**; R_i – **internal radio of** cylinder; t – **wall thickness of** cylinder; p – **internal pressure**

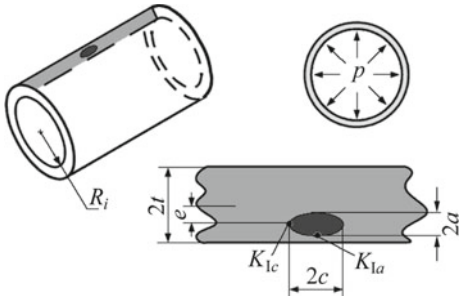

Case IV

Fig. 4 Hollow cylinder under internal pressure with off-set embedded elliptical crack: $2a$ – **depth of crack**; $2c$ – **width of crack;** R_i – **internal radio of** cylinde; $2t$ – **wall thickness of** cylinder; e – **eccentricity of crack**; p – **internal pressure**

who

$$F = \frac{M_1 + M_2\left(\frac{a}{t}\right)^2 + M_3\left(\frac{a}{t}\right)^4}{\sqrt{Q}};\ \sigma = \frac{pR_i}{t};\ M_1 = 1.13 - 0.09\frac{a}{c};$$

$$M_2 = -0.54 + \frac{0.89}{0.2 + \frac{a}{c}};\ M_3 = 0.5 - \frac{1}{0.65 + \frac{a}{c}} + 14\left(1 - \frac{a}{c}\right)^{24};$$

$$Q = 1 + 1.464\left(\frac{a}{c}\right)^{1,65}.$$

For Case IV (Fig. 4), SIF is calculated by the conditions and formulas: $0 \leq e \leq 0.5t$; $t - (a + e) \geq 0.4t$; $\frac{a}{c} \leq 1$; $\frac{R_i}{t} \geq 5$ [5]:

$$K_{Ia} = F_a \sigma \sqrt{\frac{\pi a}{Q}} \tag{3}$$

who

$$\sigma = \frac{pR_i}{2t}; \;\; F_a = h_1 h_3; \;\; F_c = h_2(\beta_1) h_2(\beta_2);$$

$$h_1 = 1 + \left[-0.04 + \frac{0.085}{0.34 + \alpha} \beta_2^2 + (0.05 - 0.03\alpha)\beta_2^4 \right];$$

$$h_2(\beta_i) = 1 + \left[-0.03 + \frac{0.075}{0.3 + \alpha} \beta_i^2 + \left(0.08 - \frac{0.024}{0.1 + \alpha} \right) \beta_i^4 \right];$$

$$h_3 = 1 + \left[-0.06 + \frac{0.07}{0.25 + \alpha} \beta_1^2 + (0.643 - 0.343\alpha)\beta_1^4 \right]; \;\; Q = 1 + 1.464 \left(\frac{a}{c} \right)^{1.65};$$

$$\alpha = \frac{a}{c}; \;\; \beta_1 = \frac{a}{t - e}; \;\; \beta_2 = \frac{a}{t + e}.$$

Discussion

The criterion for the assessment of strength and reliability of structures with crack-like defects is proposed on the base of the concept "resistance of structural element to crack growth" $z_* = (a/t)_*$, characterising the stress intensity factor (SIF) rate variation at the crack tip during its development in a considered structural element.

It has been found that there is some defect size a_*, beginning from which the rate of SIF K_I variation significantly increases. This size of defect is considered to be a characteristic for the assessment of strength and reliability of structural elements with crack-like defects. A defect for which the value of a_* is the lowest one was accepted as the most hazardous from the viewpoint of fracture risk.

For many cases values a_* are lower than critical size of defect a_c. Therefore it can be concluded that within the range $a_* \leq a \leq a_c$ of defect size the specific zone of increased risk of fracture exists. In some cases this "red zone" should be omitted under calculation of the residual durability of the defected structural component.

Based on the dependence of parameter $z_* = (a/t)_*$ on the geometry of structural element and its loading mode, and also on the shape and location of crack-like defects, it is possible to assess the fracture risk of structures or their components and also to formulate the requirements to the procedure of technical diagnostics of structures during their operation.

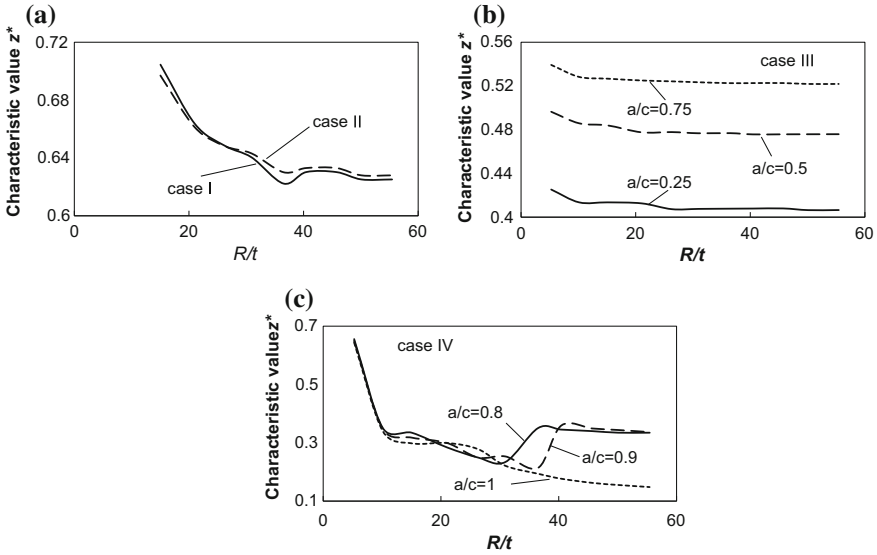

Fig. 5 Dependences of the characteristic value $z*$ on R/t for different pipelines with defects of different shapes and geometry: **a** – case I та II; **b** – case III, **a/c** = 0.25; 0.5; 0.75; **c** – case IV, **a/c** = 0.8; 0.9; 1

In order to improve the rapid analysis of piping systems the dependences of the characteristic defect size on the ratio of the characteristics of pipe sizes are constructed. Such dependencies are constructed for all of the above cases, and, if the first two cases are given in comparison with each other (Fig. 5a), cases III, IV are given for defects of various forms (Fig. 5b, c).

Cases I and II are almost identical, but it should be noted that the ratio of standard sizes R/t is the most dangerous for values 35–40 and therefore pipelines should be more monitored for the presence of longitudinal internal and external cracks defects. In Case III, it was considered that defects with smaller ratios a/c are more dangerous than defects with larger ones. There are some differences in case IV. If the graph with the ratio gradually decreases to $a/c = 1$, then in other situations considered there is a leap value. Moreover, this jump, as in the cases of I and II, is observed for values between 30 and 40. Therefore, such pipelines should be subjected to more detailed monitoring of available cracks defects.

Conclusions

The strength and durability assessment of structures with crack-like defects are presented based on the concept of index of structural element resistance to crack growth. This index is a characteristic of the SIF rate at the crack tip during its propagation in a considered structural element.

The received data may be used in the field of design, technical diagnostics and operation of the critical structures in different branches of industry (mechanical engineering, power generation industry, pipeline transport, etc.).

References

1. Pluvinage, G. A review of fracture toughness transferability with constraint and stress gradient [Text]/ G. Pluvinage, J. Capelle, M. Hadj M liani// Fatigue & Fracture of Engineering Materials & Structures. – 2014. – Vol. 37, Issue 11. – P. 1165–1185. https://doi.org/10.1111/ffe.12232.
2. Panasyuk V.V. A method for the Assessment of the Serviceability and Fracture Hazard for Structural Elements with Crack-like Defects/ V.V. Panasyuk, I.M. Dmytrakh, L. Toth, O.L. Bilyi, and A.M. Syrotyuk// Materials Science (Springer Science + Business Media New York). – 2014. – V. 49, No 5. – P. 565–576.
3. Fremy, F. A scaling approach to model history effects in fatigue crack growth under mixed mode I + II + III loading conditions for a 316L stainless steel [Text]/ F. Fremy// International Journal of Fatigue. – 2012. – Vol. 42. – P. 207–216. https://doi.org/10.1016/j.ijfatigue.2011.10.013.
4. B. E. Paton (editor), Purposeful Complex Program of Scientific Investigations of the Ukrainian National Academy of Sciences "Problems of the Service Life and Safety of the Operation of Structures, Buildings, and Machines," Collection of Scientific Papers Based on the Results Accumulated in 2010–2012 [in Ukrainian], E. O. Paton Institute of Electric Welding, Kyiv (2012).
5. Toth, L. Crack propagation sensitivity index as the tool to promote the fracture mechanics concepts [Text]/ L. Toth// Fiz.-khim. mekhanika materialiv. – 2001. – Vol. 2. – P. 63–68.
6. Kumar V., German M.D., Shih C.F. An Engineering Approach for Elastic-Plastic Fracture Analysis: Report, NP-1931. – EPRI, 1981 (July).
7. Kumar V. et al. Combined Fifth and Sixth Semianual Report to EPRI: Report, SRD-82-048. – General Electic, 1982 (March).
8. Newman J. C., Raju I. S. Stress Intensity Factors for Internal Surface Cracks in Cylindrical Pressure Vessels// Trans. ASME: J. of Press. Vess. Technol. – 1980. – 102 (November). – P. 342–349.

Formation of Preferential Paths in Cracked Hele-Shaw Cells by Water Injection—An Experimental Study

S. de Santiago, I. V. Lijanova, C. O. Olivares-Xometl and N. V. Likhanova

Introduction

The efficient recovery of remnant oil (approximately 50%) is an important world problem regarding brownfields [1–3], and offshore oil [4, 5], for the primary and secondary recovery exploitations are at declining stages.

Up to now, water injection has been the main method for oil recovery due to its simplicity, availability, and cost. The efficiency of this method is determined by intrinsic factors such as hydrocarbon properties, the efficient oil displacement through pores, rock-oil properties and reservoir heterogeneities. The characteristics of the chemical composition of crude oil, water, and rocks play a major role in their interactions, for the reservoir rocks can be more wettable either by oil or water and in some cases, these rocks display mixed wettability [6–10]. Any of these factors can limit the oil extraction if they are not analyzed at the beginning of the reservoir exploitation [11, 12].

When a study is carried out in capillary or porous media, experiments to obtain information that can help understand these phenomena are performed [5, 13]. Generally, porous medium systems on glass cells are used, which enable the direct

S. de Santiago · I. V. Lijanova (✉)
Instituto Politécnico Nacional, CIITEC, Cerrada Cecati S/N,
Colonia Santa Catarina, 02250 de Azcapotzalco, CDMX, Mexico
e-mail: irinalijanova@yahoo.com.mx

C. O. Olivares-Xometl
Facultad de Ingeniería Química, Benemérita Universidad Autónoma de Puebla,
Av. San Claudio, Ciudad Universitaria. Col. San Manuel, 72570
Puebla, P.U.E, Mexico

N. V. Likhanova
Instituto Mexicano del Petróleo, Programa de Investigación y Posgrado,
Eje Central Norte Lázaro Cárdenas No. 152, Col. San Bartolo Atepehuacan,
07730 Mexico City, CDMX, Mexico

R. R. Ambriz et al. (eds.), *Proceedings of the 17th International Conference on New Trends in Fatigue and Fracture*, https://doi.org/10.1007/978-3-319-70365-7_22

observation of the imbibition process; an example of these elements is the Hele-Shaw cells, which allow the construction of simple physical models in order to see the spontaneous or forced oil displacement by water. A Hele-Shaw cell consists of two flat parallel glass plates with a thin gap between them through which fluids flow [14, 15]. Hele-Shaw cells were studied as idealized systems by Saffman and Taylor [16] who were the first to report the interactions between two immiscible and different-density fluids.

Experimentation in this kind of cells has helped the oil industry to acquire a better understanding of the flow through cracked porous media, for with these experiments, it is possible to appreciate the low or zero flow zones. In the study of oil recovery using Hele-Shaw cells, it has been found that with surfactant solutions, the displacement depends on two main factors: the displacement coefficient and interfacial tension. If these two variables are in equilibrium, a maximum oil displacement is obtained [17, 18].

Feder [19], who mentioned that the viscous fingering problem in porous media is very important for the oil industry and a very interesting one for hydrodynamics and porous medium physics, showed, like other authors, that the flow rate in porous media is governed, in principle, by Darcy's law, which depends on the viscosity, permeability, pressure and gravity in the case of vertical cells. He also found that the interfacial pressure between two fluids is controlled by the capillary forces. In his experimental development with Hele-Shaw cells.

But reports on the interactions of these agents, comparing heterogeneous (porous with a cracked) and homogeneous (porous media), and particularly with Mexican oil, in idealized systems, such as the cracked Hele-Shaw cells, were not found.

According to the aforementioned, the present research work is based on the observation and analysis of fingering formed by unstable fronts in heterogeneous and homogeneous media. The cell configurations of the cited authors change with respect to the one used in this work, for the main aim was focused on the non-swept zones when locating strategically the holes simulating the injection and production wells. With the cracked (scratches on the glass), the changes in the fingering formations would be appreciated; it would also be possible to observe how these cracked affects the oil production.

Materials and Methodology

The experiments were carried out at room temperature (approximately 21 °C) and the materials were selected to idealize the physical model as well as possible according to their properties.

Deionized water with $\rho = 998$ kg/m^3 and $\mu = 0.001$ Pa s was used to sweep Mexican oil with $\rho = 872$ kg/m^3 and $\mu = 0.02$ Pa s. Viscosities were measured with a Brookfield viscometer.

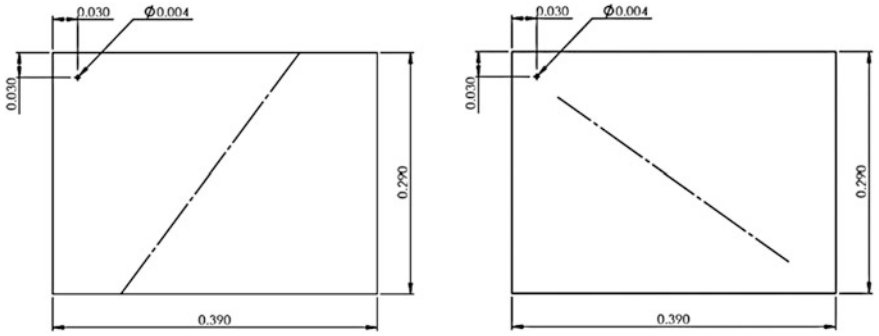

Fig. 1 The units in the schematic representation of the glass plates forming the cell are in meters (m). To left hand the dash-dot line shows the cracked position perpendicular to the holes representing the wells. To right hand the dash-dot line shows the cracked position parallel to the holes representing the wells

The oil was trapped in a Hele-Shaw cell. The commercial glass plates were arranged to form three different cells with different characteristics regarding the contact surfaces. The rough medium cell had $\varphi = 0.373$ and $K = 367$ mD$(3.621 \times 10 - 13$ m$^2)$. The cracked rough medium 1 and cracked rough medium 2 cells had similar characteristics to those of the rough medium cell, but with perpendicular and parallel cracked to the fluid flow, respectively, see Fig. 1.

The purpose of the surface cracked is to analyze, during each experiment, the effect exerted by the medium physical properties on the oil sweep and contrast the results in order to establish if the medium modifications affect the oil recovery. According to the literature [16, 20], a change in the medium geometry, like the cracked in the cells, would be responsible for the preferential water paths.

The characterization of the porous medium was carried out by the stereology method [21–24]; for this purpose, a Hitachi SEM (Scanning Electron Microscope) was used, which scanned the materials and showed glass surface images; afterwards, by means of the software 3D image viewer (v.1.01 by the Denshi Kougaku Kenkyusyo Company), administered with the SEM, the surface images were analyzed, obtaining a 3D mapping of the material surfaces, generating surface graphs along a line, which helped establish the porosity and pore radius.

The pieces of equipment used to carry out the experiments featured in the present work are described according to their main characteristics as follows: water was pumped by means of an ELDEX Optos pump 2SM, which kept constant the injection rate. Illumination was possible using LED lamps, which have the advantage of not generating heat from their internal elements. Beakers were used to collect oil-deionized water mixtures. Hoses and fittings by Festo were used in the test systems. All the procedures were recorded with a video camera Panasonic H85.

Rectangular glass plates (0.290 m $\times$ 0.390 m and 0.006 m in thickness), which were frosted to produce a rough surface on one of their faces, were used.

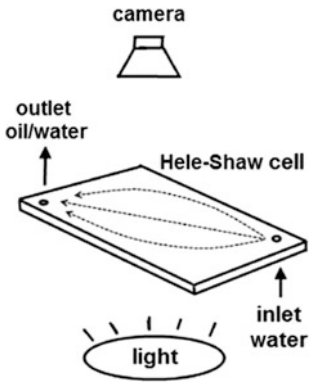

Fig. 2 Schematic representation of the experimental arrangement using a cracked Hele-Shaw cell

Afterwards, a hole with a diameter of 0.006 m was drilled at 0.030 m of each edge to place the hoses that would simulate the injection and production wells. The cleaning process was carried out using a (10% soap—90% water) solution. After drying, the glass plates were immersed for 6 h in a (3% nitric acid—97% deionized water) solution.

The glass plates were put together by the rough surfaces to form porous and cracked porous media (depending on the experiment). Then, the four edges were sealed in order to have flow only through the wells. It is worth noting that there was no separation between the faces; only that formed by the roughness of the plates. The employed hoses were joined to the cell holes to simulate the injection (inner diameter of 0.001 m) and production (inner diameter of 0.004 m) wells. The injection hose was connected to the continuous flow pump and the production hose was connected to a container to collect oil, see Fig. 2.

Experimental

Characterization of the Cracked Porous Media

The characterization of the porous media was performed by the stereology method [22, 25, 26], which consists in a SEM mapping over the cell rough surfaces using the SEM equipment software. The surface with a transversal cracked was analyzed randomly, showing its crests and valleys, which were exported and analyzed by means of a CAD program. The transversal areas of the rough samples on the surface and on the transversal section of the cracked or scratch were obtained.

The medium porosity and hydraulic radius were obtained according to the methods reported in the literature [27–29], using random samples of the rough surface based on the pore transversal areas and the materials used in the experimentation:

With the porosity and hydraulic radius data obtained by the stereology method, the Carman-Kozeny equation can be used to calculate the permeability, for conditions such as laminar flow (Re = 54.032 at the cell inlet) and no electrochemical reactions are satisfied as mentioned by Carrier [30] as follows:

$$K = (D^2\varphi^3)/180(1-\varphi)^2 \quad (1)$$

where, K is the medium permeability as a function of the pore diameter (D) and the medium porosity (φ).

From Eq. 1, the permeability of the porous medium, which was formed by the rough surfaces of the glass plates used in the experiments featured in this work, was $K = 3.621 \times 10^{-13}$ m^2 = 367 mD. By comparing this value with the information available in the literature [27, 31, 32], it was possible to confirm that the medium permeability is similar to that of sandstone found in oil reservoirs

Oil-Swept-By-Water Experimentation

The physical characteristics of the Mexican oil and deionized water used in the experiments were mainly two: density and viscosity, which were measured with a Brookfield viscosimeter at room temperature. The characteristics of the cells, which were made with commercial glass, were discussed previously.

The experiment began by placing the cell as shown in Fig. 2. Once the porous medium was saturated with oil, deionized water started to be injected, using beakers every 15 min to collect the oil/water mixtures in order to separate them and quantify the recovered oil volume. The whole procedure was recorded to analyze the formation of fingers or preferential water paths.

Figure 3 shows the formation of unstable fronts which produce the fingering. Since this is not a uniform radial front, oil drops end up trapped and cannot be moved by water.

The results obtained from the experiment series are shown in Fig. 4, where the average secondary recovery of the experiments carried out with imbibed oil in three types of media (rough, cracked rough medium 1 and cracked rough medium 2) is also shown. Three experiments were performed in every case. Figure 4 shows that the oil recovery is around 45% of the total oil imbibed in the cell with a water sweep time of 135 min for the rough medium experiments. It can be seen that there is a higher oil recovery of 56.6% but with more time (195 min) for the cracked rough medium 1 and cracked rough medium 2 experiments.

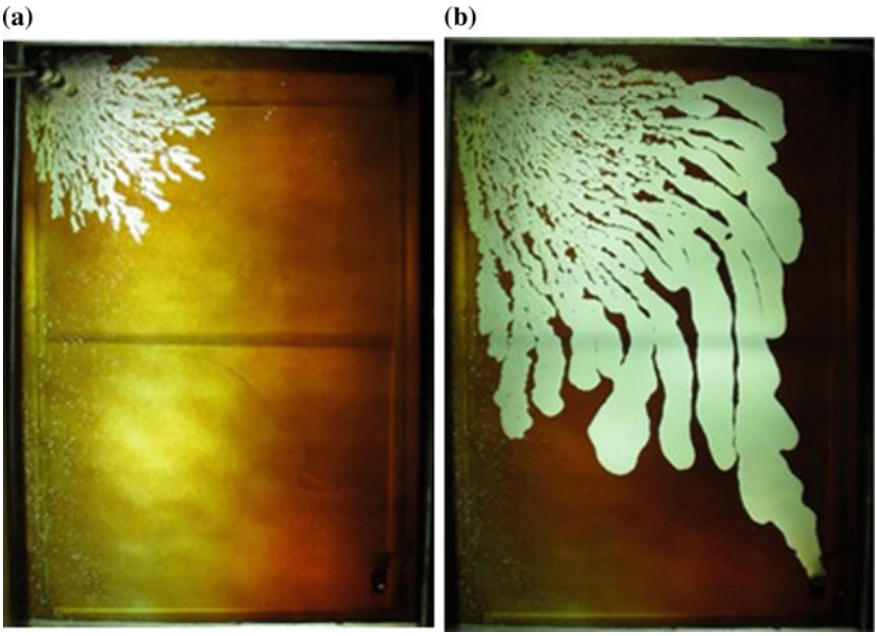

Fig. 3 Experiment using a Hele-Shaw cell saturated with oil: **a** shows the injection of water after 10 s, and **b** shows the formation of preferential paths after 150 s

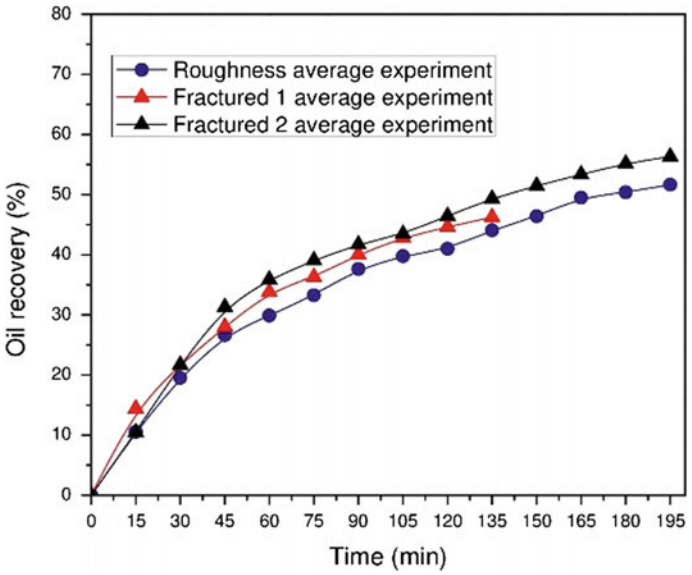

Fig. 4 Comparison of the average experimental results

Conclusions

The analysis of porous media proved that the permeability, porosity, and wettability obtained by means of the Hele-Shaw cells used in the present work can be considered to characterize an idealized system testing the oil recovery.

From the experimental results, it can be observed that the oil recovery corresponds to the worldwide production percentages and resemble brown reservoirs, where it is necessary to apply the EOR to produce 45–55% of the remnant oil. With the experiments, it was possible to find the best time to start the enhanced recovery procedure, which varies according to the geometry of the medium, i.e., if it is a rough medium, it is proposed to start the enhanced recovery after 90 min; if they are cracked rough medium 1 and cracked rough medium 2, it is proposed to start the enhanced recovery after 120 and 105 min, respectively. The EOR results will be supported with a numerical solution in a future work, where the experimental parameters will be viscosity, density, interfacial tension of the fluids and porosity and permeability of the porous medium.

References

1. Bailey B, Crabtree M, Tyrie J, et al (2000) Control del agua. Oilf Rev 32–53.
2. Gunning J, Paterson L, Poliak B (1999) Coning in dual completed systems. J Pet Sci Eng 23:27–39. https://doi.org/10.1016/S0920-4105(99)00006-6.
3. Sandrea I, Sandrea R (2007) Global oil reserves – recovery factors leave vast target for EOR technologies. Oil Gas J 1–8.
4. Fakhru'l-Razi A, Pendashteh A, Abdullah LC, et al (2009) Review of technologies for oil and gas produced water treatment. J Hazard Mater 170:530–551. https://doi.org/10.1016/j.jhazmat.2009.05.044.
5. Han M, Xiang W, Zhang J, et al (2006) Application of EOR Technology by Means of Polymer Flooding in Bohai Oil Fields. Soc Pet Eng 6.
6. Al-Aulaqi T, Fisher Q (2012) Crude oil, brine salinity and sandstone interaction - nanoscale resolution. Soc Pet Eng 1–41.
7. Ameri A, Shojai Kaveh N, Rudolph ESJ, et al (2013) Investigation on interfacial interactions among crude oil–brine–sandstone rock–co2 by contact angle measurements. Energy & Fuels 27:1015–1025. https://doi.org/10.1021/ef3017915.
8. Cuiec L (1984) Rock/crude-oil interactions and wettability: an attempt to understand their interrelation. Soc Pet Eng. https://doi.org/10.2118/13211-MS.
9. Pan C, Feng J, Tian Y, et al (2005) Interaction of oil components and clay minerals in reservoir sandstones. Org Geochem 36:633–654. https://doi.org/10.1016/j.orggeochem.2004.10.013.
10. Santanna VC, Curbelo FDS, Castro Dantas TN, et al (2009) Microemulsion flooding for enhanced oil recovery. J Pet Sci Eng 66:117–120. https://doi.org/10.1016/j.petrol.2009.01.009.
11. Larter S, Adams J, Gates ID, et al (2008) The origin, prediction and impact of oil viscosity heterogeneity on the production characteristics of tar sand and heavy oil reservoirs. J Can Pet Technol 47:52–61. https://doi.org/10.2118/2006-134.
12. Wang J, Dong M, Asghari K (2006) Effect of oil viscosity on heavy oil-water relative permeability curves. Soc Pet Eng 1–9. https://doi.org/10.2118/99763-MS.

13. Renqing L (2013) Development of enhanced oil recovery in Daqing. J Pet Gas Eng 4:46–50. https://doi.org/10.5897/JPGE2012.0136.
14. Chen J-D, Wilkinson D (1985) Pore-scale viscous fingering in porous media. Phys Rev Lett 55:1892–1895. https://doi.org/10.1103/PhysRevLett.55.1892.
15. Woods AW (2015) Flow in porous rocks, energy and environmental applications., First edit. Cambridge University Press.
16. Saffman PG, Taylor G (1958) The penetration of a fluid into a porous medium or Hele-Shaw cell containing a more viscous liquid. Proc R Soc A Math Phys Eng Sci 245:312–329. https://doi.org/10.1098/rspa.1958.0085.
17. Zajic JE, Seffens W, Gurrola A, Ban T (1989) Chapter 5 Oil recovery by bacterial and polymer solutions in the Hele-Shaw model. Dev Pet Sci 22:99–112. https://doi.org/10.1016/S0376-7361(09)70093-7.
18. Zajic JE, Ban T, Gurrola A, Seffens W (1989) Chapter 9 Oil displacement in the Hele-Shaw model using microbes and synthetic surfactants. Dev Pet Sci 22:165–180. https://doi.org/10.1016/S0376-7361(09)70097-4.
19. Feder J (1988) FRACTALS. https://doi.org/10.1007/978-1-4899-2124-6.
20. Córdoba J (1993) Interfases caprichosas. Para Saber, Exp Y Simular 4:32–38.
21. Datta AK, Sahin S, Sumnu G, Ozge Keskin S (2007) Porous media characterization of breads baked using novel heating modes. J Food Eng 79:106–116. https://doi.org/10.1016/j.jfoodeng.2006.01.046.
22. Rouquerol J, Avnir D, Fairbridge CW, et al (1994) Recommendations for the characterization of porous solids. Pure Appl Chem 66:1739–1758. https://doi.org/10.1351/pac199466081739.
23. Willson CS, Lu N, Likos WJ (2012) Quantification of grain, pore, and fluid microstructure of unsaturated sand from X-ray computed tomography images. Geotech Test J 35:1–13. https://doi.org/10.1520/GTJ20120075.
24. Zhihang F, Kuang-Ting H, Suresh G. A (2004) Experimental investigation of dispersion during flow of multi-walled carbon nanotube/polymer suspension in fibrous porous media. Carbon N Y 42:871–876. https://doi.org/10.1016/j.carbon.2004.01.067.
25. Nimmo JR (2004) Porosity and pore size distribution. In: Encycl. Soils Environ. London. Elsevier, pp 295–303.
26. Peng S, Hassan A, Loucks RG (2016) Permeability estimation based on thin-section image analysis and 2D flow modeling in grain-dominated carbonates. Mar Pet Geol 77:763–775. https://doi.org/10.1016/j.marpetgeo.2016.07.024.
27. Bear J (1972) Dynamics of fluids in porous media.
28. Desbois G, Urai JL, Hemes S, et al (2016) Multi-scale analysis of porosity in diagenetically altered reservoir sandstone from the Permian Rotliegend (Germany). J Pet Sci Eng 140:128–148. https://doi.org/10.1016/j.petrol.2016.01.019.
29. Dullien FAL (1992) Porous media: Fluid transport and pore structure. In: Acad. Press. Inc. p 572.
30. Carrier WD (2003) Goodbye, Hazen; Hello, Kozeny-Carman. J Geotech Geoenvironmental Eng 129:1054–1056. https://doi.org/10.1061/(ASCE)1090-0241(2003)129:11(1054).
31. Dutton SP, Loucks RG (2010) Diagenetic controls on evolution of porosity and permeability in lower Tertiary Wilcox sandstones from shallow to ultradeep (200-6700 m) burial, Gulf of Mexico Basin, U.S.A. Mar Pet Geol 27:69–81. https://doi.org/10.1016/j.marpetgeo.2009.12.010.
32. Ehrenberg SN, Nadeau PH (2005) Sandstone vs. carbonate petroleum reservoirs: a global perspective on porosity-depth and porosity-permeability relationships. Am Assoc Pet Geol Bull 89:435–445. https://doi.org/10.1306/11230404071.

Smith Watson and Topper Model in the Determination of the Fatigue Life of an Automotive Steel

F. F. Curiel, R. R. Ambriz, M. A. García, M. C. Ramírez and S. García

Introduction

Fails due to fatigue are an issue in automotive components that are subjected to cyclic loading during its operations. The presence of high loads and variation for long times leads to crack formation and propagation because of the local damage occurred in the vicinity of the cracks [1]. Some of the main components used in the automotive industry include frames, crank shafts, axles etc. The design for this parts involves not only metallurgical properties, but the use of tools such high cycle fatigue (HCF), low cycle fatigue, (LCF) and mathematical models to predict the fatigue life [2, 3]. The safety of the components depends on the degree of intensity of the loads to which it will be exposed throughout its operation [4]. It's well known that HCF and LCF can predict the fatigue life in the elastic and plastic regime respectively [5]. Nevertheless, it was necessary to develop mathematical models to combine both the HCL and LCF to have a better context on the fatigue life of components subjected to completely reversible loads [6]. In this regard, L.F. Coffin and S.S. Manson developed a mathematical form called Coffin-Manson relationship that contemplates the elastic-plastic behavior of the components, giving us a more successful panorama of the elastic-plastic transition and fatigue life [6].

F. F. Curiel (✉) · M. A. García · S. García
Universidad Autónoma de Coahuila. Facultad de Metalurgia, Carretera 57, Monclova, Coahuila, Mexico
e-mail: franciscocl7@gmail.com

R. R. Ambriz
Instituto Politécnico Nacional CIITEC-IPN, Cerrada de Cecati S/N Col. Sta. Catarina, Azcapotzalco 02250, DF, Mexico

M. C. Ramírez
Instituto Tecnológico Superior de Monclova, Ejercito Mexicano, Carretera 57 km 4.5, Unidad Tecnológica y Universitaria, Monclova, Coahuila, Mexico

R. R. Ambriz et al. (eds.), *Proceedings of the 17th International Conference on New Trends in Fatigue and Fracture*, https://doi.org/10.1007/978-3-319-70365-7_23

On the other hand, the Smith Watson and Topper (S.W.T.) model predicts the fatigue life of components with a mean stress equal to zero [7].

This study seeks to determine the fatigue life of an automotive steel by the use of LCF, HCF and S.W.T. tools.

Experimental

Material Characterization

The chemical composition of the material used in this study is show in Table 1. Figure 1 shows a microstructure of the initial material used in this study. It can be seen that the material is composed of ferritic microstructure whit pearlite islands aligned along the rolling direction.

Monotonic Test

In order to determine the initial parameters for HCF and LCF test, a tensile test was performed according to ASTM E646 [8]. The true stress, $\sigma = \sigma(1 + \epsilon)$, and the true

Table 1 Chemical composition of the steel in the fatigue life study

C	Cr	Mn	Mo	Ni	Si	Fe
1.4	0.08	0.83	0.055	0.18	0.53	Bal

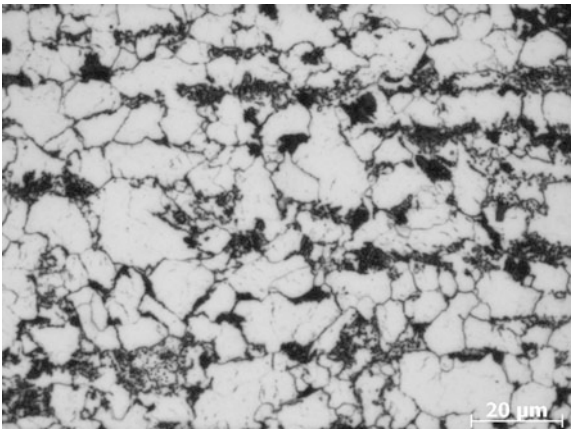

Fig. 1 Microstructure of the base metal used for fatigue life testing

strain, $\epsilon = \ln(1 + \epsilon)$, were calculated from the engineering stress-strain data. The sample was tested at 10 mm/min in displacement mode.

Fatigue Tests

Fatigue test were carried out in the stress amplitude and strain amplitude. The specimens were machined to the final dimensions according to ASTM E466 standard in order to perform the high cycle fatigue (HCF) and low cycle fatigue (LCF) tests [9]. Figure 2 shows the dimensions of the specimens.

High Cycle Fatigue Tests

For stress amplitude, HCF tests were performed on a MTS-370 machine equipped with 250KN MTS load frames and calibrated cells. The tests were carried out according to the requirements of ASTM E466. The frequency used for this study was 12 Hz and stress ratio $R = -1$ at room temperature in air. The specimens were tested until reach the failure during the positive and negative load application.

Low Cycle Fatigue Tests

Strain tests (LCF) were performed according to the specifications of ASTM E606 at 0.5 Hz. An extensometer of 25 mm gage was attached during the strain tests and a MTS software was used to acquire the data.

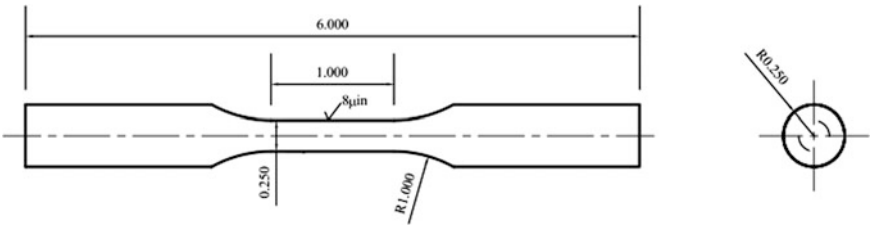

Fig. 2 Samples used for the HCF and LCF tests

Fracture Observation

After failure, several samples were cut and prepared for fracture observation. The samples were analyzed in a JEOL JSM-7600F field emission scanning electron microscope equipped with EDX analyser. The microstructure was observed with secondary electrons.

Results and Discussion

Monotonic Test

Samples of 1.4 C steel, 0.250 in diameter were tested to investigate the monotonic properties of the material used in this study. The mechanical properties are listed in Table 2. Yield strength at 0.2% offset, tensile strength and fracture strain were calculated directly from the plot (433 MPa, 743 MPa and 0.37 MPa respectively), The Elastic modulus (208 GPa) was calculated in the slope of the elastic portion of the curve in Fig. 3.

Table 2 Mechanical properties of the MB studied

Yield strength (Mpa)	Tensile strength (Mpa)	Fracture strain	Elastic modulus (GPa)	Strain hardening exponent	Strength coefficient (MPa)
433	743	0.37	208	0.241	1065.19

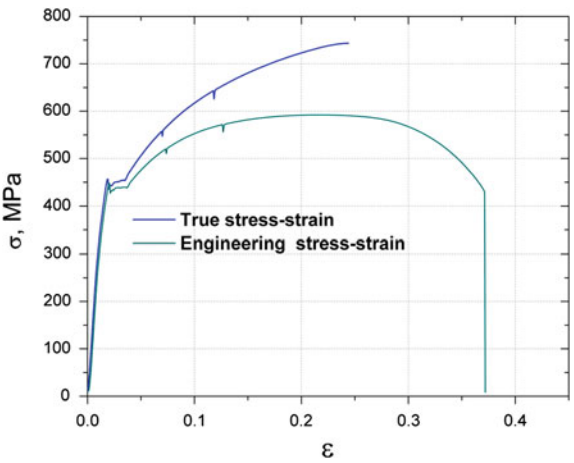

Fig. 3 Stress-strain curve of the base metal

On the other hand, the strength coefficient (K = 1065.19 MPa) and the strain hardening exponent (n = 0.241) were determined from the true stress-strain curve regression and analysis. Ramber-Osggod relationship describes the mathematical representation of stress-strain curve, which can be written as [10].

$$\varepsilon = \varepsilon_{elastic} + \varepsilon_{plastic} = \frac{\sigma}{E} + \left(\frac{\sigma}{K}\right)^{1/n} \quad (1)$$

High Cycle Fatigue Properties

The results obtained from the HCF test are summarized in Table 3. A set of 8 specimens were placed in the load control fatigue test and 7 fail during the trials, only one continued without failure. The reversals to failure were gathered with different levels of applied load.

The data obtained from the stress tests were used to plot the *S-N* curve for the material used in this study. The fatigue failure of this material may occur beyond 10^7 cycles, this is, fracture occurred between 10^5 and 10^7 cycles. This plot can decreases usually from megacycle to gigacycle range. The data obtained from the stress tests from Fig. 4 were used to plot the S-N curve for the material used in this study.

From the plotted data the stress life properties were calculated by means of the data regression. The stress life exponent (b = −0.7137), stress life coefficient (A = 1607 MPa) and fatigue strength coefficient (σ'_f = 1689 MPa) are shown in Table 4.

Low Cycle Fatigue Properties

In order to determine the fatigue life of the steel, mechanical behaviour due to the low cyclic load was determined. Low cycle fatigue test specimen of 6 mm in diameter were polished and prepared for been testing. For this, strain-controlled fatigue tests were carried out at different levels.

Table 3 High cycle fatigue data for the steel

Sample	Stress amplitude (MPa)	Applied load (kN)	Reversals to failure	Notes
01	350	11.390	142,380	Failure
02	350	11.270	102,072	Failure
03	325	10.617	194,901	Failure
04	325	10.714	430,304	Failure
05	300	9.869	1,392,017	Failure
06	300	9.823	1,278,208	Failure
07	275	9.051	4,196,994	→
08	250	8.123	6,133,923	Failure

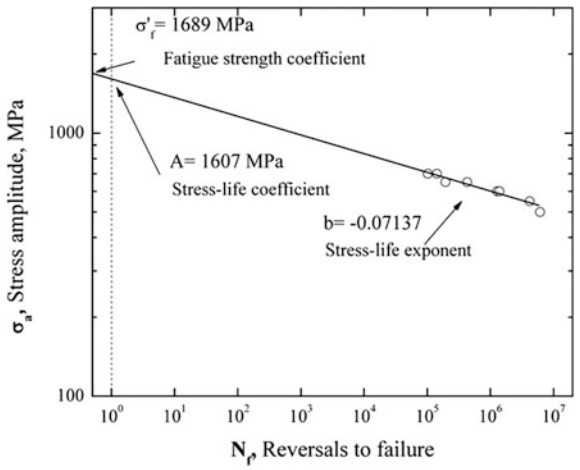

Fig. 4 Stress amplitude versus reversal to failure plot

Table 4 Stress life properties

Fatigue strength coefficient	σ'_f	1689 MPa
Stress-life coefficient	A	1607 MPa
Stress-life exponent	b	−0.07137

Table 5 summarises de cyclic data obtained from the strain-controlled tests. In here, the highest strain amplitude range (0.02334) reaches only 133 cycles until the fail, meanwhile the value for the lowest strain range (0.00694) reaches 7414 cycles.

With this data, the ε-N curve was built in order to obtain the cyclic properties.

Figure 5 shows the strain versus reversals to failure plot generated from the data of LCF tests. From this plot, the fatigue ductility coefficient and the fatigue ductility exponent were calculated doing a regression analysis of the log-log linear plot.

Table 5 Low cycle fatigue data for the steel

Sample	Strain amplitude	Reversals to failure	Notes
01	0.00694	7414	Failure
02	0.00694	7112	Failure
03	0.00972	3150	Failure
04	0.00972	3380	Failure
05	0.00948	2056	Failure
06	0.00948	2138	Failure
07	0.01861	570	Failure
08	0.01861	423	Failure
09	0.02334	358	Failure
10	0.02334	133	Failure

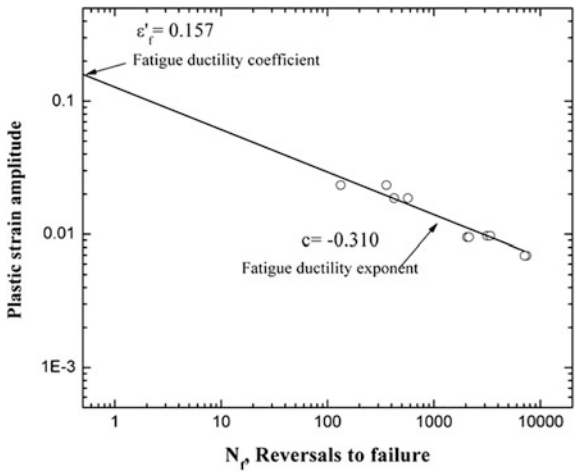

Fig. 5 Strain amplitude versus reversals to failure plot

Table 6 Strain life properties

Cyclic elastic modulus	E	170 GPa
Cyclic yield strength	σ'_y	105 MPa
Cyclic strain hardening exponent	n′	0.048
Fatigue ductility coefficient	ε'_f	0.157
Fatigue ductility exponent	c	−0.310
Fatigue strength exponent	b	−0.07137
Cyclic strain hardening coefficient	K′	862 MPa

On the other hand the elastic modulus and cyclic yield stress were calculated from a portion of the hysteresis loop, 170 Gpa and 105 Mpa were obtained respectively.

On the other hand the elastic modulus, cyclic yield stress were calculated from a portion of the hysteresis loop, 170 Gpa and 105 Mpa were obtained respectively.

Beyond the elastic portion of the hysteresis loop, the cyclic strain hardening coefficient (K' = 862 MPa) and the cyclic strain hardening exponent (n' = 0.048) were calculated in the plastic region of the loop.

The strain life properties are show in Table 6.

Smith Watson and Topper

The Smith Watson and Topper parameter is a model based on the damage induced on the material and the inherent properties determined from LCF tests [11]. The determination of this parameter in fact is due to the ratio, $R = -1$, which is an energy criterion. This approach can be used for determining the fatigue damage induced in components subjected to complete reversal loads.

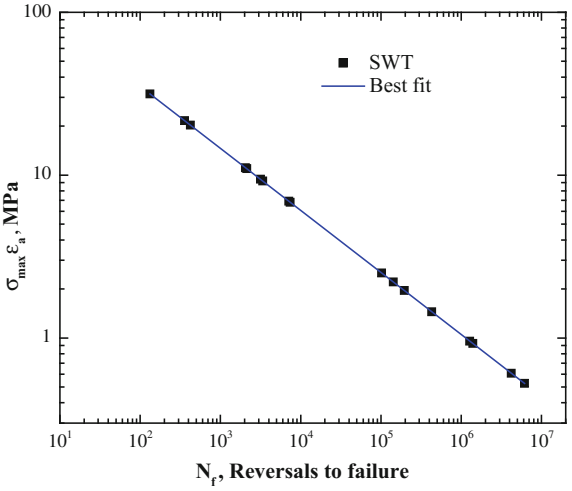

Fig. 6 S.W.T. curve for the steel

The S.W.T. parameter is also used usually as Ramber-Osgood and Coffin-Manson equations for structures or components tested under stress control [12, 13].

The relationship that defines the SWT parameter is described by:

$$\sigma_{max}\varepsilon_a = \frac{\left(\sigma_f'\right)^2}{E}\left(2N_f\right)^{2b} + \sigma_f'\varepsilon_f'\left(2N_f\right)^{b+c} \tag{2}$$

This approach assumes that the life for any situation of mean stress depends on the product, this parameter was calculated with the fatigue life properties at $\sigma_m = 0$.

The S.W.T. parameter was determined for each sample at the failed cycle [14].

Figure 6 is a plot of the above equation. The points represent the experimental data. The best fit for the data are plotted in the blue line. The coefficient and the exponent of the Smith Watson and Topper parameter were determinate from a log-log linear regression of the data showed in the graph, such data are $C = 203.5$ MPa and $\gamma = -0.381$ respectively.

Fractography

Figure 7 shows the fracture surfaces obtained from the failed specimens for the HCF test. In Fig. 7a it can be appreciate the crack initiation in the edge of the specimen, the appearance is flat and forms a semi-ellipse, but the fracture becomes a little rough. A radial ridge pattern parallel to the crack propagation is formed through the fracture [15]. A fish-eye is observed in the center of the sample, suggesting that the fatigue crack could takes place at an inclusion located inside the material tested. On the other

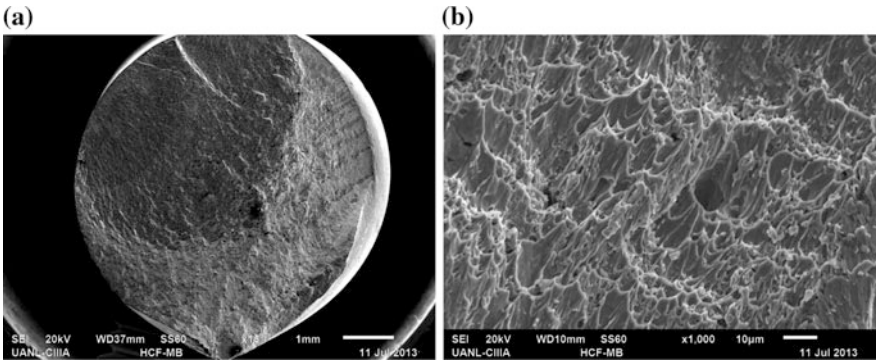

Fig. 7 Fracture surface of the HCF specimen

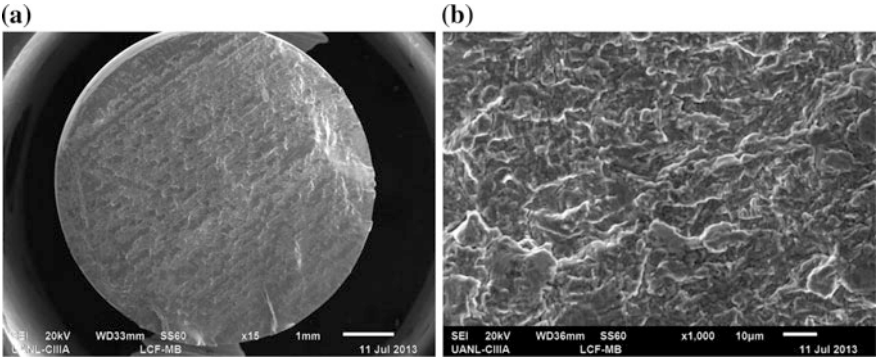

Fig. 8 Fracture of the LCF specimen

hand, Fig. 7b shows the fracture near the fish-eye displaying elongated and quite flat shear dimples as well as decohesion along grain boundaries of elongated grain. Crude steps have formed, suggesting that some degree of pulsation occurred during the test.

The surface fracture for the LCF tests is shown in Fig. 8. Extrusion and intrusions at the surface can be seen. Due this material contains ferrite-pearlite microstructure, fatigue crack can initiate trough the ferrite and the stronger pearlite colonies tended to retard the crack growth.

Figure 9 shows another region of the fracture were striation-like and cleavage-like are observed. This feature could be caused due to the rubbing of the surfaces as the test push and pull was performed (R = −1) [16].

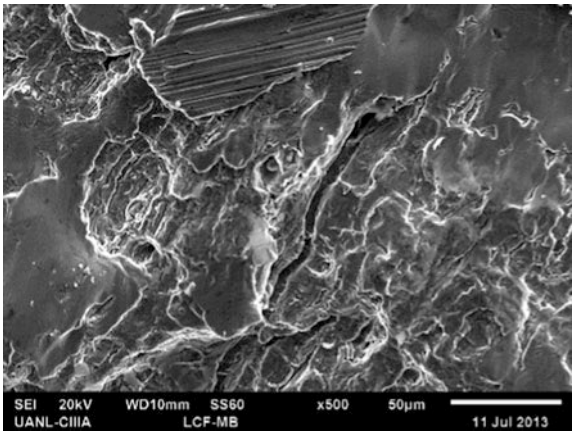

Fig. 9 Fracture of LCF with cleavage facets

Summary

The SWT parameters were calculated from LCF and HCF tests carried out in a carbon steel. The fatigue live properties of LCF and HCF were used in the SWT relationship where the coefficient and the exponent are $C = 203.5$ MPa and $\gamma = -0.381$ respectively.

The range of the fatigue live for the steel is between 10^5 and 10^7 cycles for HCF. Nonetheless, the range for LCF is between 133 and 7414 cycles.

Fish-eye fracture was observed in HCF suggesting that the failure occurred in an inclusion. For LCF cleavages-like facets were observed in the fracture surface due to the push-pull process during the fatigue test.

References

1. Singh SSK., Abdullah S., Nikabdullah N., Eng Fail Anal, 2017, 80, 464–471
2. Sadek S., Olsson M., Int J Fatigue, 2016, 92, 1, 147–158
3. Schmitz S., Seibel T., Beck T., Rollman G., Krause R., Gottschalk H., Comp Mater Sci, 2013, 79, 584–590
4. Sonsino CM., Franz R., Int J Fatigue, 2016 100, 2, 489–501
5. Zhixin Z., Weiping Hu., Fei S., Qingchun M., Jing P., Zhidong G., Int J. Fatigue, 2017, 208–223
6. Dowling NE., Mechanical Behavior of Materials, Pearson, 4th ed, USA, 2013, p. 732–733
7. Dowling NE., Mechanical Behavior of Materials, Pearson, 4th ed, USA, 2013, p. 745–736
8. ASTM E646, Tensile Strain-Hardening Exponents of Metallic Sheet Materials, ASTM International, USA, 5p
9. ASTM E466, Conducting Force Controlled Constant Amplitude Axial Fatigue Tests of Metallic Materials, ASTM International, USA, 5p
10. Dowling NE., Mechanical Behavior of Materials, Pearson, 4th ed, USA, 2013, p. 130–131
11. Özler Karakas., Int J Fatigue, 2013, 49, 1–17

12. Ramberg W., Osgood WR,. Description of stress–strain curves by three parameters, Technical note no. 902, National Advisory Committee for Aeronautics, Washington, DC; 1943
13. Manson SS., Behavior of materials under conditions of thermal stress, National Advisory Committee on Aeronautics, report 1170, Cleveland: Lewis Flight Propulsion Laboratory; 1954
14. Koh SK., Int J Pres Ves Pip, 2012, 79, 791–798
15. Sakai T., Sato Y., Oguma N., Fatigue Frac Eng Mat Struc, 2002, 8–9, 765–773
16. Sankarana S., Sarmab VS., Padmanabhanc KA., Mat Sci Eng A, 2003, 1–2, 328–335

Influence of Weld Parameters and Filler-Wire on Fatigue Behavior of MIG-Welded Al-5083 Alloy

Vidit Gaur, Manabu Enoki, Toshiya Okada and Syohei Yomogida

Introduction

Most of the experimental studies on fatigue behavior of metal alloys containing defects revealed the crack initiation from pores, specifically located at or near to the surface [1, 2]. Nearly all of these studies were done at constant R-ratio and less data is available on influence of mean stress on fatigue behavior and damage mechanisms for fatigue cracks initiating from natural defects [3, 4]. While the fatigue behavior of welded structures has been studied extensively, but the combined influence of weld-parameters, filler-wire and mean-stress is lacking. Thus aim of this study is to contribute to this gap. 50 mm thick Al-Mg alloy (Al-5083) plates with different groove angles (70° and 90°) of double-V type butt joint were welded using single pass and double pass MIG welding and using two different filler-wire materials: Al-5183 (commonly used) and Al-5.8%Mg (special hardened alloy). Load-controlled fatigue tests were conducted on the cylindrical specimens taken out from the weld bead, at different stress ratios (R-ratios = $\sigma_{min}/\sigma_{max}$), followed by fracture surface examination. Using the experimental data, the performance of well-known fatigue life model, Walker's model [5], was analyzed and it was found that the model was not best suited to capture the observed mean stress effects. Thus, an alternative criterion based on Walker's model was proposed with best predictions of fatigue lives and endurance limits.

V. Gaur (✉) · M. Enoki
Department of Materials Engineering, The University of Tokyo, 7-3-1 Hongo, Bunkyo-ku, Tokyo 113-8656, Japan
e-mail: gaur@rme.mm.t.u-tokyo.ac.jp

T. Okada · S. Yomogida
Research & Development Division, UACJ Corporation, 3-1-12 Chitose, Minato-ku, Nagoya-City, Aichi Pref 455-8670, Japan

R. R. Ambriz et al. (eds.), *Proceedings of the 17th International Conference on New Trends in Fatigue and Fracture*, https://doi.org/10.1007/978-3-319-70365-7_24

Material and Procedures

The material investigated is Al-5083 alloy welded with Al-5183 alloy and Al-5.8% Mg alloy. The respective tensile properties are reported in Table 1. The average grain sizes under respective weld conditions are also reported in Table 1. The material exhibit a dendritic type micro-structure with nearly spherical magnesium (Mg) precipitates. Different weld conditions induced an impact on average grain size. No significant texture could be observed in longitudinal or cross-sectional direction. Pores with an average size of 45 μm were found in the weld region. The distribution of these pores was not affected by change in welding conditions investigated in this study. These pores were often responsible for fatigue crack initiation as illustrated and discussed later.

Cylindrical specimens of diameter 5 mm (Fig. 1a) were cut along the weld bead in longitudinal direction from the welded plates under different cases of welding. Load-controlled push-pull fatigue tests were done using sinusoidal waveform at 30 Hz at different R-ratios (−1, −0.5, 0.1 and 0.5) in air. The tests were stopped at 10^7 cycles and the corresponding stress amplitude was considered as the endurance limit for that R ratio. Fracture surfaces of broken specimens were observed using JEOL JCM-6000 SEM. The fatigue life data obtained from experiments were used in Walker's model to study its performance:

Table 1 Tensile and micro-structural properties of weld under different conditions of welding (different filler material, groove angle and welding passes)

Material-groove angle-Pass	Tensile strength (MPa)	Average grain size (μm)
Al-5083/5183-70°-1	284	64
Al-5083/Al-5.8%Mg-70°-1	289	78
Al-5083/5183-90°-1	291	55
Al-5083/5183-90°-2	281	58

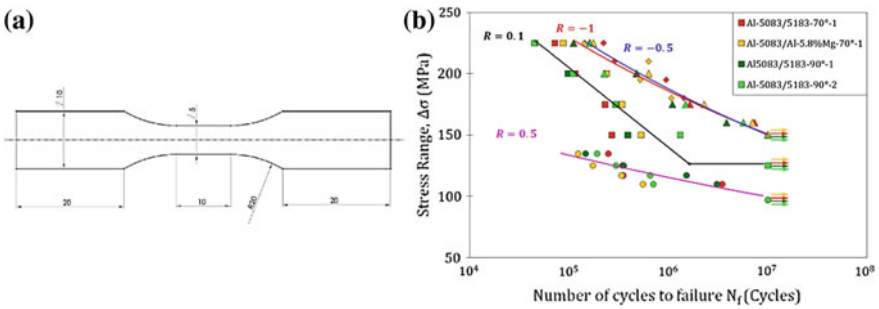

Fig. 1 **a** Geometry of cylindrical specimen used for fatigue tests. **b** Wöhler curve (S-N curves) for different welding conditions: code: Material-Groove angle-Number of pass, Markers code: 'triangle' is for R = −1, 'diamond' is for R = -0.5, 'square' is for R = 0.1 and 'circle' is for R = 0.5

$$\sigma_a \left(\frac{2}{1-R} \right)^{\gamma} = A\left(N_f\right)^b \quad (1)$$

where 'R' is the R-ratio, 'γ' is the walker's parameter and 'N_f' is the number of cycles to failure. 'A' and 'b' are constants. The parameters 'A', 'b' and 'γ' were identified by performing the multiple linear regression analysis using the experimental fatigue life data. The performance of this model is discussed later.

Experimental Results

Both the endurance limit and the fatigue lives tend to decrease with increasing R-ratio (Fig. 1b). Difference in weld groove angle, welding pass and filler material did induce some scatter in fatigue lives but not significant enough and could be fitted within same scatter band. The detrimental effect of R-ratio was negligible for R = −0.5. The slopes of S-N curves varied non-monotonically: first increases then decreases. The SEM examination of fracture surfaces revealed the influence of mean stress on crack initiation sites: dominated surface-induced failures for $R < 0.1$ (Fig. 2a) while, for $R \geq 0.1$, defect-induced failures were dominant (Fig. 2b). The typical size of the crack-initiating pores was between 40 and 160 μm. The pores responsible for fatigue failure were always located on/near to the surface.

The shapes of these entire defects were nearly spherical suggesting the gas porosities. The fracture surface in the initiation region around the pore or surface was rough (crystallographic). Some topographic measurements were done around the initiation are to estimate the approximate inclination of facets around the initiation area and an average inclination of 45° ± 8° was found: suggesting a shear driven stage-I type crack initiation. But as the crack grew, the crack propagation plane became normal to the loading axis, suggesting a stage-I to stage-II transition.

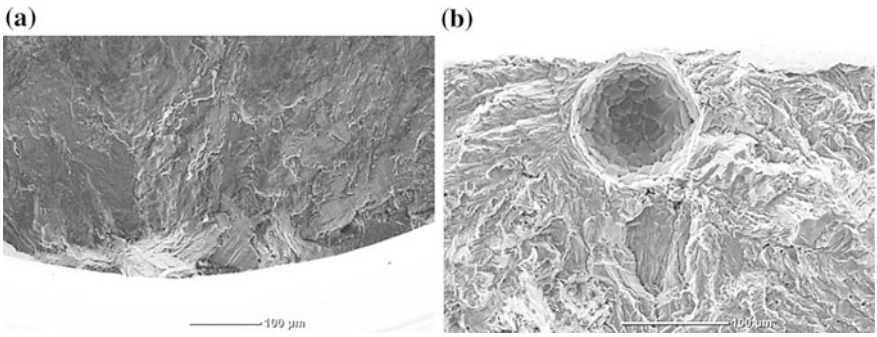

Fig. 2 SEM images of fracture surface **a** Surface-initiated fracture. **b** Defect-initiated fracture from pore at surface (size approx. 100 μm)

Discussion

The fracture surfaces of specimens of different welding conditions revealed no difference in crack initiation or crack growth mechanisms. The fraction of fatigue failures that initiated from defects tends to increase with increase in R-ratio: 25% for R = −1, 69% for R = −0.5, 87% for R = 0.1 and 100% for R = 0.5. Similar influence of mean stress on crack initiation sites (with pores) was also reported in Cr-Mo steels [6] and Ti-8Al-1Mo-1V titanium alloys [7]. Most of the defects that initiated fatigue cracks were often located on/near to the surface. A symmetrical model of a cylinder containing half of a pore of size 100 μm was studied in ABAQUS using quadratic tetrahedron elements (C3D10) (Fig. 3a). The pore position was defined using the ratio of distance of its center from the surface (r) to its radius (R): r/R = 0 means surface cutting hemispherical pore and r/R = 1 means surface touching pore. The estimation of stress concentration factor (K_t) for different positions of pore (r/R) revealed higher K_t values for sub-surface pores as compared to internal ones (Fig. 3b). For a specific case with r/R = 1.1, typical for most of the experimentally observed pores, 500 load cycles were simulated and plastic strain was estimated at the edge of pore after the end of first peak load. The values of plastic strain were higher for higher mean stress, suggesting mean tensile stress induced plastic flow occurred during ramp load of high R-ratio fatigue tests.

The size of defects responsible for fatigue failures was comparable to mean grain size and thus fracture mechanics approach is questionable [8, 9]. Fatigue striations were easily visible at lower R-ratios (R < 0.1) while for higher R-ratios, they were very difficult to locate; probably because of low stress intensity factor range (ΔK) at

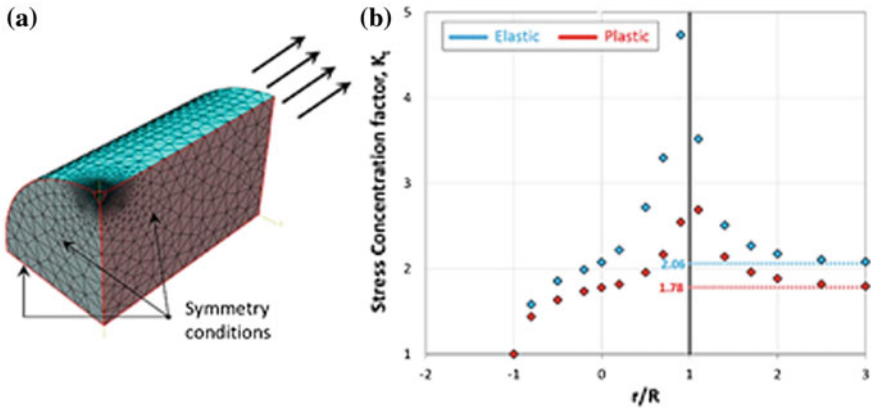

Fig. 3 **a** ABAQUS 3D meshed model of ½ of a pore. **b** Evolution of stress concentration factor (K_t) with different positions of pore with respect to surface (r/R): where r is the distance of center of pore from surface and R is the pore radius

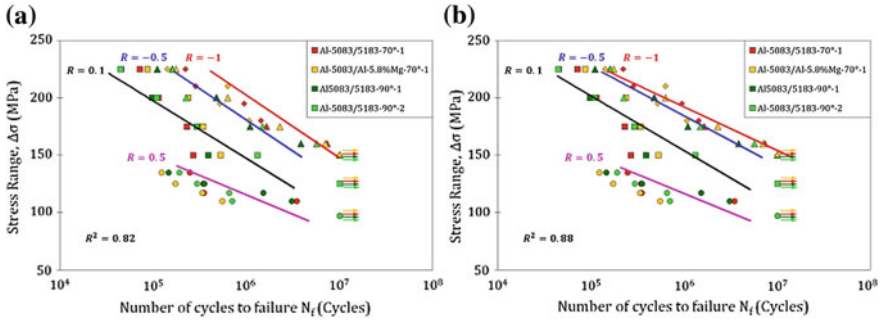

Fig. 4 The S-N curves (solid lines) predicted by **a** Walker's model. **b** Proposed model, against the experimental fatigue data (denoted by markers, for code refer to Fig. 1)

higher R-ratios, thus implying role of plasticity-induced crack closure in crack growth. Fracture surface roughness also appeared (under SEM) to vary with mean stress: rougher surface for higher R ratio.

Different welding conditions did not change fatigue live significantly, thus combined fatigue data was used to analyze performance of Walker's model. Figure 4a shows the S-N curve predicted by Walker's model (described earlier). Although, the predictions of fatigue lives were acceptable but it predicts monotonic decrease in slope of S-N curves; contradictory to experimental observations. Thus, an additional term was introduced in the walker's equation (Eq. 1) as:

$$\sigma_{ar} = e^{-\left(\frac{x+x^2}{2}\right)}\sigma_a\left(\frac{1}{1-R}\right)^{\gamma} \tag{2}$$

$$x = \frac{\sqrt{\sigma_m \sigma_a}}{\sigma_u} \tag{3}$$

where σ_a and σ_m are the amplitude and mean stress while σ_u is the ultimate tensile strength of the material. An average value of σ_u (285 MPa) was used. The term 'x' induced the non-monotonic variation of slope using the stress state parameter which is the product of mean stress and stress amplitude. Figure 4b shows the predicted S-N curve which is more accurate and compliant with experimental observations of non-monotonic behavior of slopes and thus, the fatigue life prediction as better than Walker's model (by comparing the respective correlation coefficient values i.e. R^2). The applicability of the proposed model on different materials is in progress so as to check the robustness of the proposed model.

Conclusions

- Nearly no effect of weld groove angle (70° and 90°, double-V type butt joint), number of welding passes (single pass and double pass) and filler material (Al-5183 and Al-5.8%Mg) on fatigue lives and endurance limits could be observed.
- Increase in mean-stress had detrimental effect on fatigue lives; attributed to higher stress concentration factors for sub-surface pores thus higher local cyclic plasticity and the crack closure effects. A non-monotonic trend in slopes of S-N curves was observed: first increased and then decreased. Higher R-ratios promoted higher fraction of fatigue failures from pores.
- Proposed fatigue model captures the mean stress effect much better than the Walker's model. However, analysis on robustness of the proposed model is in progress.

References

1. M. Couper, A. Neeson, J. Griffiths, "Casting defects and the fatigue behavior of an aluminum casting alloy", Fatigue & Fracture of Engineering Materials & structures Vol. 13(3), pp. 213–227, 1990
2. Q.G. Wang, D. Apelian, D.A. Lados, "Fatigue behavior of A356-T6 aluminum cast alloys. Part I. Effect of casting defects", Journal of Light Metals Vol. 1(1), pp. 73–84, 2001
3. Y. Murakami, Metal Fatigue: Effect of small defects and nonmetallic inclusions, 2002
4. Z. Lei, Y. Hong, J. Xie, C. Sun, A. Zhao, "Effects of inclusion size and location on very-high-cycle fatigue behavior for high strength steels", Material Science and Engineering A Vol. 558, pp. 234–241, 2012
5. K. Walker, "The effect of stress ratio during crack propagation and fatigue for 2024-T3 and 7075-T6 aluminum, Effects of Environment and Complex Load History on Fatigue Life", ASTM STP 462, West Conshohocken, PA, pp. 1–14, 1970
6. V. Gaur, V. Doquet, E. Persent, C. Mareau, E. Roguet, J. Kittel, "Surface versus internal fatigue crack initiation in steel: Influence of mean stress", International Journal of Fatigue Vol. 82, pp. 437–448, 2015
7. K. Yang, C. He, Q. Huang, Z. Yong Huang, C. Wang, Q. Wang, Y. Jie Liu, B. Zhong, "Very high cycle fatigue behaviors of a turbine engine blade alloy at various stress ratios", International Journal of Fatigue Vol. 99, pp. 35–43, 2016
8. K.J. Miller, "The behavior of short fatigue cracks and their initiation, Part I - A review of two recent books", Fatigue & Fracture of Engineering Materials and Structures Vol. 10(1), pp. 75–91, 1987
9. A. McEvily, "The growth of short fatigue cracks: A review", Transactions on Engineering Sciences Col. 13, ISSN 1743–3533, 1996

Mechanical Evaluation of IN718-AL6XN Dissimilar Weldment

R. Cortés, R. R. Ambriz, V. H. López, E. R. Barragán, A. Ruiz and D. Jaramillo

Introduction

Ni-Cr-Fe alloys have a wide variety of applications in aircraft, power generation, and petrochemical industries due to their excellent mechanical properties at cryogenic and high temperatures as well as corrosion resistance in aggressive environments. The Ni-Cr-Fe alloys hardened by precipitation are used when corrosion resistance and mechanical strength at high temperatures are needed [1]. On the other hand, superaustenitic stainless steel AL6XN is a relatively new material that owing to its high contents of Cr, Ni, Mo, and N exhibits a good resistance to chloride corrosion and stress corrosion cracking. Also, the AL6XN presents a high resistance as well as excellent ductility and formability, due to that the AL6XN has a wide variety of applications [2, 3]. Recently, the application of Ni-Cr-Fe alloys and superaustenitic stainless steel AL6XN has been increased because of the aforementioned. As consequence, the welding metallurgy became an active field of research, especially because these materials are used in fundamental components of gas turbines in aeronautic, nuclear power, oil and food industries [2–4].

Several welding processes can be used to weld Ni-Fe-Cr alloys and superaustenitic stainless steels. However, some metallurgical problems related with the fusion zone (FZ) and heat affected zone (HAZ) could be presented. Solidification cracking, undesirable secondary phase formation and segregation of elements such as Nb and Mo are the most important weldability problems in the FZ. Whereas, for the HAZ, the liquation cracking, Laves precipitation, δ phase and carbides formation

R. Cortés (✉) · R. R. Ambriz · E. R. Barragán · D. Jaramillo
Instituto Politécnico Nacional CIITEC-IPN, Cerrada de Cecati S/N Col. Sta. Catarina, Azcapotzalco, Ciudad de México 02250, Mexico
e-mail: crafiux@gmail.com

R. Cortés · V. H. López · A. Ruiz
Instituto de Investigación en Metalurgia y Materiales, Universidad Michoacana de San Nicolás de Hidalgo, A.P. 888, 58000 Morelia, Michoacán, Mexico

R. R. Ambriz et al. (eds.), *Proceedings of the 17th International Conference on New Trends in Fatigue and Fracture*, https://doi.org/10.1007/978-3-319-70365-7_25

are the principal phenomena to decrease the reliability of the welded joints. For instance, precipitation of secondary phases in Inconel 718 (IN718) and the formation of Mo depleted zones in AL6XN are caused by the Nb and Mo segregation during solidification, respectively. This behavior tends to increase with Fe presence in the matrix [1]. Additionally, the presence of Laves phase and NbC in the welded joints tends to produce low strength, low ductility and increase the fracture tendency in the FZ [5]. On the other hand, the precipitation of NbC in the HAZ reduces the available Nb for the γ'' formation [6]. Even when the IN718 weldments are subjected to an annealing treatment, the NbC presence is not suppressed because those carbides precipitate during the aging treatment [7]. Another factor that decreases mechanical properties in the HAZ is the reversion of precipitates which partially dissolves the γ' and γ'' phases due to the temperatures reached during welding [8].

This article is concerning with the microstructural and mechanical properties of IN718-AL6XN dissimilar GTAW welded joints. Results are reported considering the as-welded and hardening recovery provided by post weld heat treatment (HRPWHT) conditions.

Experimental

IN718 and AL6XN plates of 1500 × 150 × 6.35 mm were used. The material was supplied in annealed condition with the following mechanical properties: Vickers hardness number of 236.4 ± 5.2 (IN718) and 203.3 ± 3.5 (AL6XN), yield strength of 430.3 ± 5.7 MPa (IN718) and 396.3 ± 16.9 MPa (AL6XN), tensile strength of 842.9 ± 15.3 MPa (IN718) and 725 ± 5.7 MPa (AL6XN), elongation of 51.4 ± 0.7% (IN718) and 62.6 ± 1.5% (AL6XN). Metallographic samples of 60 × 10 × 6.35 mm of base material were mirror polished using conventional techniques. The microstructure was revealed by immersion of the samples in a 67% HCl + 33% HNO_3 solution for IN718 and $CuCl_2$ (2g) + 40%HCl + 60% C_2H_5OH solution for the AL6XN. Optical microscopy was used to analyze the structure of the material as well as the different zones of the welded joints. The chemical composition of the base and filler metals is shown in Table 1.

Table 1 Chemical composition of the materials used (wt%)

Material	C	Cr	Fe	Mn	Ni	Mo	Ti	Al	Other
Inconel 718	0.05	18.2	Bal.	0.07	52.97	2.89	0.65–1.15	0.57	Nb 4.98
ERNiFeCr-2	0.05	17.7	20.3	0.08	51.7	3.1	0.98	0.45	Nb 5.45
AL6XN	0.02	21	Bal.	1.0	24.5	6.5	–	–	Si 0.5 N 0.22

Determined by optical emission spectroscopy (OES)

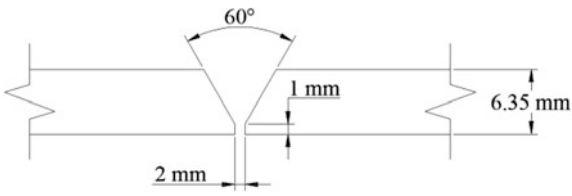

Fig. 1 Single V-groove joint used

Plates of 150 × 75 × 6.35 mm of base material were machined to obtain a single V-groove joint according to dimensions shown in Fig. 1.

Before welding, the IN718 plates were hardened by precipitation, which is the typical condition to use the IN718 alloy. The plates were heat treated by solubilization at 1065 °C for 1 h, aged at 720 °C for 8 h and finally furnace cooling. This treatment provided a Vickers hardness number of 408.5 ± 3.2, yield strength of 822.7 ± 9.6 MPa, tensile strength of 1090.3 ± 4.6 MPa and elongation of 41.2 ± 3.9%. After welding, some plates were subjected to the HRPWHT by using the same treatment conditions mentioned before. No heat treatment was used for the AL6XN plates.

A semiautomatic gas tungsten arc welding (GTAW) process was used to weld the IN718-AL6XN plates. An ER NiFeCr-2 with 1.1 mm in diameter was added by a semi auto feeding mechanism (at 170 mm s^{-1}). The GTAW torch was located at approximately 15° with respect to the normal of the plates. A mixture of H_2 (2%), CO_2 (0.12%), He (30%) and Ar (67.88%) was used as shielding gas at a flow rate of 16.50 dm^3 min^{-1}. Alternating current and tungsten-thorium electrode were used in conjunction with the following welding parameters: voltage of 29 V, current of 356 A, travel speed of 4 mm s^{-1}. These parameters provided a heat input of 1806.7 J mm^{-1}; considering a thermal efficiency of 70%.

After welding, optical and scanning electron microscopes were used to analyze the microstructure of the welded joints in as welded condition as well as HRPWHT.

For the microstructural analysis, transversal weld profiles were cut from the welded joints. The FZ, partially melted zone (PMZ) and HAZ was analyzed to determine the microstructural characteristics of the welds. Additionally, energy-dispersive X-ray spectroscopy (EDS) was used to determine the chemical composition of the matrix and some secondary phases. This technique was also used to obtain elemental concentration maps in certain areas to observe the distribution of some elements. X-ray diffraction was used to identify secondary phases at the microstructure by using Cu Kα radiation and 2θ angle from 30° to 120° with steps of 0.02° and 2 s at each step.

Vickers microhardness measurements were performed to analyze the hardness variation along the weld profile. The indentations were realized by using a load of 1.0 kg (9.81N) and dwell-time of 15 s. The distance between indentations was 500 μm and the length of the profiles was 25 mm approximately (12.5 mm from the middle the welding bead to both sides).

Tensile tests of the welded joints were performed on standard specimens (sub-size specimens), according with ASTM E8M [9]. The cross-head travel speed was 1 mm min^{-1}. The length increment during the test was measured by using and extensometer with a gauge length of 25 mm.

Results and Discussion

The microstructure of the IN718 alloy in annealed and aged conditions and AL6XN as received is shown in Fig. 2. In both alloys, an austenitic matrix γ with equiaxed grains and the presence of twinning was observed. This microstructure was produced by the mechanical deformation during rolling and annealing treatment. Annealing twins are very common in materials with FCC crystallographic structure [10]. Additionally, it is possible to observe the presence of secondary phases in form of dispersed precipitates at IN718.

An EDS analysis showed the presence of C, Mo, Ti and Nb in localized areas, which provided the evidence of MC and M_6C type carbides. The presence of these

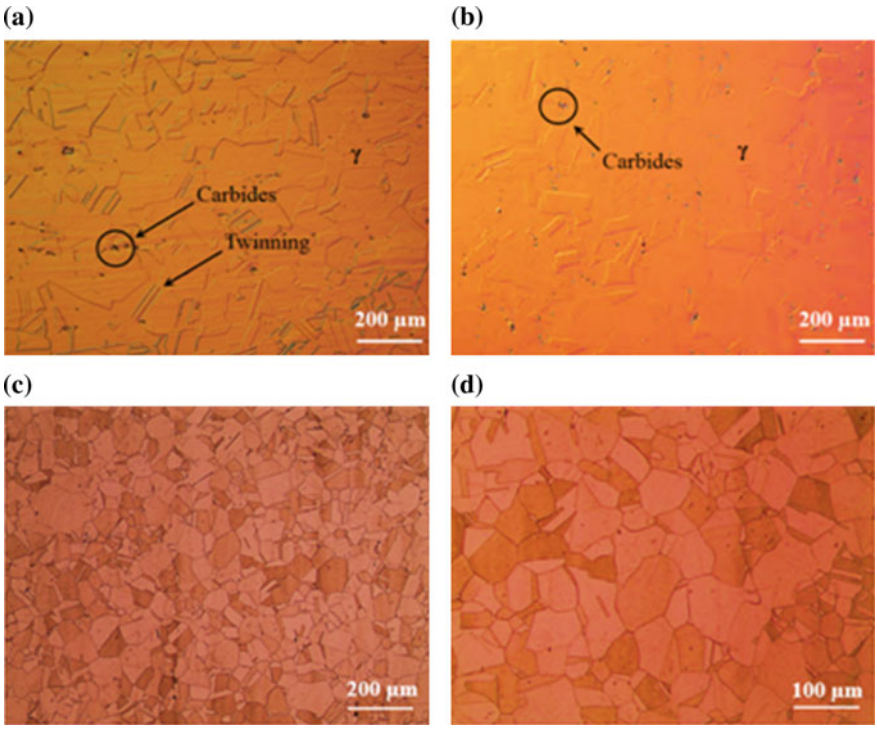

Fig. 2 Base material microstructure **a** IN718 in annealed condition. **b** IN718 in aged condition. **c** and **d** AL6XN as received

secondary phases could be produced because the Nb and Mo tend to segregate during the solidification [1]. In addition, due to the partition of these elements, the Laves phase formation is possible. The precipitation of Laves is promoted by the Fe contents in the austenitic matrix, which is related with the formation tendency of this secondary phase [11–13].

Figure 3 shows the transversal profile of the dissimilar IN718-Al6XN weld. It is possible to observe that there was full penetration of the weld, the geometry of the top was not excessive. A complete lateral fusion and no evidence of porosity or defects of the weld bead was observed. The distortion was prevented constraining the plates during welding.

The peaks shown in Fig. 4 corresponding to 37.36° and 40.68 as well as 34.73° and 40.32 represent the Laves and NbC secondary phases, respectively. This is similar with the results found by others in IN718 [14, 15]. It is evident that the peaks intensity is lower at the weldments with HRPWHT in comparison with the welded joints that were not subjected to this treatment. The greater presence of the Laves and NbC in the FZ of the weldments without HRPWHT explains why the failure appeared in this region during the tensile test, similar behavior was found by Hirose et al. [5].

The structure of the fusion zone of the IN718-AL6XN is observed in Fig. 5a. The characteristic dendritic columnar microstructure was observed. Different growing directions of the dendrites are present in the FZ, this is produced because

Fig. 3 Profile of dissimilar weldment IN718-AL6XN

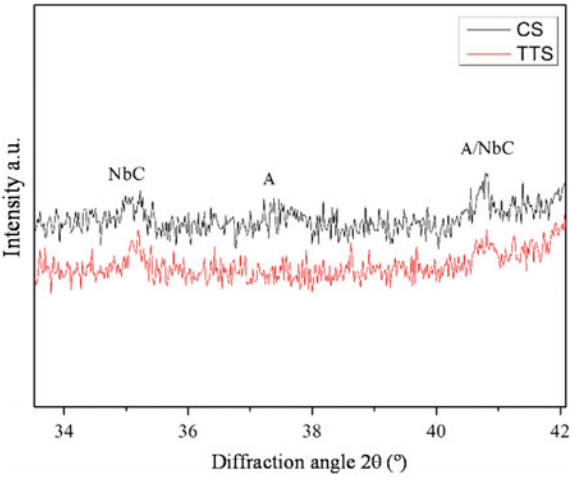

Fig. 4 XRD profile at FZ in IN718-AL6XN weldments: as-welded (CS) and with HRPWHT (TTS)

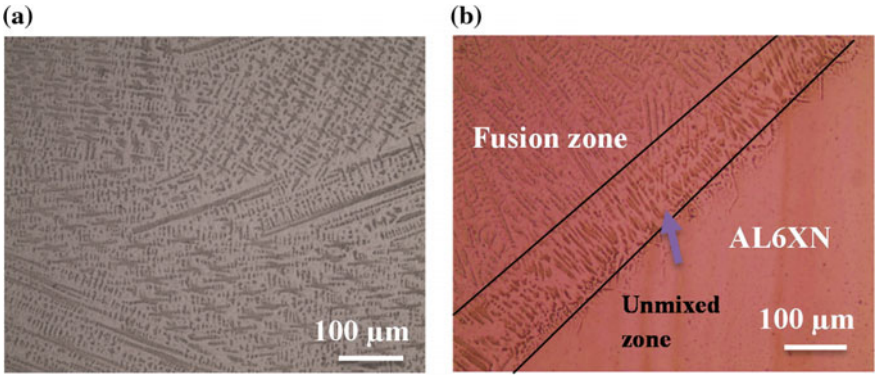

Fig. 5 **a** Microstructure of the FZ in the IN718-AL6XN weldment. **b** Unmixed zone at the interface between FZ and AL6XN

during solidification there are some favorable directions for growing than others. For IN718 (fcc structure) the easy growth directions are ⟨100⟩. The aforementioned mechanism is known as columnar competitive growth [16].

Figure 5b shows the morphology of the interface between the fusion zone and the AL6XN. As can be observed, there is an unmixed zone. This region was formed owing to the differences in chemical composition and melting point between base material and filler material. In this case, the melting point of the AL6XN material is higher than the filler material (ERNiFeCr-2). Under these conditions, convection currents were unable to produce an adequate flow and mix of the molten material at the interface. The unmixed zone tends be wider if differences in chemical composition and melting points of the material are higher [17].

The hardness profile on the IN718-Al6XN in both conditions, with and without HRPWHT is shown at Fig. 6. Owing to the welding process, it was observed a severe decreased of microhardness at the HAZ and FZ in the IN718 side of the weldment (Fig. 6a). In the case of the FZ the factor that contributes to the hardness decrement is the Nb segregation during solidification, which produces the NbC precipitation, decreasing the Nb amount for the formation of the γ'' phase [6]. Whereas, for the HAZ the decrease in hardness was associated to the reversion of precipitates, that generates a partial dissolution of the secondary phases in the region close to the FZ. In this zone, the peak temperature is higher than the precipitation temperature of the γ' and γ'' phases. This behavior was previously described for Hirose et al. [8]. At the AL6XN side there was no significant change among the hardness of the FZ and the base material. There was a slight decrease at the interface of the FZ and HAZ, which corresponds to the unmixed zone, however, the hardness values tend to reach the hardness values of base material.

Figure 6b shows the hardness distribution in the plates subjected to the HRPWHT. The hardness values practically were fully recovered at the FZ after the heat treatment. In the HAZ an increment in hardness was observed, however, these values did not reach the hardness of the base material in aged condition

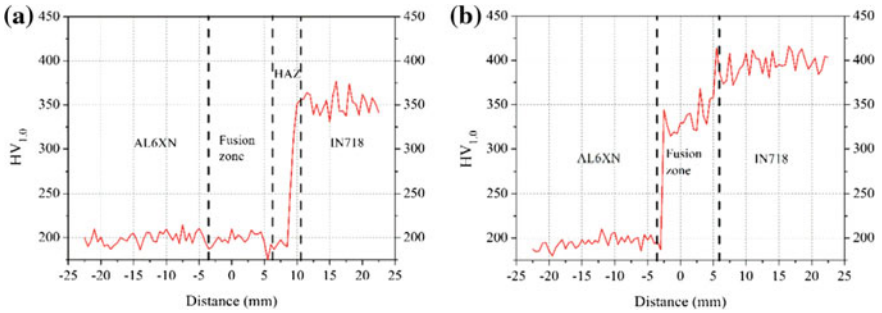

Fig. 6 Hardness distribution of the welded joints **a** microhardness profile for as-welded condition, **b** microhardness profiles for HRPWHT condition

(408.5, ±3.2). This behavior could be attributed to the reverse of precipitate mechanism and that even when the plates were solubilized the NbC precipitate during the ageing treatment. These two factors and their negative impact were discussed previously. Besides, the Nb segregation is not totally suppressed because it is considered that solid state diffusion of substitutional elements is negligible [1].

Tensile behavior of the welded joints is shown in Fig. 7a. The samples in as-welded condition presented the necking phenomenon in the HAZ due to the plastic deformation; however, the failure was presented in the FZ. It was observed that this area did not present an evident plastic deformation as in the HAZ. This behavior is not consistent with hardness results obtained for this condition, because the lowest hardness values were obtained for the HAZ of the IN718 side and the fracture was expected on that area. The failure occurs in the FZ due to the presence of brittle secondary phases that act as fracture starting points. A similar behavior was found by Hirose et al. [5]. Figure 7a also shows the tensile behavior of the welded joints with HRPWHT the average yield stress (385.5 MPa ± 3.5) and maximum stress (723.5 MPa ± 10.5) are very similar with the values of the base material AL6XN (396.3 ± 16.9 and 725 ± 5.7, respectively) as can be observed in

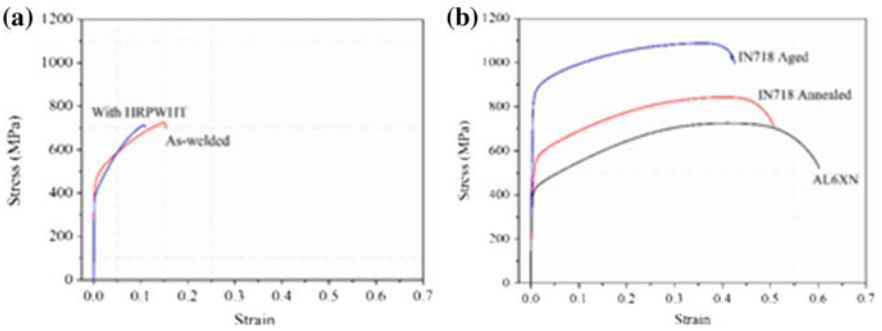

Fig. 7 Conventional stress-strain curves for **a** dissimilar welded joints in as-welded and HRPWHT conditions and **b** IN718 and AL6XN base materials

Fig. 7b. After the heat treatment, secondary phases are partially solubilized as shown in Fig. 4, in addition, both, the FZ and BM increase their hardness values. Thus, these samples failed in the AL6XN side along the fusion line between BM and FZ (that correspond to the unmixed area) which is the weakest region of the dissimilar weldment owing to the conditions in the interface described before, the failure was ductile type.

It is evident that the yield stress (∼426 MPa as-welded and ∼385 MPa with HRPWHT) and maximum stress (∼690 MPa as-welded and ∼738 MPa with HRPWHT) are close in both conditions. The most important difference is the percentage of elongation (∼14%) in the as-welded samples which is higher than the samples with HRPWHT. On the other hand, the energy absorbed by the weldments is inferior in comparison with the base materials due to the loss of ductility. This reduction was attributed to the brittle secondary phases formed during the welding process and to the increment in hardness.

Conclusions

Tensile mechanical properties of the IN718-AL6XN dissimilar weldments are severely reduced; they can be improved by hardening recovery provided by the post weld heat treatment. However, this heat treatment does not have any effect on the AL6XN side. After the HRPWHT the values of yield stress and maximum stress are very similar. Therefore, the application of a post-weld heat treatment can be suppressed without sacrificing the mechanical resistance of the IN718-AL6XN weldment.

Acknowledgements It is appreciated the financial support given for this project by the National Council of Science and Technology of the Mexican government. In addition, we are grateful with the technical and academic support given by the Instituto de Investigación en Metalurgia y Materiales of the UMSNH and the Centro de Investigación e Innovación Tecnológica of the IPN.

References

1. DuPont JN, Lippold JC, Kiser SD (2011) Welding metallurgy and weldability of nickel-base alloys. John Wiley & Sons, Hoboken, New Jersey
2. Kalnaus S, Fan F, Vasudevan AK, Jiang Y (2008) An experimental investigation on fatigue crack growth of AL6XN stainless steel. Engineering Fracture Mechanics 75 (8):2002-2019. doi:http://dx.doi.org/10.1016/j.engfracmech.2007.11.002
3. Nemat-Nasser S, Guo W-G, Kihl DP (2001) Thermomechanical response of AL-6XN stainless steel over a wide range of strain rates and temperatures. Journal of the Mechanics and Physics of Solids 49 (8):1823–1846. doi:http://dx.doi.org/10.1016/S0022-5096(00)00069-7

4. Mortezaie A, Shamanian M (2014) An assessment of microstructure, mechanical properties and corrosion resistance of dissimilar welds between Inconel 718 and 310S austenitic stainless steel. International Journal of Pressure Vessels and Piping 116:37–46. doi:http://dx.doi.org/10.1016/j.ijpvp.2014.01.002
5. Hirose A, Sakata K, Kobayashi KF (1998) Microstructure and mechanical properties of laser beam welded Inconel 718. International Journal of Materials and Product Technology 13 (1–2):28-44
6. Hinojos A, Mireles J, Reichardt A, Frigola P, Hosemann P, Murr LE, Wicker RB (2016) Joining of Inconel 718 and 316 Stainless Steel using electron beam melting additive manufacturing technology. Materials & Design 94:17–27. doi:http://dx.doi.org/10.1016/j.matdes.2016.01.041
7. Padilha AF, Rios PR (2002) Decomposition of Austenite in Austenitic Stainless Steels. ISIJ International 42 (4):325–337
8. Hirose A, Sakata K, Kobayashi KF (1997) Paper presented at the Solidification Processing 1997, Sheffield, UK,
9. ASTM (2004) Standard Test Methods for Tension Testing of Metallic Materials [Metric]. vol ASTM E8 M-04.
10. Mahajan S, Pande CS, Imam MA, Rath BB (1997) Formation of annealing twins in f.c.c. crystals. Acta Materialia 45 (6):2633–2638. doi:http://dx.doi.org/10.1016/S1359-6454(96)00336-9
11. Cieslak M (1991) The welding and solidification metallurgy of Alloy 625. Welding journal 70 (2):49s–56s
12. Cieslak MJ, Headley TJ, Knorovsky GA, Romig AD, Kollie T (1990) A comparison of the solidification behavior of INCOLOY 909 and INCONEL 718. Metallurgical Transactions A 21 (1):479–488. https://doi.org/10.1007/BF02782428
13. Cieslak MJ, Headley TJ, Romig AD, Kollie T (1988) A melting and solidification study of alloy 625. Metallurgical Transactions A 19 (9):2319–2331. https://doi.org/10.1007/BF02645056
14. Manikandan S, Sivakumar D, Kamaraj M, Rao KP (2012) Laves phase control in Inconel 718 weldments. In: Materials Science Forum, vol 710. Trans Tech Publ, pp 614–619
15. Chen S, Zhang C, Xia Z, Ishikawa H, Yang Z (2014) Precipitation behavior of Fe 2 Nb Laves phase on grain boundaries in austenitic heat resistant steels. Materials Science and Engineering: A 616:183–188
16. Chalmers B (1964) Principles of Solidification. Wiley, New York
17. Sireesha M, Shankar V, Albert SK, Sundaresan S (2000) Microstructural features of dissimilar welds between 316LN austenitic stainless steel and alloy 800. Materials Science and Engineering: A 292 (1):74–82. http://dx.doi.org/10.1016/S0921-5093(00)00969-2

Fatigue Life of Resistance Spot Welding on Dual-Phase Steels

J. H. Ordoñez Lara, R. R. Ambriz, C. García, G. Plascencia and D. Jaramillo

Introduction

Dual-phase steels are composed by a ferrite matrix and martensite as second phase. This characteristic allows to obtain an excellent combination of high strength and ductility, which is very attractive for the automotive industry to reduce the total weight of the vehicles. Resistance spot welding (RSW) is commonly used in the automotive industry to join the automobile parts, i.e. a vehicle has around three thousand welding points. However, due to the welding process (heat input), microstructural changes can be induced, which affects the mechanical behavior of the welded joints. In this context, several studies have been carried out [1–4]. Nayak et al. [1] studied the soft zone generated in the heat affected zone (HAZ) in RSW in dual-phase steels. They observed a tempering of the martensite in the HAZ, which affects the tensile properties of the joints. Additionally, Farabi et al. [5] analyzed the microstructure and mechanical properties of dissimilar laser welding in dual-phase steels. It was found that a microstructural change (almost 100% martensite) in the fusion zone (FZ) increases the hardness (50 HV), also they observed that the failure zone after tensile tests was presented in the soft zone formation in the HAZ. In contrast, the fatigue failure was attribute to the stress concentration effect produced by the nugget zone. Mediratta et al. [6] studied the influence of ferrite and martensite microstructure in fatigue life considering low cyclic fatigue. They found that the different microstructure of the material exhibits a cyclic hardening effect. The lower hardening occurs when there is a uniform

J. H. Ordoñez Lara (✉) · R. R. Ambriz · G. Plascencia · D. Jaramillo
Instituto Politécnico Nacional CIITEC-IPN, Cerrada de Cecati S/N,
Col. Sta. Catarina, 02250 Azcapotzalco, Ciudad de México, Mexico
e-mail: pure_evil_h@hotmail.com

C. García
Facultad de Ingeniería, Universidad Autónoma de San Luis Potosí,
Av. Manuel Nava no. 8, Zona Universitaria, 78290 San Luis Potosí, S.L.P., Mexico

R. R. Ambriz et al. (eds.), *Proceedings of the 17th International Conference on New Trends in Fatigue and Fracture*, https://doi.org/10.1007/978-3-319-70365-7_26

distribution of dislocations due to the dispersion of martensite. In contrast, fine grains and continuous martensite around the ferrite grains present the best performance for the fatigue life. Pouranvari [2] performed a study on the susceptibility to interfacial failure in RSW of DP600 dual phase steel. He found a transition from interfacial failure to pullout failure which depends of the size of the melting zone. The high carbon content of the steel promotes the martensite formation, as well as the propagation of cracks through the melting zone. There is no direct correlation between the equivalent carbon and the tendency to interfacial fracture in shear tensile test. Dancette et al. [4] carried out a study on the tensile shear fracture of advanced high-strength steel spot welds. They identified two fracture mechanisms, the first one was related with the localized deformation in the base material, the second one was associated with the ductile shear at the interface of the nugget zone. Giri and Bhattacharjee [7] studied the fatigue life in DP590 steel; they reported that the stress concentration generated in the fusion zone reduces the fatigue life of the welded joints. In contrast, Sherman and Davies [8] conducted a study of the effect of martensite content on fatigue life in dual-phase steels, reporting that the strength of the joints tends to improve when the martensite volume increases.

This work reports a comparative scenario between the DP590 and DP980 steels welded by RSW. The results are reported in terms of microhardness, shear and fatigue tests. The fatigue life of the joints and the analysis of the fracture surface also are reported.

Experimental Procedure

Materials and Welding

DP590 (σ_0 = 362 MPa σ_u = 596 MPa, and ε = 23.5%), and DP980 (σ_0 = 930 MPa σ_u = 1135 MPa, and ε = 11.5%) steel sheets were used (chemical composition shown in Table 1). Conventional techniques of cutting, machining, grinding and mirror polishing were used to obtain metallographic samples of the materials. The grain structure of the materials is presented in Fig. 1. As it can be observed, the microstructure of the DP590 steel presents a lower volume of martensite in comparison to the DP980, also an important difference in terms of grain size was observed. These characteristics provided an important difference in hardness.

Resistance spot welding (RSW) equipment with alternating current was used. A current of 9.5 kA, with a frequency of 60 Hz and force of 40 kN were used to perform RSW lap joint according with the standard dimensions dictated by the AWS D8.9 specification. Uncoated copper electrodes were used during the welding process. Tips of the electrodes were machined to obtain a circular section of 5 mm in diameter with an angle of 120°.

Table 1 Chemical composition of the materials employed (wt%)

	C	Si	Mn	P	S	Cr	Mo	Ni	Al	Cu	Ti	V	Fe
DP590	0.054	0.43	1.95	0.019	0.0057	0.030	0.0022	0.018	0.038	0.021	0.0017	0.0050	97.43
DP980	0.15	0.2	1.5	0.0096	0.0033	0.037	0.013	0.045	0.034	0.0075	0.0012	0.01	97.98

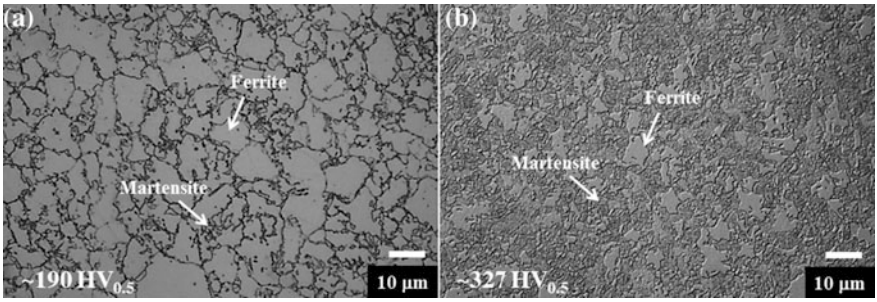

Fig. 1 Dual-phase steel optical microstructure showing a ferrite and martensite phases, **a** DP590 and **b** DP980

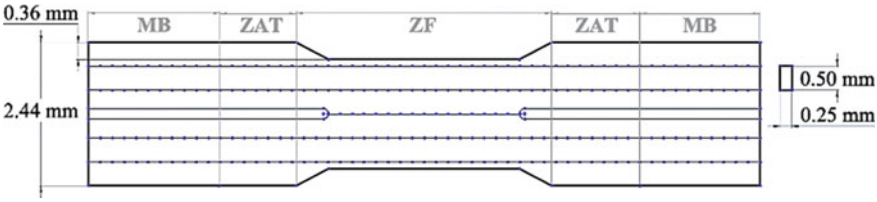

Fig. 2 Schematic welding profile and virtual mesh for microhardness measurements

After welding Vickers microhardness measurements with a load of 0.5 kg and dwell-time of 15 s were taken following the scheme shown in Fig. 2.

Tensile shear tests were performed for the welded joints with head-cross displacement of 0.25 mm min^{-1}. An extensometer with a gage length of 25 mm was used. The specimen dimensions for tensile shear and fatigue tests were 105 mm × 45 mm × 1.22 mm with an overlap of 35 mm. These dimensions were established according with the AWS D8.9 specification. Fatigue tests were performed with a cyclic loading sinusoidal wave form at a stress ratio of $R = 0.1$ by using a frequency of 30 Hz and room temperature (∼22 °C). After fatigue tests, some specimens were analyzed by using a scanning electron microscope to observe the fracture surface.

Results and Discussion

Microstructure

Figure 3 shows the macro and microstructure of the cross-section resistance spot welding points obtained. From this figure it is possible to observe the fusion zone (FZ), the heat affected zone (HAZ), and the base material (BM). In both welded

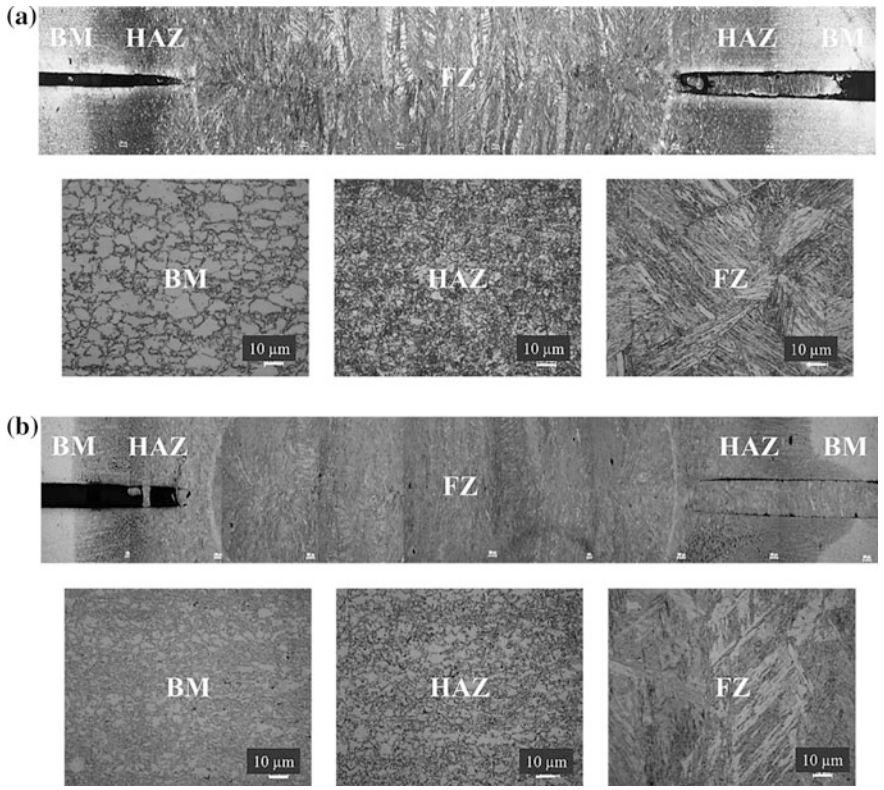

Fig. 3 Microstructure of resistance spot welds **a** DP590 and **b** DP980 steels

joints (DP590 and DP980) the heat input produced during welding produces an evident microstructural change. The FZ is formed by martensite with a lath morphology, which is characteristic for steels with low carbon contents. In the HAZ a grain size refinement was observed with an increment in volume of martensite, especially for the DP980 steel (Fig. 3b).

Microhardness

Figure 4 shows the hardness profile for the DP590 and DP980 spot welds. According to figure it is possible to observe a hardness increment in the center of the FZ, which represents approximately 130 $HV_{0.5}$ and 120 $HV_{0.5}$ for the DP590 and DP980 steels in comparison with the base material hardness. This hardness tends to increase as function of distance from the center of the FZ to the HAZ, reaching values (near to the interface between HAZ and FZ) at about 370 $HV_{0.5}$ and 430 $HV_{0.5}$ for DP590 and DP980 steels, respectively [1]. Considering that the

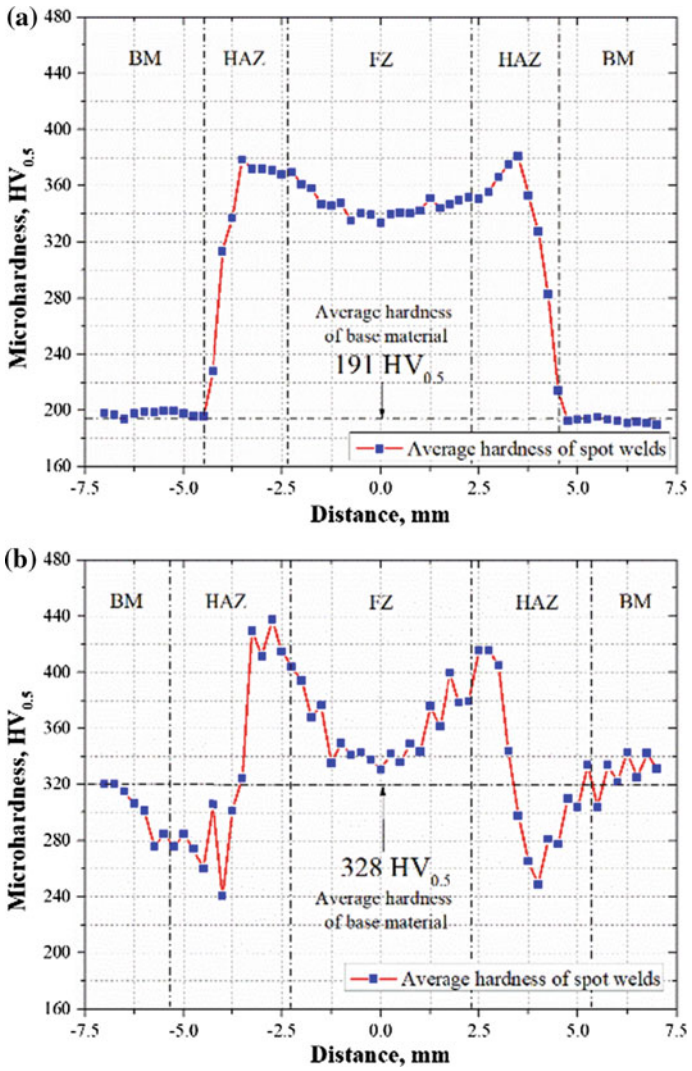

Fig. 4 Microhardness profiles for **a** DP590 and **b** DP980

applied current during welding in both materials is similar, as well as the thermo-physical properties, we can consider that the cooling rate in both materials is also similar. Thus, the increase in hardness on the FZ can be attributed to the chemical composition of the materials [9, 10], as well as the fast cooling rate, i.e. the cooling rate curve traverses the martensitic transformation line of the continuous cooling transformation. Later, a hardness decrement is observed reaching the base material hardness for the DP590 steel. However, in the case of the DP980 steel, a

soft zone formation [5, 11] with hardness values below of that of the base material (320 $HV_{0.5}$) have been observed. This zone was attributed to the weld thermal cycle producing a tempering process (tempered martensite).

Shear Testing

Figure 5 shows the representative (average of three samples) shear load-displacement curves for the DP590 and DP980 steels welded joints. As can be seen, the maximum load is similar in both welded joints ($F_{max} \sim 18$ kN). However, an important difference in terms of displacement was observed for the DP590 ($\sim$1.73 mm) joints in comparison to the DP980 ($\sim$0.9 mm) joints. This aspect can be attributed to the microstructural transformation, which tends to increase tensile strength but a decrement in ductility [4, 12, 13] for the DP980 welds. Then, an improvement in fracture energy (fracture toughness) can be deduced for the DP590 welds. In addition, it is possible to note a pullout failure mode after shear testing.

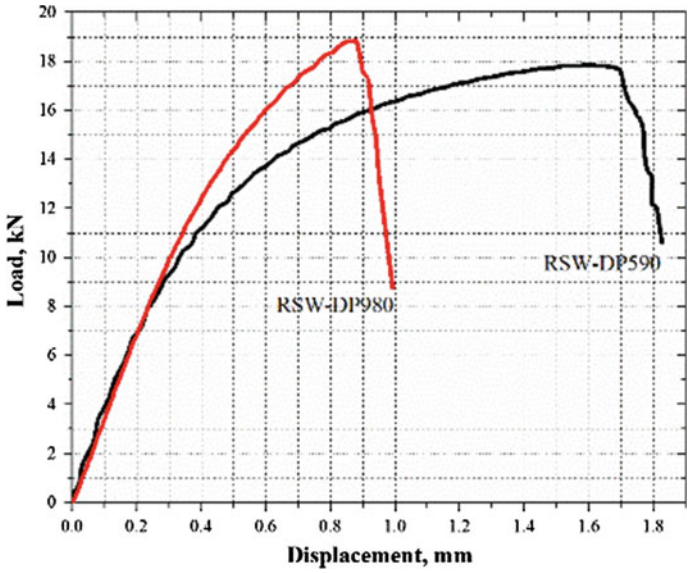

Fig. 5 Shear load-displacement curves for resistance spot welding in DP590 and DP980 steels

Fatigue Behavior (Wöhler Curves)

Resistance spot welds were subjected to a cyclic loading as previously indicated. Figure 6 shows the experimental results obtained for the RSW in DP590 and DP980 steels and its respective comparison with the Wöhler curve found in the literature.

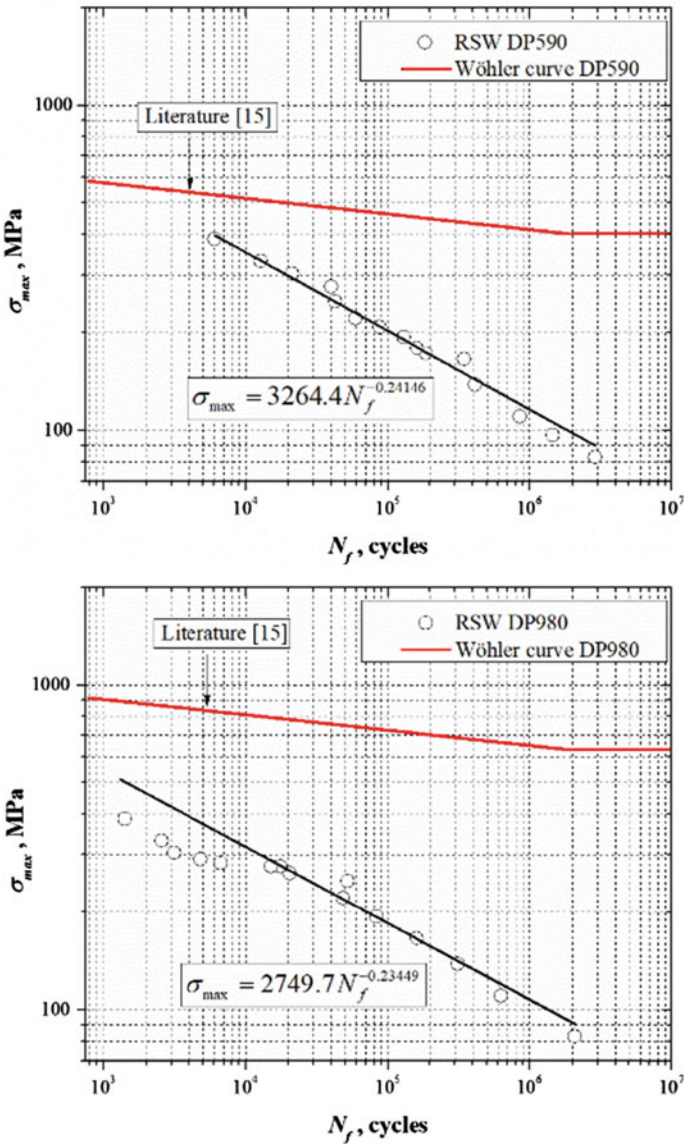

Fig. 6 Experimental Wöhler curves obtained for resistance spot welding in DP590 and DP980 steels and its respective comparison with the base material found in the literature [14]

The experimental data found were fitted to the traditional Basquin's equation:

$$\sigma_{\max} = AN_f^b \tag{1}$$

where A and b are the experimental constants.

Considering the results shown in Fig. 6, it is possible to observe an important effect of the spot welding geometry on the fatigue life with respect to the base material. It is to say that the stress concentration factor is the dominant aspect to decrease the fatigue life of the joints. This aspect was observed in both materials (DP590 and DP980). Thus, it is important to note that the high resistance of the DP980 steel should not be consider as a predominant aspect to design welded structures subjected to cyclic loading. On this context, the authors are carrying out experiments related with overloads to induced compressive residual stresses to improve the fatigue resistance of the RSW in DP980 steel.

In terms of fatigue cracks, it was observed that all the samples tested nucleated the crack at the fusion zone (stress concentration factor), and grew trough the HAZ to the base material, as shown in Fig. 7.

From Fig. 7, two predominant fracture modes can be observed. Mode I from which the crack nucleated and propagates due to the stress concentration produced by the spot welding and the interface between both sheets. Then it changes to Mode III, in which the crack grows throughout the interface between the FZ and the HAZ perpendicular to the applied load across the thickness of the joints [15].

The fracture surface of the joints is shown in Fig. 8. Five sites of the fracture surface were analyzed as indicated by details a1–a5, b1–b5.

The fracture appearance reveals that the crack was nucleated at the interface between sheets (rectangle marked as position 5 in Fig. 8). Later, the crack propagated across the thickness and surface of the sheets in a combination mode I/III. During the propagation of the crack striations were detected, which represents the steps of the cyclic load applied during the fatigue test. On the other hand, microcracks also were observed, which can be attributed to the martensitic microstructure (hard and brittle phase). A larger number of microcracks can be observed in the case of DP980, which can be attributed to the higher volume of martensite, compared to DP590.

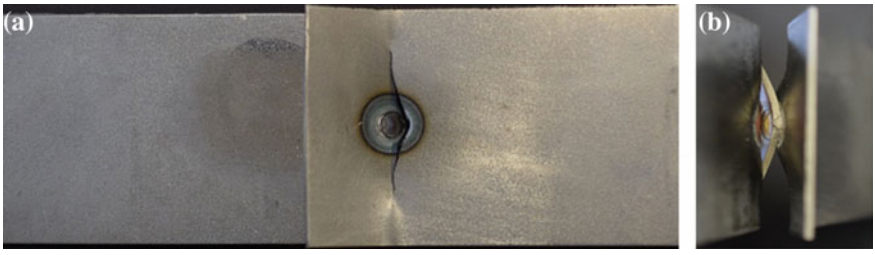

Fig. 7 General fatigue fracture appearance for **a** DP590 sample and **b** DP980 sample

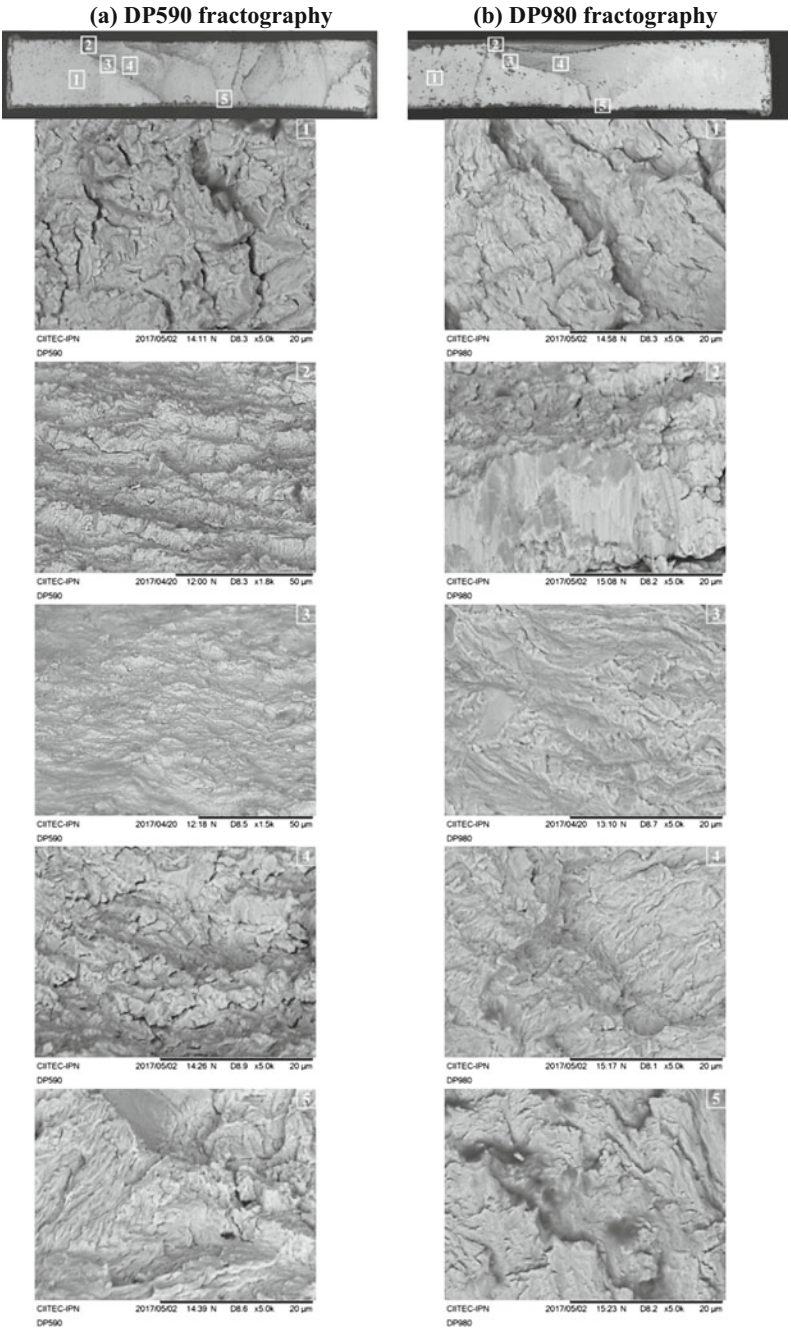

Fig. 8 Fracture surface appearance

Conclusions

The welding parameters have a great importance in the mechanical behavior of the resistance spot welds. The microstructural transformation in DP980 steel is higher severe than for the DP590 steel. This change was attributed to thermal input, which affects directly the mechanical properties of the material. In the case of DP980 steel a soft zone in the heat affected zone was detected, which is produced by the chemical composition of the material and the cooling thermal cycle of the resistance spot welding process. On the other hand, the tensile shear test shows a similar resistance in both steels, however, the displacement is higher than for the DP590 steel. It was observed that the stress concentration factor produced by the spot weld is the predominant aspect to decrease the fatigue resistance of the joints. A better fatigue behavior was observed for the DP590 steel.

Acknowledgements The authors thank to CONACyT-México (project 736) and SIP-IPN for funding this research. José Humberto Ordoñez Lara thanks CONACyT-México for the scholarship provided.

References

1. S. Nayak, Y. Zhou, V. Baltazar Hernandez and E. Biro, "Resistance spot welding of dual-phase steels: heat affected zone softening and tensile properties," in *Proceedings of the 9th International Conference on Trends in Welding Research, Chicago, Illinois, United States*, 2012.
2. M. Pouranvari, "Susceptibility to interfacial failure mode in similar and dissimilar resistance spot welds of DP600 dual phase steel and low carbon steel during cross-tension and tensile-shear loading conditions," Materials Science and Engineering: A, vol. 546, pp. 129–138, 2012.
3. R. W. Rathbun, D. Matlock and J. Speer, "Fatigue behavior of spot welded high-strength sheet steels," Welding Journal, vol. 82, no. 8, pp. 207–218, 2003.
4. S. Dancette, D. Fabregue, V. Massardier, J. Merlin, T. Dupuy and M. Bouzekri, "Investigation of the tensile shear fracture of advanced high strength steel spot welds," Engineering Failure Analysis, vol. 25, pp. 112–122, 2012.
5. N. Farabi, D. Chen and Y. Zhou, "Microstructure and mechanical properties of laser welded dissimilar DP600/DP980 dual-phase steel joints," Journal of Alloys and Compounds, vol. 509, no. 3, pp. 982–989, 2011.
6. S. Mediratta, V. Ramaswamy and P. R. Rao, "Influence of ferrite-martensite microstructural morphology on the low cycle fatigue of a dual-phase steel," International journal of fatigue, vol. 7, no. 2, pp. 107–115, 1985.
7. S. K. Giri and D. Bhattacharjee, "Fatigue behavior of thin sheets of DP590 dual-phase steel," Journal of materials engineering and performance, vol. 21, no. 6, pp. 988–994, 2012.
8. A. Sherman and R. Davies, "The effect of martensite content on the fatigue of a dual-phase steel," International Journal of Fatigue, vol. 3, no. 1, pp. 36–40, 1981.
9. M. Xia, M. Kuntz, Z. Tian and Y. Zhou, "Failure study on laser welds of dual phase steel in formability testing," Science and Technology of Welding and Joining, vol. 13, no. 4, pp. 378–387, 2008.

10. M. Xia, N. Sreenivasan, S. Lawson, Y. Zhou and Z. Tian, "A comparative study of formability of diode laser welds in DP980 and HSLA steels," Journal of Engineering Materials and Technology, vol. 129, no. 3, pp. 446–452, 2007.
11. M. Xia, E. Biro, Z. Tian and Y. N. Zhou, "Effects of heat input and martensite on HAZ softening in laser welding of dual phase steels," ISIJ international, vol. 48, no. 6, pp. 809–814, 2008.
12. N. Chen, H.-P. Wang, B. E. Carlson, D. R. Sigler and M. Wang, "Fracture mechanisms of Al/steel resistance spot welds in lap shear test," Journal of Materials Processing Technology, vol. 243, pp. 347–354, 2017.
13. M. Marya, K. Wang, L. G. Hector and X. Gayden, "Tensile-shear forces and fracture modes in single and multiple weld specimens in dual-phase steels," Journal of Manufacturing Science and Engineering, vol. 128, no. 1, pp. 287–298, 2006.
14. A. Mittal, "Dual Phase steels," in Automotive Worldwide, 2017, p. 9.
15. W. Xu, D. Westerbaan, S. Nayak, D. Chen, F. Goodwin, E. Biro and Y. Zhou, "Microstructure and fatigue performance of single and multiple linear fiber laser welded DP980 dual-phase steel," Materials Science and Engineering: A, vol. 553, pp. 51–58, 2012.

Failure Analysis by Hot Cracking Root HAZ in Welding SMAW Type

M. Arzola, J. L. González, S. J. García, D. I. Rivas and E. Sandoval

Introduction

This research aims to identify the damage mechanism experienced by a elbow welded to a class 600 flange, which were removed from the Spool of a 20 in. pipeline.

During the inspection of the component, there were cracks in the weld bead of the long radius elbow and flange, located at three hours of technical hours. The pipeline operates at 18 kg/cm^2, with a maximum historical pressure of 52 kg/cm^2, an operating temperature of 30 °C and a maximum historical temperature of 100 °C. The elbow is 90°, with 20 in. in diameter, a thickness of 0.938″; and its material of manufacture is carbon steel (MS SSP75WPH 65). The flange is of class 600 carbon steel; this type of accessories are usually made of steel ASTM A 105 (Fig. 1).

Experimental

The present failure analysis was performed under the methodology developed specifically for GAID-IPN by Dr. Jorge Luis González Velázquez, which is in accordance with the approach and procedure described in the standard ASTM E 2332-04 [1] "Standard Practice for Investigation and Analysis of Physical Component Failures" and consisting of the following activities:

M. Arzola (✉) · J. L. González · S. J. García · D. I. Rivas · E. Sandoval
Instituto Politécnico Nacional, ESIQIE-IPN, GAID-IPN,
UPALM Edif, 7 Planta Baja, Av. Instituto Politécnico Nacional s/n, Col, 07738
Col. Lindavista, CDMX, Mexico
e-mail: k_david_77@hotmail.com

R. R. Ambriz et al. (eds.), *Proceedings of the 17th International Conference on New Trends in Fatigue and Fracture*, https://doi.org/10.1007/978-3-319-70365-7_27

Fig. 1 Long radio elbow removed from Spool due to cracking

1. Collection of Evidence and Failure Information.
2. Tests of the failed component:
   - 2.1 Visual examination for verification of dimensions and condition "as received", photographic record, identification of physical characteristics, cleaning and preparation of samples.
   - 2.2 Chemical analysis.
   - 2.3 Mechanical tests: Hardness tests (ASTM E10 [2]) and uniaxial stress (ASTM E8 [3]).
   - 2.4 Metallographic examination: according to standards: ASTM E3 [4], ASTM E1122 [5] and ASTM E1382 [6].
   - 2.5 Fractographic and superficial examination.
3. Analysis of results:
   - 3.1 Mechanisms that led to component failure.
   - 3.2 Failure sequence (by events and in timeline).
   - 3.3 Physical cause, intrinsic and extrinsic factors that contributed to the failure.
4. Conclusions

Results

Visual Examination

The sample is observed in Fig. 2 in the condition as received for its study. The piece consists of a section of the elbow and flange connected by field welding with the coated electrode welding process (SMAW). The significant measurements are as follows: 49.6 cm (19.52″) long, 18 cm wide (7.08″), The thickness of the elbow is 28 mm (1.102″) and reduced in the bevel to 21 mm (0.826″), the thickness of the

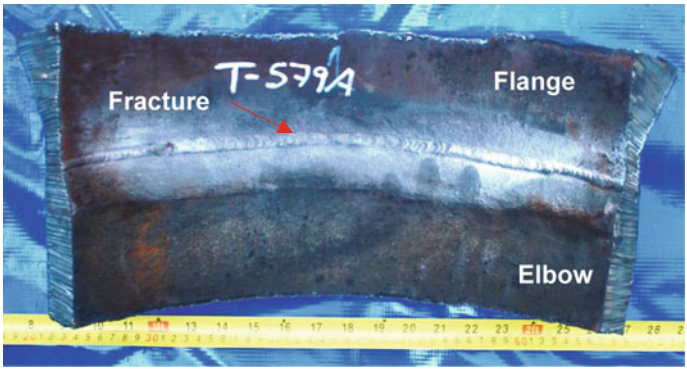

Fig. 2 Section of elbow and flange containing failure in condition as received for study by GAID-IPN

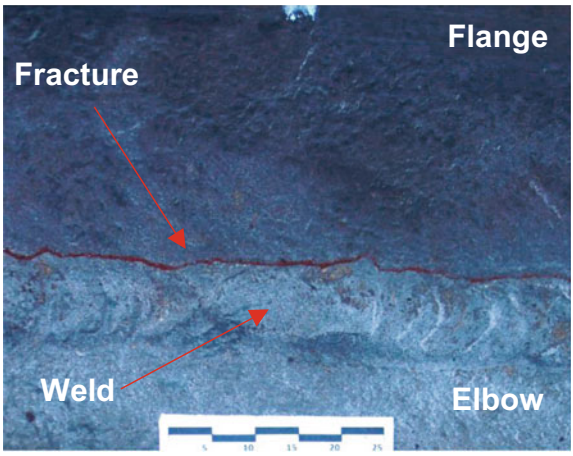

Fig. 3 Detail of the fault zone showing the location of the cracking

flange is variable, the lowest in its neck and adjacent to the weld is 18 mm (0.708″), the main feature observed in the sample, is a radial cracking adjacent to the weld bead.

The fracture is simple, without branching, without secondary or multiple cracking, the fracture plane is in the circumferential direction, there is no plastic deformation associated with the fracture, no localized or generalized metal losses are observed, no deposits of products of corrosion. The cracking length was estimated to be 30 cm delimited by inspection by penetrating liquids. Figure 3 shows a close-up of the cracking, it can be seen that this is given adjacent to the weld, on the side of the flange.

Chemical Analysis

The carbon (C), sulfur (S), silicon (Si), manganese (Mn) and phosphorus (P) contents of the elbow and flange steel were determined by spectrophotometry using the atomic absorption technique. Table 1 shows the results of the chemical analysis and what is established in the specification ASTM A-105 and in MMS-**SP75.**

Hardness Tests

Rockwell hardness tests were performed on the B scale on elbow and flange steels. The test conditions were as follows: carbide indenter of 1/16 tungsten, preload of 10 kg and a total load of 100 kg. Table 2 shows the results.

Uniaxial Tensile Tests

Tension tests were performed on specimens drawn from the elbow and flange, following the guidelines described in ASTM E 8M. The tests were performed at room temperature in laboratory air, using an electromechanical machine equipped with extensometer and controlled with application software. The results are presented in Table 3. And are compared with ASTM specifications A-105 and MMS-SP75.

Table 1 Results of chemical analysis in weight%

ID	C	Mn	S	P	Si	Cr	Cu	Mo	Ni	Nb	V
Flange	0.075	1.193	0.026	0.014	0.285	0.193	0.075	0.131	0.399	0.041	0.081
ASTM A105	0.35 max	0.6–1.05	0.04 max	0.035 max	0.10–0.35	0.30 max	0.40 max	0.12 max	0.4 max	NE	0.08
Elbow	0.168	0.884	0.021	0.011	0.190	0.083	0.006	0.016	0.028	0.028	0.007
MSS SP-75	0.30 max	1.60 max	0.06 max	0.05 max	0.5 max	0.25 max	1.50 max	0.25 max	1.0 max	0.10 max	0.13 max

Table 2 Rockwell hardness values on scale B

Sample	Number of identations	Average	Minimum value	Maximum value	Uncertainty
Flange	10	91	91	92	±1.78
Elbow		79	78	80	±2.01

Table 3 Uniaxial tensile strength properties

Sample	Direction	Area reduction (%)	Elongation (%)	Yield stress (psi)	UTS (psi)
Flange	Longitudinal	77	28	71,693	91,127
ASTM A 105	NE	22 min	36,000 min	70,000 min	
Elbow	Longitudinal	77	38	47,835	68,253
MSS-SP75-WPG-46	NE	20 min	46,000	63,000	

Metallographic Analysis

The Fig. 4 show the non-metallic inclusions present in the materials, which were characterized as D type, globular oxides, in both cases.

Subsequently, the samples were etched with the nital reagent 3, to reveal their microstructure, and were observed in the image analyzer. The results are shown in Fig. 5, the steel microstructure is constituted by a matrix of fine grains of ferrite with the presence of a second phase with grains coarse and dissimilar in size (large and multiple small grains). The condition of heat treatment corresponds with a thermomechanical treatment of controlled rolling to obtain a fine grain. As part of

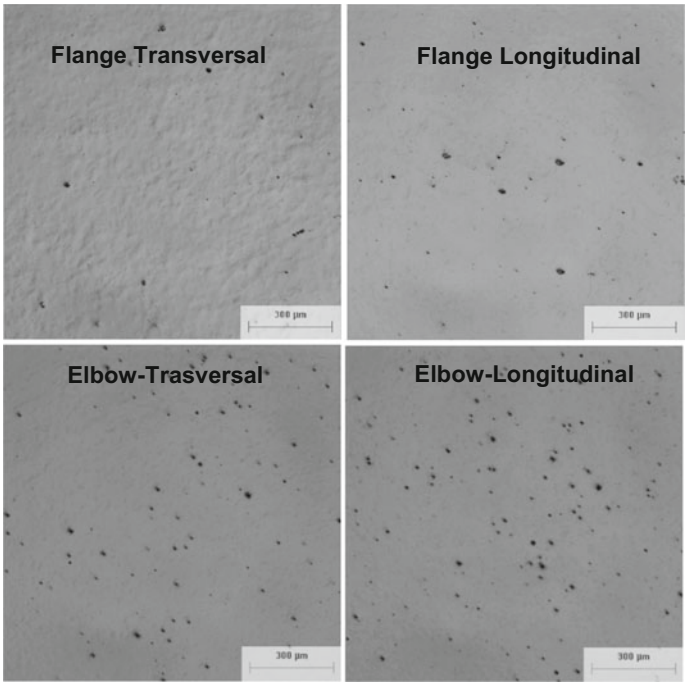

Fig. 4 Non-metallic inclusions present in steel making the flange and elbow respectively, globular oxides

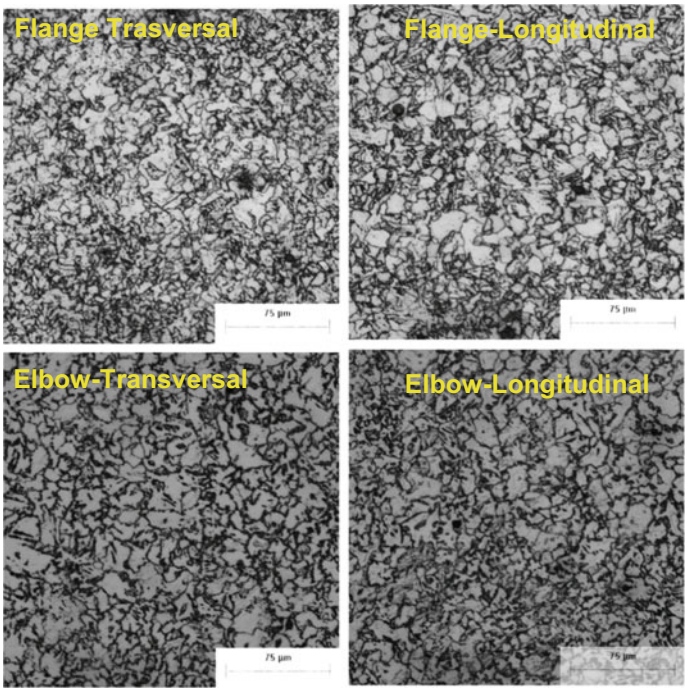

Fig. 5 Microstructure of the pipe section steel, consisting of a ferrite matrix, 500X fine-grained

Table 4 Stereological parameters of the microstructure

Sample	Direction	Inclusion content	Inclusion type	Ferrite (%)	Second phase (%)	Grain size ASTM
Flange	Transversal	0.25	D	82.85	17.25	10
	Longitudinal	0.47		80.18	19.85	
Elbow	Transversal	0.93		66.02	33.98	9
	Longitudinal	0.83		69.24	30.76	

the metallographic study, a quantification of the stereological parameters of the microstructure was performed, the results are presented in Table 4.

Analysis of the Failure Zone

The center of the fracture was cut, in order to observe the fracture surface. Figure 6 shows the result in a macro-view and in a detail seen under the microscope stereoscope. It is not observed a high degree of plastic deformation. On the other hand, fine steps distributed throughout the surface, which are marks closely parallel

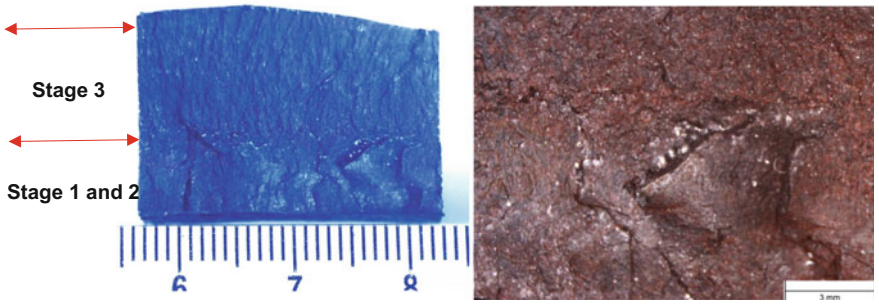

Fig. 6 Surface of fracture in a macro view and under microscope stereoscope, note the steps and layer of corrosion products

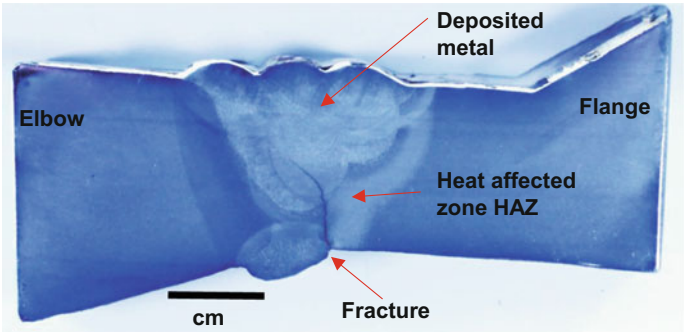

Fig. 7 Cross section containing cracking, observe its location and feed path

to the direction of cracking are observed. Also, the fracture plane initially is the circumferential direction and represents approximately the 40% of the fracture surface. This zone corresponds to stage 1 (nucleation) and 2 (stable propagation) of the general fracture model [7]. As the cracking propagates, there is a deflection closely Oblique towards the longitudinal direction, without representing a total change in direction and corresponding to step 3 (unstable propagation) representing the remaining 60% of the fracture surface; On the other hand, a layer of red and brown corrosion products adhering to the surface is observed, which prevents microscopic observations with scanning electron microscopy (SEM).

The sectioning was continued, and a section cross-section was prepared for metallography containing the cracking just at its end, Fig. 7 shows the result, it can be seen that the onset of cracking occurs just in the ZAC of the root of the cord Of welding on the side of the flange and that it propagates by the wall thickness, entering the deposited metal advancing in it, and culminating towards the crown. The images of Fig. 8 show close-up of the crack seen under the optical microscope, it is possible to observe the presence of microscopic cracks adjacent to the main

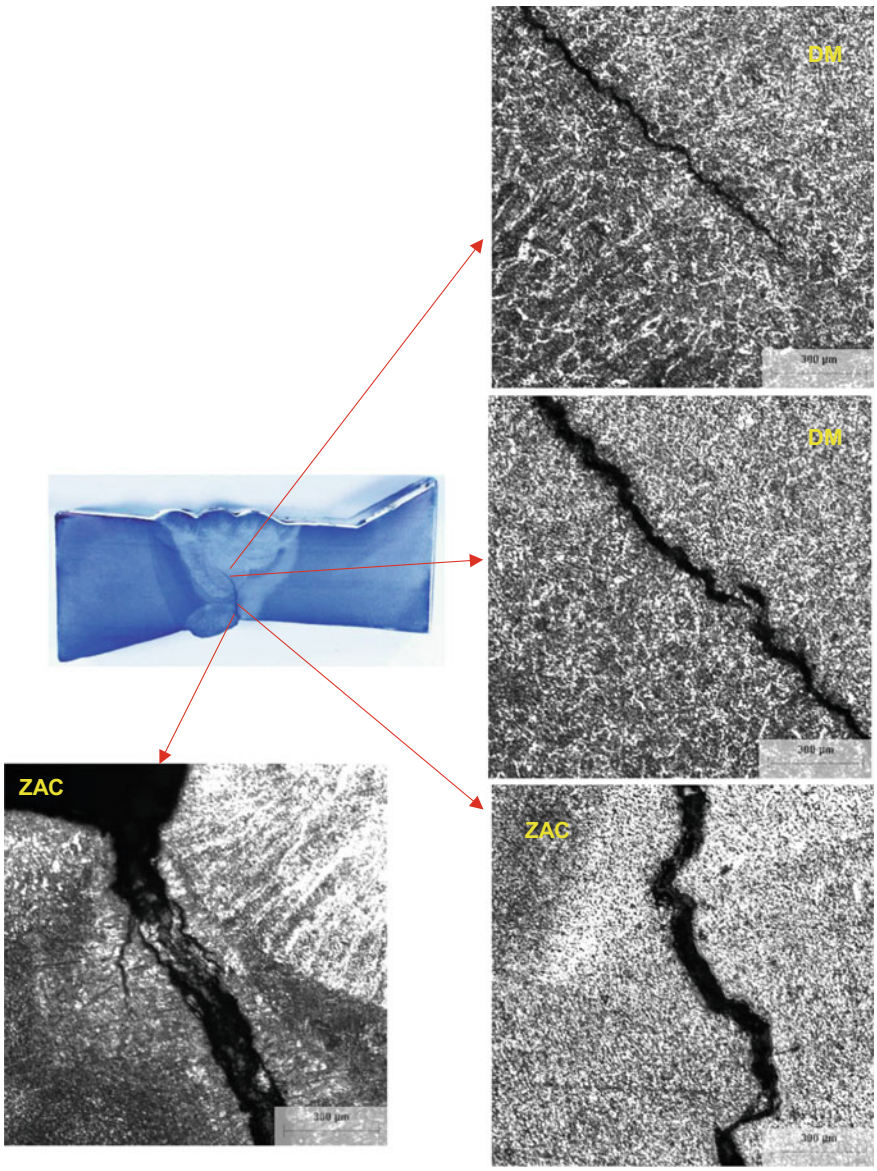

Fig. 8 Trajectory and morphology of cracking, observe tiny micro cracks adjacent to the main

crack, the crack is observed to be staggered, the cracking path through the microstructure is granular and not Notes that it follows preferential guidance.

Analysis of Results

The chemical, metallurgical and mechanical characteristics (Tensile strength and hardness) observed in the flange making steel generally comply with an ASTM A105 steel, only a slightly high manganese content is observed, although this is not necessarily transcendental in the Cause of failure. However this type of materials commonly are manufactured in steel ASTM A105; The yield strength and the maximum strength observed in this steel are high and well above that recommended in ASTM A105, therefore this material surpasses the intended design needs. The elbow material generally meets MSS SP-75 grade WPHY42 steel, which differs from that indicated in the elbow bending, which refers to a steel MSS SP WPHY65, yield strength values and Maximum strength do not meet the specified minimum of 65 KSI at yield and 77 KSI at maximum, for this type of steel, therefore the material of the elbow was characterized as a low carbon MSS SP75 grade WPHY42.

The damage consisted of a closely radial cracking that started in the heat affected area of the root of the weld bead joining the elbow and the flange, this is a weld defect that is generated during the construction, is known as Cracking in the heat-affected area at the root of the HAZ (Cracking Root). As welding cracks are known, they can have their origin, in solidification points, high stresses present in the joint, presence of hydrogen and bad practices of the welding process.

In this case, to be a cracking that starts in the zone affected by the heat at the root of the weld could be thought of a problem of weldability however the carbon equivalent in the material of the flange was 0.36 the reference standard ASTM A105 indicates that the CE must be a maximum of 0.48; With respect to the elbow the value of the equivalent carbon was estimated at 0.35, in the reference standard MSS SP 75 the maximum value of CE is 0.45, therefore both materials have an adequate weldability taking as reference what is recommended by the regulations.

A weldability problem is not expected because it has an extremely hard material or a high carbon content. The hardness in both materials is in order for structural steels without special heat treatments. Both materials have chemical characteristics (low carbon content) and metallurgical characteristics, which rules out the problem of weldability.

From the foregoing it is inferred that the failure of the welding occurred as a consequence of the application of the process itself, for one of the following reasons: an inadequate working temperature between passes, a delay in time during the anchoring and the passage Hot, differences in height of weld beads and use of old or wet electrodes.

The sequence of events leading to the weld failure joining the flange and elbow of the Spool of the 20″ line can be listed as follows:

During the welding process and the cooling of the joint there is the formation of a cracking in the area affected by the heat in the root of the side of the flange.

There is a stable propagation of the fracture which represented approximately 40% of the fracture surface.

Under normal service conditions unstable and lost ligament propagation occurred because the loads provided by the working fluid generated stresses high enough for the weld material to reach its fracture toughness and propagate in a manner Unstable and there was loss of ligament, then there was the lack of tightness in the union and emanation of the working fluid.

Conclusions

The type of failure was a fragile circumferential fracture in the area affected by the HAZ heat at the root of the H (HAZ).

Flange fabrication was characterized as ASTM A105 carbon steel, during which the elbow material was characterized as MSS SP75 grade carbon steel grade WPHY42.

The weldability of the materials was considered adequate since the equivalent carbon in both cases was within the permissible limits indicated in the specification of the materials.

The source of the damage was an incorrect application of the welding process.

Acknowledgements The authors would like to acknowledge the National Polytechnic Institute (IPN), the National Council of Science and Technology (CONACYT) and the Analysis Integrity of Pipelines Group (GAID-IPN) for the support to carry out this research.

Reference

1. ASTM E 2332-04 Standard Practice for Investigation and Analysis of Physical Component Failures.

Effect of Electromagnetic Field on the Microstructure and Mechanical Properties of the Dissimilar 2205/316L Welded Joint

S. L. Hernández-Trujillo, V. H. López-Morelos, R. García-Hernández, M. A. García-Rentería, A. Ruiz-Marines and J. A. Verduzco-Martínez

Introduction

Welding of dissimilar stainless steels has been increasingly considered in many applications in the petrochemical, pulp and paper, chemical and oil industries as well as in power and desalination plants due to several benefits including reduction of material costs and improvements in design and components [1–3]. The practice of welding dissimilar materials represents a major challenge owing to the differences in physical, mechanical and metallurgical properties and the use of a filler that may does not match the chemical composition of any of the parent plates. Thus, a deeper understanding of the behavior of dissimilar welded joints is needed and assessment of their performance is being carried out to establish the relative benefits of welding two different stainless steels based on cost, weight, mechanical properties and corrosion resistance to fulfill safety and structural requirements. Proper selection of the filler metal is an important aspect to evaluate in the design of a dissimilar weld for a satisfactory performance in service [4].

On their own, ASS and DSS are widely used in many engineering applications. These steels present excellent combination of corrosion resistance, ductility, toughness and mechanical strength. Weldability studies of DSSs and ASSs have been extensively carried out, but only a few studies have been reported on dissimilar welds between these alloys [2–4]. ASS grade 316L is one of the most popular stainless steels due to its excellent weldability and reduced susceptibility to

S. L. Hernández-Trujillo (✉) · V. H. López-Morelos · R. García-Hernández · A. Ruiz-Marines · J. A. Verduzco-Martínez
Instituto de Investigación en Metalurgia y Materiales, Universidad Michoacana de San Nicolás de Hidalgo, Edificio "U", Ciudad Universitaria, Morelia, Michoacán, Mexico
e-mail: saullht@yahoo.com.mx

M. A. García-Rentería
Facultad de Metalurgia, Universidad Autónoma de Coahuila, Carretera 57 Km 5, Los Bosques, 25710 Monclova, Coah, Mexico

R. R. Ambriz et al. (eds.), *Proceedings of the 17th International Conference on New Trends in Fatigue and Fracture*, https://doi.org/10.1007/978-3-319-70365-7_28

localized corrosion in virtue of its metallurgical design with low carbon content and significant amounts of Cr, Ni and Mo [5]. The 316L has a small thermal conductivity and a large coefficient of thermal expansion and it is prone to produce residual stress and deformation upon welding [6]. DSSs are compositionally formulated and thermomechanically processed to provide a two-phase microstructure with nearly equal proportions of ferrite and austenite. The outstanding properties of these alloys strongly depend on their phase balance. Welding of DSS yields a HAZ with a microstructure very different to the base metal due to elevated temperatures reached in this zone. Heating up of the alloy leads to a fully ferritic region with grain growth and precipitation of austenite during cooling. However, the time for the regeneration of austenite is not sufficient to restore the initial phase balance and the HAZ is prone to corrosion as the fillers for welding DSS are designed to enhanced formation of austenite during cooling [7]. Recent studies have shown some benefits when welding 304 ASS and 2205 DDS with the simultaneous application of an external magnetic field [8–11]. In principle, this practice induces an electromagnetic stirring (EMS) of the weld pool and affects the solidification mode. In the solid state, it generates vibration of the crystal structure and alters diffusion processes in short distances so that sensitization in the HAZ may be avoided [12]. This study is addressed to evaluate the effects on the microstructure and mechanical properties of the application of an external axial electromagnetic field of low intensity during welding plates of 2205 DSS and 316L ASS.

Materials and Experimental Methods

The plates employed in this study were 150 mm × 70 mm × 6.35 mm of 2205 DSS (UNS 31803) and 316L ASS (UNS S31603). Table 1 lists the chemical composition of the base materials along with the filler wire used for welding. The plates were machined to a single V-groove butt joint configuration (30° bevel, 1.5 mm root face and 2.5 mm root gap). Gas metal arc welding (GMAW) was performed in a sole pass with reverse polarity and a heat input of 1.2 kJ/mm (75% efficiency). An ER-2209 filler wire, 1.2 mm in diameter, fed at 160 mm/s was used along with the mixture 95% Ar + 3% N_2 + 2% O_2 as shielding gas flowing at 19 L/min. Welding was performed normal to the rolling direction of the plates at 3.6 mm/s with a stick out of 10 mm. The experimental setup for welding with the application of an external axial magnetic field is shown elsewhere [9, 10]. Briefly, it consists of a coil placed around the joint fed with an external power supply to

Table 1 Chemical composition of the base materials and filler wire employed (wt%)

Material	C	Mn	P	S	Si	Cr	Ni	Mo	N	Cu	Fe
2205	0.01	1.81	0.03	0	0.54	22.5	5.7	3.1	0.16	0.21	Bal.
316L	0.02	1.15	0.03	0	0.54	16.69	10.03	2.02	0.05	0.46	Bal.
ER-2209	0.012	1.75	0.02	0.01	0.5	23	8.8	3.2	0.14	0.1	Bal.

induce a magnetic field of 3 mT. This magnetic field interacts with the magnetic field inherent to the welding process and both generate an electromagnetic interaction of low intensity (EMILI).

The microstructural features were characterized in the optical microscope by preparing metallographic samples with standard procedures and chemical etching with Glyceregia reagent (15 cc HCl +10 cc Glycerol + 5 cc HNO_3). Vickers microhardness profiles were generated applying a load of 100 g during 15 s across transverse sections of the welds at the mid height of the welds. Three microhardness scannings were performed in each weld with a separation of 200 μm between line and punctual measurements. Dog bone shape specimens were machined from the base materials and welded joints to perform tensile testing with a cross head speed of 0.016 mm/s.

Results and Discussion

Figure 1 shows the characteristic microstructure in the rolling direction of the base materials in the as-received condition. The microstructure of the 2205 DSS, Fig. 1a, consists of elongated grains of austenite and δ-ferrite with an approximate fraction of 55 and 45%, respectively, approaching the ideal 50/50 ratio for the optimum mechanical and corrosion behavior. The 316L presents equiaxed grains of austenite, as seen in Fig. 1b, with a grain size of 15.11 ± 5.73 μm. It is also observed bands of residual δ-ferrite oriented in the rolling direction. The presence of this phase is due to segregation of chromium that promotes its precipitation during solidification and thermomechanical secondary processing [7].

The geometry of the welded joints is shown in the images of Fig. 2. Fully penetrated welds with no observable macro defects were obtained for both welding conditions. Chemical etching disclosed the profile of the weld bead and the HTHAZ of the 2205 DSS. The straight lines depict the initial configuration of the joint. Area measurements revealed that the size of the HTAZ of the 2205 DSS reduced from 6.77 to 4.04 mm^2 for the welds without and with magnetic field, respectively.

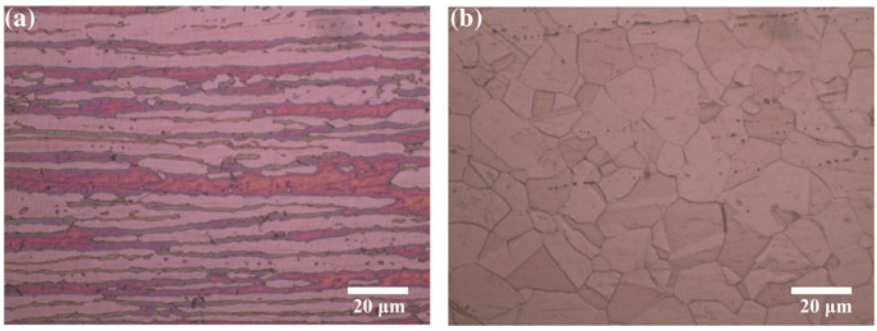

Fig. 1 Microstructure of the as-received base materials; **a** 2205 DSS and **b** 316L ASS

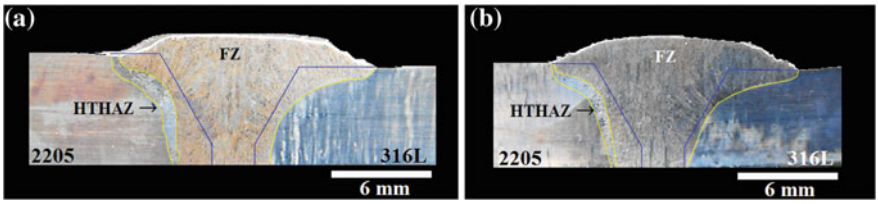

Fig. 2 Macrographs of the transverse views of the welded joints; **a** 0mT and **b** 3mT

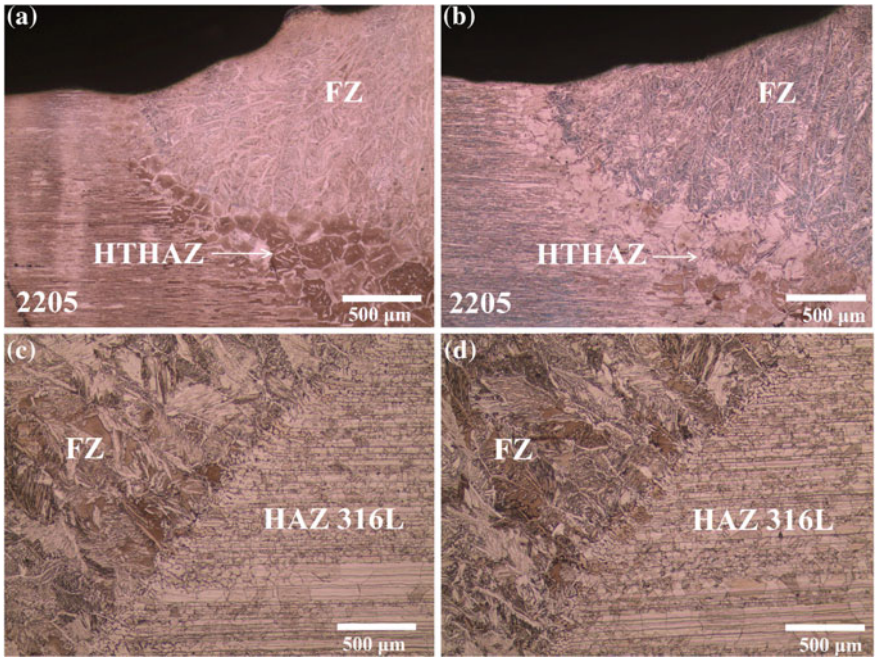

Fig. 3 Optical micrographs of the microstructure at the fusion line of the welds; **a–b** 2205 DSS and **c–d** 316L. Left 0 mT and right 3 mT

This effect is related to the EMS induced during welding [10, 13]. It promotes detachment of partially molten base material with its subsequent incorporation into the weld pool.

Figure 3 shows some details of the microstructure of the welds at the fusion line of every side of the welds. Figure 3a, b compare the side of the 2205 DSS without and with magnetic field, respectively. The microstructure in the HTHAZ for both welds is the typical one characterized by a ferritized region with austenite precipitating mainly in the limits of the coarse grains of ferrite. Measurement of the ferritic grain size, in equivalent locations in the HTHAZ, indicated a reduction of 10 µm in the average grain size and a reduction in the range size when using magnetic field.

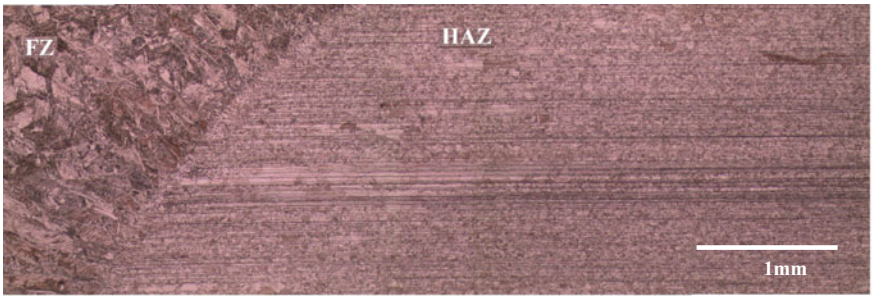

Fig. 4 Microstructural transitions of the weld at the side of the 316L ASS

A complex phenomenon involving magnetization and diffusion of substitutional elements may restrict coarsening of the ferritic matrix [14, 15]. In the fusion zone, the weld metal solidifies from the partially molten coarse ferritic grains of the HTHAZ growing toward the thermal gradient within the weld pool. The content of austenite in the weld metal is abundant owing to the high content of gammagenous elements in the metallurgical design of the filler wire. On the counter side, Figs. 3c, d compare the microstructure at the weld metal/316L ASS interface without and with magnetic field, respectively. This side of the welds is composed by a coarser microstructure in the fusion zone (as compared to the side of the 2205 DSS), a thin band of partially molten grains and the HAZ characterized by irregular grain growth. The bands of ferrite are clearly seen in the austenitic matrix. Figure 4 shows that grain growth in the HAZ occurred mostly at the mid height of the 316L plates where the concentration of stresses and ferrite caused by rolling of the plates is larger. In this zone, the size of the grains increased to an average value of 75 ± 29 μm. The presence of these large grains delimited the width of the HAZ up to 3 mm. Physical properties may revert to the previous state before cold-working caused by the welding thermal cycle. Such restoration results from two different processes that occur at elevated temperatures: recovery and recrystallization, may be followed by grain growth [16].

The variations in microhardness along the transverse section of the welds is shown in Fig. 5. In the side of the 2205 DSS, the results indicate that depending on the distance, the values are kept approximately constant at 258 ± 10 HV_{100}, lightly increasing in the HTHAZ to 272 ± 2 HV_{100} (closely to the as-received 2205 DSS). In the fusion zone, the values exhibited a slight decrease to 248 ± 7. Hardness of DSS is determined mainly by three factors; (i) nitrogen in solid solution in austenite. The content of 3% N_2 in the shielding gas compensates for the nitrogen loss during welding. (ii) The precipitation of hard secondary phases such as the nitrides, carbides and sigma phase may significantly increase hardness of DSS. (iii) The content of ferrite and its grain size. Ferrite is considered a strengthening phase in DSS and it is hardened by solution of alloying elements such as Cr and Mo, increasing the probability of precipitation of detrimental phases.

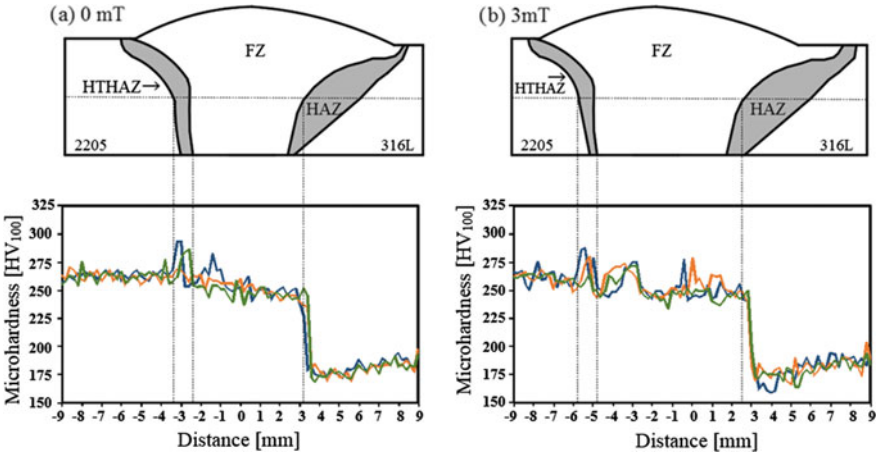

Fig. 5 Microhardness profiles along the different zones of the welds; **a** 0 mT and **b** 3 mT

The HTHAZ of 2205 DSS exhibited the highest microhardness values may be due to a combination of the following factors: (a) ferrite grains supersaturated with Cr and Mo and an increased ferrite content; (b) precipitation of hard Cr_2N; and (c) more nitrogen in solid solution in the primary austenite and the precipitation of Widmanstätten and acicular austenite [17]. The HAZ of the 316L ASS decreased its microhardness 18.5% (174 ± 8) as compared to the alloy in the as-received condition (215 ± 8).

Typical stress versus strain curves of the tensile test of the as-received base materials and welded joints are plotted in Fig. 6. The results of these tests are listed in Table 2. As expected, a higher mechanical strength is shown by the 2205 DSS whereas the 316L ASS exhibits significantly larger toughness. The welded joints essentially presented the same behavior independently of the welding condition with failure consistently occurring far away from the weld bead and beyond the HAZ. The mechanical strength of the dissimilar welds was slightly above the value of the 316L ASS with an elongation close to the 2205 DSS. These results mean that sound metallurgical dissimilar welds were obtained and an evaluation in corrosion properties is needed to further assess the effect of the application of the magnetic field during welding.

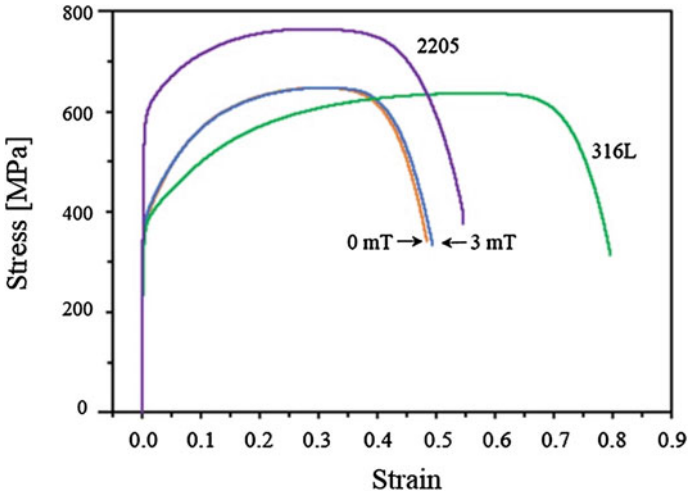

Fig. 6 Stress versus strain curves of the tensile specimens of the as-received base materials and welded joints

Table 2 Mechanical properties of base materials in the as-received condition and welded joints

Material	Yield stress (MPa)	Tensile strength (MPa)	Elongation %	HV_{100}
2205 DSS	558 ± 6.4	765 ± 1.5	55 ± 2	272 ± 9
316L ASS	344 ± 9.6	635 ± 9	81 ± 2.6	215 ± 8
Weld, 0 mT	358 ± 4	643 ± 5	50.7 ± 2	–
Weld, 3 mT	368 ± 15	644 ± 2	48.4 ± 2	–

Conclusion

Sound dissimilar 2205 DSS/316L ASS welded joints were obtained by the GMAW process with and without the application of an external axial magnetic field. In terms of microstructure, the use of the magnetic field during welding reduced the size of the HTHAZ of the DSS. The hardest region of the welded joints was the HTHAZ of the DSS irrespective of the welding condition. The thermal affection in the 316L ASS resulted in a moderate reduction in hardness and irregular grain growth at the mid height of the plates. Despite this effect, failure of the welds consistently occurred in the 316L ASS beyond the softened zone with a strength slightly above that of the base material in the as-received condition.

References

1. Mortezaie, A. and M. Shamanian, *An assessment of microstructure, mechanical properties and corrosion resistance of dissimilar welds between Inconel 718 and 310S austenitic stainless steel.* International Journal of Pressure Vessels and Piping, 2014. **116**(0): p. 37–46.
2. Verma, J., et al., *Microstructure, Mechanical and Intergranular Corrosion Behavior of Dissimilar DSS 2205 and ASS 316L Shielded Metal Arc Welds.* Transactions of the Indian Institute of Metals, 2017. **70**(1): p. 225–237.
3. Ibrahim, O.H., I.S. Ibrahim, and T.A.F. Khalifa, *Effect of Aging on the Toughness of Austenitic and Duplex Stainless Steel Weldments.* Journal of Materials Science & Technology, 2010. **26**(9): p. 810–816.
4. Moteshakker, A. and I. Danaee, *Microstructure and Corrosion Resistance of Dissimilar Weld-Joints between Duplex Stainless Steel 2205 and Austenitic Stainless Steel 316L.* Journal of Materials Science & Technology, 2016. **32**(3): p. 282–290.
5. Kianersi, D., A. Mostafaei, and A.A. Amadeh, *Resistance spot welding joints of AISI 316L austenitic stainless steel sheets: Phase transformations, mechanical properties and microstructure characterizations.* Materials & Design, 2014. **61**: p. 251–263.
6. Li, L.C., et al. *Effect of welding heat input on grain size and microstructure of 316L stainless steel welded Joint*. in *Applied mechanics and Materials*. 2013. Trans Tech Publ.
7. Lippold, J.C. and D.J. Kotecki, *Welding Metallurgy and Weldability af Stainless Steels*. 2011: Wiley India Pvt. Limited.
8. Curiel, F.F., et al., *Effect of magnetic field applied during gas metal arc welding on the resistance to localised corrosion of the heat affected zone in AISI 304 stainless steel.* Corrosion Science, 2011. **53**(7): p. 2393–2399.
9. García Rentería, M.A., et al., *Effect on the microstructure and mechanical properties of the electromagnetic stirring during GMA welding of 2205 DSS plates.* Materials Science Forum, 2013. **755**: p. 61–68.
10. García-Rentería, M., et al., *Improvement of localised corrosion resistance of AISI 2205 Duplex Stainless Steel joints made by gas metal arc welding under electromagnetic interaction of low intensity.* Applied Surface Science, 2014. **321**: p. 252–260.
11. García-Rentería, M., et al., *Effect of electromagnetic interaction during fusion welding of AISI 2205 duplex stainless steel on the corrosion resistance.* Applied Surface Science, 2017. **396**: p. 1187–1200.
12. Curiel, F.F., et al., *Transmission electron microscopy in the heat affected zone of an AISI 304 austenitic stainless steel welded with the application of a magnetic field of low intensity.* Materials Transactions, 2013. **54**(1): p. 122–125.
13. Villafuerte, J. and H. Kerr, *Electromagnetic Stirring and Grain-Refinement in Stainless-Steel GTA Welds.* Welding journal, 1990. **69**(1): p. S1-S13.
14. Liu, X.J., et al., *Effect of external magnetic field on thermodynamic properties and phase transitions in Fe-based alloys.* Journal of Alloys and Compounds, 2008. **459**(1–2): p. 169–173.
15. Liu, X.J., et al., *Effects of external magnetic field on the diffusion coefficient and kinetics of phase transformation in pure Fe and Fe–C alloys.* Calphad, 2011. **35**(1): p. 66–71.
16. Callister, W., *Materials Science and Engineering: An Introduction.*
17. Zhang, Z., et al., *Effects of nitrogen in shielding gas on microstructure evolution and localized corrosion behavior of duplex stainless steel welding joint.* Applied Surface Science, 2017. **404**: p. 110–128.

Heat Input Effect on the Mechanical Properties of Inconel 718 Gas Tungsten Arc Welds

N. K. Rodríguez, E. R. Barragán, I. V. Lijanova, R. Cortés, R. R. Ambriz, C. Méndez and D. Jaramillo

Introduction

Inconel™ 718 is a precipitation hardened Nickel based alloy, which is widely used in gas turbines and aerospace engines due to its excellent mechanical properties from cryogenic to elevated temperatures (−253 and 700 °C) [1, 2]. Elements such as Nb is added to form the γ'' metastable phase (Ni_3Nb) whereas Ti and Al are added to precipitate in the form of γ' intermetallic phase. Other phases found in Inconel 718 include carbides like Nb(Ta)C, TiC and M_6C, TiN, Laves and sigma. The Nb(Ta)C, TiC and TiN phases tend to increase the corrosion resistance, as well as the high temperature resistance. Laves and sigma phases are brittle intermetallic, which decrease the mechanical properties [3].

As a consequence of the corrosive environment and high temperatures that the alloy is exposed, the mechanical behavior of the components tend to present some problems related with cracking or wear. To repair damaged components, it is possible to use welding processes such as gas tungsten arc welding (GTAW) [4, 5]. Nevertheless, after welding process some metallurgical problems related with the fusion zone (FZ) and heat affected zone (HAZ) could be presented. Cracking solidification and undesirable secondary phase formation are the most important weldability problems in the FZ, as well as in the HAZ [6, 7].

N. K. Rodríguez (✉) · E. R. Barragán · I. V. Lijanova · R. Cortés · R. R. Ambriz
C. Méndez · D. Jaramillo
Instituto Politécnico Nacional CIITEC-IPN, Cerrada de Cecati
S/N Col. Sta. Catarina, Azcapotzalco, 02250 Ciudad de México, Mexico
e-mail: karr2502@yahoo.com.mx

R. Cortés
Instituto de Investigación en Metalurgia y Materiales,
Universidad Michoacana de San Nicolás de Hidalgo,
A.P. 888, 58000 Morelia Michoacán, Mexico

R. R. Ambriz et al. (eds.), *Proceedings of the 17th International Conference on New Trends in Fatigue and Fracture*, https://doi.org/10.1007/978-3-319-70365-7_29

This work reports some results in terms of mechanical behavior in Inconel 718 joints welded by GTAW. The heat input effect produced by two welding conditions was analyzed in terms of microstructure, tensile, microhardness and instrumented impact Charpy results.

Experimental Methodology

An Inconel™ 718 plate was used. It was supplied in annealed condition with the following mechanical properties: Vickers hardness number of 236.4 ± 5.1, yield strength of 537 MPa, tensile stress of 850 MPa and elongation of 47.5%. Metallographic samples of base material of 25 × 7× 6.35 mm were obtained by using conventional metallographic techniques. The microstructure was revealed by immersion of the samples in 15 ml HCl, 10 mm CH_3C_2H and 10 ml HNO_3 reagent.

Optical microscopy was used to analyze the microstructure of the base material, as well as the different zones of the welded joints. Plates of 115 × 75 × 6.35 mm of base material were machined to obtain a single V-groove preparation with an angle of 60°. Later, the plates were fixed by mechanical press to form a butt joint with 2 mm in separation. Before welding, the plates were hardened by precipitation (solubilization at 1065 °C for 1 h, aged at 720 °C for 8 h, and finally furnace cooling). This treatment provided a Vickers hardness number of 408.5 ± 3.2, yield strength of 809 MPa, tensile stress of 1080 MPa and elongation of 38.5%.

A semiautomatic gas tungsten arc welding (GTAW) process was used to weld Inconel™ 718 plates. An ER NiFeCr-2 with 1.1 mm in diameter was fed automatically (at 170 mm s^{-1}) by a gas metal arc welding (GMAW) torch. A mixture of H_2 (2%), CO_2 (0.12%), He (30%) and Ar (67.88%) was used as shielding gas at a flow rate of 14.15 L s^{-1}. Alternating current (tungsten-thorium electrode) was used. Two different heat input welding conditions were used with the parameters shown in Table 1.

After welding, optical and scanning electron microscopes were used to analyze the microstructure. Additionally, energy-dispersive X-ray spectroscopy (EDS) was used to determine the chemical composition of the matrix and some secondary phases. The samples were obtained from the transverse direction of the welding bead.

Table 1 Operative parameters used in welding joints

Condition	C1	C2
Feed speed, mm s^{-1}	169	122
Current	AC	AC
Gas flow, L s^{-1}	14.15	14.15
Voltage (V), V	29	29
Intensity (I), A	356	356
Travel speed (v), mm s^{-1}	4	8
Thermal efficiency (η)	0.7	0.7
Heat input (q), J mm^{-1}	1806.7	903.3

Mechanical properties of welds were determined by microhardness measurements and tensile test according with the ASTM E8M-04 [8].

Results and Discussion

Microstructure

Figure 1 shows the base material microstructure in annealed and aged condition. An austenitic matrix γ in both conditions was observed characterized by equiaxed grains. In Fig. 1a (annealed condition), the presence of twinning can be appreciated and secondary phases in form of dispersed precipitates. Figure 1b shows that the number of twinning after heat treatment decrease because of the hardening heat treatment (dispersed phases in the γ matrix are observed).

Figure 2 shows the elemental concentration obtained from the EDS element mapping of base material. It is possible to observe the γ matrix with contents in Cr, and secondary phases in form of dispersed precipitates showing precipitates MC (M could be Ti and Nb), M_6C (M could be Fe, Cr, Mo, W and Nb) due to Mo segregation with Nb during solidification. Laves precipitates could be present because they have the same composition as MC and M6C precipitates.

Welding profiles for both welding conditions is shown in Fig. 3. From this figure, it is possible to observe the fusion zone (FZ), the heat affected zone (HAZ) and the base material.

Figure 4 shows the microstructures for the welding condition C1. A traditional competitive columnar dendritic microstructure produced by the solidification during welding (Fig. 4a) was observed. Also, partially melted grains with an epitaxial growth in the interface of the FZ and HAZ (Fig. 4b) was detected. In the case of the C1 condition with PWHT the optical microstructure obtained does not present an important difference with respect to the as-welded condition (C1). For this reason only the C1 without PWHT condition is shown. However, it is well known that precipitation process due to the PWHT increases the hardness as is possible to observe in the microhardness profiles (Fig. 7).

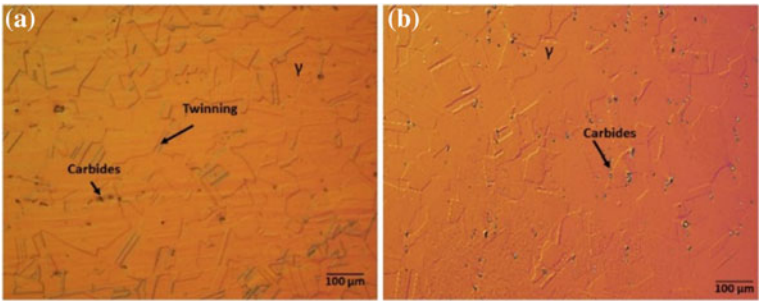

Fig. 1 Inconel 718 microstructure, **a** annealed condition, and **b** aged condition

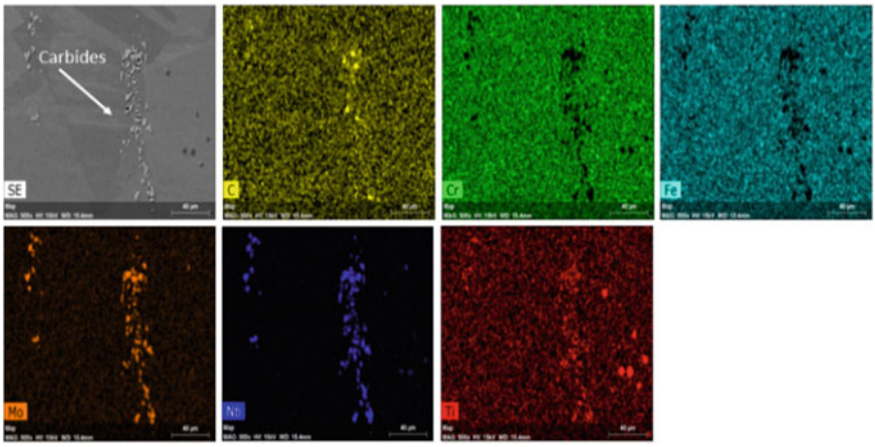

Fig. 2 Elemental concentration of IN718 base material in aged condition **a** SE, **b** C, **c** Cr, **d** Fe, **e** Mo, **f** Nb, and **g** Ti

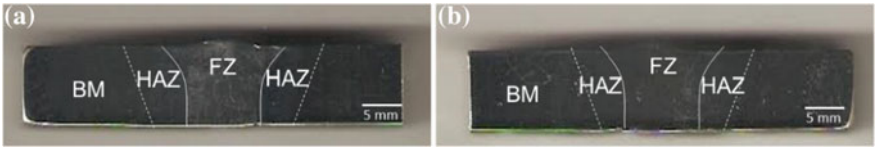

Fig. 3 Gas tungsten arc welding profiles for an Inconel™ 718 alloy, **a** C1 (only one pass of welding), and **b** C2 (three welding passes)

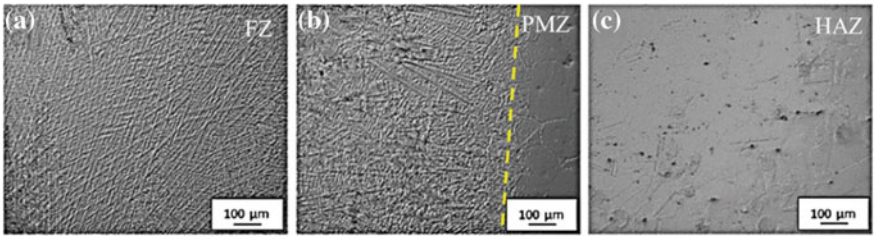

Fig. 4 Microstructures of Inconel 718 welds obtained for the application of only one welding pass (C1 condition)

The microstructure for the C2 condition is shown in Fig. 5. A grain size improvement in the FZ can be appreciated (Fig. 5a) in comparison with the C1 condition. A dendritic equiaxed microstructure was observed with an absence of carbides formation. Figure 5b shows the partially melted zone with an epitaxial columnar solidification from partially melted grains of base material. In HAZ

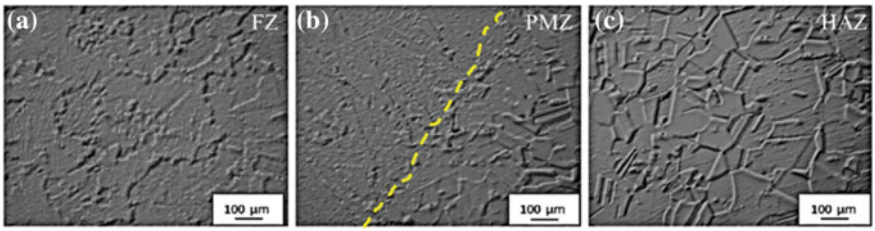

Fig. 5 Microstructures of Inconel™ 718 welds obtained for the application of three welding passes (C2 condition)

(Fig. 5c) a lower amount of secondary phases can be observed due to the solubilization effect by the application of multiple welding beads.

Hardness and Tensile Test

The microhardness distribution of the Inconel™ 718 welded joints is presented in Figs. 6 and 7. It has been observed different zones of hardness due to the heat input produced by the welding process.

For both conditions (C1 and C2) in as welded condition (Figs. 6) a remarkable difference in hardness with respect to the base material in aged condition ($HV_{0.1} = 408.5 \pm 3.2$) for the FZ ($HV_{0.1} \sim 250$) and HAZ ($HV_{0.1} \sim 220$) was observed. In the case of the HAZ this hardness values are produced by the microstructural transformation of γ'' and γ' precipitates. Whereas for the FZ in as-welded condition, the ageing hardening is not present, instead the only hardening mechanism was provided by solid solution and grain size refinement generated by the solidification process.

On the other hand, it is possible to identify that hardness increased after the PWHT (Fig. 6b, d). In the case of the FZ, the hardness reached values between 400 and 450 $HV_{0.1}$, which was generated by the hard disperse and brittle phases such as γ'' and γ'. Even though a recovery was observed for the HAZ, the hardness was not similar than for the FZ or even the base material. This aspect, was more remarkable for the C1 welding condition (Fig. 6b), where the hardness increment was lower than for the C2 welding condition (Fig. 6d). This phenomenon can be referred to the NbC phase, which precipitate during the ageing process, as well as to the very limited Nb segregation in solid state. Thus, we can infer that the application of multipass welding beads in Inconel™ 718 welds tend to be less severe in terms of microstructural changes, and obviously it increases the mechanical behavior of the welded joints.

Conventional stress-strain curves for Inconel™ 718 base material and welded joints are presented in Fig. 7. A summary of the obtained tensile results is presented in Table 2.

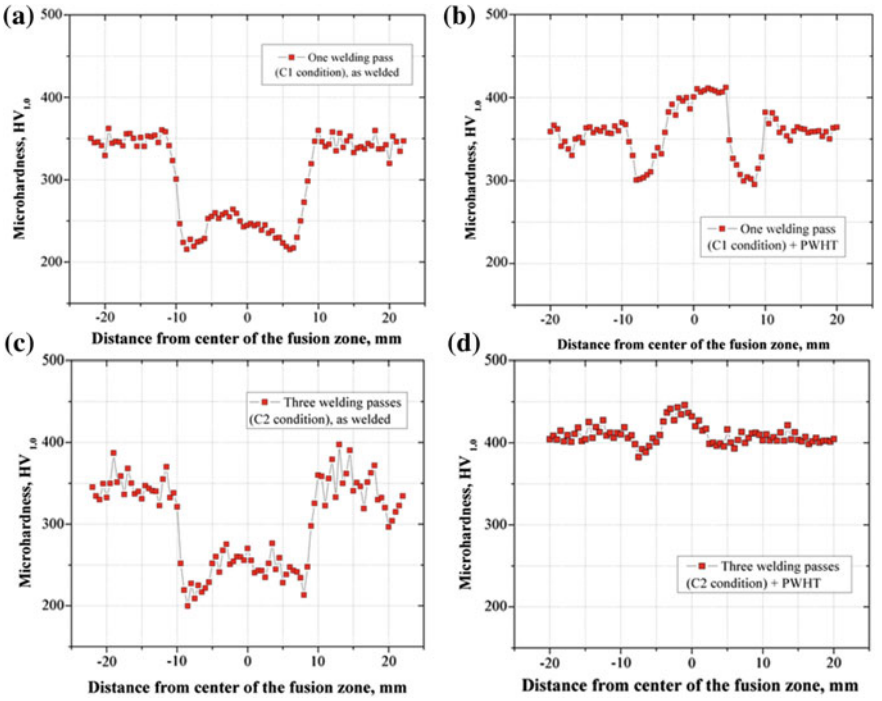

Fig. 6 Microhardness distribution of the Inconel 718 welded joints, **a** C1 condition (as-welded, one welding bead), **b** C1 condition after post weld heat treatment, **c** C2 (as welded, three welding beads), and **d** C2 after post weld heat treatment

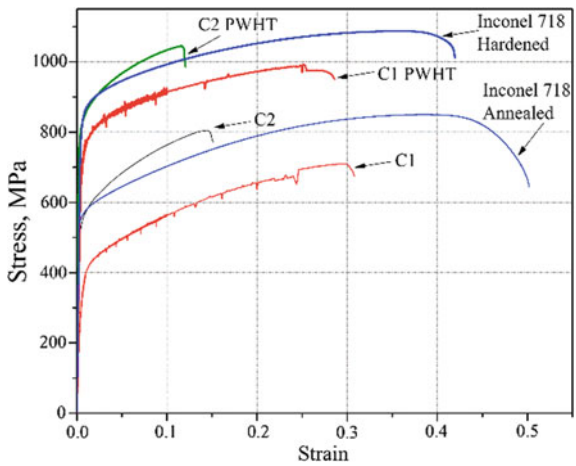

Fig. 7 Conventional stress-strain curves for Inconel™ 718 base material and welded joints

Table 2 Tensile test results

	Inconel™ 718 base material	Inconel™ 718 welded joints				
	Annealed	Hardened	C1	C1 PWHT	C2	C2 PWHT
σ_0, MPa	537	809	371	719	528	770
σ_{max}, MPa	850	1080	660	988	804	1044
Energy to fracture, MJ m^{-3}	372.3	430.2	147	246	106	115.8
Elongation, %	47.5	38.5	25.7	26.8	16.2	16
σ_0/σ_{max}	1.58	1.33	1.77	1.37	1.52	1.35

From Fig. 7 and Table 2 we can observe a tensile properties decrement in both welded joint conditions. For instance, the yield strength for the as welded joints in C1 and C2 conditions, decreased in more than 54 and 34% in comparison to the base material (annealed condition), respectively. Also, it is possible to observe that the PWHT increases the resistance of the joints. In this context, we can note that yield and tensile strength of the welded joints in C2 condition tend to be similar than the base material (aged condition), however, the joints performed with the C1 condition presented the lowest resistance, but a better ductility, i.e. the joints in C2 condition are more brittle than C1 condition.

Conclusions

The use of low heat input during welding (multiple welding beads) in Inconel™ 718 alloy increases the strength of the joints. According with the results obtained the use of only one welding bead precipitated fragile phases in the material as a result of heat input induced by the welding process. In contrast, a heat input reduction tends to avoid the carbides formation that prevent the precipitation of hardening phases in the base material that deteriorates the mechanical resistance of HAZ.

Acknowledgements The authors thank to CONACyT-Mexico and SIP-IPN for funding this research. Nadia Karina Rodríguez Rodríguez thanks CONACyT-Mexico for the scholarship provided.

References

1. M. Anderson, A.-L. Thielin, F. Bridier, P. Bocher and J. Savoie, “δ Phase precipitation in Inconel 718 and associated mechanical properties”, *Materials Science and Engineering A,* pp 48–55, 2016.
2. X. Ma, Z. Duan, H. Shi, R. Murai, E. Yanagisawa, “Fatigue and Fracture behavior of nickel-based superalloy Inconel 718 up to the very high cycle regime”, Journal of Zhejiang University-Science A (Applied Physics & Engineering), pp 727–737, 2010.
3. K. Devendranath, R. Jagat, V. Santhosh, “Effect of filler wires and direct ageing on the microstructure and mechanical properties in the multi-pass welding of Inconel 718”, Journal of Manufacturing Processes, pp 23–45, 2015.
4. J. C. L. John N. DuPont, Sammuel D. Kiser, *Welding metallurgy and weldability of nickel-base alloys*: John Wiley & Sons, Inc., 2009.
5. S. Kou, *Welding Metallurgy*: John Wiley & Sons, 2003.
6. R. Cortés, E.R. Barragán, V.H. López, R.R. Ambriz, D. Jaramillo, Mechanical properties of inconel 718 welds performed by gas tungsten arc welding, The International Journal of Advanced Manufacturing Technology, 2017.
7. E. Barragan, “Comportamiento Mecanico y Evaluacion Estructural en soldaduras GTAW de Inconel 718”, Tesis Maestria CIITEC IPN, 2017.
8. ASTM (2004) Standard Test Methods for Tension Testing of Metallic Materials [Metric]. vol ASTM E8M-04.

A Case Study of Corrosion Fatigue in Aluminium Casing Bolt Holes

Siew Fong Choy

Background

An aluminium alloy (A2618) casing belonging to a large civil engine was sent to the laboratory for investigation after cracks were found around 56 of the 58 bolt holes in the casing during an overhaul service visit. These bolt holes were responsible for securing steel outlet guide vanes (OGV) to the casing. Thirty previous instances of cracking around the bolt holes have been reported but the number affected in this instance was the highest.

Visual Examination

The casing was returned in the dirty condition (Fig. 1). Square regions of epoxy paint around the affected bolt holes on the inner surface of the casing had been removed, presumably for localized fluorescent penetrant inspection (FPI). Visual examination found cracks around 56 of the bolt holes, with most of the cracks parabolic-shaped and concentrated on the 11 o'clock and 1 o'clock positions of the bolt hole inner face; 12 o'clock being the forward direction.

Close examination revealed contact witness marks (with the OGV outboard surfaces) for the majority of the bolt holes. The completeness of these witness marks varied from bolt hole to bolt hole, possibly a result of the manual grinding process performed to remove the epoxy paint coating prior to FPI. Within and in the periphery of these contact witness markings, black scale and fibrils of suspected

S. F. Choy (✉)
Applied Technology Group, Materials Services Laboratory,
Rolls-Royce Singapore Pte Ltd., 1 Seletar Aerospace Crescent, 797565
Singapore, Singapore
e-mail: siewfong.choy@rolls-royce.com

R. R. Ambriz et al. (eds.), *Proceedings of the 17th International Conference on New Trends in Fatigue and Fracture*, https://doi.org/10.1007/978-3-319-70365-7_30

Fig. 1 Overview (left) and close-up (right) showing contact witness mark and fretting around the vane bolt holes. The typical parabolic shape of the cracks was also shown

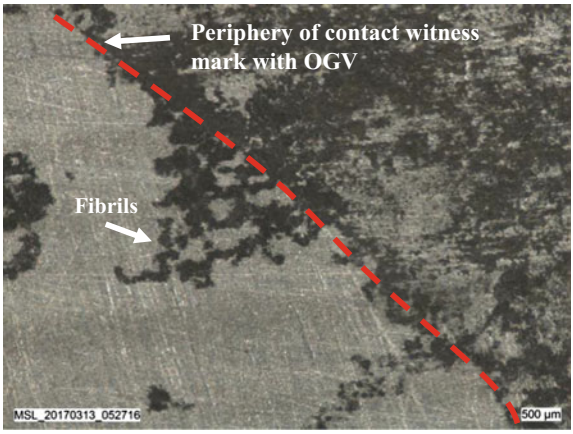

Fig. 2 Corrosion fibrils observed around the contact witness mark around the cracked bolt holes

corrosion products were seen extending outwards (Fig. 2). Some of these fibrils followed the direction of surface machining marks but others did not. However, most of the cracks were located within the region of contact witness marks.

Fractography

The four longest cracks were identified using FPI and forced open for fractographic examination. Figures 3 and 4 shows the surface view and opened fracture surface of a typical crack. All fracture surfaces appeared dull, fairly rough and facetted, with multiple arrest bands and some radial marks pointing to multiple origins. It was noted that all cracks had initiated from the inner surface of the casing, and not from the bore of the bolt hole, even if the crack had breached the bolt hole.

SEM examination of forward growing crack around bolt hole #24 found a badly oxidized fracture surface, particularly at the crack origins (Fig. 5). A relatively flat, feathery fracture exhibiting multiple arrest banding was observed on the cleaner

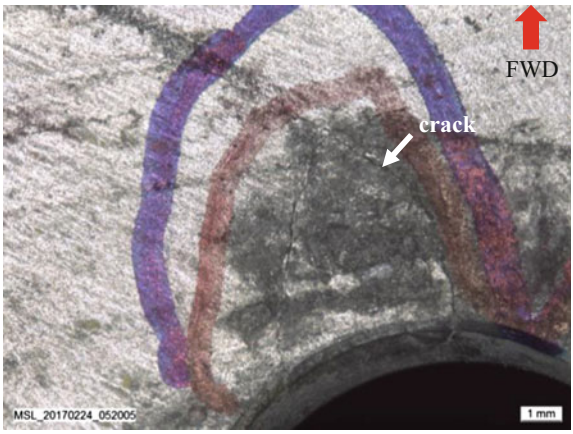

Fig. 3 Top view of crack on bolt hole #24

Fig. 4 Fracture surface of crack on bolt hole #24

parts of the fracture. Closer examination within the bands found no resolvable fatigue striations even though aluminium is known to striate easily [1]. Instead, irregularly spaced micro-bands suggestive of a high cycle fatigue mode of propagation were observed (Fig. 6). Alternate light and dark bands indicate possible passage through two or more alternating transient fatigue modes. However, due to a lack of comparative engine data, quantitative fracture analysis with regards to crack propagation life was not possible. On some cracks, localized patches of corrosion pitting were observed (Fig. 7).

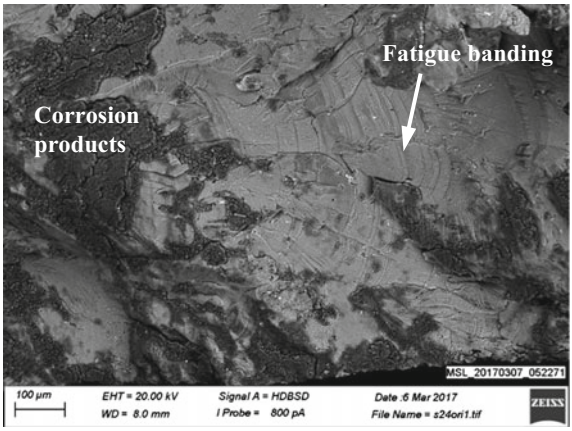

Fig. 5 Copious oxidation/ contamination observed on fracture surface (#24)

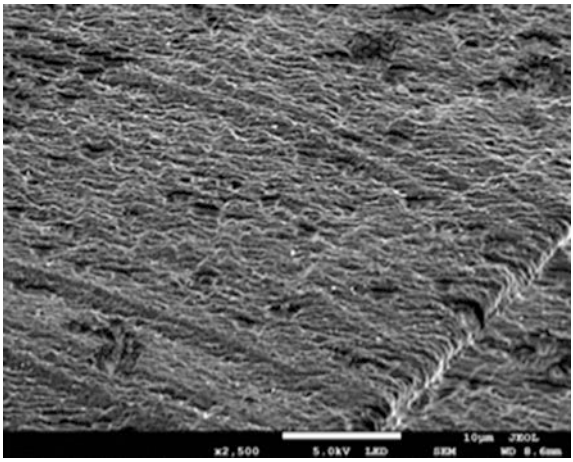

Fig. 6 Multiple micro-bands with alternate light and dark bands suggestive of HCF observed near crack front

Metallographic Examination and EDX Analysis

A micro-section of the crack in bolt hole #24 was hot mounted in Clarocit and polished through the origin for metallographic examination. Black corrosion pits with ~1.6 wt% of chlorine (via EDX) were observed propagating inwards from the fracture surface (Fig. 8) while no pitting was seen on the adjacent break-open surface. EDX elemental mapping revealed chlorine (Cl) and oxygen (O) only within the pits, which suggested chlorine was trapped within the oxide in a Cl-related corrosion process. Immersion etching with Kellers Reagent revealed elongated grains with copper-rich precipitates lined up in the long direction of the grains (Fig. 9).

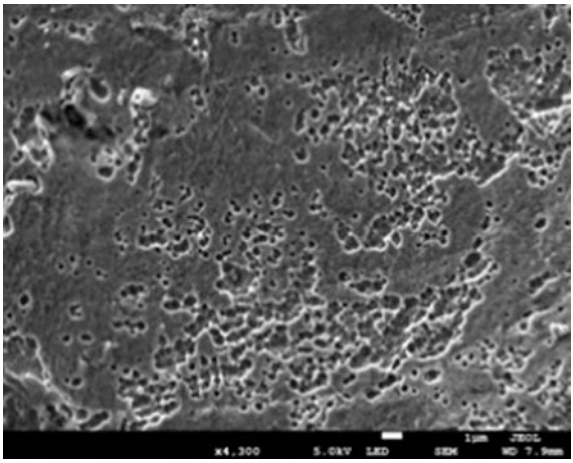

Fig. 7 Localized regions of corrosion pitting observed on some parts of the fractures

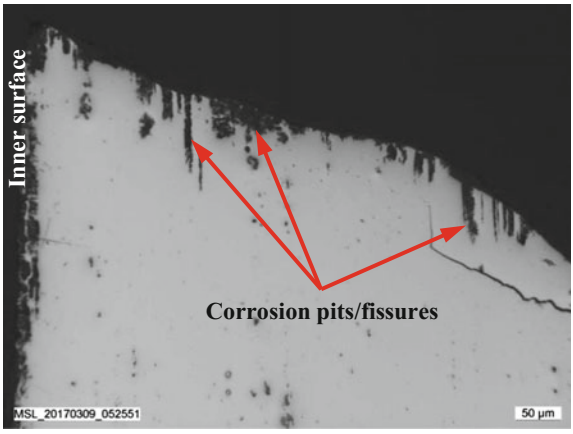

Fig. 8 Micro-section showing corrosion pits propagating inwards

Discussion and Conclusion

The location of the crack origins on inner surface of the bolt hole (rather than the bore) suggests that failure was not stress-related. Instead, corrosion [2, 3] appeared to have played a significant role in the cracking of the bolt holes examined. The presence of black corrosion scale/fibrils in the crack region, badly oxidized fractures as well as the corrosion pits/fissures observed were all indicative of corrosion. The level of chlorine (~ 1 wt%) and its presence only within the pits indicated that it was not a post-contaminant. Fractographically, the presence of multiple arrest bands and micro-banding observed suggest a HCF mode of propagation. It was considered likely that the cracks had initiated due to corrosion pitting [2], which reduced initiation life, and subsequently propagated via HCF.

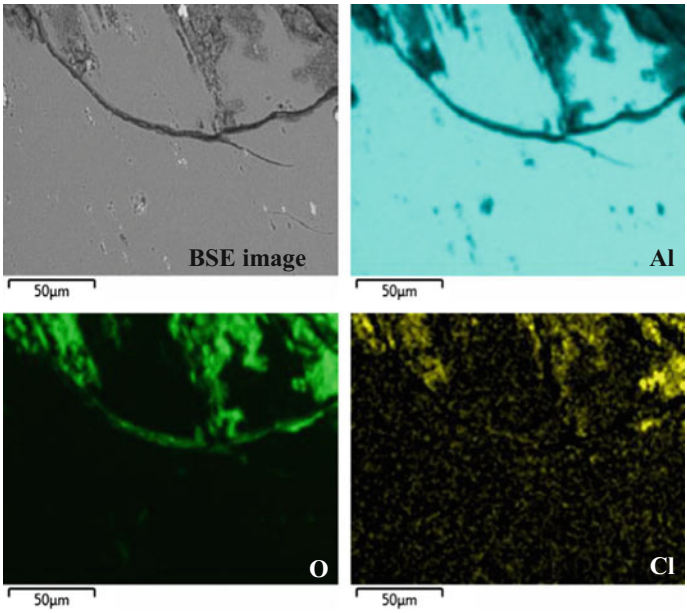

Fig. 9 Back-scattered electron image and EDX element maps of Al, O and Cl

Acknowledgements The author wishes to thank Mr. Tan Teck Siong of JEOL Asia Pte Ltd. for his support in FESEM usage during our equipment downtime and Edward A. Saunders of Rolls-Royce for his valuable inputs.

References

1. N.W. Sachs, Journal of Failure Analysis and Prevention, Vol. 5(2), April 2005, p 12.
2. Chen, G.S., Gao, M., Harlow, D.G. and Wei, R.P., *Corrosion and Corrosion Fatigue of Airframe Aluminium Alloys*, FAA/NASA International Symposium on Advanced Structural Integrity Methods for Airframe Durability and Damage Tolerance, NASA Conference Publication 3274, Langley Research Center, Hampton, VA (1994), 157–173.
3. Foley, R.T., *The Localised Corrosion of Aluminium Alloys – A Review*, CORROSION. 1986; 42(5): 277–288.

Study of the Modal Effect of 1045 Steel Pre-stressed Beams Subjected to Residual Stress

Erasto Vergara Hernández, Brenda Carolina Pérez Millán, Juan Manuel Sandoval Pineda and Luis Armando Flores Herrera

Introduction

The frequencies at which vibration naturally occurs, and the modal shapes, which the vibrating system assumes, are properties of the system, and can be determined analytically by using modal analysis. Analysis of vibration modes is a critical component of design structural elements, inherent vibration modes in structural components or mechanical support systems can reduced the life of the equipment, and cause premature or completely unanticipated failure. Detailed fatigue analysis is often required to assess the potential for failure or damage. Detailed modal analysis determines the fundamental vibration modes and their corresponding frequencies. Different fatigue-analysis approaches are available, i.e. vibration-fatigue analysis is one that is very suitable when the stress response occurs mainly as a consequence of structural dynamics [1–4].

Experimental Details

AISI 1045 steel beams were used; their square sections were of 12.5 mm (side) by 300 mm (length). In order to eliminate the previous stresses, the steel beams were heat treated at 660 °C for 60 min and cooled to room temperature (23 °C) inside of

E. V. Hernández (✉)
Instituto Politécnico Nacional, UPIIH, San Agustín Tlaxiaca, 42080 Hidalgo, Mexico
e-mail: erasto99@hotmail.com

B. C. Pérez Millán
Instituto Politécnico Nacional, UPIITA, 07738 Ciudad de México, Mexico

J. M. Sandoval Pineda · L. A. F. Herrera
Instituto Politécnico Nacional, ESIME-SEPI, U., 02250 Azcapotzalco, Mexico

R. R. Ambriz et al. (eds.), *Proceedings of the 17th International Conference on New Trends in Fatigue and Fracture*, https://doi.org/10.1007/978-3-319-70365-7_31

the furnace. To avoid any oxidation and decarburization, the beams were packed in stainless steel sheets.

To induce stresses into the treated beams, they were placed in a four-point flexural test bench and subjected to different loads up to 125 kN. Five different beams labelled B1, B2, B3, B4 and B5 were obtained. The B1 sample had no previous history or residual stresses. The specimens were pre-strained at 5600 με for B2 specimen, 9000 με for B3, 9,600 με for B4 and 16,000 με for B5. At one end of each beam, it was placed a Kistler 8632C accelerometer, and it was attached on the free end of the laminate using small portion of wax by firmly pressing it down.

Experimental Results and Discussion

The first three modes of vibration of each of the beams were studied by the finite element method and experimentally, in Table 1 the results obtained for B1 beam are observed.

The results by the finite element method and the experiments coincide with the vibration modes of a bar attached at one of its ends. Figure 1 shows the values of the first vibrational mode of the beams, while in Fig. 2, the second mode is shown and finally in Fig. 3 the third vibrational mode.

The vibration frequencies for the first mode of the beam, where the results obtained indicated a maximum change of 4 Hz between the frequencies of the sample free of residual stress with respect to the beams of 9600 and 9000 με, reduced for the other two specimens to a maximum of 2 Hz. These results show that

Table 1 Vibrational modes for B1 beam

Mode number	Numerical analysis	Experimental
	Frequency (Hz)	
1°	850	848
2°	1277	1276
3°	2618	2620

Fig. 1 First vibrational mode

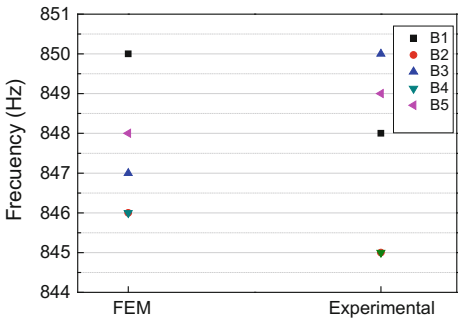

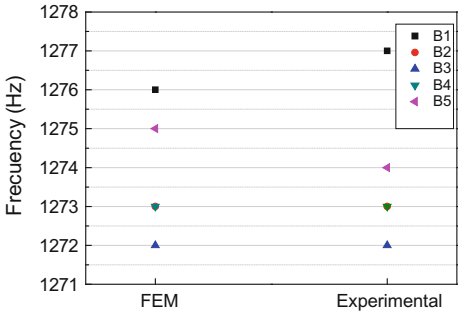

Fig. 2 Second vibrational mode

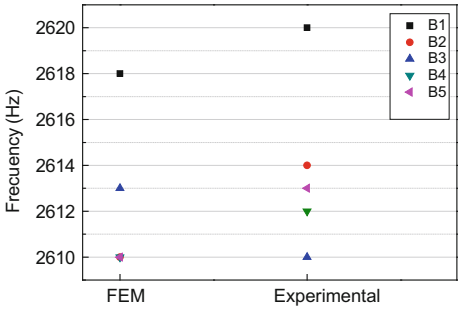

Fig. 3 Third vibrational mode

there is no change in the natural frequency of the beam in the first mode of vibration. In the second mode of vibration it is has been observed a better behavior between the two methods. In addition, there is only one change of 0.005 kHz between the frequency of a beam free of residual stresses and others with a field of induced residual stresses. Both methods are validated with respect to each other by their proximity. They does not change the frequency of vibration of the specimen with residual stresses and the specimen without previous history. Finally, by evaluating the frequency of the third mode of vibration, there is a maximum change of 8 Hz between the test beam free of residual stress and without previous history, which were subjected to a pre-strain of 5600, 9600 and 16,000 με.

Conclusions

The residual stresses present in the mechanical components play a very important role in the design, planning and manufacture of mechanical parts. They can play a positive or negative role in the applications where the importance of prior knowledge of them is used. The evaluation of the frequencies of the three main modes of vibration of a 1045 steel was carried out through an external excitation in the stable state, and with the aid of a system of acquisition and treatment of signals. The

values of these fundamental frequencies of vibration which can generally have negative effects on the mechanical components. The experimental results were compared with the finite element method (FEM), with errors less than 5% between values with both methods. The results show that the natural frequencies do not present a significant change when there are fields of residual stresses and predictions of different magnitude in the material. In addition there is a better behaviour of the value of the natural frequency as the residual stress field change.

References

1. Matjaž Mršnik, Janko Slavič, Miha Boltežar. Vibration fatigue using modal decomposition, Mechanical Systems and Signal Processing, Volume 98, 1 January 2018, Pages 548–556.
2. Habtour, W.S. Connon, M.F. Pohland, S.C. Stanton, M. Paulus, A. Dasgupta. Review of response and damage of linear and nonlinear systems under multiaxial vibration Shock Vib., 2014 (2014).
3. A. Nieslony, E. Macha. Spectral Method in Multiaxial Fatigue, Springer-Verlag, Berlin, Heidelberg (2007).
4. M. Mršnik, J. Slavič, M. Boltežar. Multiaxial vibration fatigue – a theoretical and experimental comparison, Mech. Syst. Sig. Process., 76–77 (2016), pp. 409–423.

Experimental Analysis of Fatigue Cracks Emanating from Corner Notches in the Presence of Variable Residual Stress Fields

J. L. Cuevas, C. Garcia, A. Amrouche, R. R. Ambriz and D. Jaramillo

Introduction

The study of fatigue of engineering materials has been motivated by the occurrence of catastrophic accidents over the history. For instance, the DeHavilland Comet [1], the Boeing 737 of Aloha's Airlines [2] and the F-15C fighter jet of the Missouri National Guard [3]. A fatigue crack growth process from local stress raisers was among the reasons for the occurrence of these accidents. The fatigue crack growth is an irreversible physical process produced by cyclic loading of engineering systems and components. The result of the fatigue crack growth is a reduction of the carrying load capacity for the engineering materials.

An undesirable consequence of traditional thermo-mechanical processes is a negative distribution of residual stresses within the manufactured pieces. The residual stresses are locked-in and at equilibrium within the engineering materials despite the absence of any type of external load or temperature gradient [4].

J. L. Cuevas
Edificio de Posgrado, Instituto Tecnológico de Pachuca,
Carretera México-Pachuca Km. 87.5, Col. Venta Prieta, 42080 Pachuca
Hidalgo, Mexico

C. Garcia (✉)
Facultad de Ingeniería, Universidad Autónoma de San Luis Potosí,
Av. Dr. Manuel Nava No. 8, Zona Universitaria, 78290
San Luis Potosí, S.L.P., Mexico
e-mail: christian.lopez@uaslp.mx

A. Amrouche
Laboratoire de Génie Civil et géo-Environnement LGCgE, EA 4515,
Faculté des Sciences Appliquées FSA Béthune, Université d'Artois, Arras, France

R. R. Ambriz · D. Jaramillo
Instituto Politécnico Nacional CIITEC-IPN, Cerrada de Cecati S/N, Col. Sta. Catarina,
02250 Azcapotzalco, Ciudad de México, Mexico

R. R. Ambriz et al. (eds.), *Proceedings of the 17th International Conference on New Trends in Fatigue and Fracture*, https://doi.org/10.1007/978-3-319-70365-7_32

The relevance of the residual stress fields is their ability to modify the mechanical behavior of the engineering materials. The residual stress fields modify the mean stress in a mechanical component subjected to a fatigue process, as well as the fatigue crack growth rate [5]. Tensile residual stress fields increase the fatigue crack growth rate, while a reduction of the fatigue crack growth rate is produced by compressive residual stress fields [6].

A combination of fracture mechanics theory and empirical data from fatigue crack growth tests is the traditional approach for the analysis of damaged components with the presence of a dominant crack. The effects of residual stresses have been included into this traditional approach by means of either a superposition assumption [7] or a crack closure effect [8]. Both approaches are based on an estimation of the stress intensity factor K. The superposition considers a total stress intensity factor that considers the applied external load and the residual stress field. The crack closure effect uses an effective stress intensity factor that considers the local stiffness of the cracked component. Several works in the literature had reported numerical models based on the superposition approach for the inclusion of residual stress effects into fatigue crack growth. Fewer results are reported for numerical models based on the crack closure effect. However, most of the models have considered a constant residual stress fields through the thickness of the mechanical component or specimen. The results of Beghini et al. [9, 10] showed that the superposition approach provide inadequate estimations of the fatigue crack growth rate in variable residual stress fields. Stuart [11] also used a superposition approach for variable residual stress fields. Stuart reported that for cracks emanating from corner notches, the crack shape evolution seemed to play a significant role for the estimation of the residual stress effects in the fatigue crack growth rate. Corner cracks are traditionally developed in the real structures, but the crack shape evolution is regularly not considered by the stress intensity factor computation. Instead, the crack front is regarded as a simple straight line. LaRue and Daniewicz [12] compared numerical models based on a superposition assumption and a crack closure effect, but they considered a straight line for the crack front. Both models showed adequate fatigue crack growth rate estimation, but the residual stresses were constant through the thickness of the specimen.

The present work presents the fatigue crack growth process from corner notches in an specimen with a variable distribution of residual stresses. The specimen was subjected to a cold worked operation prior to a fatigue crack growth test. The cold worked operation produced a variable residual stress distribution through the thickness of the specimen.

Materials and Methods

A 6061-T6 aluminum alloy plate of 6.35 mm (1/4 plg) thick was used for the fabrication of the specimen. Figure 1 presents the details of the specimen of 200 mm length, 100 mm width and 6.35 mm thick. The results from a tensile test

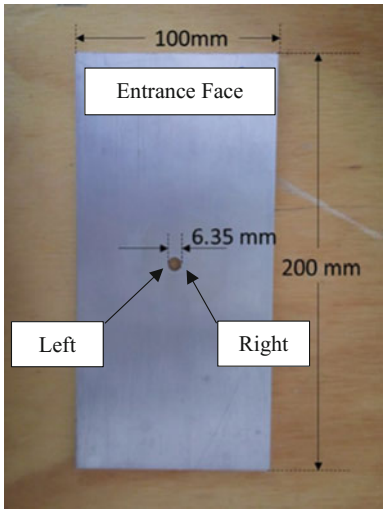

Fig. 1 Geometry details of the 6061-T6 Al alloy specimen. Entrance face is a reference for the cold worked operation. Left and right are a reference for the corner notches

of a dog-bone specimen of the 6061-T6 Al alloy plate indicated an elastic modulus of 70 GPa, a yield strength of 200 MPa and a tensile strength of 250 MPa. The Poisson's ratio for the 6061-T6 Al alloy is 0.3.

The specimen with a 6.35 mm diameter was subjected to a customized cold worked operation via a conical mandrel that was passed through the hole along the thickness of the specimen. The maximum diameter of the mandrel was 6.32 mm. The entrance face of the specimen as indicated in Fig. 1 corresponded to the specimen side touched by the mandrel first during the cold work operation. Meanwhile, the exit face designation corresponded to the opposite side of the specimen. Further details of the customized cold worked operation had been already reported in the literature [13]. Figure 2 presents the distribution of the residual stresses in the specimen determined via a finite element simulation and the hole drilling method [13].

Corner notches of approximately 1 mm depth were machined at the hole's edge with a jeweller saw cut after the cold worked operation. The left and right side of the hole were machined with the corner notches (Fig. 1) for the prevalence of a symmetry condition during the fatigue crack growth test. A servo-hydraulic fatigue testing machine was used for the fatigue crack growth test of the specimen. The maximum load capacity of the fatigue testing machine was of 100 kN. Both sides of the specimen were hydraulically clamped by the machine grips with a pressure of approximately 15 MPa. The fatigue crack growth test was conducted under constant amplitude loading cyclic and sinusoidal wave form conditions at a frequency of 20 Hz. The maximum load applied was of 36 kN. The loading ratio was of 0.1. The initial crack length was of 4.28 mm for the left side and 4.23 mm for the right side. A pre-cracking fatigue test was previously conducted under the same fatigue crack growth test conditions, except for a maximum load of 42 kN. The pre-cracking fatigue test was conducted until an increment of 0.75 mm was

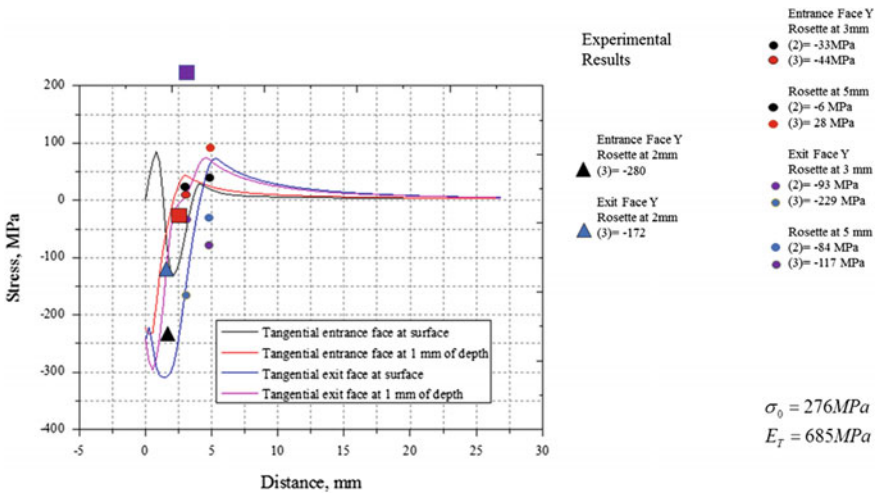

Fig. 2 Residual stress distribution induced by a customized cold worked operation into the specimen [13]

measured for the fatigue crack length. The fatigue crack length was measured with a traveling optical microscope.

Results and Discussion

The entrance and exit face were monitored during the pre-cracking fatigue test to detect the appearance of the initial crack. In spite that the corner notches were machined at the entrance and exit face sides of the specimen, the fatigue crack was firstly produced on the entrance face side of the specimen. Afterwards, the crack was only monitored for the entrance face. The initial crack length was 4.28 and 4.23 for the left and right hole's edge positions, respectively. The crack length during the fatigue test was measured from the center of the expanded hole. Figure 3 presents the crack length as a function of the number of cycles (a vs. N curve) for the 6061-T6 specimen with residual stresses. Both a versus N curves for the left and right hole's edge position were determined.

The final fatigue crack length was of 28.5 mm with a corresponding number of cycles of 2.8×10^6. A narrow difference in the fatigue crack length was observed between the left and right hole's edge position, but in general the initiation and propagation stages of the fatigue crack were symmetrical between both hole's edge positions. For instance, the fatigue crack length at the left and right position was of approximately 7.9 and 5.9 mm at 1.5×10^6 cycles. The narrow differences in the number of cycles for the fatigue crack length between the left and right positions can be associated with local microstructural features. The symmetrical fatigue crack

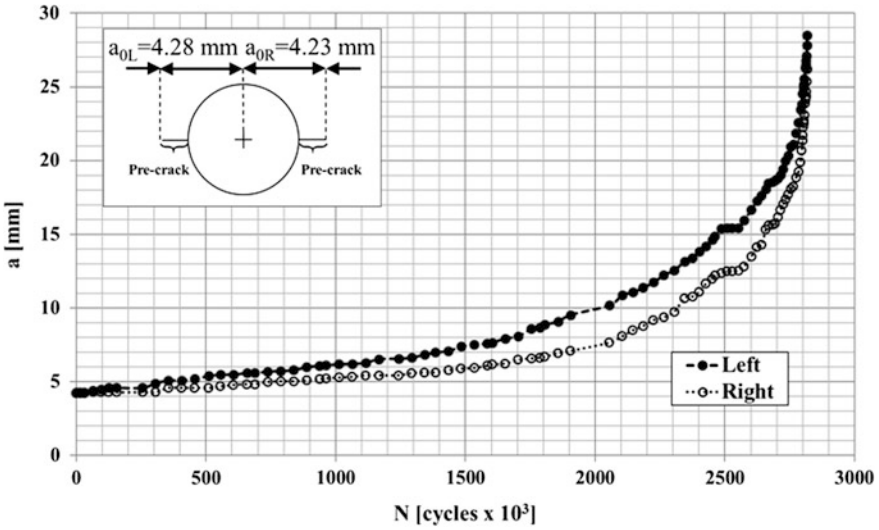

Fig. 3 Crack length versus number of cycles curves for the 6061-T6 Al alloy specimen with residual stresses. As a reference, initial crack length is shown

growth has several implications with respect to the residual stress field and the fatigue crack propagation mode. Regarding the initial residual stress condition, the symmetrical growth is an indication of a uniform residual stress distribution around the hole in the specimen (annular direction). The uniform residual stress distribution in the annular direction is an advantage of the customized cold work operation, because the applied load is not restrictive to a specific angular direction. On the contrary, a uniform annular residual stress distribution allows for an arbitrary direction of the external applied loads. The annular direction should not be confused with the thickness direction where a variable residual stress distribution was presented because of the cold worked operation. Regarding the fatigue crack propagation mode, the symmetry is an indication of a dominant mode I loading condition.

Figure 4 presents the fatigue crack growth rate as a function of the fatigue crack length (*da/dN* vs. *a* curve) for the left and right hole's edge positions. The fatigue crack growth rate was below 0.1 μm/cycle during the initial 20 mm of the fatigue crack length. This fatigue crack length corresponded to the stable regimen of the fatigue crack growth, which for the current specimen with residual stresses represented 2.7×10^6 loading cycles.

After the 20 mm fatigue crack length, the da/dN rate increased up to approximately 0.6 μm/cycle. This region corresponded to the final stage of the fatigue crack growth, where the final fracture is imminent. This interval of the final stage of the fatigue crack growth represented less than 5% of the total fatigue life for the specimen with residual stresses.

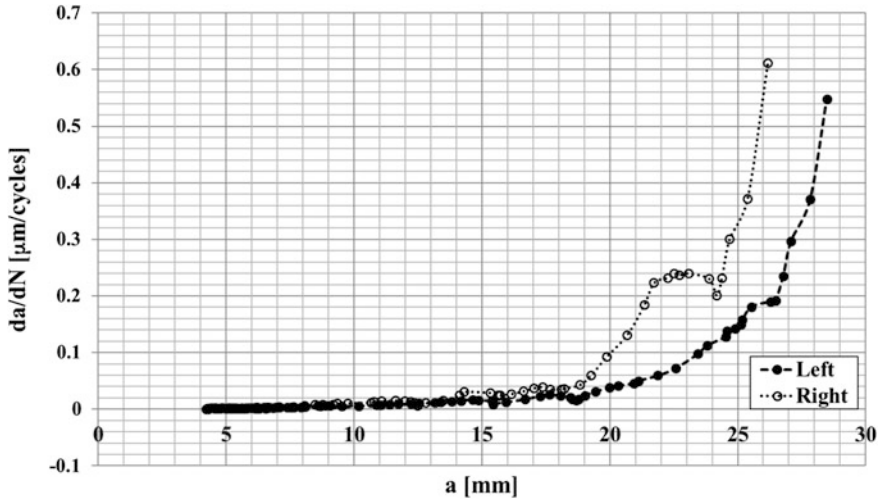

Fig. 4 Fatigue crack growth rate as a function of the crack length for the 6061-T6 Al alloy specimen with residual stresses

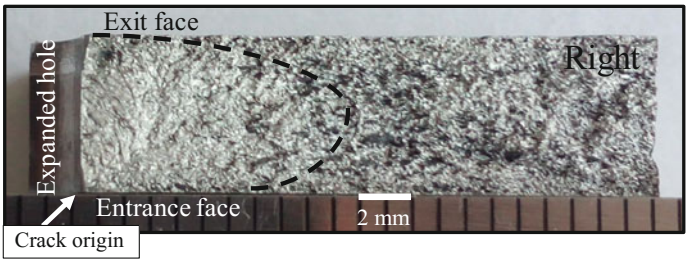

Fig. 5 Macroscopic view of the fracture surface

Figure 5 presents a macrofractography of the fatigue failure corresponding to the right hole's edge position of the specimen with residual stresses. The entrance face, exit face and expanded hole references are shown in Fig. 5. The corner notches at the entrance and exit face locations are observed in the macro. The beach markings may possible to detect the crack origin at the corner notch of the entrance face side (see arrow in Fig. 5). In addition, a preferential propagation occurred along the entrance face and the expanded hole directions that resulted in an irregular crack front as schematically indicated by the black line. Also, the fracture surface exhibited several peaks and valleys that indicated different transitions for the fatigue crack path. It seemed that the fatigue crack propagated in a tortuous manner because of the residual stress field, which may be a result of local mode loading transitions.

Conclusions

- Variable residual stress fields along the thickness direction were generated by the cold worked operation. The variable residual stresses resulted in an irregular crack front as demonstrated by the macroscopic view of the fracture surface. The fatigue crack origin was traceable to the corner notches located at the hole's edge of the entrance face side of the specimen.
- Symmetry conditions between the left and right fatigue cracks emanating from the corner notches prevailed during the fatigue crack growth. This indicate also a symmetry distribution of the residual stresses in the specimen between the left and right hole's edge positions.
- The stable fatigue crack growth stage represented 95% of the fatigue life for the specimen with residual stresses, introduced by the cold worked operation. The fatigue crack growth rate over this period of fatigue life were below 0.1 μm/cycle. The low fatigue crack growth rates associated with beneficial compressive residual stresses in the specimen resulted in a fatigue life of 2.8×10^6 cycles.

References

1. S. Suresh, Fatigue of materials, Cambridge, U. K.: Cambridge University Press, 1998.
2. S. S. Manson and G. R. Halford, Fatigue and Durability of Structural Materials, ASM International, 2006.
3. A. Butler, Manufacturing defect at root of F-15 grounding, Aviation Week and Space Technology, Vol. 168, 2008.
4. P. J. Withers and H.K.D. H. Bhadeshia, Residual stress part II: Nature and origins, Materials Science and Technology, pp. 366–375, 2001.
5. P.J. Withers, Residual stress and its role in failure, Reports on Progress in Physics, vol. 70, pp. 2211–2264, 2007.
6. S. Y. Lee, Y. Sun, K. An, H. Choo, C. R. Hubbard and P. K. Liaw, "Evolution of residual-strain distribution through an overload-induced retardation period during fatigue-crack growth," Journal of Applied Physics, vol. 107, 2010.
7. Bueckner HF. The propagation of crack and the energy of elastic deformation. Transactions of the ASME, Series A-D 80, 1958; 1225–1230.
8. W. Elber, "Fatigue crack closure under cyclic tension," Engineering Fracture Mechanics, vol. 2, pp. 37–44, 1970.
9. Beghini M, Bertini L. Fatigue crack propagation through residual stress fields with closure phenomena. Engineering Fracture Mechanics 1990; 3:379–87.
10. Beghini M, Bertini L, Vitale E. Fatigue crack growth in residual stress fields: experimental results and modelling. Fatigue and Fracture of Engineering Materials and Structures 1994; 17:1433–44.
11. Daniel Haines Stuart, Evaluation of linear elastic fracture mechanics predictions of one and two-dimensional fatigue crack growth at cold-expanded holes, M.Sc. Thesis, University of California, 2006.
12. J. E. LaRue and S. R. Daniewicz, "Predicting the effect of residual stresses on fatigue crack growth," International Journal of Fatigue, pp. 508–515, 2007.
13. Oswaldo Kaleb Reséndiz Yañez, Esfuerzos residuales generados por expansión de un orificio en aluminio 6061-T6, M.Sc. Thesis, Instituto Politécnico Nacional, 2016.

Fatigue Crack Initiation and Growth on Welded Joints of 2205 Duplex Alloy: The Effect of Electromagnetic Interaction During Welding

J. Rosado-Carrasco, J. González-Sánchez, V. H. López-Morelos and G. R. Domínguez

Introduction

Austenite-Ferrite duplex stainless steels (DSS) offer superior mechanical properties and resistance to localized corrosion than austenitic and ferritic stainless steels. However, during fusion welding, these alloys undergo thermal cycles which induce severe microstructural transformations, affecting the phase distribution and balance in the different regions of the welded zone. The microstructural evolution affects the fracture toughness, the mechanical strength and the resistance to localized corrosion [1]. The welding thermal cycles also promote the grain growth of the ferritic phase (δ) due to the total or partial dissolution of the austenitic phase (γ) in the high temperature heat affected zone (HTHAZ) [1–4]. It is well know that σ phase can nucleate and growth in the HTHAZ reducing impact toughness and the resistance to localized corrosion due to the Cr and Mo depleted zones created adjacent to this phase [4–6]. Another undesirable phase that could decrease the fracture toughness is the CrN which precipitates within the δ phase grains and along the δ-δ and δ-γ grain boundaries owing to the high affinity of N by Cr [1, 2, 4, 7]. It has been reported that the pitting corrosion resistance (PCR) decrease at the HTHAZ of DSS welds due to the increase of δ phase in this region, which has lower pitting resistance equivalent number (PREN) than austenite [2, 4, 7].

J. Rosado-Carrasco · J. González-Sánchez (✉) · G. R. Domínguez
Centre for Corrosion Research, Autonomous University of Campeche,
Av. Agustín Melgar s/n Cal. Buenavista, 24039 Campeche, Cam., Mexico
e-mail: jagonzal@uacam.mx

V. H. López-Morelos
Metallurgy and Materials Research Institute, Universidad Michoacana
de San Nicolás de Hidalgo, AP 888, 58000 Morelia, Michoacán, Mexico

R. R. Ambriz et al. (eds.), *Proceedings of the 17th International Conference on New Trends in Fatigue and Fracture*, https://doi.org/10.1007/978-3-319-70365-7_33

The regeneration of austenite in the HTHAZ must be enhanced in order to reduce the volume fraction of δ ferrite because in this phase is more possible the nucleation and growth of brittle Cr-rich phases increasing the susceptibility to attack nucleation and growth.

Material and Procedures

Plates of AISI 2205 DSS (6.35 × 70 × 150 mm) with a single V groove configuration were joined using the GMAW process with an ER-2209 filler wire, 1.2 mm in diameter, fed at 160 mm/s and a shielding gas mixture of 98% Ar + 2% O_2 flowing at 17 L/min. The welding torch was displaced at 3.6 mm/s with a stick out of 10 mm. A constant voltage power supply was used with direct current-electrode positive. The welding parameters were adjusted to obtain an approximate heat input of 1.4 kJ/mm considering an efficiency of 75% for the GMAW process. The experimental setup for welding with the application of EMF using an external power supply consisted in placing a coil in the same plane of the plates to be welded as reported elsewhere [7]. The EMF applied was 3 mT and other welds were made without EMF for comparison. The chemical composition of the base metal (BM) and filler wire are listed in Table 1.

Cylindrical samples of diameter 5.1 mm and length 70 mm were cut transverse to the weld bead as shown in Fig. 1.

The fatigue tests were performed in a rotating bending machine Gunt Hamburg WP-140 with the parameters indicated in Table 2. The specimen was placed in the machine as shown schematically in Fig. 2.

Load-controlled rotating bending fatigue tests were conducted using a sinusoidal waveform at 60 Hz in air. To obtain the load for the test, the Eq. 1 was used,

$$\sigma_a = \frac{M_b}{w_b} = 32\frac{a}{\pi d^3}F \tag{1}$$

where σ_a is the stress amplitude, M_b is the flexural moment and w_b is the moment of resistance, d is the diameter of the specimen and a is the distance from the bending point to the load application.

In order to follow the crack initiation and growth, the samples were subjected to grinding with abrasive SiC paper and polished to mirror surface finish. Acetate

Table 1 Chemical composition of base metal (AISI 2205) duplex stainless steel and filler metal (ER-2209)

Material	C	Cr	Ni	Mo	N	Fe
2205	0.030	22.94	5.62	3.015	0.17	Bal
ER-2209	0.012	23.00	8.80	3.20	0.14	Bal

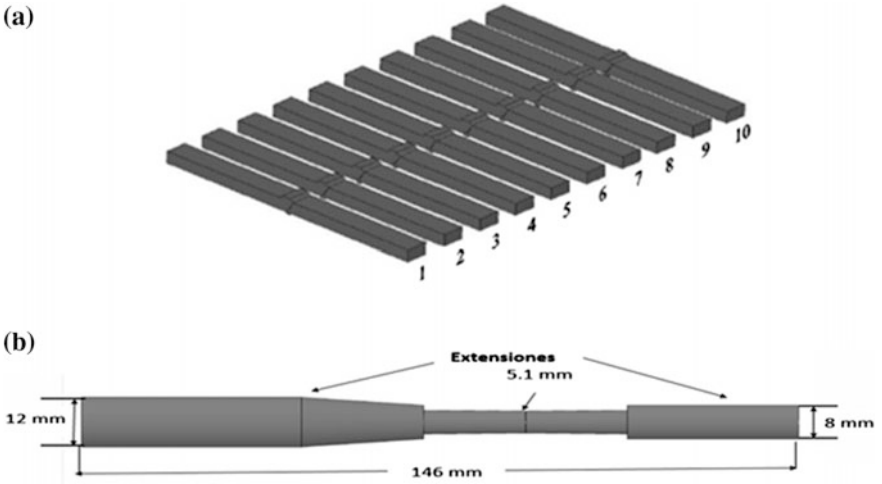

Fig. 1 **a** First cut from AISI 2205 duplex stainless steel welded plates. **b** Geometry of cylindrical specimens along with extensions for assembling to the fatigue machine

Table 2 Experimental parameters for the rotating bending fatigue tests

Condition	σ_{max} (MPa)	σ_{min} (MPa)	R	F (N)	f (Hz)	a (cm)	d (mm)
Metal base	337.9	−337.9	−1	62.8	60	7	5.1
0 mT	337.9	−337.9	−1	62.8	60	7	5.1
3 mT	337.9	−337.9	−1	62.8	60	7	5.1

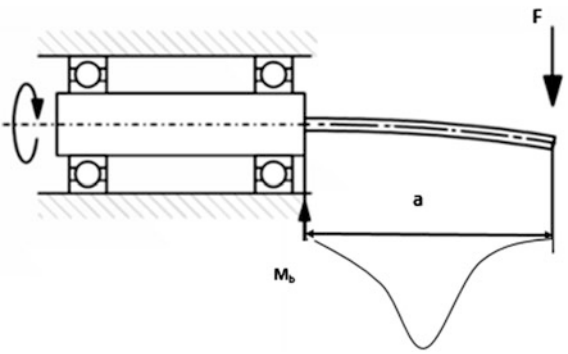

Fig. 2 Schematic diagram of experimental setup during fatigue test

replicas were obtained after every 20,000 load cycles. The fracture surface of samples at the end of the fatigue tests were analyzed by stereoscopic microscopy.

Experimental Results

The crack growth rate (da/dN) was calculated as a function of the crack length (a) and the diagram is shown in Fig. 3a where the blue line corresponds to the weld with the EMF and the black line to the conventional weld. The values of fracture toughness (K_{IC}) are listed in Fig. 3b and they were calculated using Eq. 2 and the last crack length measured, before the final fracture, as critical length.

$$K_{IC} = \beta\sigma\sqrt{\pi a} \tag{2}$$

where β is the geometric factor of the specimen, σ is the applied stress in MPa and a, is the crack length in m.

The cracks propagated on the surface of the specimen following a transgranular path, along the δ-γ grain boundaries of the welding pool, as it can be observed in the pictures shown in Fig. 4, obtained using acetate replicas during testing.

Discussion

The crack growth behavior in the diagram in Fig. 3a revealed, first for both welding conditions two slope changes, the first one indicates a decrease in the growth rate, this is due to phase boundaries that represent an efficient barrier to crack propagation, this mechanism is characteristic in duplex stainless steel as reported by Marinelli et al. [8, 9].

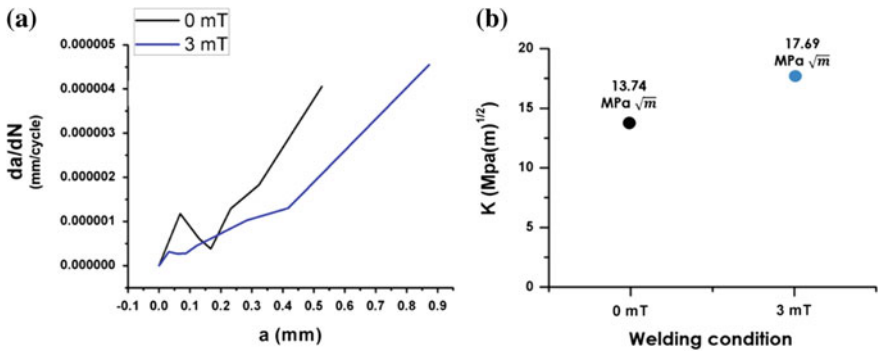

Fig. 3 **a** Crack growth rate as a function of crack length, the blue line represent the welding with EMF. **b** Fracture toughness values for comparison

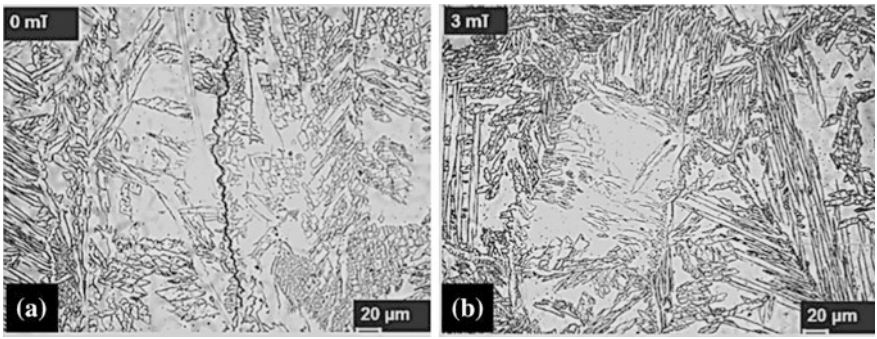

Fig. 4 Cracks propagating along the δ-γ grain boundaries in the welding pool of the **a** conventional weld and **b** the weld with EMF of 3 mT. Pictures taken after N = 60,000 cycles

The 3a diagram shows that, for 3 mT weld condition, there exist a decreased crack growth rate and a larger critical crack length before final fracture than 0 mT, this indicates a better endurance than conventional GMAW. This can be correlated with an influence of the grain refinement, austenite regeneration and electromagnetic stirring in the welding pool, due to EMF reported by García et al. [4] in a former research work.

The electromagnetic stirring also increases the grain misorientation, which, in further investigations, Krupp et al. [9, 10] reported as significative microstructural barriers for crack growth and this improves the fatigue life of the duplex stainless steel.

By calculating the value of fracture toughness, an increase for 3 mT weld in comparison with 0 mT weld, was noticed as it was expected and analyzing the surface pictures of Fig. 4, it can be observed that for the same number of cycles, the crack separation between the new created surfaces is wider for 0 mT weld than 3 mT. This is strongly correlated with the behavior shown in the diagram of crack growth rate and the fracture surfaces of specimens of different welding conditions shown in Fig. 5a, b, revealed that the fast fracture zone is bigger for 0 mT weld than 3 mT weld, this is an evidence of the improved fracture toughness of the latter condition.

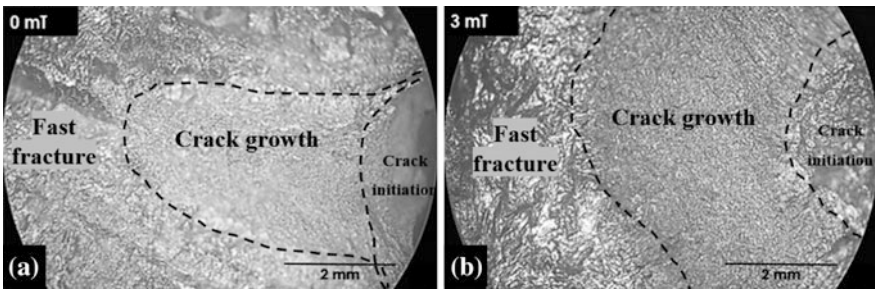

Fig. 5 Fracture surface observed with stereoscopic microscopy. **a** Corresponds to a 0 mT weld condition and **b** is the 3 mT weld. The dotted lines delimit the different zones of the surface

Conclusions

- The crack growth rate was decreased when and EMF of 3 mT was applied during GMAW in comparison with a conventional GMAW (without EMF).
- Due to the microstructural evolution such as grain refinement and γ regeneration, the fracture toughness of the 3 mT weld condition was increased and therefore the fatigue life was increased too.
- For both welding conditions, the cracks propagated on the surface of the specimen following a transgranular path, along the δ-γ grain boundaries of the welding pool.

References

1. R. Strubbia, et. al. "Short crack nucleation and growth in lean duplex stainless steels fatigued at room temperature", International Journal of Fatigue, pp. 90–94, 2012.
2. Lacombe, P., B. Baroux and G. Beranger (1993), Stainless Steels, Les Ulis Cédex, France: Les editions de physique.
3. Nilsson, J-O, Super Duplex Stainless Steel, Materials Science and Technology, Volume 8, Issue 8, Pages 685–700, 1992.
4. M. A. García, V. H. López, R. García, E. Bedolla, J. A. González, "Electrochemical Characterization of AISI 2205 Duplex Stainless Steel Welded Joints with Electromagnetic Interaction.", International Congress of Science and Technology of Metallurgy and Materials, SAM–CONAMET, 2013.
5. M. Martínez, "Corrosión por Picaduras y Sensibilización." de Las Tecnicas Electroquimicas Aplicadas, 2002.
6. J. Gong, "Evaluation of intergranular corrosion susceptibility of UNS S31803 duplex" Electrochimica Acta, vol. 55, p. 5077–5083, 2010.
7. M. A. García-Rentería, V.H. López-Morelos, R. García-Hernández, L. Dzib-Pérez, E.M. García-Ochoa, J. González-Sánchez, "Improvement of localised corrosion resistance of AISI 2205 Duplex Stainless Steel joints made by gas metal arc welding under electromagnetic interaction of low intensity" Applied Surface Science, Elsevier, vol. 321, p. 252–260, 2014.
8. I. Alvarez-Armas, H. Knobbe, M. C. Marinelli, M. Balbi, S. Hereñú y U. Krupp, "Experimental characterization of short fatigue crack kinetics in an austeno-ferritic duplex steel" Elsevier, Procedia Engineering, vol. 10, p. 1491–1496, 2011.
9. M.C. Marinelli, U. Krupp, M. Kübbeler, S. Hereñú, I. Alvarez-Armas, "The effect of the embrittlement on the fatigue limit and crack propagation in a duplex stainless steel during high cycle fatigue", Engineering Fracture Mechanics, vol. 110, p. 421–429, 2013.
10. Ulrich Krupp, Helge Knobbe, Hans-Jürgen Christ, Philipp Köster, Claus-Peter Fritzen, "The significance of microstructural barriers during fatigue of a duplex steel in the high- and very-high-cycle-fatigue (HCF/VHCF) regime", International Journal of Fatigue vol. 32, p. 914–920, 2010.

Nondestructive Monitoring of Rail Surface Damage Via Barkhausen Noise Technique

M. Neslušan, K. Zgútová, I. Maňková, P. Kejzlar and J. Čapek

Introduction

Large axle loads of the trains usually cause serious wear and structure transformations of the rails. Near surface region of the rail surface appears white under the metallographic observation [1–3]. For this reason this region is named white etching layer (WEL). Origin of WEL was widely discussed. Newcomb and Stobbs reported that WEL is initiated by the repetitive and severe plastic deformation [4]. On the other hand, phase analyses reveal retained austenite which indicates that WEL is thermally initiated process when the near surface region undergoes heating above austenitizing temperature followed by rapid self—cooling [1–3, 5]. Such process hinders full transformation of austenite to pearlite and certain volume of austenite retains in the WEL. WEL was subjected to many studies in which variable techniques were employed to identify stress state, phase composition, chemical and other alterations [1–5]. It was reported [1] that WEL is a product of rolling-contact fatigue caused by the alternating stresses associated with rolling contact bodies. Operation of the rails containing WEL regions may be risky with the respect to possible rails macro cracking initiated by micro cracks in the WEL. Furthermore, rails are subjected to grinding process in order to remove damaged layer and surface asperities [3].

M. Neslušan (✉) · K. Zgútová
University of Žilina, Univerzitná 1, 01026 Žilina, Slovakia
e-mail: miroslav.neslusan@fstroj.utc.sk

I. Maňková
Technical University of Košice, Mäsiarska 74, 04001 Košice, Slovakia

P. Kejzlar
Technical University in Liberec, Studentská 1402/2, 46117 Liberec, Czech Republic

J. Čapek
ČVUT Praha, Trojanova 13, 12000 Prague, Czech Republic

R. R. Ambriz et al. (eds.), *Proceedings of the 17th International Conference on New Trends in Fatigue and Fracture*, https://doi.org/10.1007/978-3-319-70365-7_34

For these reasons the suitable nondestructive method would be beneficial to revelation of the surface damage degree. Magnetic Barkhausen noise (MBN) is sensitive to microstructure and stress state [6–10]. Being so, this study deals with sensitivity of MBN technique for such purpose. MBN originates from irreversible and discontinuous Bloch Walls (BW) motion during the cyclic magnetization. The main reason can be viewed in pinning strength of variable microstructure features interfering with BW in motion. Irreversible and discontinuous BW motion produces acoustic as well as electromagnetic pulses. Electromagnetic pulses propagate towards free surface and can be detected by the use of a suitable pick up coil. It is well known that MBN is a function of stress state as well as microstructure. However, stress state affects mainly the domain and corresponding BW alignment whereas microstructure affects the free path of BW motion [7]. Microstructure of matrix can be expressed in many terms and it is worth to mention that BW interferes with all crystalline defects. Being so, in many studies MBN is studied as a function of dislocation density [9], carbides precipitation [10], grain size or presence of non-ferromagnetic phases [7]. Transformations in WEL are very complex and fully change character of the matrix. Being so, MBN could be a promising technique for monitoring of surface state of rails in operation. This pilot study reports about monitoring of surface damage in the rail by the use of MBN.

Experimental Part

The experimental study was carried out on hot rolled rail steel R220 (strength 785 ± 50 MPa, hardness 215 ± 35 HB) of chemical composition indicated in Table 1.

The rail was subjected to the 20 years accumulated passing tonnage about 0.8 million tons per year. Figure 1 shows a photo of the rail profile with indication of the analyzed zone. The rail surface was measured and analyzed within the whole rail width in which the possible contact of the rail and wheel can be expected. Metallographic observation, micro hardness alterations, XRD and MBN measurements were carried in certain points regularly distributed within the rail width (distance between the neighboring points is kept 6 mm).

MBN was measured by the use of RollScan 350 and software μScan 500 (magnetizing voltage 5 V, magnetizing frequency 125 Hz, 10 bursts, sensor type S1-18-12-01, frequency range of MBN from 10 to 1000 kHz). MBN values were obtained by averaging 10 MBN bursts (5 magnetizing cycles). MBN refers to the rms (effective) value of the signal. Estimated sensing depth of the MBN signal is

Table 1 Chemical composition of the rail steel R220 in wt%

Fe	C	Mn	Si	Cr	Ni	Cu	P
Bal	0.60	1.05	0.21	0.12	0.13	0.07	0.02

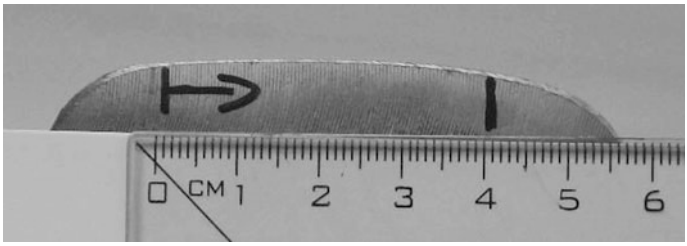

Fig. 1 The rail cross section with indication of measured width

about 50 μm. Magnetization of the rail surface was carried out in the direction of traction. Except conventional MBN parameter (rms value of the signal) also Peak positions were analyzed. Peak position of MBN refers to the position of magnetic field in which MBN envelope attains the maximum (corresponds to the magnetic hardness of the body). Units for Peak position are indicated as arbitrary units (a.u.) since measuring system normalize the scale of magnetic field (±100 a.u.). For this reason calibration was executed. This supplementary measurement found that the normalized scale of magnetic field ±100 a.u. corresponds to the real scale ±5.83 kA m^{-1} at magnetization frequency 125 Hz and voltage 5 V.

Residual stresses and phase analysis were measured via X-ray diffraction technique (XRD) ({211}, α-Fe, CrKα, 40 kV, 30 mA, average sensing depth approx. 5 μm, X'Pert PRO). Except stress state also Full Width at Half Maximum (FWHM) was analyzed since this parameter is closely connected with micro hardness of the matrix. To reveal the microstructure transformations induced by severe plastic deformation 10 mm long pieces were routinely prepared for metallographic observations (etched by 3% Nital for 8s). Microstructure was observed in the direction longitudinal with the track direction.

Vickers micro hardness readings were conducted by Zwick Roel ZHm micro-hardness tester by applying the force 50 g for 10 s. Micro hardness was determined by averaging 3 repetitive measurements (3 micro hardness profiles spaced 0.1 mm). All measurements were conducted at 7 points within the rail surface region indicated in Fig. 1. The first position was placed 3 mm from the left side. The following positions were spaced 6 mm each to other (also bulk structure was investigated).

Results of Experiments

Figure 2 illustrates microstructure of the rail surface at different positions. Bulk microstructure is entirely composed of pearlite with the equiaxed grains whereas the sub surface regions exhibit preferential orientation of the pearlite matrix due to hot rolling process. WEL is superimposed on this preferentially oriented matrix. Figure 2 also shows that thickness of WEL varies within the investigated rail width.

(a) distance 3 mm

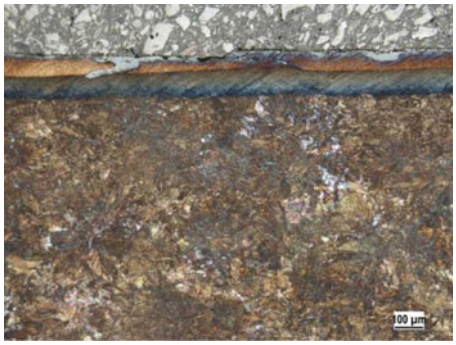

(b) distance 15 mm

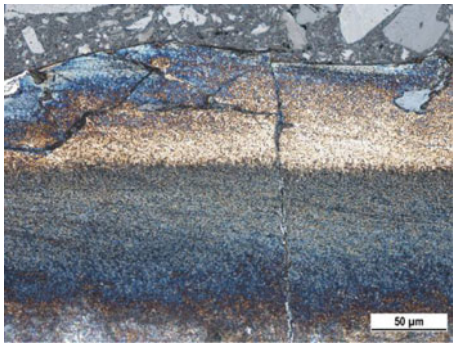

(c) distance 15 mm -detail

Fig. 2 Metallographic observation of the rail surface

Thin and discontinuous WEL can be found on the left side of the rail width (distance 3 mm) whereas thick and continuous WEL is located at the distance 9 and especially 15 mm from the left side of the rail. Distances 21 and 27 mm also exhibit thin and discontinuous WEL whereas positions 33 and 39 mm indicate no WEL in the surface region.

It can be easily understood that the main rail load is positioned in the zones of thick and continuous WEL. Micrographs also indicate that the rail surface is polluted the long term oxidation. Oxides initiated on the rail free surface contaminate not only WEL region but also the whole rail width and process of plastic deformation dips oxides into the deeper layer beneath the free surface. Micrographs also reveal surface cracking since WEL regions becomes hard and brittle. Further loading of such structure together with oxidizes initiate micro cracking contributing to the remarkable irregularities in the rail surface profile. The rail height varies due to pulling out small micro particles entirely surrounded by microcracks as that illustrated in details of the rail surface (at the thick WEL).

Surface oxidation can be verified by phase analyses executed by the use of XRD technique. Table 2 indicates that all regions contain Fe_2O_3 and first 3 regions also FeO. Table 2 also shows that bulk structure is entirely composed of pearlite phase. On the other hand, thick WEL regions contains martensite matrix of high tetragonality mixed with retained austenite whereas the right side of the rail width is composed of ferrite (low degree of lattice tetragonality) without retained austenite. Phase analyze verifies that WEL is thermally induced structure since retained austenite indicates that the near surface region undergoes heating above the austenitizing temperature. Table 2 and Fig. 3 also indicate that original pearlite structure is completely decomposed. Cementite lamellas are broken into very fine particles and certain volume of carbon is dissolved in the matrix [2, 5], see also SEM pictures in Fig. 3. Moreover, SEM technique clearly distinguishes between near surface WEL and deeper untouched structure.

High hardness of the WEL (see Fig. 4) corresponds with the high tetragonality of matrix (see Table 2) and associated dislocation density. Such matrix is due to rapid self—cooling from austenitizing temperature and results into remarkable surface hardening [1, 2, 5]. Thick and continuous WEL corresponds with quite deep extend of high hardness for distances 9 and especially 15 mm. On the other hand, it is worth to mention that micro hardness profiles for distances 3, 21 and 27 mm are debatable since WEL in these areas are discontinuous; they can occur in the form of localized spots thus indentation results can remarkably vary especially in the near

Table 2 Phases on the rail surface indicated by XRD technique

Dis. (mm)	Fe α	Fe γ	Fe_3C	Fe_2O_3	FeO	C	Fe fct
3	–	●	–	●	●	●	$●^+$
9	–	●	–	●	●	●	$●^+$
15	–	●	–	●	●	●	$●^+$
21	–	–	–	●	–	●	$●^+$
27	–	–	–	●	–	●	$●^-$
33	–	–	–	●	–	●	$●^-$
39	–	–	–	●	–	●	$●^-$
Bulk	●	–	●	–	–	–	–

$●^+$—high degree of lattice tetragonality
$●^-$—low degree of lattice tetragonality

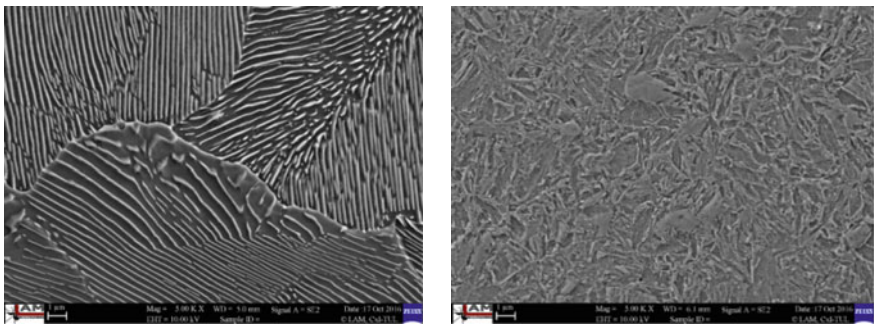

(a) bulk (b) WEL zone

Fig. 3 SEM observation of the rail surface

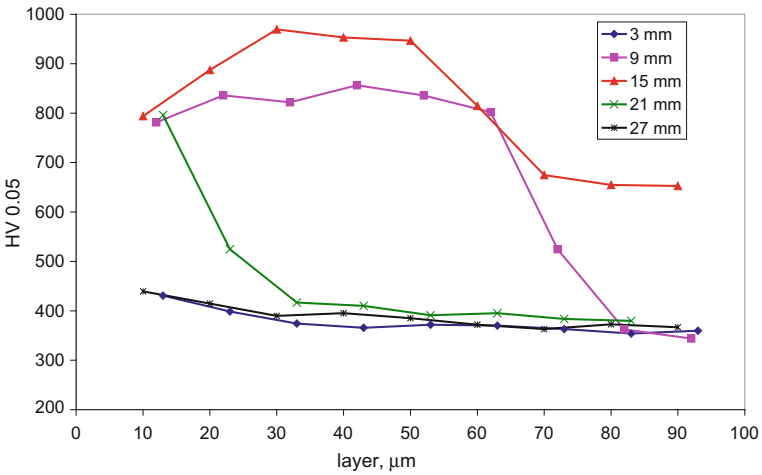

Fig. 4 Micro hardness profiles

surface region. Being so, it could be considered that microhardness for distances 3 and 27 mm could also attain microhardness approximately 800 HV as that for distance 21 mm, see Fig. 4.

As it was expected, compressive stresses can be found within the whole rail width, see Table 3. The left side exhibits the higher magnitude of compressive stresses compared to the rest of the rail surface. Analyzing the correlation between residual stresses and WEL thickness (on the base of data from Fig. 5 and Table 3) it can be found that the residual stresses exhibit poor sensitivity against the thickness of WEL since the thick WEL gives nearly the same residual stresses as the regions containing thin discontinuous WEL or regions free of WEL. Pearson coefficient correlation between WEL thickness ad residual stresses is only 0.356. The main reasons can be found as follows:

Table 3 Residual stresses and FWHM of XRD (stress is 191 MPa and FWGM 1.75 for bulk)

	3 mm	9 mm	15 mm	21 mm	27 mm	33 mm	39 mm
Stress (MPa)	−478 ± 30	−248 ± 38	−132 ± 45	−141 ± 11	−174 ± 19	−166 ± 9	−172 ± 10
FWHM	6.88	6.05	6.58	2.8	3.18	3.15	3.05

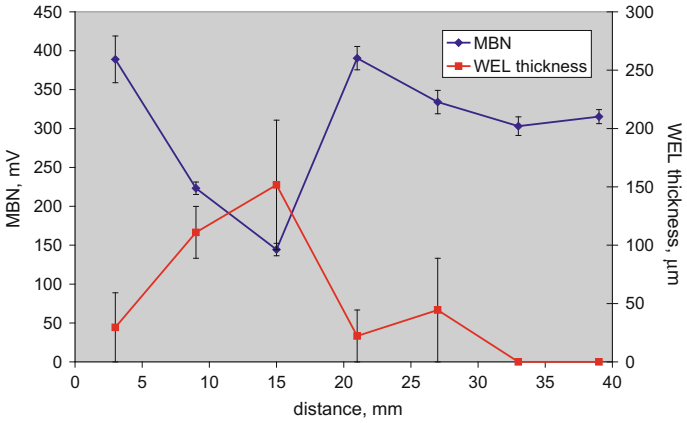

Fig. 5 Distribution of MBN and WEL thickness within the rail width

- sensing depth of XRD technique is too low (about 5 μm) compared with thickness of WEL; thus stress state cannot distinguish between thin and thick WEL,
- surface cracking releases the stresses in the WEL and other regions,
- due to long term cyclic loading WEL region undergoes repetitive periods of surface hardening followed by the matrix dynamic recovery and the corresponding stress relaxation [2].

On the other hand, FWHM is more sensitive to the structure alterations; thus regions containing thick WEL exhibit high values of FWHM a vice versa, see Fig. 5 and Table 3. The high values of FWHM correspond to high hardness and associated high dislocation density. Compared to the stress state, relationship between WEL thickness and FWHM exhibits better correlation (expressed in the term of Pearson coefficient of correlation 0.555).

Figures 5 and 7 illustrate very good sensitivity of MBN (rms value of signal) versus WEL thickness. Relation between MBN and WEL thickness is nearly linear and increasing WEL thickness can be directly linked with decreasing magnitude of MBN signal. The main reasons can be found as follows:

- much higher sensing depth of MBN technique (compared with XRD technique),
- martensite matrix of the high degree of lattice tetragonality containing carbon in the supersaturated state, high dislocation density and the corresponding high hardness associated with high magnetic hardness,
- retained austenite in the WEL strongly hinder BW motion,
- oxides (FeO and Fe_2O_3) as hard ferromagnetic particles embedded in the martensite matrix strongly pin BW motion,
- microcracks such as defects not producing MBN emission.

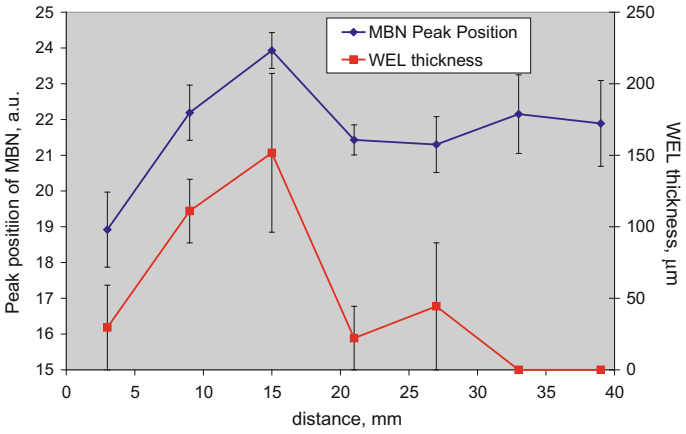

Fig. 6 Distribution of Peak position of MBN and WEL thickness within the rail width

Figure 7 shows that thickness of WEL can be obtained from MBN signal; thus damaged rail layer can be monitored in a non-destructive manner.

An alternative parameter for nondestructive monitoring of the rail damage via MBN can be viewed in Peak position. Figure 6 shows that the high hardness in the thick WEL correspond with the high Peak positions a vice versa. Expressed in other words, stronger magnetic fields are needed for irreversible BW motion in thick WEL compared to thin WEL or surface free of WEL. Information about Peak positions can be obtained directly from μScan software or MBN envelopes as that reported in the previous study [11]. An alternative parameter for nondestructive monitoring of the rail damage via MBN can be viewed in Peak position. Figure 6 shows that the high hardness in the thick WEL correspond with the high Peak positions a vice versa. Expressed in other words, stronger magnetic fields are needed for irreversible BW motion in thick WEL compared to thin WEL or surface free of WEL. Information about Peak positions can be obtained directly from μScan software or MBN envelopes as that reported in the previous study [11].

Conclusions

Micro cracking in the hard and brittle WEL arises from the cyclic long term loading and potentially can initiate rail macro cracking. For this reason, rails should be subjected to the re-grinding process in order to remove the damaged layer and refresh the surface state. MBN technique could be potentially employed for the assessment of WEL thickness as a layer removed by grinding. Finally, this is the pilot study which would suggest a possible concept for prevention of unexpected rails deformation (or cracking) due to their thermal dilatation (and the corresponding stresses) initiated by the ambient temperature fluctuations via MBN

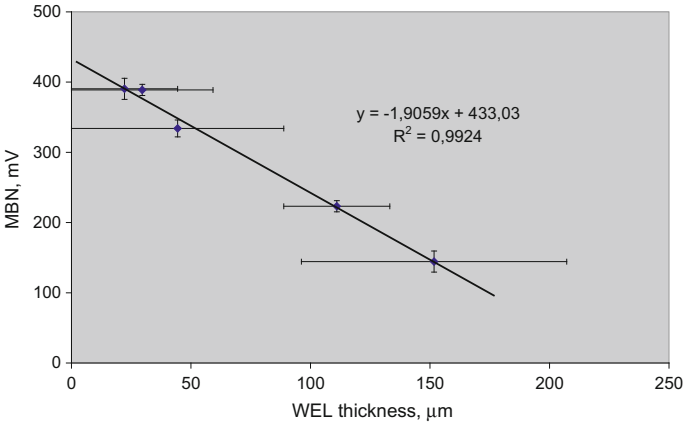

Fig. 7 MBN versus WEL thickness, Pearson coefficient of correlation is −0.996

technique. However, MBN emission initiated by external stresses superimposes with MBN from the accumulated damage of the rail surface due to its cyclic severe loading.

Acknowledgements This work was supported by the VEGA projects n.1/0254/15 and n.1/0170/17 as well as project: University Science Park of the University of Zilina (ITMS: 26220220184).

References

1. S. Pal, J.T. Daniel, H.G. Valente, A. Wilson, A. Atrens. Surface damage on new AS60 rail caused by wheel slip, Engineering Failure Analysis, 22, (2012), pp. 152–165.
2. J. Takahashi, K. Kawakami, M. Ueda, Atom probe tomography analysis of the white etching layer in a rail track surface, Acta Materialia 58, (2010), pp. 3602–3612.
3. J.F. Santa, A. Toro, R. Lewis, Correlation between rail wear rates and operating conditions in a commercial railroad, Tribology International 95, (2016), pp. 5–12.
4. Newcomb, S.B. Stobbs, W.M., A transmission electron microscopy study of the white-etching layer on a rail head, Materials and Science Engineering Materials and Engineering, 66, 1984, pp. 195–204.
5. L. Wang, A. Pyzalla, W. Stadlbauer, E.A. Wener, Microstructure features on rolling surfaces of railways rails subjected to heavy loading, Materials and Science Engineering Materials and Engineering A 359, (2003), pp. 31–43.
6. Karpuschewski, B., Bleicher, O., Beutner, M., 2011. Surface integrity inspection on gears using Barkhausen noise analysis. Processing Engineering 19, pp. 162–171.
7. Moorthy, V., Shaw B.A., Mountford, P., Hopkins, P., 2005. Magnetic Barkhausen noise emission technique for evaluation of residual stress alteration by grinding in case – carburized En36 steel. Acta Materialia 53 (19), pp. 4997–5006.
8. Gatelier-Rothea, C., Chicois, J., Fougeres, R., Fleischmann, P., 1998. Characterization of pure iron and (130 p.p.m.) carbon-iron binary alloy by Barkhausen noise measurements: study of the influence of stress and microstructure. Acta Metallurgica 46 (14), pp. 4873–4882.

9. J. Čížek, M. Neslušan, M. Čilliková, A. Mičietová, O. Melikhova: Modification of steel surfaces induced by turning: non-destructive characterization using Barkhausen noise and positron annihilation, Journal of Physics D, Applied Physics 47/2014, pp. 1–17.
10. Neslušan, M., Čížek, J., Kolařík, K., Minárik, P., Čilliková, M., Melikhová, O., Monitoring of grinding burn via Barkhausen noise emission in case-hardened steel in large-bearing production, Journal of Materials Processing Technology, Vol. 240, 2017, pp. 104 – 117.
11. Neslušan, M., Zgútová, K., Kolařík, K., Šramek, J., Čapek, J. Analysis of structure transformation in rail surface induced by plastic deformation via Barkhausen noise emission, Acta Physica Polonica A, Vol. 131/4, 2017, pp. 1096 – 1101.

Failure Analysis of Stress Corrosion Cracking of Two Tees in a Pressurized Drainage System

D. Rivas, J. L. González, A. Casarrubias and M. Beltran

Introduction

The circuit where the specimens were located presented component substitutions in the years 2011 and 2012. On January 12th 2016, the Tee E-277 presented cracking, while the Tee E-182 presented a leak at February 5th 2016. The schemes shown in Fig. 1 indicate the location of the samples. The operating conditions are shown in Table 1.

Materials and Methods

The present failure analysis was performed under the methodology developed by the procedure described in ASTM E 2332-04 "Standard Practice for Investigation and Analysis of Physical Component Failures".

A visual examination of the Tee E177 and E182 was realized, where the dimensions are the following; Tee E177: diameter 4.445 cm (1.750″), wall thickness of 8.28 mm (0.303″) and a length of 12 cm (7.72″) also has a section of welded tube 13.5 cm long (5.31″); the Tee E 182, diameter 4.445 cm (1.750″), wall thickness of 7.874 mm (0.310″) and a length of 13 cm (5.11″); As shown in Fig. 2.

Subsequently, a chemical analysis of the steel was performed by spectrophotometry, using the atomic absorption technique. The samples were prepared fol-

D. Rivas (✉) · J. L. González · A. Casarrubias · M. Beltran
Instituto Politécnico Nacional, ESIQIE-IPN, GAID-IPN, UPALM Edif. 7 Planta baja, Av. Instituto Politécnico Nacional s/n, 07738 Col. Lindavista, CDMX, Mexico
e-mail: drivas_lopez@yahoo.com.mx

R. R. Ambriz et al. (eds.), *Proceedings of the 17th International Conference on New Trends in Fatigue and Fracture*, https://doi.org/10.1007/978-3-319-70365-7_35

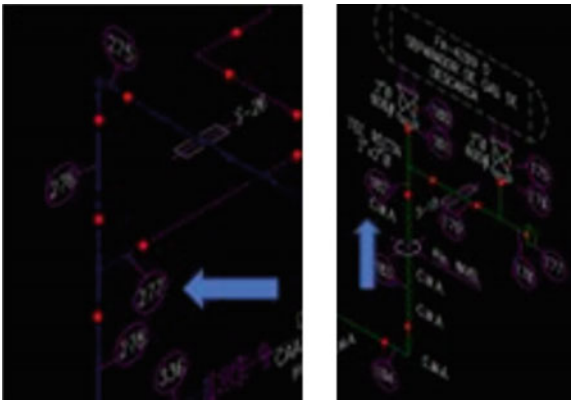

Fig. 1 Location of study samples, in an isometric view

Table 1 Technical information on the valve control

General data	
Circuit description	Pressurized module in 2″ Ø
Operating pressure[a]	0.80 kg/cm^2 (1109.4 psi)
Operating temperature[a]	27 °C (95 F)
Work service	High pressure condensate

[a]Value provided by operating data

Fig. 2 Tee E177 and E182 in as received conditions

lowing the procedure described in ASTM E3, for afterwards observe by optical microscope. Finally, it analyzed the fault zone and the deposits by E.D.S., Rockwell hardness tests were carried out on the B scale. Hardness tests were developed based on ASTM E-18.

Results

Visual Examination

The general characteristic observed in both samples is the fracture in a perpendicular direction to the straight side. The fractures propagation for the Tee E177 and the Tee E182 were of 16 and 15.5 cm respectively. For both samples, the fracture plane is in the circumferential section, the plastic deformation associated to the fractures is null, there are no abrupt changes of the fracture planes, only steps are observed and the fracture surfaces are close to smooth. However, on the fracture surfaces, a layer of corrosion products by aqueous attack, as well as oxides of weathering are observed. The images of Fig. 3 show the fracture surfaces.

Chemical Analysis

Table 2 shows the results of the chemical analysis and the specified values of the ASTM A 234 WPB standard.

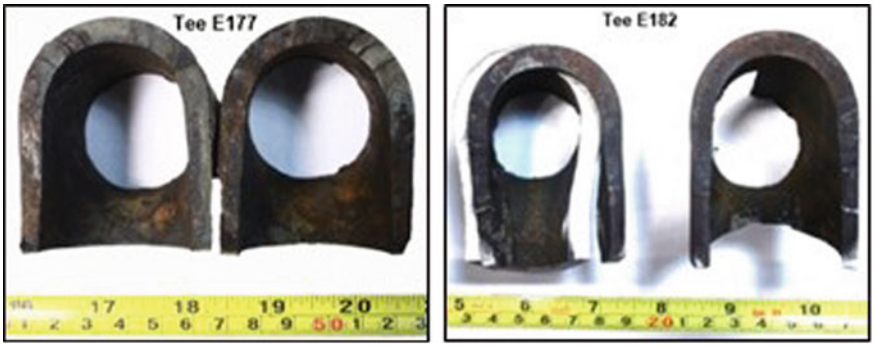

Fig. 3 Fracture surface observed on Tee E177 and Tee E182 respectively. Note the steps and the null plastic deformation in both samples

Table 2 Shows the results of the chemical analysis in %W

ID	C	Mn	P	S	Si	Cu(1)	Cr(1)	Mo(1)	Ni(1)	V
E177	0.248	0.722	0.023	0.041	0.383	0.288	0.055	0.019	0.045	0.015
E182	0.181	0.765	0.007	0.018	0.322	0.057	0.084	0.015	0.059	0.006
ASTM A 234 WPB	0.30 max.	0.29–1.06	0.030 max.	0.035 max.	0.10 min.	0.400 max.	0.400 max.	0.150 max.	0.400 max.	0.08 max.

Specified residual elements, the maximum total of these elements must be less than 1%

Hardness Tests

Table 3 shows the results of the hardness tests.

Metallographic Examination

The results of the microstructure are presented in Table 4, which is constituted by a matrix of ferrite crystals and pearlite colonies. The distortion of the microstructure is related to its forging process.

Analysis of the Failure Zone

Figure 4 shows the failure zone, where the steps and grooves are closely parallel to the propagation direction of the crack and perpendicular to the propagation front. A layer of corrosion products (possibly aqueous) covering the fracture surface was observed. This layer prevents further observations, as indicated in the visual inspection. Non significate plastic deformation associated to the fracture was observed.

Table 3 Rockwell hardness values in B-scale

Specimen	No. of indentations	Middle value	Minimum value	Maximum value	HB	UTS ASTM [KSI]	Uncertainty
E177	10	99	98	99	234	114	1.41
E182		99	98	99	234	114	1.57

[a]The value of UTS is assumed approximate to be quantified by correlation with the hardness test

Table 4 Stereological parameters of the microstructure

Specimen	Volume fraction of inclusions	Type of inclusion	% ferrite	% pearlite	ASTM grain size
E 177	0.63	D	76.50	23.50	9
	0.77		74.65	25.35	
E 182	0.38		84.15	15.85	
	0.48		82.19	17.81	

Fig. 4 Fracture surfaces are observed in both parts, the steps and the null plastic deformation associated to the fracture are observed

Analysis of Deposits by E.D.S.

The corrosion products in the internal wall of the two Tee were removed, in order to realize a chemical characterization of the sample by the use of the Energy Dispersive X-Ray Spectroscopy (EDS) technique. The results are shown in Fig. 5, where it can be seen that the corrosion products are formed primarily of iron, oxygen and sulfur. These elements are the constituents of chemical compounds such as iron oxide and iron sulfide.

Analysis of Results

The chemical and metallurgical characteristics observed in the steel of both Tee's meet the design specifications. However, the mechanical strength of the steel, in both cases, was found to be well above than that specified for an ASTM A234 grade WPB steel. This specification indicates (Point No. 9) that the fittings should not exceed 197 HB (Brinell Hardness). However, as seen in Table 3, the hardness value reported in laboratory was estimated as 234 HB. At this hardness value, the maximum strength of these steels would be approximately 114 KSI, which is well above the maximum specified strength for an ASTM A-234 WPB steel (65–85 KSI).

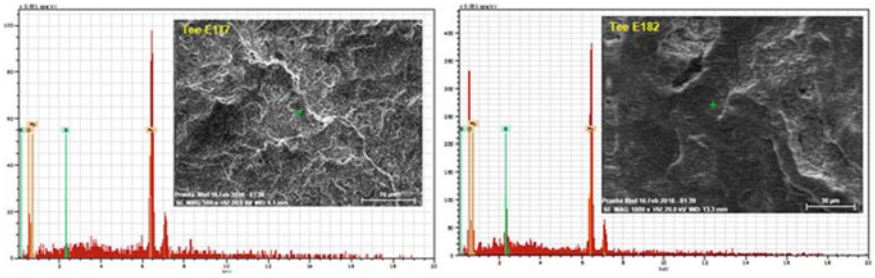

Fig. 5 Energy spectra EDS, of solid products removed from the inner wall of the two Tee's

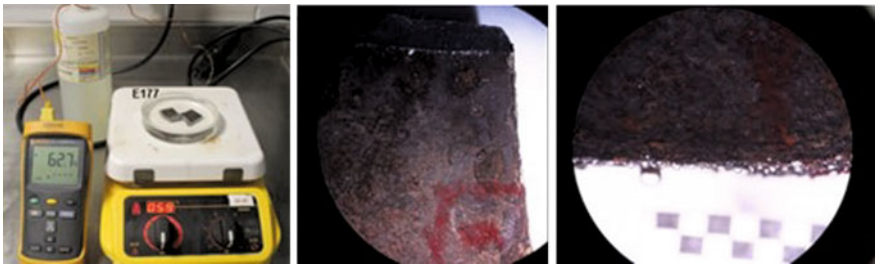

Fig. 6 Sample removed near the fracture of the tee E177; notice bubble formation from the material's surface

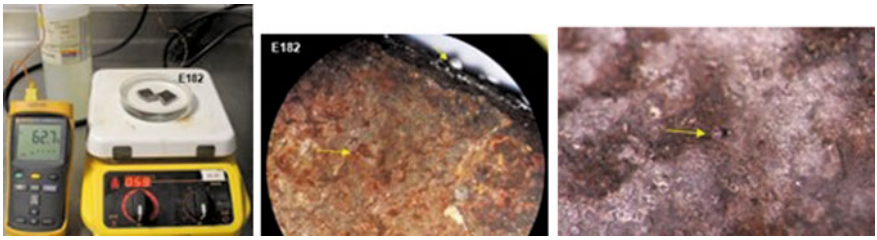

Fig. 7 Sample removed near from the fracture of the tee E182; notice bubble formation from the material's surface

The form of damage consisted of a brittle fracture characterized by null plastic deformation and the presence of steps and grooves at the macro level. The fracture mechanism was identified as a corrosion cracking and efforts (SCC). The SCC is a form of fracture that occurs through the interaction of a corrosive environment, susceptible material and a stress high enough to propagate the cracking.

The EDS characterization of the corrosion products, show that the chemical composition of the oxides and sulphides deposits are formed by the presence of H_2S and H_2O. The H_2S reacts with the iron of the steel, forming the iron sulphide which is deposited in the wall. Initially, the deposits of corrosion products tends to protect the steel. However, the deposit layer is porous, changing its cathodic character to the anodic. This behavior promotes the cavities formation; these cavities are sites for nucleation and initiation of cracking.

According to the macroscopic observations and the EDS results of the corrosion products, the hypothesis of the presence of hydrogen (H) inside the samples was proposed. In order to demonstrate the H presence, sections close to the fracture (of approximately 2 cm $\times$ 2 cm), were submerged in glycerin for heating at 60 °C. The objective was to promote the absorbed H displacement inside the steel. Figures 6 and 7 show bubbles in the steel surface, whose quantity increase as increasing the temperature. As known, the H is the only chemical species able to diffusing inside the steel in its atomic form, as a consequence of its lower

atomic radius. The effect of the H presence within the steel has not been completely understood, however it has been demonstrated that the embrittlement of the material is one of its effects. The H absorption is generated in sour media; with the presence of hydrogen sulphide, CO_2 and water; as the one that contains the pressurized drainage circuit.

Conclusions

- The failure mechanism, observed in T E177 and E182, is identified as stress corrosion cracking in the presence of hydrogen, in a hard material.
- The steel of both Tee's has a high hardness, this type of steels are susceptible to stress corrosion cracking.
- The presence of hydrogen was determined empirically and qualitatively.
- The effect of adsorbed hydrogen is the embrittlement of the material.
- The manufacture material of the both Tees partially meets with the specifications of the steel ASTM A234° WPB.

References

1. ASTM E 2332-04 "Standard Practice for Investigation and Analysis of Physical Component Failures".
2. ASTM E 18-17 "Standard Test Methods for Rockwell Hardness of Metallic Materials".
3. ASTM E3-11 (2017) "Standard Guide for Preparation of Metallographic Specimens".
4. González Velázquez Jorge Luis (2013), Mecánica de la Fractura, México D.F., Limusa Noriega.
5. ASTM E-1245 (2016), Standard practice for determining the inclusions or second-phase constituent content of metals by automatic image analysis.
6. ASTM E-45 (2013), Standard Test Methods for Determining the Inclusion Content of Steel.
7. ASTM E-1382 (2015), Standard test method for determining average grain size using semiautomatic and automatic image analysis.
8. González Velázquez Jorge Luis (1999), Metalurgia Mecánica, México D.F., Limusa Noriega, ISBN 968-18-5782-8.

Fatigue Life Extension of 2205 Duplex Stainless Steel by Laser Shock Processing: Simulation and Experimentation

V. Granados-Alejo, C. A. Vázquez-Jiménez, C. Rubio-González and G. Gómez-Rosas

Introduction

Laser Shock Processing (LSP) has been successfully utilized for extending the fatigue life of critical engineering components [1–4]. Through LSP it is possible to delay the fatigue cracks initiation and growth by introducing a compressive residual stresses field. According with the iteration of radiation with matter, the laser beam is directed and focused on the sample surface as shown in Fig. 1. When it touches the surface, a thin layer of the surface is vaporized. Consequently, due to high energy concentration in a reduced area, the temperature increases rapidly and the gas is ionized, giving rise to the formation of plasma between sample surface and confined medium (thin water layer). Over time, the plasma expands and generates a high pressure on the material surface in the order of GPa [5]. This pressure transmits shock waves into the material plastically deforming the surface and inducing a compression residual stresses field.

In the last decade, the prediction of residual stress field introduced by The LSP technology through Finite Element Analysis software which involves the simula-

V. Granados-Alejo · C. Rubio-González
Centro de Ingeniería y Desarrollo Industrial, Pie de la Cuesta 702, Desarrollo San Pablo, 76125 Querétaro, Qro., Mexico

C. A. Vázquez-Jiménez · G. Gómez-Rosas
Universidad de Guadalajara, Blvd. Marcelino García Barragán 1421, 44430 Guadalajara, Jal., Mexico

V. Granados-Alejo (✉)
Universidad Politécnica de Guanajuato, Av, Universidad Sur 1001 Juan Alonso, 38483 Cortazar, Guanajuato, Mexico
e-mail: vgrandos@posgrado.cidesi.edu.mx

C. A. Vázquez-Jiménez
Universidad de Colima, Carretera Colima-Coquimatlán Km 9, 38483 Coquimatlán, Colima, Mexico

R. R. Ambriz et al. (eds.), *Proceedings of the 17th International Conference on New Trends in Fatigue and Fracture*, https://doi.org/10.1007/978-3-319-70365-7_36

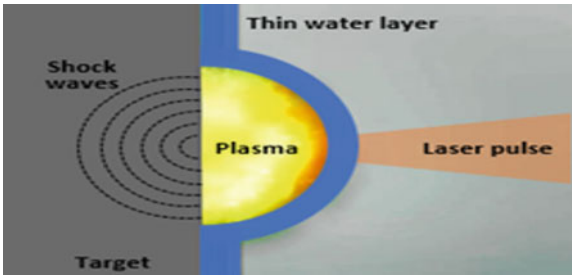

Fig. 1 Laser shock penning principle

tion of the metal behavior and the pressure profile of the shock waves, has been used to optimize the process [6–11]. In this work, FEM software ABAQUS was employed in order to analyze the treatment and predict its beneficial effects on cyclic response and residual stress fields of 2205 DSS. The 3D model was verified by comparing simulated surface residual stress with experimentally measurements and then, the commercial code FE-Safe was used to predict fatigue lives of samples.

Materials and Methods

2205 DSS notched samples (flat plate) of 100 × 40 mm with radius notches of 5 mm were employed. The chemical composition is: 22.13 Cr, 5.56 Ni, 3.08 Mo, 1.22 Mn, 0.42 Si, 0.19 Cu, 0.188 N, 0.14 Co. The offset tensile yield stress is 520 MPa, ultimate tensile strength is 710 MPa and elastic modulus is 190 GPa. The LSP experiments were performed using a Q switched Nd:YAG laser operating at 10 Hz with a wavelength of 1064 nm and FWHM of 6 ns. The experimental set-up of LSP is shown in Fig. 2. A convergent lens was used to deliver 0.85 J/pulse. The spot diameter was 1 mm and the pulses density was 2500 pulses/cm^2.

Fatigue tests were performed on a MTS 810 servo-hydraulic system at room temperature in the air. Load ratio $R = P_{min}/P_{max}$ was maintained at $R = 0.1$

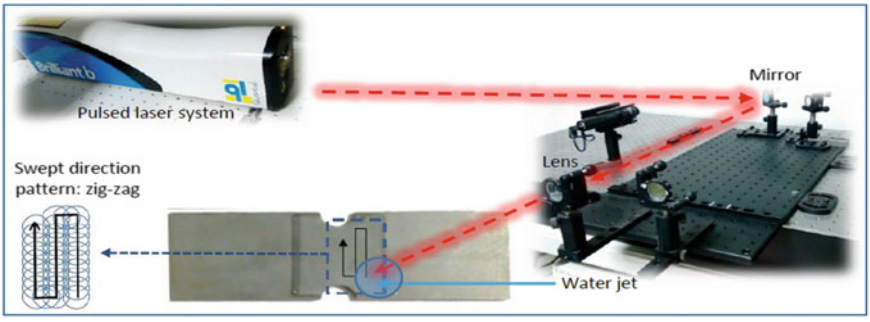

Fig. 2 Schematics of experimental set up of LSP

with 20 Hz. Each specimen was tested to maximum stress applied of 275 MPa. The residual stress was measured using the strain gage rosettes CEA-06-062UL-120 by the hole drilling method according to ASTM 837 standard.

Modelling: Finite Element Analysis

FEA analysis of the LSP treatment was performed using the Abaqus software. The model is shown in Fig. 3 in which 224,826 C3D8R linear hexahedron elements were used. Encastre boundary condition was applied on the specimen border while LSP was applied on the front face and then the process was applied on the back face.

The simulated loading condition was a pressure pulse on 25 × 25 mm square, with time evolution given in Table 1. Peak pressure of 5.21 GPa according with [12–15].

The material model used to simulate the behavior of the material under the shock conditions was the Johnson-Cook model with parameters material constants: A (MPa) = 520 MPa, B = 840.5 MPa, C = 0.0124, n = 0.1904, m = 0.965, $\varepsilon_0 \doteq 1$ [16, 17].

Fatigue lives under constant amplitude loading were correlated by the Coffin–Manson equation:

$$\frac{\Delta_\varepsilon}{2} = \frac{\sigma'_f}{E}\left(2N_f\right)^b + \varepsilon'_f\left(2N_f\right)^c \tag{1}$$

The maximum principal strain analysis is a critical plane multi-axial fatigue algorithm; this algorithm uses the strain-life curve defined by Eq. 1. Maximum shear strain analysis is a critical plane multi-axial fatigue algorithm [18]. Several relations to estimate Coffin-Manson parameters from monotonic properties have been proposed in the literature [19–21]. Life Principal Strain and Maximum Shear

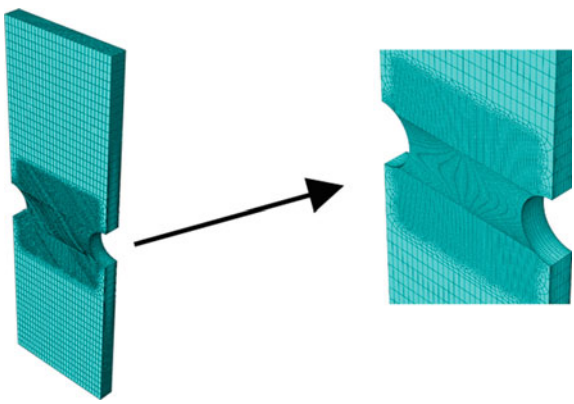

Fig. 3 Finite element model of the specimen

Table 1 Load distribution

Time (ns)	0	3	5	7	9	12	15	19	26	33	59	80	120	178	200
Pressure (GPa)	0	0.7	1.4	2.9	4.8	5.2	5.1	4.2	2.7	2.1	1.3	1.0	0.57	0.19	0

Strain Stress theories for fatigue analysis are considered with the Morrow and SWT correction for mean stress.

Results and Discussion

Residual stress profiles as a function of depth with LSP treatment are shown on Fig. 4a. It is noted the similitude of hole drilling technique and FEM simulation result in samples treated with LSP. The maximum tensile stress for material as received is 260 MPa, while for the treated samples; the maximum compressive residual stress is 780 and 720 MPa for the experimental and simulation, respectively. Figure 4b shows the fatigue life results. The experimental results for untreated specimen was 836,700 cycles to failure, whereas for the treated specimen was 4,318,000, which corresponds to 416% improvement.

Figure 5a shows the residual stress distribution induced by LSP. Figure 5b show the number of cycles to fatigue crack initiation.

Figure 6a, b show details of the striations and FCG for untreated and treated samples, respectively. Figure 6c shows that the FCI starts at the surface for untreated sample. While for treated sample the FCI stars in the centre of thickness (Fig. 6d).

The average of striation length for specimens with LSP treatment is 0.16 μm, while for untreated specimens is 0.213 μm. The striation length is directly related with the fatigue crack growth rate and represents the distance of the crack growth

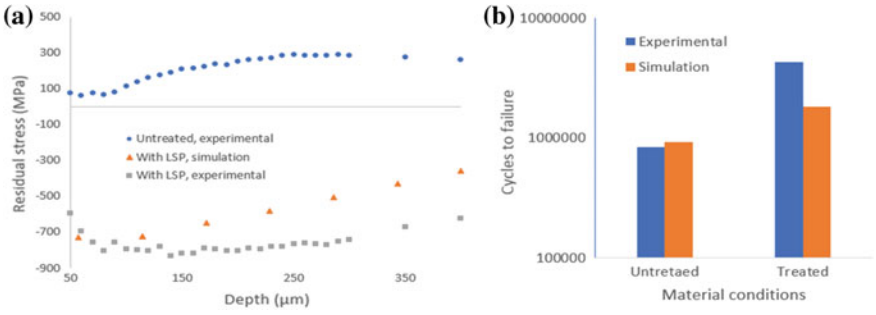

Fig. 4 Comparison of untreated and treated samples for **a** residual stress and **b** fatigue life

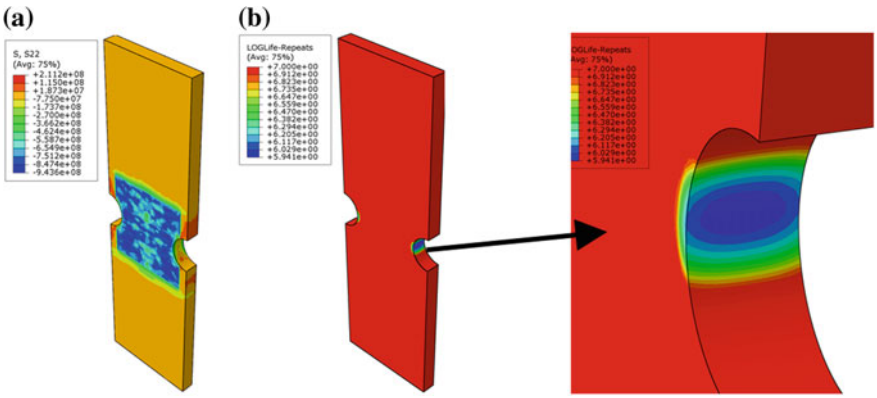

Fig. 5 Simulations results of **a** residual stress distribution after LSP, **b** cycles to failure for untreated specimens

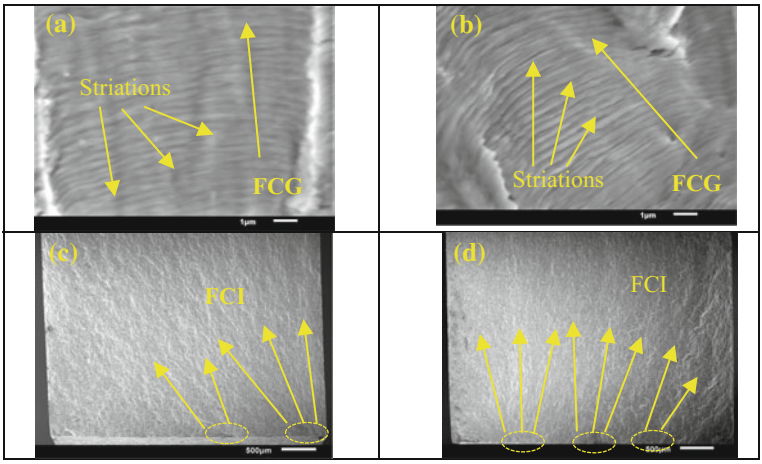

Fig. 6 Fracture surface images: **a** striations of untreated sample, **b** striations of untreated sample, **c** FCI of untreated sample and **d** FCI of treated sample

per cycle. Thus, according to striation length measured for specimens with LSP, the crack growth rate is reduced in comparison with untreated specimen. This decreases of fatigue crack growth rate is attributed to superficial residual stress induce by LSP. Similar observations have been reported in Titanium and Aluminium alloys [22].

Conclusions

The effect of LSP treatment on residual stress and fatigue life of 2205 DSS was studied. FEM simulation and experimental data were correlated. Both exhibited an extension of fatigue life due to the compressive residual stress induced by LSP. It is observed that the compressive residual stresses field decreases the effect of external load near-surface and according with SEM analysis and FEM simulation, the fatigue crack initiation zone is changed to the centre of thickness delaying significantly the fatigue crack initiation.

References

1. Lloyd Hackel, Jon Rankin, Tracy Racanellia, Tim Mills, John H. Campbell. Procedia Engineering 133 (2015) 545 – 555.
2. Anoop Vasu, Koorosh Gobal, Ramana V. Grandhi. International Journal of Fatigue 70 (2015) 395–405.
3. Qiao Hongchao. Applied Surface Science 351 (2015) 524–530.
4. M. J. Leap, J. Rankin, J. Harrison, L. Hackel, J. Nemeth, J. Candela. International Journal of Fatigue 33 (2011) 788–799.
5. R. Fabbro, J. Fournier, P. Ballard, D. Devaux, J. Virmont. Journal of applied physics 1990; 68: 775–84.
6. F. Z. Dai, J. Z. Lu, Y. K. Zhang, D. P. Wen, X. D. Ren, J. Z. Zhou. Applied Surface Science 316 (2014) 477–483.
7. Y. W. Fang, Y. H. Li, W. F. He, P. Y. Li. Materials Science & Engineering A 559 (2013) 683–692.
8. Sagar Bhamare, Gokul Ramakrishnan, Seetha R. Mannava, Kristina Langer. Surface & Coatings Technology 232 (2013) 464–474.
9. Benxin Wu, Sha Tao, Shuting Lei, Applied Surface Science 256 (2010) 4376–4382.
10. César A. Vázquez Jiménez, Gilberto Gómez Rosas, Carlos Rubio González, Vignaud Granados Alejo, Silvina Hereñú, Optics and Laser Technology 97 (2017) 308–315.
11. C. Rubio-González, C. Felix-Martinez, G. Gomez-Rosas, J. L. Ocaña, M. Morales, J. Porro, Mater. Sci. Eng. A 528 (2011) 914–919.
12. G. Ivetic, *et al*, Mater. Sci. Eng. A 534 (2012) 573–579.
13. V. Granados Alejo, C. Rubio Gonzalez, Y. Parra Torres, J. A. Banderas, G. Gómez-Rosas, Structural Engineering and Mechanics, Vol. 62, No. 6 (2017) 739–748.
14. P. Peyre, I. Chaieb, C. Braham, Model. Simul. Mater. Sci. Eng. 15 (2007) 205–221.
15. C. Correa A., Gil-Santos, J.A. Porro, M. Díaz, J.L. Ocaña, Materials and Design 79 (2015) 106–114.
16. Mohammed Asif. M, Kulkarni Anup Shrikrishana, P. Sathiya, Engineering Science and Technology, an International Journal 18 (2015) 704–712.
17. Peñuelas, I., Rodríguez, C., García, T.E., Belzunce, F.J., vol 258 (2014)8 22–831.
18. User manual, fe-safeTM 6 (2014), Durability Analysis Software, ©Safe technology limited, Volume 1 14–13.
19. K.S. Kim, X. Chen, C. Han, H.W. Lee, International Journal of Fatigue 24 (2002) 783–793.
20. Yingyu Wang, Luca Susmel, International Journal of Fatigue 83 (2016) 135–149.
21. V. T. Troshchenko, L. A. Khamaza. Strength of Materials, Vol. 42, No. 6, 2010.
22. X. Q. Zhang, *et al*. Materials and Design 65 (2015) 425–431.

Fracture Toughness of Fiber Metal Laminates Through the Concepts of Stiffness and Strain-Intensity-Factor

Jesús Gerardo Martínez Figueroa and Perla Itzel Alcántara Llanas

Introduction

There is no a great amount of bibliography regarding the fracture toughness of Fiber metal laminates (FMLs). Authors have focused to obtain critical fracture parameters. Fracture toughness has been experimentally determined in terms of the J-integral and the Crack Tip Opening Displacement (CTOD).

In the work of Rios [1] for carbon epoxy with aluminum 6061, it is concluded that the elastic-plastic approach seems to be suitable to examine the behavior of this type of materials. Castrodeza et al. [2] used the parameter *Jc* to estimate a critical crack length, and experimentally validated this proposal, showing that the fracture toughness of the Laminate is higher than those of each constituent evaluated separately. Afaghi et al. [3] studied the effect of stress concentrators and the adhesion inter-lamina on the crack propagation stability throughout the laminate. For the evaluation of the dynamic fracture behavior, Tarpani et al. [4] has used the Charpy pendulum in Titanium-Graphite FMLs, in that work the energy of crack propagation is reported. Among other studies in dynamic behavior of FML, Garcia [5] analyses the sensibility of structural elements to high-speed projectile impact and preloads.

The main purpose of this document is to describe a simple general methodology to analyze the fracture of FMLs based on a twofold approach: the use of a stiffness model and a Strain Intensity Factor concept, assuming linear elastic fracture mechanics (LEFM).

The laminate studied in this document is made of a composite carbon-epoxy DA-4518, called woven. It consist of plane weave of carbon fibers embedded in an epoxy resin. The second material is an aluminum alloy 2024-T3, consisting of

J. G. M. Figueroa (✉) · P. I. A. Llanas
Centro de Ingeniería y Desarrollo Industrial, Pie de la Cuesta 702,
Desarrollo San Pablo, 76130 Querétaro, Mexico
e-mail: jmtzfigueroa@gmail.com

R. R. Ambriz et al. (eds.), *Proceedings of the 17th International Conference on New Trends in Fatigue and Fracture*, https://doi.org/10.1007/978-3-319-70365-7_37

Table 1 Elastic properties, density of each material of the laminate

	Carbon-epoxy woven	Aluminum 2024-T3
E_x (GPa)	49.816	66.902
E_y (GPa)	53.34	66.902
ν_{xy}	0.048	0.3
G_{xy} (GPa)	3.51	25.731
ρ (kg/m^3)	1505.8	2780

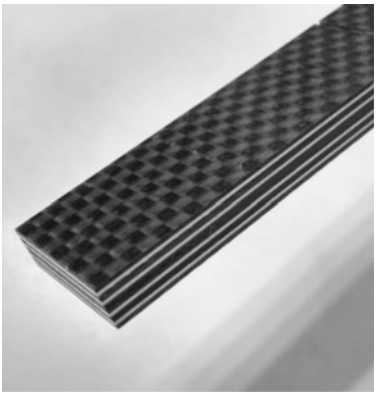

Fig. 1 Detail of woven-aluminum laminate specimen

sheets of 0.32 mm width, chemically treated (P2 etching) to assure optimal surface condition for adhesion with the woven resin. The woven is considered especially orthotropic with the same properties in the z and y directions. Both materials were tested separately to obtain their elastic constants, shown in Table 1.

The laminate was stacked-up in vacuum bag following the sequence [[0°/0°/0°/Al/0°/0°] s] s, where the 0° is the woven warp direction woven, and the rolling of the aluminum. The arrangement was cured in autoclave. The thickness of the cured laminate is 6.4 mm. A number of Single Edge Notch Bending (SENB) specimens were extracted and a slit that simulates the central crack. The specimen's dimensions are (Fig. 1):

- Total length: 100 mm (woven warp, x-direction)
- s = 80 mm
- a = 10 mm
- W = 20 mm

Analysis Approach: Stiffness Model and Strain Intensity Factor

Stiffness Model

FMLs are composed by alternated thin laminae. Here, it is assumed that each lamina supports a portion of the mechanical load and that all laminae of the same material behave similarly if the load on the specimens is distributed evenly throughout the laminate thickness. The expression of the Stress Intensity Factor (SIF) in modeI [6]:

$$K_I = F\frac{C_1}{B} \tag{1}$$

where F is the force applied, B is the specimen thickness and C_I is a specimen shape constant:

$$C_1 = \frac{f\left(\frac{a}{W}\right)}{\sqrt{W}} \tag{2}$$

According to [7] the SIF in function of the CTOD is:

$$K_I = CTOD(C_e)(C_2) \tag{3}$$

C_e is the elastic constant proposed in [7] and C_2 is a typical r-singularity function for LEFM:

$$C_2 = \frac{\pi}{\sqrt{2\pi r}} = \frac{1}{2}\sqrt{\frac{2\pi}{r}} \tag{4}$$

Equating expressions (1) and (3), the force received by the specimen, F is:

$$F = (CTOD)C_e(B)\frac{C_2}{C_1} \tag{5}$$

The product $C_e(B)$, is designed the Crack Tip Stiffness (CTS), as it represents the force necessary to open the Crack tip by 1 length unit. Expression (5) is analogous to the linear spring model, where the spring deflection is substituted by the CTOD, and a convenient range of r should be defined. When two or more springs are connected in parallel, the total stiffness of the ensemble is the sum of the individual stiffness and the force received by each spring is proportional to its individual stiffness. The behavior of FML specimens can be investigated as an ensemble of linear springs, each spring representing the particular elasticity and total laminae thickness of each material. Consider the SENB specimen loaded in three-point-bending in Fig. 2, composed by many laminae of 2 different materials A and B, each material having a particular stiffness $CTS_{A,B}$.

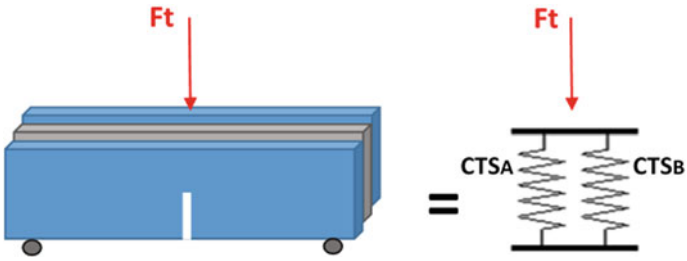

Fig. 2 SENB specimen of a 2-material laminate, modeled as two springs in parallel

The thickness of each spring is split in the material's total number of laminae. The total specimen's rigidity is the sum of the two particular rigidities. The total force *Ft* can be separated into two forces. If a common CTOD is imposed the next formulae can be proposed:

$$F_{A,B} = (CTOD)CTS_{A,B}\frac{C_2}{C_1} \tag{6}$$

$$F_A + F_B = F_t \tag{7}$$

$$\frac{F_A}{F_B} = \frac{CTS_A}{CTS_B} \tag{8}$$

The model can be extended for three or more materials. The CTOD substitutes the typical displacement δ of the force-application point and must be the same for both materials. Expressions (6)–(8) are the reference stiffness model proposal of this work.

Strain Intensity Factor for Isotropic and Especially Orthotropic Plane Stress

The Strain Intensity Factor K_ε in this work is a parameter to be related to the SIF of each material of the FML. In front of the crak tip (θ = 0°) the crack-plane-normal strain profile, ε_I is defined as:

$$\varepsilon_I = \frac{K_\varepsilon}{\sqrt{2\pi r}} \tag{9}$$

The constitutive stress-strain equations for isotropic materials in plane stress [8]:

$$\varepsilon_x = \frac{\sigma_x}{E} - \frac{v}{E}\sigma_y, \quad \varepsilon_y = \frac{\sigma_y}{E} - \frac{v}{E}\sigma_x, \quad \gamma_{xy} = \frac{\tau_{xy}}{G} \tag{10}$$

In LEFM mode I, there is no shear stress in the crack plane. Also the x and y normal stresses are:

$$\sigma_x = \sigma_y = \frac{K_I}{\sqrt{2\pi r}} \tag{11}$$

Combining Eqs. (10) and (11), the strain profile is:

$$\varepsilon_I = \frac{K_I}{\sqrt{2\pi r}} \left[\frac{1-\nu}{E} \right] \tag{12}$$

A similar arrangement for especially orthotropic materials in plane stress [8]:

$$\varepsilon_x = \frac{\sigma_x}{E_x} - \frac{\nu_{yx}}{E_y}\sigma_y, \quad \varepsilon_y = \frac{\sigma_y}{E_y} - \frac{\nu_{xy}}{E}\sigma_x, \quad \gamma_{xy} = \frac{\tau_{xy}}{G_{xy}} \tag{13}$$

According to [9], being the x-direction normal to the crack plane, the principal stresses are:

$$\sigma_x = \frac{K_I}{\sqrt{2\pi r}}, \quad \sigma_y = r'\sigma_x \tag{14}$$

where r' is an orthotropic stress ratio. The Strain profile in plane stress expressed by combining Eqs. (13) and (14) is:

$$\varepsilon_I = \varepsilon_x = \frac{K_I}{\sqrt{2\pi r}} \left[\frac{1}{E_x} - \frac{r'\nu_{yx}}{E_y} \right] \tag{15}$$

Having defined $K\varepsilon$ in (9), it can be expressed in terms of K_I as:

$$K_\varepsilon = K_I C_\varepsilon \tag{16}$$

$$C_\varepsilon = \frac{1-\nu}{E} \quad \text{(Isotropic plane stress)} \tag{16.1}$$

$$C_\varepsilon = \frac{1}{E_x} - \frac{(r')\nu_{yx}}{E_y} \quad \text{(Especially orthotropic plane stress)} \tag{16.2}$$

The term C_ε is called here constitutive coefficient. Equations (11) and (14) come from the assumption of a crack in an infinite elastic field. In praxis the ratio σ_y/σ_x is different from 1 so an r' for ν is required in (16.1); it also differs from the ideal orthotropic r' by [9]. This is due to finite-geometry restrictions in real practice. However, the following expression of C_ε is easily deduced:

$$C_\varepsilon = \frac{K_\varepsilon}{K_I} = \frac{\varepsilon_I}{\sigma_I} \tag{17}$$

In this manner, constitutive coefficients can be obtained empirically as the ratio of the reference stress and strain in front of the crack tip.

Finite Element Analysis

Model, Load and Restraints Description

The Finite Element Model, made in ANSYS® is presented in Fig. 3. A SENB specimen described in Section "Introduction" was modeled with 4-node quadrilaterals and plane stress option declared with the total thickness of each material. There are two sets of elements and nodes overlapped with the same exact mesh, located in the same coordinates. Material 1 is the woven, modeled as an especially orthotropic solid. Material 2 is the isotropic alloy 2024-T3. The elastic properties and density are declared as in Section "Introduction". The reference parameters used in this analysis are listed in Table 2. Five load cases were run for every run the supporting nodes were restraint in x and y direction as shown in Fig. 3. The first load case (Lc1) applies loads to the woven and aluminum separately, each one receiving the proportional force fraction from a total force Ft of 500N. In load case 2, a displacement δ is imposed at the two application nodes obtained from the Load case 1 (-1.14819×10^{-4} m in y). Also a node-to-node coupling (each pair of nodes in the same location) in the x and y degrees-of-freedom is applied to both models. This assures the same displacement field for both geometries, including the CTOD.

Load cases 3–5 have the same restrictions and couplings as Lc2, except that the displacements δ were calibrated to correspond to higher values of Ft:

- Lc3: −2.29638e−4 m for Ft = 1000N
- Lc4: −3.44457e−4 m for Ft = 1500N
- Lc5: −4.59276e−4 m for Ft = 2000N

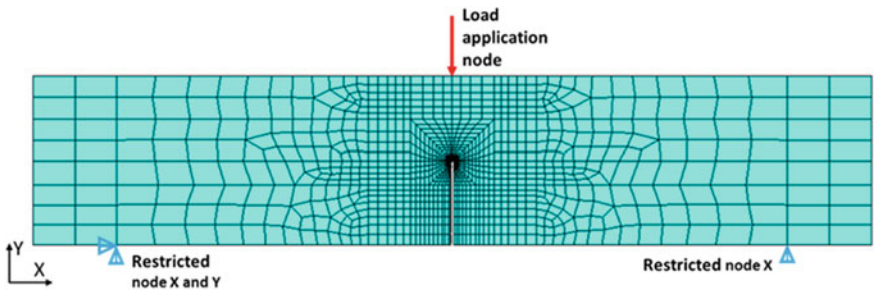

Fig. 3 FEA model geometry, load and restrictions

Table 2 Reference parameters of the two materials comprising the laminate FEA model

	Carbon-epoxy woven	Aluminum 2024-T3
C_1 ($\sqrt{m}$)	75.3068	75.3068
Ce (GPa)	12.8752	33.451
B (m)	0.00512	0.00128
CTS (N/m)	6.5921E+07	4.2817E+07
F(N)	303.132	196.878
K_I (MPa $\sqrt{m}$)	4.458578	11.58302
Cε (Pa^{-1})	1.9144E−11	1.0463E−11

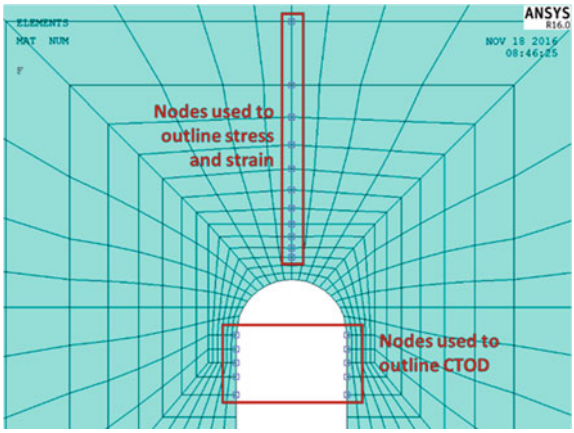

Fig. 4 Crack tip mesh detail and nodes used to outline stress, strain and CTOD

Figure 4 shows the crack tip mesh and the nodes used to trace the profiles of stress, strain and CTOD. The crack is a 0.4 mm width slit with a semicircle-shaped tip. This is because specimens used in this work have this geometry. The meshing has been validated to behave according to LEFM in background work [7].

FEA Results

A comparison between Lc1 (the two materials deforming freely) and Lc2 (coupling, perfect bonding) is presented in Fig. 5a, b showing the effect of the coupling on stress and CTOD profiles. The stiffness model straightforwardly predicts the same CTOD for both materials as they have equal parameters C_1, and C_2.

The dotted lines are the reference profiles from the stiffness model and parameters of Table 2. Deviations (errors) are reported with respect to these references. The nodal coupling creates an increase in the woven stress profile. The error of the

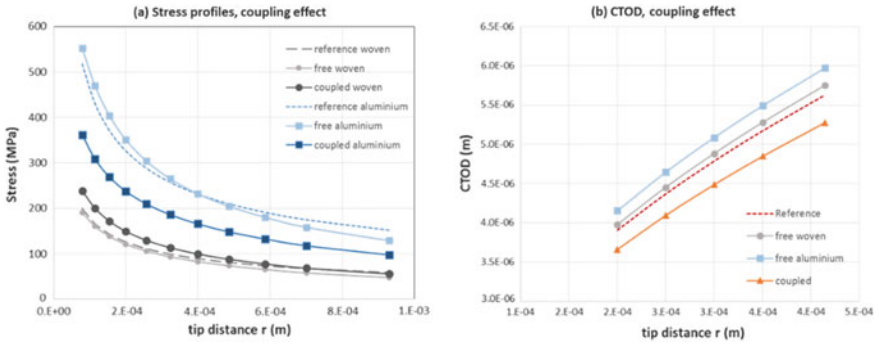

Fig. 5 Coupling effect in **a** stress profiles. **b** CTOD profiles

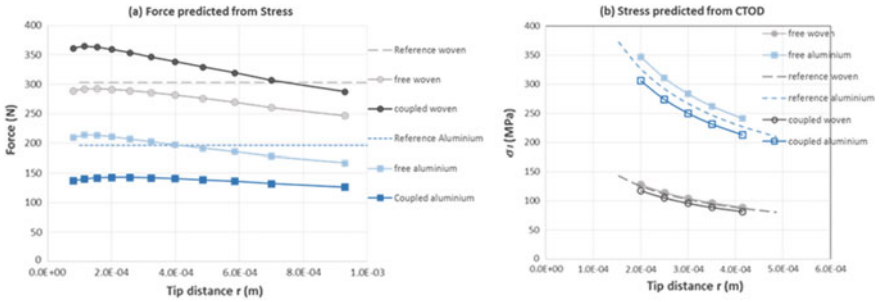

Fig. 6 **a** Forces from nodal stress profiles. **b** CTOD-derived stress profiles

free case (Lc1) ranges from −3.5 to −18% with increasing r, the coupling effect (Lc 2) offsets this error to a range from 20 to −5%. The effect on aluminum is an important decrease: from a free case error range from 8.7 to −15%, the coupled stress error varies from −27.3 to −35.7%. The free CTOD of the woven is around 2% higher than the reference, the free aluminum CTOD, by 6%. The coupled CTOD is smaller than the reference profile, by 6.3%. The force expected to be taken for each material can be predicted from the stress profiles by combining Eqs. (3), (5) and (12), and from K_I using Eq. (1), as presented in expression (18), remarking the independence from the material elastic properties of the relation of F to σ_I and K_I. This force prediction is shown in Fig. 6a. The error percentages of the forces and K_I are the same as those in the stress profiles.

$$F = \frac{B\sigma_I}{C_1}\sqrt{2\pi r} = \frac{BK_I}{C_1} \tag{18}$$

The stress profiles from the diametrically opposed CTOD presented in Fig. 6b are obtained according to the simplified form reported in [7]:

$$\sigma_I = \frac{CTOD(C_e)}{2r} \tag{19}$$

From the stress profiles obtained from the CTOD, it can be noted that the reduction of stress and eventual force and K_I calculated from it will remain small and at a constant variation of −6% for both materials.

This is consistent with the decrease of CTOD due to the coupling observed in Fig. 5b. However, it is not with respect to the stress and force offsets observed in Figs. 5a and 6a.

Strain Analysis

The nodal strains ε_I from lc1 and lc2 are presented in Fig. 7a. The very good coincidence in the coupled strain profiles is in accordance with the displacement field imposed by the coupling: The free strain profiles are taken to a single trace in-between, which can be used to obtain a single strain intensity factor.

Constitutive coefficients, obtained using the direct nodal stress-strain ratio are shown in Fig. 7b. For both materials, maximum $C\varepsilon$ values are higher than the reference (25% for aluminium, 4% for woven), approaching to it as r increases. For a single value of $K\varepsilon$ useful for woven and aluminum, Eq. (10) is used and the nodes selected are those of the minimal difference of this value between both materials (1%): the nodes at r = 1.5415e−4 m, $K\varepsilon$ = 1.05678e−4 $\sqrt{\text{m}}$.

The results of the next load cases are listed in Table 3. With the selected value of $K\varepsilon$, an exact proportionality for load cases 3–5 has been verified. The load application forces match well the stiffness model reference, but the supporting forces are redistributed: the woven takes an extra fraction of the total force that would correspond to the aluminum, for lc2 is 44.36N (8.8% of the total force).

The CTOD does not seem to be appropriate to predict Stress profiles and fracture parameters for the coupled materials: it is not consistent with the rest of results because only a slight reduction of about 6% of stress and loads for both materials is

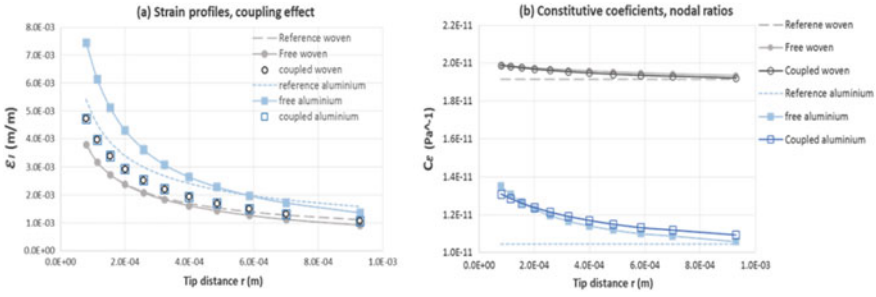

Fig. 7 **a** Coupling effect in strain profiles. **b** Constitutive coefficients comparison

Table 3 Selected fracture parameters and nodal forces obtained from load cases 2 to 5

	Lc 2 (500N)		Lc 3 (1000N)		Lc 4 (1500N)		Lc 5 (2000N)	
	Woven	Aluminum	Woven	Aluminum	Woven	Aluminum	Woven	Aluminum
load point δ (m)	-1.14819×10^{-4}		-2.29638×10^{-4}		-3.44457×10^{-4}		-4.59276×10^{-4}	
Kε ($\sqrt{m}$)	1.05678×10^{-4}		2.11356×10^{-4}		3.17034×10^{-4}		4.22712×10^{-4}	
KI (MPa $\sqrt{m}$)	5.3472	8.2947	10.6945	16.5894	16.0417	24.8841	21.389	33.1789
load point force (N)	−304.64	−195.36	−609.29	−390.72	−913.93	−586.07	−1218.6	−781.46
Supports reactions (N)	349	151	697.98	302.02	1046.98	453.02	1395.98	604.02

predicted due to the coupling. The stress and strain profiles, and the reactions queried, suggest an important redistribution of the load with respect to the stiffness model: an increase estimated between 15 and 20% for the woven, and a decrease of between 23 and 35% for the aluminum. The FEA quantification of the coupling effect can be considered a conservative baseline, as the real interlaminate adhesion is not perfectly rigid: actual behavior can be reasonably placed between the ideal free-material reference and the nodal coupling described.

Experimental Activities

Static Fracture Toughness Procedure and Results

A total of 5 SENB specimens were tested according to standard ASTM1820 [10] in an Instron 8872 machine. Each specimen was placed in the fixture base using dough to avoid slipping, as shown in Fig. 8. The load applied slowly at the mid-span edge of the specimen was recorded along with the displacement of the applying roller. The results are presented in Fig. 9 and Table 4. These tests had previously been simulated and analyzed in Section "Strain Intensity Factor for Isotropic and Especially Orthotropic Plane Stress" for F_t values of up to 2 kN.

According to the ASTM standard, the fracture toughness is the value of K_I using Eq. (1) and a critical force, F_Q interpreted as the limit beyond which the crack tip region loses LEFM validity and the specimen starts collapsing. One single value of K_I for each F_Q is not reported. Instead, there is one single value of K_ε related to the SIF of each material using the corresponding C_ε. The FEA results briefed in Table 3

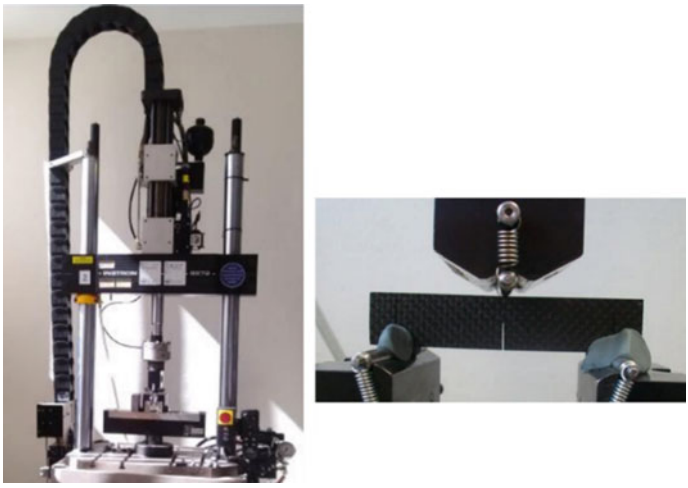

Fig. 8 Machine and fixture for quasi static tests

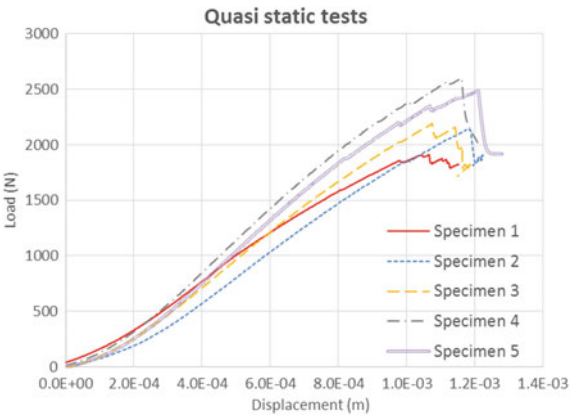

Fig. 9 Load-displacement plots of quasi-static tests

Table 4 Results of static fracture toughness tests

Specimen	F_{max} (N)	F_Q (N)	$K\varepsilon_C$ ($\sqrt{m}$)
1	1910.2	1910.2	4.0373E−04
2	2137.8	2063	4.3603E−04
3	2193.7	2193.7	4.6365E−04
4	2602.7	2370	5.0091E−04
5	2486.9	2267	4.7914E−04

Strain fracture toughness

are extrapolated in order to obtain a single value of Strain Intensity Factor for each specimen F_Q, so it can be considered the Strain Fracture Toughness, as $K\varepsilon_C$ ($\sqrt{m}$) in Table 4.

The strain fracture toughness has an average value of 4.567e−4 $\sqrt{m}$. This value and references C_ε gives a SIF for aluminum of 43.65 MPa $\sqrt{m}$ and 23.86 MPa $\sqrt{m}$ for the woven. The stiffness model using the average F_Q as Ft predicts 50.056 for the aluminum and 19.2675 for the woven. The effect of the rigid coupling is now observed in each material being −12.8 and +23.8% respectively. This variation should be considered as a maximum expected because of two reasons. First: the rigid coupling is not realistic as it has been already discussed, and second: C_ε constants used are the theoretical values from each materials' elastic properties, but they have been shown to be slightly increased as described in the previous section.

If Eq. (1) is used to obtain a comparative *SIF* with the specimens width (6.4 mm) and the average F_Q (2160.78N) a single K_{IC} of 25.425 MPa $\sqrt{m}$ is obtained. It is important to recall the need of plane strain conditions to assure that the specimens fracture toughness be considered a property of the material tested. In this case there is no way to comply with this condition as the specimen is made of thin laminae of two different materials.

Dynamic Fracture Toughness Procedure and Results

Four specimens were examined in Hopkinson bars in three-point-bending (3 PB) configuration. The schematic of the experimental device is shown in Fig. 10. The pressure bars (1800 mm) and the striker bar (156 mm) are made of 19.05 mm diameter high strength steel (Maraging C300, E = 190e9 Pa, ν = 0.29, ρ = 8000 kg/m^3). The specimens were placed between the bars and rapidly loaded in dynamic regimen at the same locations as in the static tests. A strain gage is carefully cemented close to the notch tip of each specimen, 1 mm up and 1 mm to the left to the slit tip. The strain gages signals were conditioned, visualized and stored into an oscilloscope, recorded at a sampling rate of 1 μs. Recent work [7, 11] shows that the use of the incident bar tip speed in the FEM yields less scatter than the bar tip force, in the results obtained by this methodology. This speed is calculated as:

$$V_1 = C_0(-\varepsilon_i + \varepsilon_r) \tag{20}$$

C_0 is the elastic wave speed of the bars (4873.4 m/s), and εi and εr are the experimental incident and reflected pulses on the incident bar. The FEM of Section "Stiffness Model" has been complemented to extract the evolution of $K\varepsilon$ during the dynamic tests. Standard contacts have been declared in the bars tips locations using their profile lines.

V_I, is then applied to a pilot node directing the incident bar tip profile line. The transmitter bars are modeled as links elements with the cross-section of the bar and the same tip lines, as shown in Fig. 11. Each experiment was simulated in transient analysis during 100 μs. The analyses of these simulations showed loss of contact with the three bars, in a very similar manner as reported in background studies [7, 11]. K_ε was obtained with the progression of nodal strain ε_I at r = 1.5415e−4 m, the same location as in Section "Stiffness Model", and the values of ε_I are also practically the same for both materials. The velocity V_I and the evolution of K_ε for each

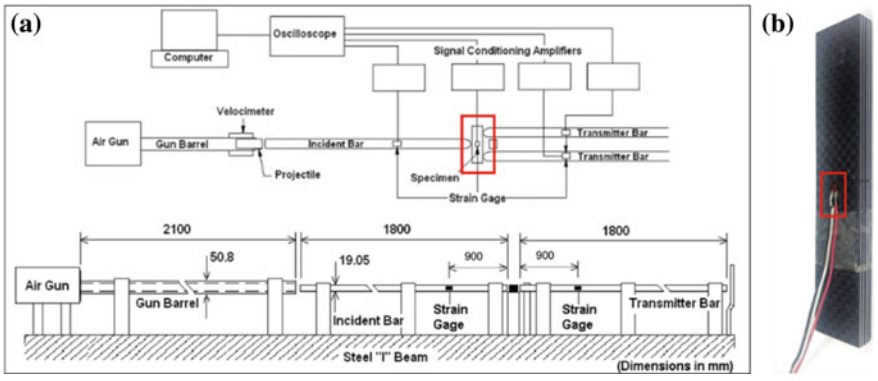

Fig. 10 **a** Experimental device for dynamic tests. **b** Specimen with strain gage

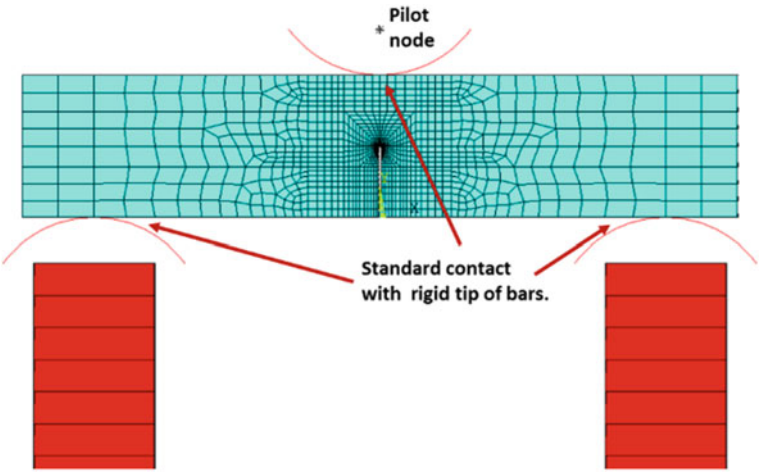

Fig. 11 FEM for dynamic fracture toughness tests

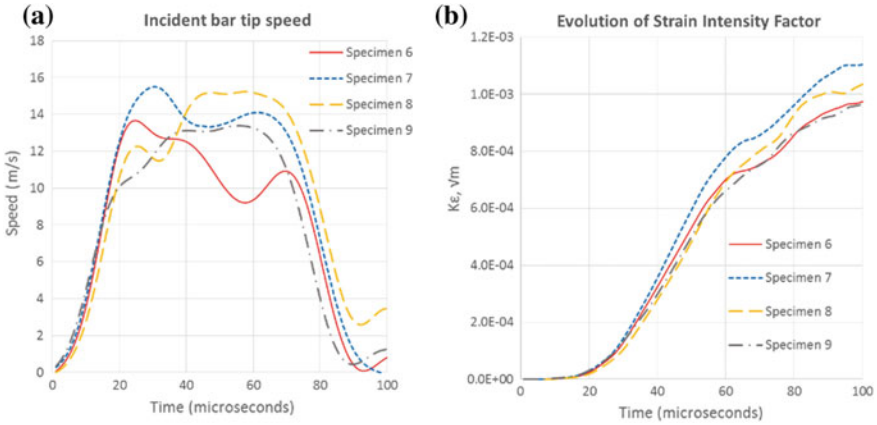

Fig. 12 **a** Incident bar tip speeds. (b) Evolution of Kε

experiment are presented in Fig. 12a, b respectively. The strain fracture toughness is the value of K_ε at the instant of specimens' strain gage signal drop (time-to-fracture).

The projectiles speed, time to fracture and strain fracture toughness ($K\varepsilon_D$) of the dynamic tests are presented in Table 5. The average $K\varepsilon_D$ is 4.619×10^{-4} $\sqrt{m}$. This is a very similar value to the one obtained in quasi static tests, so there seems to be no influence of the load rate on the fracture toughness evaluated in this laminate. The corresponding SIF for each material can also be obtained with the corresponding values of $C\varepsilon$. However, it is important to consider that this coefficients may be load-rate dependent as they are function of each materials elastic properties.

Table 5 Results of dynamic fracture toughness tests

Specimen	Projectile speed (m/s)	Time to fracture (μs)	$K\varepsilon_D$
6	16.86	44	4.0800×10^{-4}
7	16.63	45	4.7530×10^{-4}
8	17.23	51	5.0516×10^{-4}
9	15.45	48	4.5925×10^{-4}

Conclusions

This document investigates the fracture behavior of a woven-aluminum FML by a twofold approach. A stiffness model and the concept of strain intensity factor.

This proposal remains in the LEFM domain and is useful if precise behavior and interactions among laminae (shear forces, delamination, interlaminate cracks) are not needed. The values reported are considered high because of a number of remarks: plane stress conditions have been assumed; the adhesion interlaminates is considered perfectly rigid and ideal constitutive coefficients have been used.

In the other hand, K_ε is defined to be translated to K_I for each material of the Laminate, and it is not an equivalence of the concept of K_I to formally describe strain fields around the crack tip.

Finite Element Analyses have been used to verify this approach. Being the stiffness model the reference, the adhesion among laminas, modeled as nodal rigid coupling is a conservative assumption. This condition is observed to cause a redistribution of the load, transferring about 9% of the total force from the aluminum to the woven. This redistribution causes a SIF variation of −13% for the metal and +24% for the composite.

Experimental activities were carried out to obtain the fracture toughness as the critical value of K_ε. The quasi-static tests show an average of $4.567 \times 10^{-4} \sqrt{\text{m}}$. For the dynamic tests, the average value of $K\varepsilon_D$ is $4.619 \times 10^{-4} \sqrt{\text{m}}$, so there seems to be no difference between the static and dynamic fracture toughness for this FML.

The methodology to obtain fracture toughness in SENB specimens remains the same as for typical monolithic materials. The stiffness approach provides a straightforward estimation of the load distribution and SIF for each material. The Strain Intensity Factor proposed is useful as a single indicator of the fracture toughness of the FMLs examined for static and dynamic regimes and can be associated to the SIF of each constitutive material. Accordingly, the activities described in this document provide a useful proposal to perform baseline measurements of fracture toughness for FML.

References

1. J. C. Ríos, E. Chomik, J. J. Balderrama, F. Cambiasso, and E. Asta, "Determination of Fracture Toughness J on Fiber-metal Laminate Type CARALL with Sheets of Aluminium 6061," Procedia Mater. Sci., vol. 9, pp. 530–537, 2015.
2. E. M. Castrodeza, F. L. Bastian, and J. E. P. Ipina, "Critical fracture toughness, J(C) and delta (5C), of unidirectional fibre-metal laminates," Thin-Walled Struct., vol. 41, no. 12, pp. 1089–1101, 2003.
3. A. Afaghi-Khatibi, G. Lawcock, L. Ye, and Y.-W. Mai, "On the fracture mechanical behaviour of fibre reinforced metal laminates (FRMLs)," Comput. Methods Appl. Mech. Eng., vol. 185, no. 2–4, pp. 173–190, 2006.
4. J. R. Tarpani, O. Maluf, and C. M. Adami Gatti, "Charpy Impact Toughness of Conventional and Advanced Composite Laminates for Aircraft Construction 3. Materials and Test Specimens," Mater. Res., vol. 12, no. 4, pp. 395–403, 2009.
5. S. García, E. Barbero, and C. Navarro, "Análisis De Laminados De Materiales Compuestos con Precarga En Su Plano Y Sometidos a Impacto," p. 183, 2007.
6. Anderson, T. L., Fracture Mechanics: Fundamentals and Applications, CRC Press, Boca Raton, FL, 2012.
7. Martínez-Figueroa, J., Rubio-Gonzalez, C., Velasco-Reyes, F., and Benseddiq, N., "Dynamic Fracture Toughness of a Plain Weave Carbon-Epoxy Composite: Validation of Test Results with Finite Element Analyses," Materials Performance and Characterization, Vol. 3, No. 3, 2014, pp. 489–505.
8. Mallick, Pankar K. "Fiber-reinforced composites: materials, manufacturing, and design". CRC press, 2007.
9. Williams J.G. (1989) fracture mechanics of anisotropic materials, in K. Friedrich, ed. "Application of fracture mechanics to composite materials", Elsevier.
10. ASTM E1820-17, "Standard Test Method for Measurement of Fracture Toughness", ASTM International, West Conshohocken, PA, 2017.
11. Martínez-Figueroa, J., C. Rubio-Gonzalez, and F. Velasco-Reyes. "Three point bending Hopkinson bar for fracture toughness measurement: A new approach for interface analysis." Materialwissenschaft und Werkstofftechnik 46.4–5 (2015): 505–514.

Uncertainty Quantification of Fatigue Life Prediction in Welded Structures Using Microstructure-Based Simulations

Takayuki Shiraiwa, Fabien Briffod and Manabu Enoki

Introduction

Fatigue performances of welded structures are affected by many factors such as loading, materials properties, microstructures, geometry and boundary conditions. Under such background, various numerical simulation techniques related to fatigue in the welded joints have been proposed. The phase field method is one of the promising methods to predict the complex microstructure, and the crystal plasticity model which accounts for the physical deformation mechanisms such as crystallographic slip and twinning have been received considerable attention in recent years. The prediction of the fatigue crack initiation life based on the microstructure and crystal plasticity have been conducted actively. The extended finite element method (X-FEM) is a powerful and widely used tool to predict the fatigue crack propagation. However, most of these studies have not explicitly taken account of the uncertainty such as data uncertainty, model uncertainty and error. It is essential to systematically account for these sources of uncertainties in order to ensure the scattering in fatigue life of welded structures. The objective of this study is to develop an extensible framework for uncertainty quantification of fatigue life prediction in welded structures by integrating aforementioned computational techniques. The computing system that automatically executes a series of these calculations has been constructed. As an example, a fatigue problem in widely used butt joint with low carbon steel (0.15% C) was assessed by the proposed method.

T. Shiraiwa (✉) · F. Briffod · M. Enoki
Department of Materials Engineering, The University of Tokyo,
Tokyo 113–8656, Japan
e-mail: shiraiwa@rme.mm.t.u-tokyo.ac.jp

R. R. Ambriz et al. (eds.), *Proceedings of the 17th International Conference on New Trends in Fatigue and Fracture*, https://doi.org/10.1007/978-3-319-70365-7_38

Analytical Methods

Overview of proposed method for predicting fatigue life of welded joints is shown in Fig. 1. In the first part of the proposed method, various material properties were calculated from chemical composition, using commercial software JMatPro v9.0. The continuous cooling transformation (CCT) diagram, density, specific heat, thermal conductivity, Young's modulus, Poisson's ratio, coefficient of thermal expansion, yield stress, and hardening slope were derived from the chemical composition shown in Table 1. The second step is a welding simulation to analyze the residual stress and the microstructure distribution. A two-dimensional finite element model was created by Abaqus CAE 6.14 based on the shape parameters such as plate thickness and the toe radius. The heat input distribution was defined by the Goldak's double-ellipsoidal heat source model [1]. The heat source traveled along the center line of the plate at a speed of 1 mm/s. The total amount of the heat input was defined by 1.5 kJ/mm. After the single-pass welding is completed, the butt joint was allowed to cool down to room temperature. In the phase transformation analysis, diffusion type and martensitic type phase transformations were predicted by Kolomogorov-Johnson-Mehl-Avrami (KJMA) model [2] and Koistinen-Marburger (KM) model [3], respectively. The distribution of Vickers hardness was also derived from the chemical composition and the cooling rate at 700 °C (V_r) according to the following empirical equations [4]. The austenite grain size was also calculated by the incremental equation proposed by Leblond and Devaux [5]. After the heat transfer analysis coupled with the phase transformation, thermal-elastic-plastic analysis was performed to calculate the residual stress based

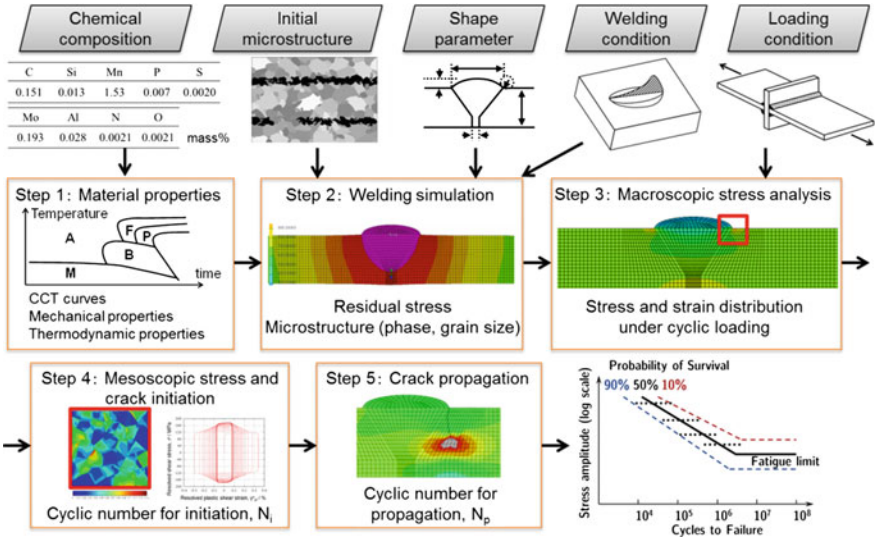

Fig. 1 Overview of proposed method for predicting fatigue life of welded joints

Table 1 Chemical composition of 0.15C steel (mass%)

	C	Si	Mn	P	S	Mo	Al	N	O
0.15C steel	0.151	0.013	1.53	0.007	0.0020	0.193	0.028	0.0021	0.0021

on the temperature distribution and phase transformation histories calculated by the heat transfer analysis. The third step is the macroscopic stress analysis. The input data of this step were hardness distribution, residual stress distribution obtained from the previous step, and loading condition. Based on the hardness distribution, the finite element model used in the previous step was divided into 10 regions, and different stress-strain curves were given to each region. The stress-strain curves were calculated by rule of mixtures. Before loading, all components of residual stress were introduced into the model. The model was subjected to 10 cyclic loadings with a stress ratio $R = -1$ and seven different stress amplitudes: 100, 150, 200, 300, 400, 500, and 600 MPa.

The forth step is analysis of mesoscopic stress field and crack initiation using crystal plasticity finite element method (CP-FEM). The geometry of the model was cut out from the region around the highest stress location in the macroscopic model. This region was assumed to be martensite single phase because the volume fraction of martensite was predicted to be approximately 100% in the second step. The average grain size of prior austenite was determined by referring to the grain size distribution calculated in the second step. The synthetic grain morphology was generated by a tessellation technique described in the previous paper [6]. In order to simulate the elastic-plastic deformation behavior of the microstructural model, the phenomenological constitutive law proposed by Hutchinson [7] was used within the Düsseldorf advanced material simulation kit (DAMASK) [8]. A non-linear kinematic hardening is also modeled by Armstrong–Frederick hardening law [9]. The elastic constant and a part of the crystal plasticity parameters were taken from the literature [6, 10]. The boundary condition of this simulation was defined by the displacement field of the macroscopic model. The crack initiation analysis was carried out based on the Tanaka-Mura model [11] which considers the irreversible energy accumulated over the slip band. The number of cycles for crack initiation, N_i, is calculated by

$$N_i = \frac{8GW_s}{\pi(1-\nu)d\left(\Delta\tau^{\alpha} - 2\tau_c^{\alpha}\right)^2} \tag{1}$$

where G is the shear modulus, W_s is the fracture surface energy per unit area, ν is the Poisson's ratio and d is the length of the slip band. The fracture surface energy was defined as $W_s = 2.0$ kJ/m^2 according to Hoshide and Kusuura [12]. The value of N_i was evaluated by averaging over the potential crack path defined parallel to the slip line. This analysis procedure follows the previous study [6]. Additionally, seven different microstructural models were randomly created using the same procedure and the same average grain size in order to evaluate the scattering in the crack initiation life.

The last step is the fatigue crack propagation analysis using X-FEM. The position and length of the initial crack obtained in the previous step was introduced into the macroscopic model. The crack growth rate was calculated from Paris' law. The stress intensity factor was computed by the virtual crack closure technique [13] within Abaqus. The constants were defined as $C = 2.7 \times 10^{-11}$ m/cycle and $m = 2.75$ according to the fatigue design recommendation for welded steel structures [14]. The system that automatically executes a series of calculations from the first step to fifth step has been constructed by python scripts.

Results and Discussion

A cumulative plastic shear strain in each slip system when the applied stress range was 300 MPa is illustrated in Fig. 2. Overall, the cumulative shear plastic strain showed a high value in the vicinity of the weld toe. As shown in the figure, the plastic strain exhibited quite heterogeneous distribution due to the difference of the crystal orientation. The value of N_i was evaluated by Eq. (1) for all slip planes and slip directions of each grain, and the crack is assumed to initiate at the slip system having the minimum N_i. In many cases, the crack initiation occurred from the surface near the weld toe. A series of simulations were conducted for a total of 49 times with a combination of seven stress levels and seven different microstructural models. All the results are plotted in Fig. 3. The open circle symbols are the crack initiation, and the closed symbols are the total number of cycles to failure. The fatigue design curves of the class C recommended by Japanese Society of Steel Construction (JSSC) [14] are also shown in the figure. The class C is classification of the butt joint with finished weld toe. The squared symbols are experimental

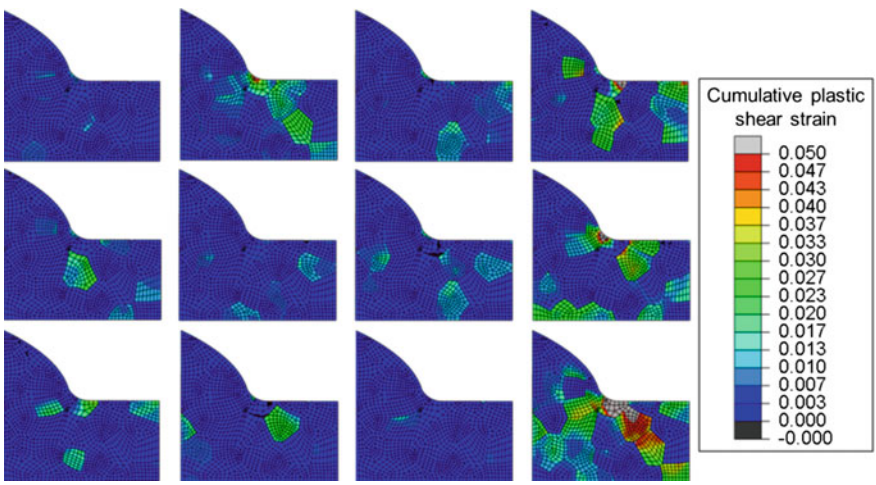

Fig. 2 Example of cumulative plastic shear strain in each slip system ($\Delta\sigma = 300$ MPa)

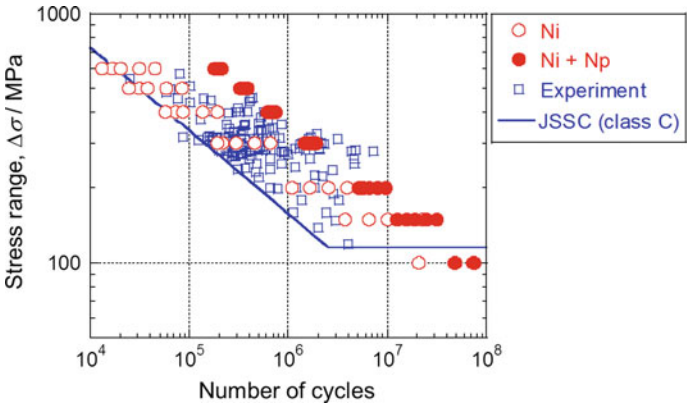

Fig. 3 Predicted fatigue life and the fatigue design curve recommend by JSSC [14]

results in the JSSC recommendation book [14]. Compared to the experimental results, the simulation provided the prediction of longer life than experimental results. This is because the current simulation assumed the completely smooth weld toe, while there is a complex shape or defects inducing stress concentration in the actual situation. As a result, the simulation predicted the fatigue life on the non-conservative side. In a different perspective, the scattering of the fatigue life increased with decreasing the stress level. Under the high stress range, the effect of the microstructure is relatively small because the most of the lifetime is spent on crack propagation. On the other hand, large scattering appeared in high cycle region. The proportion of N_i occupying N_f (number of cycles to failure) increased with the fatigue life. This indicated that the scattering in fatigue life is mainly due to the crack initiation. Similar trends were observed in the experiments of fillet welded specimens [15]. Thus, the possibility of evaluating the scattering of fatigue life using the proposed framework was demonstrated.

Conclusions

In this work, an extensible framework for uncertainty quantification of fatigue life prediction in welded structures was proposed and applied to the butt welding joint with low carbon steels. The following conclusions were drawn.

1. The proposed framework to predict the fatigue life has been developed by implementing the advanced computational techniques such as welding simulation, CP-FEM and X-FEM.

2. The mesoscopic stress field was calculated by CP-FEM and the crack initiation life was evaluated by the Tanaka-Mura model. The plastic shear strain exhibited a heterogeneous distribution due to the crystal orientation. The crack initiation was predicted at the vicinity of the weld toe.
3. Further improvement of this framework is expected by implementing uncertainty quantification and propagation analysis.

Acknowledgements This work was partially supported by the Cross-ministerial Strategic Innovation Promotion Program (SIP)—Structural Materials for Innovation—unit D62 operated by The Cabinet Office, Japan, and Japan Society for the Promotion of Science KAKENHI (Grant Number 17K14832).

References

1. J. Goldak, A. Chakravarti, M. Bibby, Metall. Trans. B, 15 (1984) 299–305.
2. A. Kolmogorov, Izvestia Akademia Nauk Serie Mathematica SSSR, 1 (1937) 355–359.
3. D.P. Koistinen, R.E. Marburger, Acta Metall., 7 (1959) 50–60.
4. R. Blondeau, P. Maynier, J. Dollet, Mémoires scientifiques de la Revue de métallurgie, 70 (1973) 883–892.
5. J.B. Leblond, J. Devaux, Acta Metall., 32 (1984) 137–146.
6. F. Briffod, T. Shiraiwa, M. Enoki, Materials Science and Engineering: A, 695 (2017) 165–177.
7. J.W. Hutchinson, Proceedings of the Royal Society of London. A. Mathematical and Physical Sciences, 348 (1976) 101–127.
8. F. Roters, P. Eisenlohr, C. Kords, D.D. Tjahjanto, M. Diehl, D. Raabe, Procedia IUTAM, 3 (2012) 3–10.
9. C.O. Frederick, P.J. Armstrong, Mater. High Temp., 24 (2007) 1–26.
10. D.D. Tjahjanto, S. Turteltaub, A.S.J. Suiker, Continuum Mech. Thermodyn., 19 (2008) 399–422.
11. K. Tanaka, T. Mura, J. Appl. Mech., 48 (1981) 97–103.
12. T. Hoshide, K. Kusuura, Fatigue & Fracture of Engineering Materials & Structures, 21 (1998) 201–213.
13. E.F. Rybicki, M.F. Kanninen, Eng. Fract. Mech., 9 (1977) 931–938.
14. JSSC, Fatigue Design Recommendations for Steel Structures, Gihodo, Tokyo, Japan, 2010.
15. N. Tagaki, A. Kondo, K. Yamada, Y. Kikuchi, Journal of Japan Society of Civil Engineers, 324 (1982) 151–159.

Prediction of Fatigue Life Induced by Defects Considering Crack Initiation

Ryota Sakaguchi, Takayuki Shiraiwa and Manabu Enoki

Introduction

Fatigue is the principal cause of mechanical failure and defects such as inclusions and void can be the origin of fatigue failure particularly in welding and casting materials. It is not practically possible to always avoid the defects and it is important to consider the effect of the defects on the fatigue properties. A large number of experiments are required to obtain a statistically representative distribution of the fatigue properties. Therefore the prediction of fatigue properties by representing characteristic variations of defects with probability distribution functions has been investigated [1]. In the case of the fatigue life, defects have been considered as pre-existent crack and the crack propagation laws have been used to predict the fatigue life in the conventional approach [2]. Most of the prediction methods of fatigue life have not considered the life spent in crack initiation. However, it is suggested that the crack initiation may consume considerable part of the total fatigue life in high cycle fatigue even if the fatigue failure is induced by defects [3].

The objective of this research is to improve the prediction of fatigue life arising from the defects by considering the crack initiation. Two models were supposed and only the life of crack propagation was predicted by Paris law in one model while the life of crack initiation as well as propagation was predicted by Tanaka and Mura model [4] in the other model. These models were applied to four types of steels and compared with the experimental results in the literature [2, 5].

R. Sakaguchi (✉) · T. Shiraiwa · M. Enoki
Department of Materials Engineering, The University of Tokyo,
Tokyo 113–8656, Japan
e-mail: sakaguchi@rme.mm.t.u-tokyo.ac.jp

R. R. Ambriz et al. (eds.), *Proceedings of the 17th International Conference on New Trends in Fatigue and Fracture*, https://doi.org/10.1007/978-3-319-70365-7_39

Analytical Methods

Voids in ductile cast iron, MnS in Cr–Mo steel, Al_2O_3 in S35C and Al_2O_3 in quenched S35C are supposed as defects in base materials. Only in cast iron and Cr–Mo steel, the data of fatigue test and the size distribution of defects were obtained in the reference [2, 5]. The probability distribution function of $\sqrt{area}$ for voids was generalized extreme value distribution where the location, scale and shape parameter are 0.501, 0.181 and 0.334 mm. The probability distribution function of $\sqrt{area}$ for MnS was lognormal distribution where the average is 2.75 μm and the standard deviation is 0.387 μm. The number of voids and MnS was assumed 98 and 26. In the case of S35C and Al_2O_3, the size and number of defects were supposed same as Cr–Mo steel and MnS.

Table 1 shows the parameter for finite element model (FEM), Tanaka and Mura model and Paris law. Young's modulus (E) and Poisson ratio (ν) of cast iron, MnS and Al_2O_3 were quoted from the literature [2, 6, 7] and the others were assumed. Shear modulus (G) was calculated by E and ν. The fatigue limit (σ_w) was calculated as the half of the tensile strength. The tensile strength of ductile cast iron and Cr–Mo steel was quoted from the literature [2, 5] and the others were assumed. The constants m and C were quoted from the literature [2, 8, 9].

Initial defects model (model A) followed the algorithm in Fig. 1a. Murakami et al. [10] proposed the formula for the stress intensity factor of defects by using $\sqrt{area}$ and this formula was translated into the following formula [11] by using equivalent diameter which was the diameter of a circle having the equivalent area.

$$\Delta K_I = Q\Delta\sigma\sqrt{\pi a_{eq}} \tag{1}$$

where Q is 0.61 or 0.47 for surface or interior defects, $\Delta\sigma$ is the applied stress range and a_{eq} is the equivalent diameter. In this study, the stress intensity factor was calculated by the Eq. (1). On the basis of Kitagawa diagram [12], the threshold size of defects was given by

Table 1 Young's modulus, Poisson ratio and parameters of Paris law

	Young's modulus (GPa)	Poisson ratio	Shear modulus (GPa)	Fatigue limit (MPa)	m	C
Ductile cast iron	136	0.25	54.4	187	4.4	9.4×10^{-14}
Cr–Mo steel	205	0.28	80.8	839	3.32	4.79×10^{-12}
S35C	200	0.3	76.9	225	2.75	1.5×10^{-11}
Quenched S35C	200	0.3	76.9	650	2.75	1.5×10^{-11}
Void	0.001	0.3	–	–	–	–
MnS	120	0.24	–	–	–	–
Al_2O_3	372	0.232	–	–	–	–

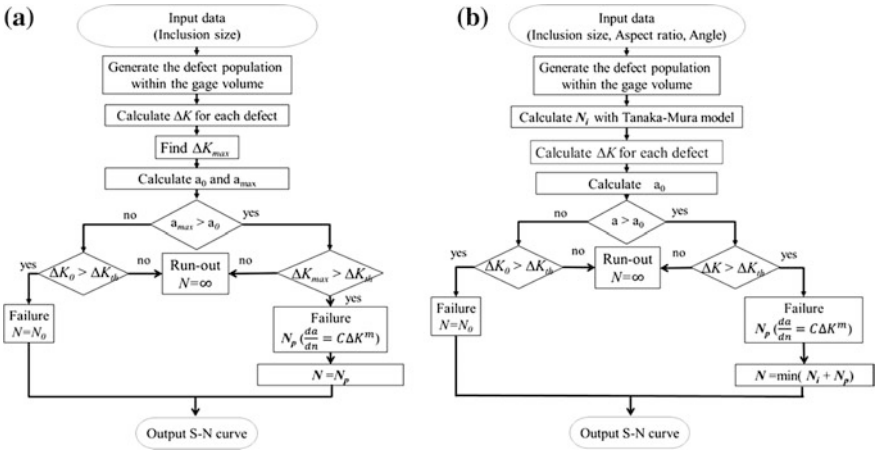

Fig. 1 **a** Calculation algorithm of model A, **b** Calculation algorithm of model B

$$a_0 = \frac{1}{\pi}\left(\frac{\Delta K_{th}}{Q\Delta\sigma_w}\right) \tag{2}$$

where ΔK_{th} is the threshold stress intensity factor range. The life of the crack propagation was predicted by the integrated Paris law, Eq. (3).

$$N_p = \frac{1}{C(Q\Delta\sigma\sqrt{\pi})^m}\int_{a_{ini}}^{a_f}\frac{dx}{(Y'\sqrt{a})^m} \tag{3}$$

where a_{ini} is the initial crack length, a_f is the fracture crack length and Y' is the shape factor [13]. It was assumed that a_{ini} is the size of defects, a_f is the size of the specimen (W) and the life of crack propagation equaled the fatigue life. If $a_0 > a_{max}$ and $\Delta K_{max} > \Delta K_{th}$, the life of crack propagation was predicted by Eq. (3) for $a_{ini} = a_0$ and $a_f = W$. If $\Delta K_{th} > \Delta K_{max}$, it was assumed that fatigue fracture did not occur.

Crack initiation model (model B) followed the algorithm in Fig. 1b. The crack initiation life was predicted by the following formula,

$$N_i = \frac{8GW_c}{\pi(1-v)d\left(kt\frac{\Delta\sigma}{M} - 2\frac{\sigma_w}{M}\right)^2} \tag{4}$$

where W_c is the fracture energy per unit area (W_c = 2 kJ/m^2 [14]), d is the length of the slip band, kt is the stress concentration factor and M is Taylor factor. On the basis of Tanaka and Mura model, the formula was derived in reference to Chan's research [15]. The length of the slip band was assumed to equal the mean grain size (50 μm). The Taylor factor was assumed 2.5. The stress concentration factor was

simulated by 2D FEM for the elastic response. The shape of defects was assumed as ellipse and the approximate formula for the arbitrary angle and aspect ratio was obtained by multiple regression analysis. The probability distribution function of the aspect ratio was assumed as normal distribution. In the case of voids, the average was assumed 0.5 because the casting voids are typically round. The standard deviation was assumed 0.05. In the case of MnS, the average was assumed 0.3 to represent the elongated MnS in rolled steels. The standard deviation was assumed 0.05. The probability distribution function of the angle was assigned uniform distribution.

If $a_{max} > a_0$ and $\Delta K_{max} > \Delta K_{th,}$ the life of crack propagation was predicted by Eq. (3) for $a_{ini} = a_0 + 50$ μm and $a_f = W$ under the assumption that the crack of 50 μm occurred. The fatigue life arising from each defect was calculated by adding the life of crack initiation to that of crack propagation. The output of model B equaled the minimum of them. In other cases, the fatigue life was predicted by the same way as model A.

Results and Discussion

The results of the fatigue life prediction by model A were presented in Fig. 2a, b. In the case of ductile cast iron including voids, the fatigue life predicted by model A was within the range of the experimental scattering. In the case of Cr–Mo steel including MnS, the fatigue life was not consistent with the experimental results under high and low stress. In this regard, it is assumed that it is incorrect to consider MnS as pre-existent crack. In the case of S35C and quenched S35C including Al_2O_3, there is no experimental data and the predicted fatigue life arising from Al_2O_3 was compared to the predicted fatigue life from the matrix. In the case of S35C, the fatigue life from Al_2O_3 was more than the fatigue life from the matrix. This means that defects in S35C does not influence on the fatigue failure. On the

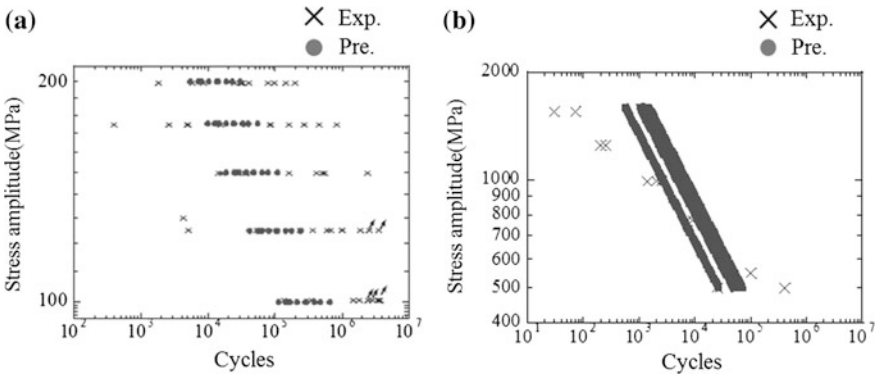

Fig. 2 Fatigue life predicted by model A in **a** cast iron (void), **b** Cr–Mo steel (MnS)

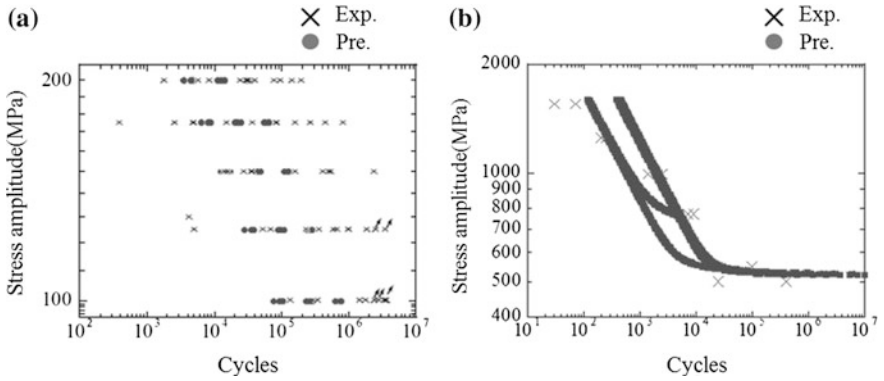

Fig. 3 Fatigue life predicted by model B in **a** cast iron (void), **b** Cr–Mo steel (MnS)

other hand, in the case of quenched S35C, the fatigue life arising from Al_2O_3 was less than the fatigue life arising from the matrix. From these facts, it is indicated that the defects in the high strength steel are likely to influence on the fatigue failure.

The results of the fatigue life prediction by model B were presented in Fig. 3a, b. Compared with the fatigue life predicted by model A, the fatigue life predicted by model B did not change in the case of ductile cast iron because the life of the crack initiation was far less than that of the crack propagation due to the high stress concentration factor in the range of loaded stress. In the case of Cr–Mo steel including MnS, the fatigue life predicted by model B mostly showed a better agreement with experimental results than the fatigue life predicted by model A. In addition, the result that the origin of the fatigue failure was the surface defect in the high stress range and the origin was the interior defect in the low stress range was also obtained. In the high stress range, the origin was the surface defect whose coefficient of the stress intensity factor applied to Paris law was higher than that of the interior defect due to Q of Eq. (1). In the low stress range, the origin was the interior defect whose stress concentration factor was stochastically higher than the surface defect and the life of crack initiation arising from the interior defect is less than that of the surface defect. In this model, the effect of the crack initiation increases as the loaded stress range decreases and the change of the origin occurred.

Conclusions

(1) Model A which predicts the fatigue life arising from defects by Paris law and model B which predicts the fatigue life by Tanaka-Mura model and Paris law were proposed.

(2) In the case of ductile cast iron including voids, there was little difference in the fatigue life predicted by both models due to the high stress concentration factor of voids.
(3) From the results of the predicted life arising from S35C and quenched S35C, it was indicated that defects in the high strength steel were likely to influence on the fatigue failure.
(4) In the case of Cr–Mo steel including MnS, the fatigue life predicted by model B mostly showed a good agreement with experimental results. The result that the origin of the fatigue failure was the surface defect in the high stress range and it was the interior defect in the low stress range was also obtained.

References

1. J.Z. Yi, X. Zhu, J.W. Jones and J.E. Allsion: Metallurgical and Materials Transactions A **38** (2007)1123–1135.
2. M. Shirani and G. Harkegard: International Journal of Fatigue **41** (2012)188–198.
3. H. Mughabi: International Journal of Fatigue **28** (2006)1501–1508.
4. K. Tanaka and T. Mura: Metallurgical and Materials Transactions A **13** (1982)117–123.
5. S. Cyril and A. Fatemi: International Journal of Fatigue **31** (2009)526–536.
6. Kavci and S. Cabuk: Computational Materials Science **95** (2014)99–105.
7. S. Sakaguchi, N. Murayama and Y. Kodama and F. Wakai: Journal of Materials Science Letters **10** (1991)282–284.
8. J. H. Chuanga, L. W. Tsayb, C. Chena: International Journal of Fatigue **20** (1998)531–536.
9. JSSC: Fatigue Design Recommendations for Steel Structures (Giho-do, Japan, 2010) 53.
10. Y. Murakami and M. Endo: Effects of defects, inclusions and inhomogeneities on fatigue strength **16** (1994)163–182.
11. X. Zhu, J.Z. Yi, J.W. Jones and J.E. Allison: Metallurgical and Materials Transactions A **38** (2007)1111–1122.
12. S. Suresh: Fatigue of Materials Second Edition (Cambridge University Press, the United Kingdom Britain and Northern Ireland, 1998) 545–547.
13. T. L. Anderson: Fracture mechanics: fundamentals and applications, Third Edition (CRC Press, United States of America, 2005) 48–54.
14. T. Hoshide and K. Kusuura: Fatigue Fract. Eng. Mat. Struct. 21 (1998)201–213.
15. S. Chan: Metallurgical and Materials Transactions A **34** (2003)43–58.

Peridynamic Modeling of Cracking in Ceramic Matrix Composites

Yile Hu, Erdogan Madenci and Nam Phan

Introduction

In the design of Ceramic Matrix Composites (CMC), the ability to promote crack growth only through the interphase and prevent fiber cracking is utmost important. In the presence of a weak interphase (coating) between the fibers and matrix, matrix cracks propagate through the dense matrix and are deflected around the fiber through the interphase region. Deflection of matrix cracks at the interphase depends on the relative strengths of the matrix, interphase and fiber and the bonding characteristics between the constituent layers. By selecting optimized strength ratio between matrix and interphase, it is possible to double the load carrying capacity of a SiC/SiC CMC with BN interphase [1]. Under axisymmetric fiber/matrix model loaded in tension, debonding or cracking at the interphase is expected to occur if the fiber is stiffer than the matrix [2]. In many cases, it is observed that the debonds or cracks in the interphase occur at some distance in front of a primary crack, and these cracks arrest or retard the growth of the primary crack [3–6]. Cook et al. [7] explained the mechanism of crack deflection as a result of the stress component parallel to the crack plane. Braginsky and Przybyla [8] employed the extended finite element method XFEM available in ABAQUS to study fiber/matrix crack deflection in SiC/SiC CMC with a BN fiber interphase. However, the model does not allow for crack coalescence; it is a major limitation when multiple cracks attempt to interact and coalesce. Therefore, this study focuses on simulating complex crack propagation/deflection in CMC by using peridynamics.

Y. Hu · E. Madenci (✉)
The University of Arizona, Tucson, AZ 85721, USA
e-mail: madenci@email.arizona.edu

N. Phan
Naval Air Systems Command (NAVAIR), Patuxent River, MD, USA

R. R. Ambriz et al. (eds.), *Proceedings of the 17th International Conference on New Trends in Fatigue and Fracture*, https://doi.org/10.1007/978-3-319-70365-7_40

Peridynamics

As an alternative to the classical continuum mechanics, the peridynamic (PD) theory introduced by Silling [9, 10] and later reviewed by Silling and Lehoucq [11] converts the existing governing equations from their local form to a nonlocal form by introducing an internal length parameter. This length parameter defines the domain of interaction of a material point. The main difference between the PD theory and classical continuum mechanics is that the former is formulated using integral equations as opposed to the classical differential form of the governing equations. This feature allows crack initiation and propagation at multiple sites without requiring external crack growth criteria. In the PD analysis, the damage at a material point can be introduced by removing the interactions between material points. These removed interactions may align themselves along surfaces that form cracks, but the equations of motion remain valid regardless. The direction and path of crack growth emerges from the PD equations of motion and the constitutive model. All of these features are predicted without the need of any special techniques; crack growth in the PD theory is unguided.

As in any computational analysis, the choice of criteria for crack nucleation and propagation in a structure strongly influences the predictions. The most commonly used failure parameter in PD is the critical stretch. The stretch, which is analogous to strain in classical continuum mechanics, is monitored between the PD material points. When the stretch reaches its critical value, the interaction between these material points is terminated. Silling and Askari [12] derived an analytical expression for the critical stretch by equating the energy required to create a unit fracture surface in PD to the critical energy release rate. The ability of PD to predict failure initiation and propagation has been well established. The non-uniform PD discretization can be generated using standard finite element mesh generation software that enables the construction of computational models to represent specific geometries.

Silling et al. [10] derived the ordinary state-based PD equilibrium equation in the form

$$\rho(\mathbf{x})\,\ddot{\mathbf{u}}(\mathbf{x},t) = \int_{H_{\mathbf{x}}} \left(\mathbf{t}(\mathbf{u}'-\mathbf{u},\mathbf{x}'-\mathbf{x},t) - \mathbf{t}'(\mathbf{u}-\mathbf{u}',\mathbf{x}-\mathbf{x}',t)\right) dV_{\mathbf{x}'} + \mathbf{b}(\mathbf{x},t) \quad (1)$$

where the region $H_{\mathbf{x}}$ defines the range of interaction for material point $\mathbf{x}$. Its extent is specified by δ, referred to as the "horizon." The integrand in this equation does not contain any spatial derivatives; thus, it is valid everywhere regardless of the presence of discontinuities. However, this equation is not usually amenable for analytical solutions. Therefore, its solution is constructed by using numerical techniques for spatial and time integrations. The spatial integration is performed by using a meshless collocation method due to its simplicity. The numerical integration is performed by dividing the domain into a finite number of specific volumes associated with the integration (material) points. Therefore, this equation can be

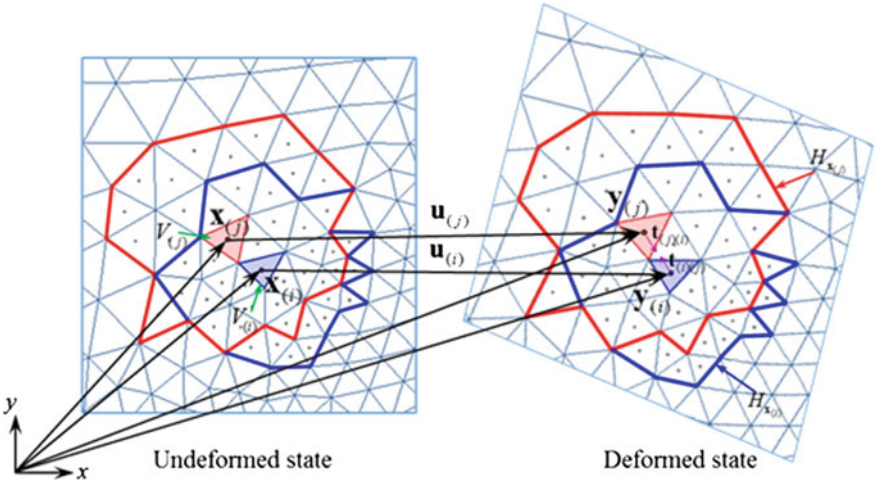

Fig. 1 Nonlocal interactions between material point $\mathbf{x}_{(i)}$ and its family member $\mathbf{x}_{(j)}$

rewritten in discretized form with $N_{(i)}$ representing the number of material points in the family of material point $\mathbf{x}_{(i)}$ as

$$\rho_{(i)}\ddot{\mathbf{u}}_{(i)} = \sum_{j=1}^{N_{(i)}} \left[\mathbf{t}_{(i)(j)}\left(\mathbf{u}_{(j)} - \mathbf{u}_{(i)}, \mathbf{x}_{(j)} - \mathbf{x}_{(i)}, t\right) - \mathbf{t}_{(j)(i)}\left(\mathbf{u}_{(i)} - \mathbf{u}_{(j)}, \mathbf{x}_{(i)} - \mathbf{x}_{(j)}, t\right)\right] V_{(j)} + \mathbf{b}_{(i)} \tag{2}$$

where $\mathbf{u}_{(i)}$ is the displacement vector and $\mathbf{b}_{(i)}$ is the body load vector at the material point $\mathbf{x}_{(i)}$. Each point occupies a finite volume, $V_{(i)}$, and is located at its centroid. The vector $\mathbf{t}_{(i)(j)}$ represents the force density that material point $\mathbf{x}_{(j)}$ exerts on material point $\mathbf{x}_{(i)}$, and $\mathbf{t}_{(j)(i)}$ represents the force density that material point $\mathbf{x}_{(i)}$ exerts on material point $\mathbf{x}_{(j)}$. The domains of interaction (family) of material points $\mathbf{x}_{(i)}$ and $\mathbf{x}_{(j)}$ are denoted by $H_{\mathbf{x}_{(i)}}$ and $H_{\mathbf{x}_{(j)}}$, respectively, as shown in Fig. 1. As illustrated in this figure, the material point $\mathbf{x}_{(i)}$ interacts with the material points in its family $H_{\mathbf{x}_{(i)}}$, and it is influenced by the collective deformation of all these material points. Similarly, material point $\mathbf{x}_{(j)}$ is influenced by deformation of the material points in its own family, $H_{\mathbf{x}_{(j)}}$. With respect to a Cartesian coordinate system, the relative position vector between these points is defined as $\boldsymbol{\xi}_{(i)(j)} = \mathbf{x}_{(j)} - \mathbf{x}_{(i)}$.

The PD family size is an important parameter. The size and shape of each family can be different. Each material point $\mathbf{x}_{(i)}$ has its own horizon size, $\delta_{(i)}$, and its extent is dictated by the nature of discretization. The horizon size $\delta_{(i)}$ is specified as $\delta_{(i)} = m\Delta_{(i)}$ with m being an integer, and with the characteristic length $\Delta_{(i)}$ is defined as

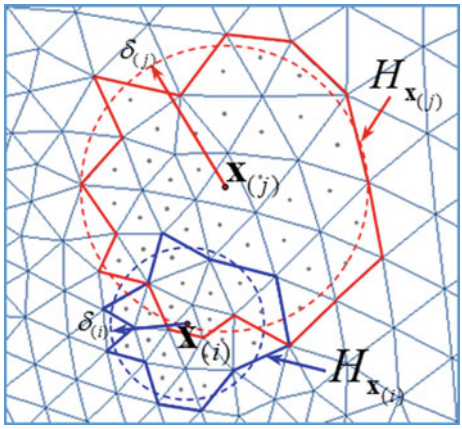

Fig. 2 Irregular domain of interactions for material points $\mathbf{x}_{(i)}$ and $\mathbf{x}_{(j)}$

$$\Delta_{(i)} = \begin{cases} \sqrt{V_{(i)}/h} & \text{2-D} \\ \sqrt[3]{V_{(i)}} & \text{3-D} \end{cases} \tag{3}$$

where h is the thickness of a two-dimensional model.

As shown in Fig. 2, the collection of material points encompassed by the horizon of material point $\mathbf{x}_{(i)}$ establishes the domain of interaction, $H_{\mathbf{x}_{(i)}}$, with an arbitrary size and shape. If the centroid of a finite volume is included within the horizon, it is included in the family of $\mathbf{x}_{(i)}$. As a result of the discretization, material points $\mathbf{x}_{(i)}$ and $\mathbf{x}_{(j)}$ may or may not be part of their families as a paired interaction. It can be resolved by deleting the material point $\mathbf{x}_{(i)}$ from the interaction domain of material point $\mathbf{x}_{(j)}$ or vice versa.

As suggested by Madenci and Oterkus [13], the force density vectors, $\mathbf{t}_{(i)(j)}$ and $\mathbf{t}_{(j)(i)}$ can be of the form

$$\mathbf{t}_{(i)(j)} = t_{(i)(j)} \frac{\mathbf{y}_{(j)} - \mathbf{y}_{(i)}}{\left|\mathbf{y}_{(j)} - \mathbf{y}_{(i)}\right|} \tag{4a}$$

and

$$\mathbf{t}_{(j)(i)} = t_{(j)(i)} \frac{\mathbf{y}_{(j)} - \mathbf{y}_{(i)}}{\left|\mathbf{y}_{(j)} - \mathbf{y}_{(i)}\right|} \tag{4b}$$

where the magnitudes of the vectors are defined as

$$t_{(i)(j)} = 2\frac{\delta_{(i)}}{\xi_{(i)(j)}}\left(d_{(i)}a\theta_{(i)} + b_{(i)(j)}\xi_{(i)(j)}s_{(i)(j)}\right) \tag{5a}$$

and

$$t_{(j)(i)} = -2\frac{\delta_{(j)}}{\xi_{(i)(j)}}\left(d_{(j)}a\theta_{(j)} + b_{(j)(i)}\xi_{(i)(j)}s_{(i)(j)}\right) \tag{5b}$$

in which the stretch between material points $\mathbf{x}_{(i)}$ and $\mathbf{x}_{(j)}$ is defined as

$$s_{(i)(j)} = \frac{\left|\mathbf{y}_{(j)} - \mathbf{y}_{(i)}\right| - \left|\mathbf{x}_{(j)} - \mathbf{x}_{(i)}\right|}{\left|\mathbf{x}_{(j)} - \mathbf{x}_{(i)}\right|} \tag{6}$$

In this equation, $(\mathbf{x}_{(j)} - \mathbf{x}_{(i)})$ and $(\mathbf{y}_{(j)} - \mathbf{y}_{(i)})$ represent the relative position vectors between material points $\mathbf{x}_{(i)}$ and $\mathbf{x}_{(j)}$ in the undeformed and deformed states, respectively.

The parameter a is a material constant related to modulus K and shear modulus G as

$$a = \begin{cases} \frac{1}{2}\left(K - \frac{5}{3}G\right), \text{ with } K = \frac{E}{3(1-2\nu)} & \text{for 3D,} \\ \frac{1}{2}(K - 2G), \text{ with } K = \frac{E}{2(1-\nu)} & \text{for 2D plane stress,} \\ \frac{1}{2}(K - 2G), \text{ with } K = \frac{E}{2(1-2\nu)(1+\nu)} & \text{for 2D plane strain,} \end{cases} \tag{7}$$

where E and ν are the Young's modulus and Poisson's ratio, respectively. In the 3D case, modulus K represents the bulk modulus κ. Through calibration against the classical SED by considering a simple loading condition of isotropic expansion, the two parameters, $d_{(i)}$, and $b_{(i)(j)}$ can be determined as

$$d_{(i)} = \frac{\mathrm{tr}(\mathbf{I})}{\delta_{(i)}\sum_{m=1}^{N_{(i)}} V_{(m)}} \tag{8a}$$

and

$$\delta_{(i)}b_{(i)(j)} + \delta_{(j)}b_{(j)(i)} = \frac{\mathrm{tr}(\mathbf{I})}{\xi_{(i)(j)}}\left(\frac{K}{2} - a\right)\left(\delta_{(i)}d_{(i)} + \delta_{(j)}d_{(j)}\right) \tag{8b}$$

The final form of the PD equation of motion is stated as

$$\rho_{(i)}\ddot{\mathbf{u}}_{(i)} = 2\sum_{j=1}^{N_{(i)}}\left[\begin{array}{l} a\delta_{(i)}d_{(i)}\theta_{(i)} + a\delta_{(j)}d_{(j)}\theta_{(j)} \\ +\xi_{(i)(j)}\left(\delta_{(i)}b_{(i)(j)} + \delta_{(j)}b_{(j)(i)}\right)s_{(i)(j)} \end{array}\right]\frac{V_{(j)}}{\xi_{(i)(j)}}\frac{\mathbf{y}_{(j)} - \mathbf{y}_{(i)}}{\left|\mathbf{y}_{(j)} - \mathbf{y}_{(i)}\right|} + \mathbf{b}_{(i)}. \tag{9}$$

In the derivation of this equation, the degree of interactions among the material points is controlled by the non-dimensional influence function, $w_{(i)(j)}$ as

$$w_{(i)(j)} = \frac{\delta_{(i)}}{\left|\mathbf{x}_{(j)} - \mathbf{x}_{(i)}\right|} = \frac{\delta_{(i)}}{\xi_{(i)(j)}} \tag{10}$$

When a failure criterion is satisfied, the PD interactions between the material points are removed to describe damage initiation and growth [12]. An energy-based failure criterion is used in this study, although other criteria can be used with this approach. Associated with an interaction between two material points $\mathbf{x}_{(i)}$ and $\mathbf{x}_{(j)}$, the force component, $f_{n(i)(j)}$ normal to a given crack surface can be expressed as

$$f_{n(i)(j)} = \left(t_{(i)(j)} - t_{(j)(i)}\right) \cos\beta_{(i)(j)} V_{(j)} V_{(i)} \tag{11}$$

where $\beta_{(i)(j)}$ is the angle between the unit normal to a crack surface and the direction of force density vector, as shown in Fig. 3. Similarly, the displacement component $u_{n(i)(j)}$ normal to that crack surface can be evaluated as

$$u_{n(i)(j)} = s_{(i)(j)} \xi_{(i)(j)} \cos\beta_{(i)(j)} \tag{12}$$

Therefore, the strain energy arising from the opening deformation mode of a crack surface can be expressed as

$$U_{n(i)(j)} = \frac{1}{2} f_{n(i)(j)} u_{n(i)(j)} = \frac{1}{2}\left(t_{(i)(j)} - t_{(j)(i)}\right) s_{(i)(j)} \xi_{(i)(j)} \cos^2\beta_{(i)(j)} V_{(j)} V_{(i)} \tag{13}$$

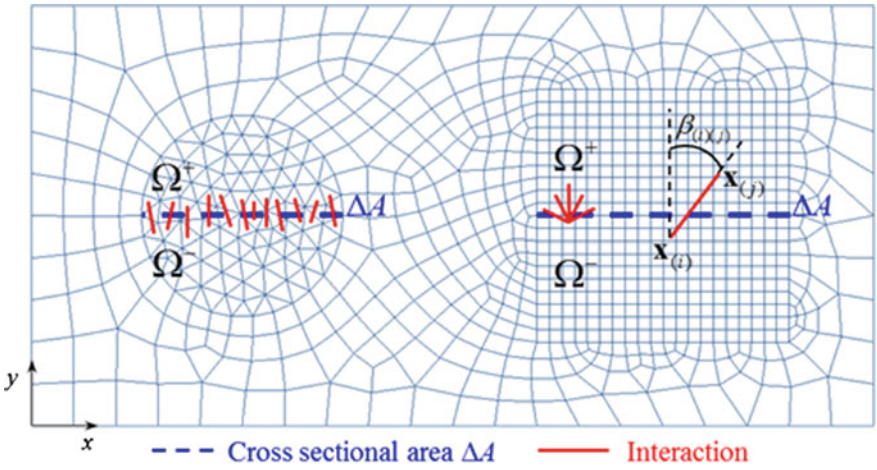

Fig. 3 Interactions across a potential crack surface

The strain energy ΔU required to eliminate all interactions across a new crack surface ΔA can be related to the mode-I critical energy release rate G_{Ic} as

$$G_{Ic} = \frac{\Delta U}{\Delta A} = \frac{\sum_{i=1}^{i\in\Omega^+} \sum_{j=1}^{j\in\Omega^-} \frac{1}{2}\left(t_{(i)(j)} - t_{(j)(i)}\right) s_{(i)(j)}\ \xi_{(i)(j)} \cos^2\beta_{(i)(j)} V_{(j)} V_{(i)}}{\Delta A} \tag{14}$$

The crack surface area ΔA can be determined from the discretized model as illustrated in Fig. 3. The strain energy ΔU required to generate a crack surface ΔA is a summation of the strain energy of the interactions between regions Ω^+ and Ω^-. Under an isotropic expansion s the critical total stretch s_c can be obtained as

$$s_c = \sqrt{\frac{2G_{Ic}\Delta A}{\mathrm{tr}(\mathbf{I})K\left(\sum_{i=1}^{i\in\Omega^+} \sum_{j=1}^{j\in\Omega^-} \left(d_{(i)}\delta_{(i)} + d_{(j)}\delta_{(j)}\right)\cos^2\beta_{(i)(j)} V_{(j)} V_{(i)}\right)}} \tag{15}$$

The critical stretch needs to be evaluated at different regions of the model because it has dependence on the local mesh density.

Numerical Procedure

The solution of PD governing equations can be achieved by employing both implicit and explicit algorithms. Under a quasi-static loading condition, the inertial term on the left side of Eq. (2) is zero. Therefore, the PD equilibrium equation can be expressed as

$$\mathbf{L}(\mathbf{u}) + \mathbf{b} = 0 \tag{16a}$$

where the internal force vector can be expressed in the form of

$$\mathbf{L}_{(i)} = \sum_{j=1}^{N} \left(t_{(i)(j)} - t_{(j)(i)}\right) V_{(j)} \mathbf{e}_{(i)(j)} \tag{16b}$$

with

$$\mathbf{e}_{(i)(j)} = \frac{\mathbf{y}_{(j)} - \mathbf{y}_{(i)}}{\left|\mathbf{y}_{(j)} - \mathbf{y}_{(i)}\right|} \tag{16c}$$

The tangent stiffness matrix is defined as

$$\mathbf{K}_{\mathrm{T}} = \frac{\partial \mathbf{L}}{\partial \mathbf{u}} \tag{17}$$

For linear analysis, the incremental equilibrium equations can be expressed in a recursive form,

$$\mathbf{K}_{\mathrm{T}}^{n} \Delta \mathbf{u}^{n+1} = \Delta \mathbf{b}^{n+1} \tag{18}$$

where $\mathbf{K}_{\mathrm{T}}^{n} = \mathbf{K}_{\mathrm{T}}(\mathbf{u}^{n})$, $\Delta \mathbf{u}^{n+1} = \mathbf{u}^{n+1} - \mathbf{u}^{n}$, $\Delta \mathbf{b}^{n+1} = \mathbf{b}^{n+1} - \mathbf{b}^{n}$, and $n = 0, 1, 2, \ldots$. At each incremental step, the tangent stiffness matrix is obtained from the previous known state $\mathbf{u}^{n}$ and is used to solve for the unknown state $\mathbf{u}^{n+1}$ in the next step. Imposing the boundary conditions reduces the size of the tangent stiffness matrix $\mathbf{K}_{\mathrm{T}}^{n}$ and renders it to be positive definite. Subsequently, the reduced linear system is solved by a Generalized Minimal Residual (GMRES) algorithm.

When the removal of an interaction is detected as part of the implicit solution, the analysis is switched to the explicit time integration, 4th-order Runge-Kutta (RK) method. The equilibrium equation Eq. (2) is modified to reflect the removal of an interaction by introducing a failure (status) parameter μ as

$$\rho \ddot{\mathbf{u}}_{(i)}^{n} = \sum_{j=1}^{N_{(i)}} \mu_{(i)(j)} \left(t_{(i)(j)}^{n} - t_{(j)(i)}^{n} \right) V_{(j)} \mathbf{e}_{(i)(j)}^{n} + \mathbf{b}_{(i)}^{n} \tag{19}$$

where $\mathbf{u}_{(i)}^{n} = \mathbf{u}(\mathbf{x}_{(i)}, t^{n})$ and superscript n indicates the step number. If constant velocity constraints are applied as boundary conditions, the reaction force density $\mathbf{F}_{\mathrm{R}}$ can be expressed as

$$\mathbf{F}_{\mathrm{R}(i)}^{n} = -\sum_{j=1}^{N_{(i)}} \mu_{(i)(j)} \left(t_{(i)(j)}^{n} - t_{(j)(i)}^{n} \right) V_{(j)} \mathbf{e}_{(i)(j)}^{n} \tag{20}$$

For the 4th Runge-Kutta method, the 2nd-order differential equation, Eq. (19) is converted to a system of two 1st-order equations as

$$\dot{\mathbf{u}}_{(i)}^{n} = \mathbf{v}_{(i)}^{n} \tag{21a}$$

and

$$\dot{\mathbf{v}}_{(i)}^{n} = \mathbf{g}^{n} \left(\mathbf{u}_{(i)}^{n}, \mathbf{u}_{(j)}^{n}, \mathbf{u}_{(k)}^{n}, \ldots, \mathbf{x}_{(i)}^{n}, \mathbf{x}_{(j)}^{n}, \mathbf{x}_{(k)}^{n}, \ldots, t \right) \tag{21b}$$

with

$$\mathbf{g}^n = \frac{1}{\rho}\left(\sum_{j=1}^{N_{(i)}} \mu_{(i)(j)}\left(t^n_{(i)(j)} - t^n_{(j)(i)}\right) V_{(j)} \mathbf{e}^n_{(i)(j)} + \mathbf{b}^n_{(i)}\right) \tag{21c}$$

where $\mathbf{v}$ is the velocity vector. The Runge-Kutta algorithm requires two initial conditions on $\mathbf{u}^n_{(i)}$ and $\mathbf{v}^n_{(i)}$: the first is obtained from the implicit solution and the second is obtained by the 2nd-order central difference formula

$$\mathbf{v}^n_{(i)} = \frac{\mathbf{u}^{n+1}_{(i)} - \mathbf{u}^{n-1}_{(i)}}{2\Delta t} \tag{22}$$

where $\mathbf{u}^{n+1}_{(i)}$ and $\mathbf{u}^{n-1}_{(i)}$ are also computed by the implicit algorithm.

Numerical Results

The numerical results concern first the investigation of a matrix-interphase-fiber microstructure, and second prediction of complex cracking path in densely distributed fibers in matrix. The computational model of a matrix-interphase-fiber microstructure is shown in Fig. 4. The length of the model is $L = 40\,\mu\text{m}$, width of the model is specified to $W = 40\,\mu\text{m}$, the thickness of the interphase is set to $h = 1\,\mu\text{m}$. On the right edge of the model, an initial crack with length $2a = 5\,\mu\text{m}$ is inserted. For this model, uniform discretization is suitable with in-plane grid spacing set to $\Delta x = \Delta y = 0.2\mu\text{m}$. The material points along the axis of symmetry is fixed in axial direction, but free to move in radial direction. Tensile displacement constraints are applied to the material points on top and bottom edges. The ceramic fiber, matrix and interphase are modeled individually with distinct material properties. The material properties of HiPerComp SiC-SiC CMCs are presented in Table 1 [14]. It is known that the relative strength of the matrix and interphase has the greatest influence on the crack propagation and interaction with the interphase [8]. Hence, variation of fracture toughness is considered to investigate the main mechanism of crack deflection for six different fracture toughness, $G_c = 5, 10, 15, 20, 25$ and $30\ \text{J/m}^2$.

Figure 5 shows the PD displacement prediction before any damage occurs in the structure. Due to the presence of an edge crack, discontinuity in the axial displacement can be observed, as shown in Fig. 5a. Due to the presence of a weak interphase between fiber and matrix, discontinuity in radial displacement can be observed as well in Fig. 5b. Figure 6 shows the damage evolution in the CMC composite under axial tension. Crack growth initiates from the tip of the primary pre-crack as presented in Fig. 6a. Subsequently, a secondary crack emerges at the interphase, in front of the crack tip of the primary crack, as illustrated in Fig. 6b.

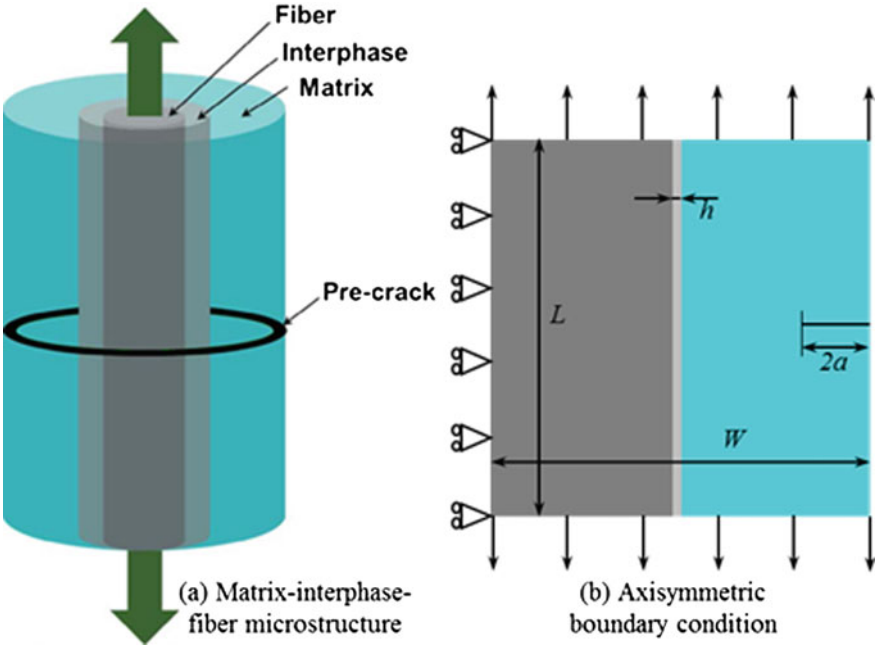

Fig. 4 Cross section of ceramic matrix composite material

Table 1 Material properties of HiPerComp SiC/SiC CMCs

	Fiber	Matrix	Interphase
Young's modulus	$E = 380$ GPa	$E = 360$ GPa	$E = 10$ GPa
Poisson's ratio	$v = 0.185$	$v = 0.185$	$v = 0.05$
Fracture toughness	$G_c = 36$ J/m^2	$G_c = 36$ J/m^2	$G_c = 5$ J/m^2

Due to the presence of a secondary crack, the primary crack is arrested and its growth rate reduces, as shown in Fig. 6c. With the increase of loading, the secondary crack continues to propagate along the interphase (Fig. 6d). Various fracture toughness values are considered to investigate the propensity of primary crack deflection. The distance of the primary crack tip from the interphase versus the ratio of the interphase to the matrix fracture toughness is given in Fig. 7. It is observed that the primary crack is arrested further away from the interphase with the reduction in the ratio of interphase to matrix fracture toughness.

The CMC model with multiple fibers distributed throughout the matrix is shown in Fig. 8. The dimensions of the computational model are length $L = 584.797$ μm, width $W = 524.132$ μm and thickness $h = 1.0$ μm. An initial crack is inserted to the top edge with initial length $a = 100$ μm. The model is generated with an irregular mesh using 64,825 material points. The horizon size is adaptive to the local mesh density, $\delta_{(i)} = 3\Delta_{(i)}$ and it results in 511,072 interactions. Tensile

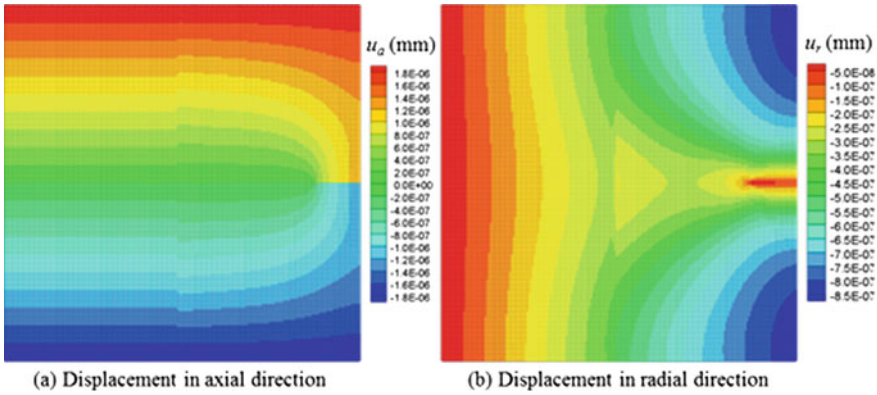

Fig. 5 Displacement field prediction before any damage occurs

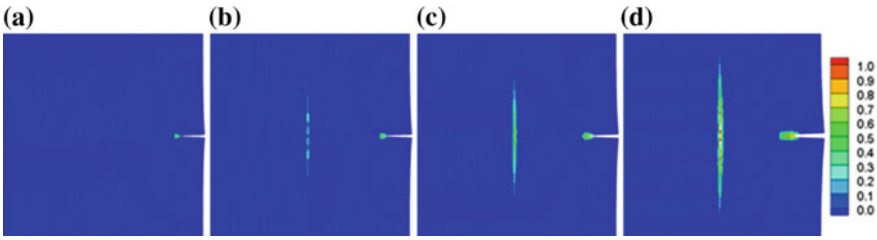

Fig. 6 Primary and secondary crack initiation and propagation in a matrix-interphase-fiber microstructure (Deformation is exaggerated)

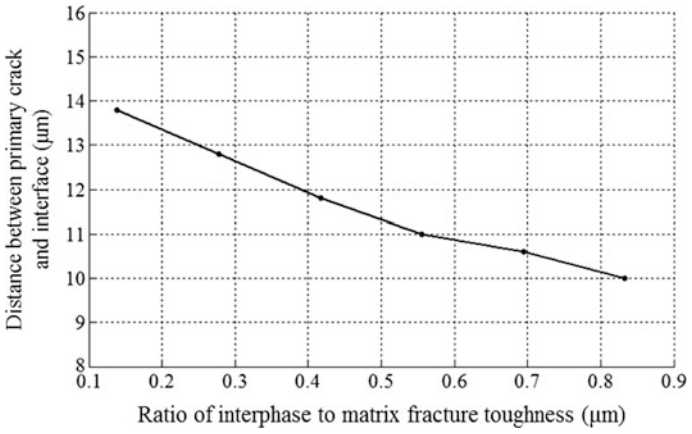

Fig. 7 Distance between the primary crack tip and the matrix-interphase interface for varying ratio of interphase/matrix fracture toughness

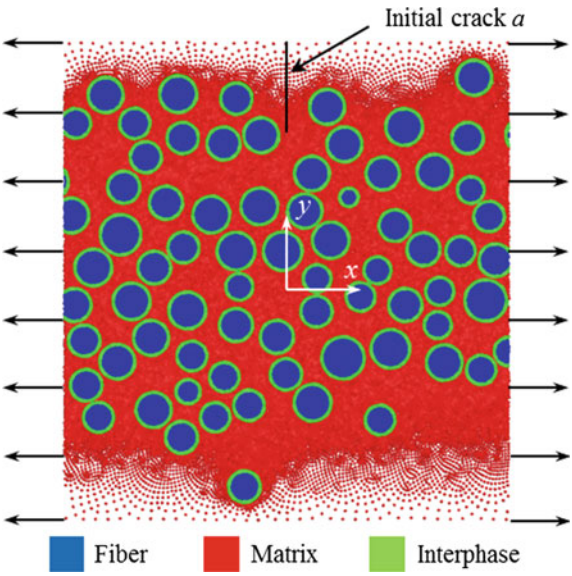

Fig. 8 Computational model of CMC

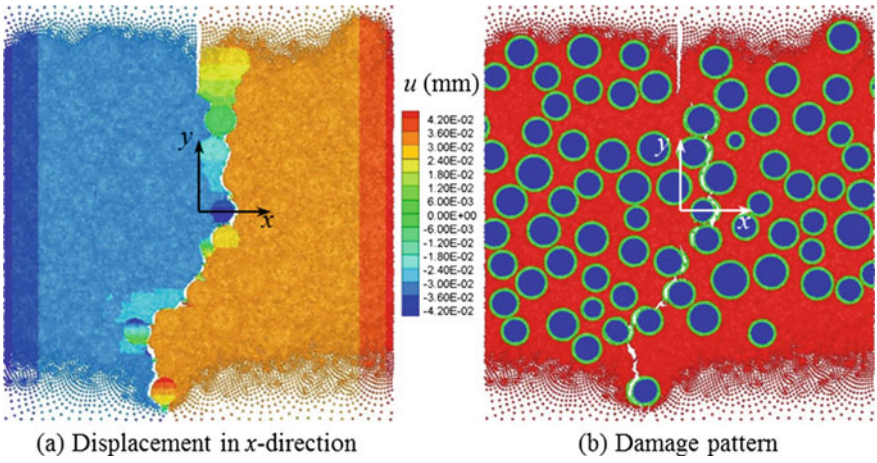

Fig. 9 PD displacement and damage predictions (deformation is exaggerated)

displacement constraints are applied to the left and right edges in the horizontal direction. Figure 9 shows that the initial crack propagates from the edge towards the other side. Due to the weak interphase between matrix and fiber, the crack deflects to the closest interphase from its crack tip and propagates along the interphase regions. As the load increases, crack jumps to the nearby interphases; thus forming

very complex damage patterns and highly arbitrary crack paths. These observation are representative of the experimental observations, and verifies the capability of the present PD approach.

Conclusions

This study presents a new nonuniform discretization capability in peridynamics to investigate crack propagation in CMCs in the presence of a fairly dense matrix, and with fine discretization of the interphase (coating) regions. Damage prediction is based on the critical energy release rates. The PD model captures the effect of relative strengths of the matrix, interphase and fiber on damage propagation path. In the presence of a weak interphase between the fibers and matrix, it predicts the propagation of cracks through the interphase regions very similar to the experimental observations available in the literature.

References

1. F. Rebillat, J. Lamon, A. Guette. The concept of a strong interface applied to SiC/SiC composites with a BN interphase. *Acta Material*, 2000, Vol. 48, 4609–4618.
2. E. Martin, D. Leguillon. Energetic conditions for interfacial failure in ther vicinity of a matrix crack in brittle matrix composites. *Int. J. of Solids and Structure*, 2004, Vol. 41, 6937–6948.
3. P.S. Theocaris, J. Milios. Disruption of a longitudinal interface by a moving transverse crack. *J. of Reinforced Plastic Composites*, 1983, Vol. 2, 18–28.
4. N.J. Pagano, H.W. Brown. The full-cell cracking mode in unifirectional brittle-matrix composites. *Composites*, 1993, Vol. 24, 69–83.
5. W. Lee, S.J. Howard, W.J. Clegg. Growth of interface defects and its effect on crack deflection and toughening criteria. *Acta Material*, 1996, Vol. 44, 3905–3922.
6. Y. Kagawa, K. Goto. Direct observation and modeling of the crack-fibre interaction process in continuous fibre-reinforced ceramics: model experiment. *Material Science Engineering A*, 1998, Vol. 250, 285–290.
7. J. Cook, J. E. Gordon, C. C. Evans and D. M. Marsh, A mechanism for the control of crack propagation in all-brittle systems. *Proc. of the Royal Society of London. Series A, Mathematical and Physical Sciences, 1964,* Vol. 282, 508–520.
8. M. Braginsky, C.P. Przybyla. Simulation of crack propagation/deflection in ceramic matrix continuous fiber reinforced composites with weak interphase via the extended finite element method. *Composite Structures*, 2016, Vol. 136, 538–545.
9. S.A. Silling. Reformulation of elasticity theory for discontinuities and long-range forces. *J Mech Phys Solids*, 2000, Vol. 48, 175–209.
10. S.A. Silling, M. Epton, O. Weckner, J. Xu, E Askari, Peridynamics states and constitutive modeling, *J. Elasticity*, 2007, Vol. 88, 151–184.

11. S.A. Silling, R.B. Lehoucq. Peridynamic theory of solid mechanics. *Adv. Appl. Mech*., 2010, Vol. 44, 73–168.
12. S.A. Silling, E. Askari, A meshfree method based on the peridynamic model of solid mechanics, *Comput. Struct.* 2005, Vol. 83, 1526–1535.
13. E. Madenci, E. Oterkus, Peridynamic Theory and Its Applications, *Springer,* New York, 2014.
14. D. Dunn. The effect of fiber volume fraction in HiPerComp SiC-SiC composites, *PhD Thesis*, Alfred University, Alfred, New York, 2010.

Evaluation of Stress Intensity Factors (SIFs) Using Extended Finite Element Method (XFEM)

Bojana Aleksić, Aleksandar Grbović, Abubakr Hemer, Ljubica Milović and Vujadin Aleksić

Introduction

Finite element analysis is a numerical method that makes it possible to solve very complex problems. This method uses physical discretization of domains, so that complex spatial structures in the calculations are considered as discrete systems. The development of engineering structures presupposes the existence of very precise calculations, which provide optimum weight, load capacity and structural safety. The idea of division of domains into a number of subdomains is very old, but the intensive development of the method of finite elements is only foreboded in the middle of the twentieth century.

The finite element is defined by its shape, number and position of the adjacent nodes. Calculation by the finite element method begins with discretization consisting of the selection of interpolation functions (element shape functions) as well as the selection of refinement of the finite element mesh. Interpolation functions (shape functions) approximately determine the true field of variables at any point within an element, interpolating the values of the variables in the nodes of that

B. Aleksić (✉)
Innovation Centre of Faculty of Technology and Metallurgy,
Karnegijeva 4, 11120 Belgrade, Serbia
e-mail: baleksic@tmf.bg.ac.rs

A. Grbović
Faculty of Mechanical Engineering, University of Belgrade,
Kraljice Marije 16, 11120 Belgrade, Serbia

A. Hemer · L. Milović
Faculty of Technology and Metallurgy, University of Belgrade,
Karnegijeva 4, 11120 Belgrade, Serbia

V. Aleksić
Institute for Testing Materials-IMS Institute, Bulevar Vojvode Mišića 43,
11000 Belgrade, Serbia

R. R. Ambriz et al. (eds.), *Proceedings of the 17th International Conference on New Trends in Fatigue and Fracture*, https://doi.org/10.1007/978-3-319-70365-7_41

element. By solving formed differential equations for the finite element mesh, the required magnitudes are calculated (displacement, strain, internal forces, stress) [1].

The finite element method is very often used to calculate the structures with the cracks-pre-cracked structures.

In addition to the classical finite elements, there is an extended Finite Element Method (XFEM) that will be discussed in this paper. The basic characteristic of XFEM is that it allows the modeling of a discontinuous physical field independently of the generated network of finite elements. Unlike the classic finite element method, where the cracks growth process requires the successive generation of a network to be able to monitor the increasing geometric discontinuity, the XFEM does not require a comfortable mapping between the network and the discontinuity geometry.

In this paper, a simulation of the central-crack propagation was conducted using the example of a finite-dimension plate, and a comparative overview of the results obtained using Abaqus and the FRANC2D/L software presented.

3D Simulation of the Central-Crack Propagation on the Finite-Dimension Plate

It is a plate of constant thickness (t = 25.4 mm) and slightly larger dimensions (508 × 254 mm), but with a central initial crack 254 mm long (Fig. 1). The model of the central-crack plate is defined in the CATIA v5 [2] software, from where it was exported to Abaqus. The initial crack in CATIA v5 is defined as a surface without thickness, while Abaqus defines the characteristics of the material

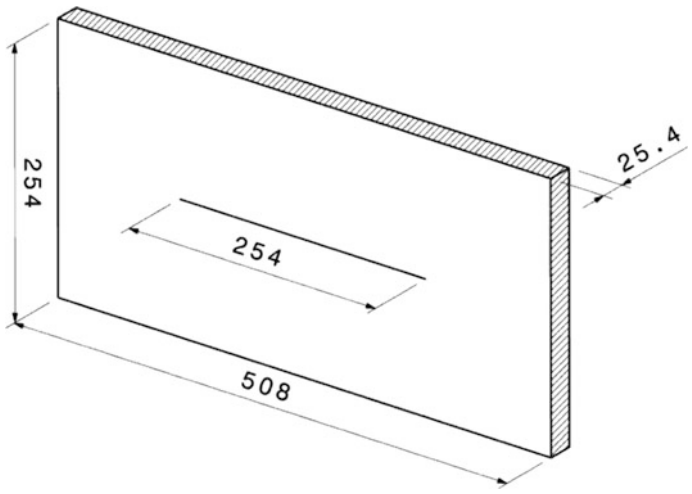

Fig. 1 Dimensions of the plate with central crack, used for 3D simulation of propagation

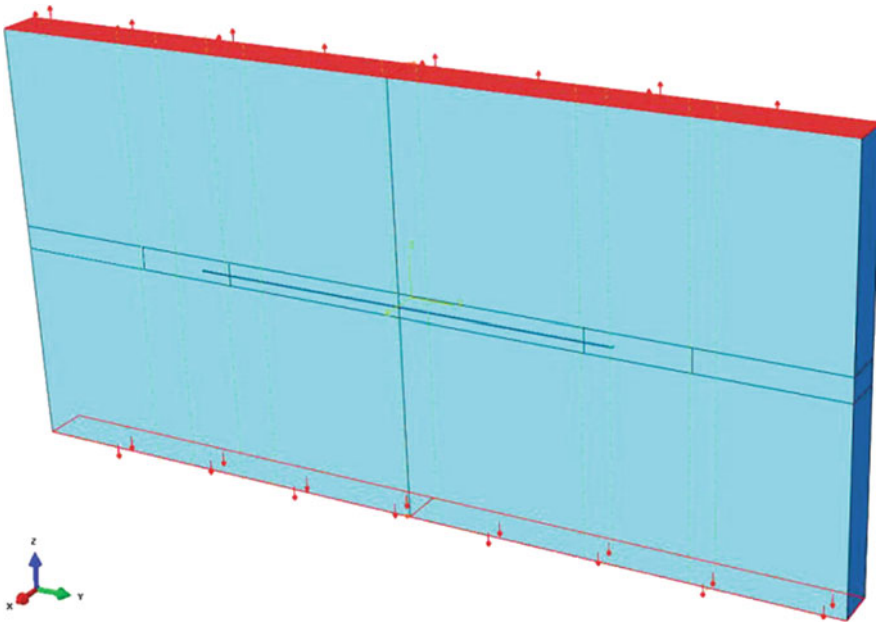

Fig. 2 Loading of the 508 × 254 mm plate with central crack (Abaqus model)

(steel with Young's modulus of elasticity 206,800 MPa and Poisson's coefficient 0.3), uniform tensile stress (value 6.89 kPa) on the upper and lower surface of the plate and the corresponding boundary conditions (Fig. 2).

In Abaqus, two meshes of finite elements—mesh with hexahedra (Fig. 3) and mesh with tetrahedra (Fig. 4) are defined to compare the results obtained for different types of elements. In Figs. 3 and 4 it can be seen that in the areas through which the crack propagates a very "thick" mesh is generated, in order to increase the accuracy of the values obtained by calculation using a larger number of nodes. The Figs show the outlook of the meshes that gave the best results and that came after several iterations through which the meshes were gradually improved. The final mesh consisting of hexahedral elements had 128,190 elements, while the tetrahedral mesh consisted of 917,880 elements.

Figures 5 and 6 show the values of von Mises stress around the crack on the hexahedral mesh after the first step of the calculation (crack opening displacement). The maximum value of the stress adjacent to the crack tip was 0.703 MPa, which is quite a low value, but it should not be surprising since the applied tensile stress at the ends of the plate was only 0.00689 MPa.

Such a low stress value was adopted to study the variation in the value of the stress intensity factor in the case of low external stress, as well as to compare the value of the stress intensity after the crack opening displacement with the value given in the literature [3], which was also obtained by the extended finite element

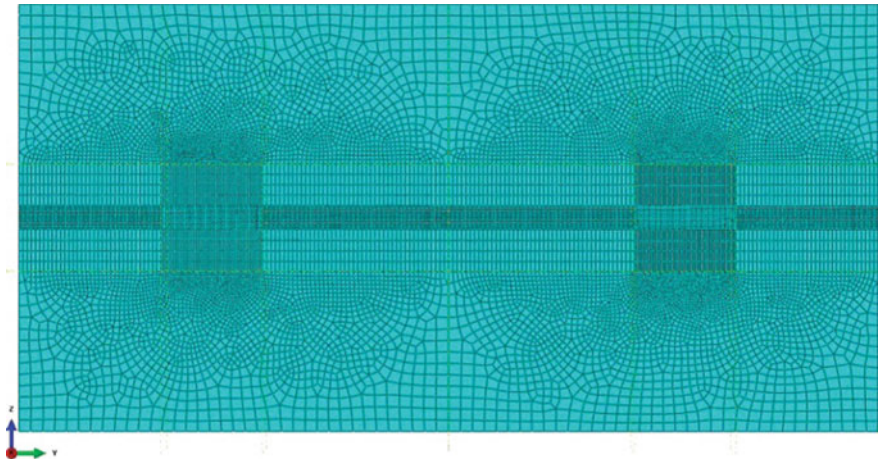

Fig. 3 The finite-element mesh of the model of pre-cracked 508 × 254 mm plate (hexahedral elements)

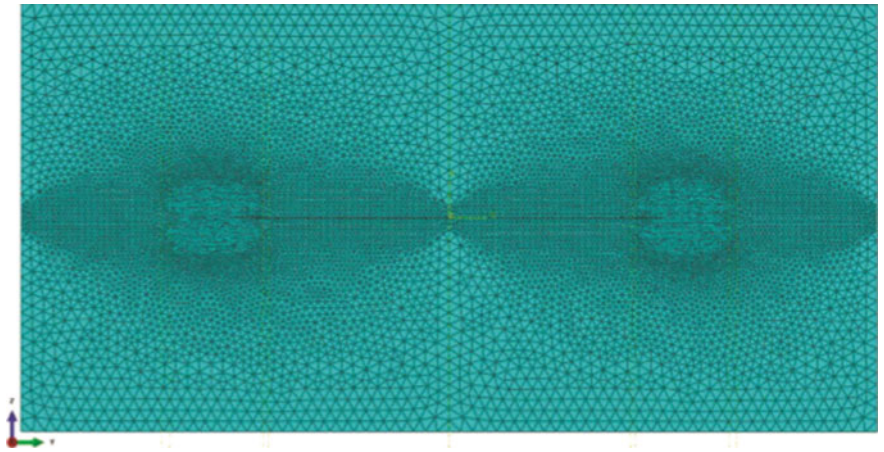

Fig. 4 Finite-element mesh of the model of pre-cracked 508 × 254 mm plate (tetrahedral elements)

method, but in 2D analysis. Otherwise, the value of the K_I intensity factor in the case of the plate with central crack can be determined by the formula:

$$K_I^{(teor.)} = \sigma \cdot f\left(\frac{a}{W}, \frac{L}{W}\right) \cdot \sqrt{\pi a} \tag{1}$$

where factor of correction $f\left(\frac{a}{W}, \frac{L}{W}\right)$ is determined from the tables of the values that also can be found in literature [4]. In this case $\frac{a}{W} = \frac{254}{508} = 0.5$, $\frac{L}{W} = \frac{254}{508} = 0.5$, then

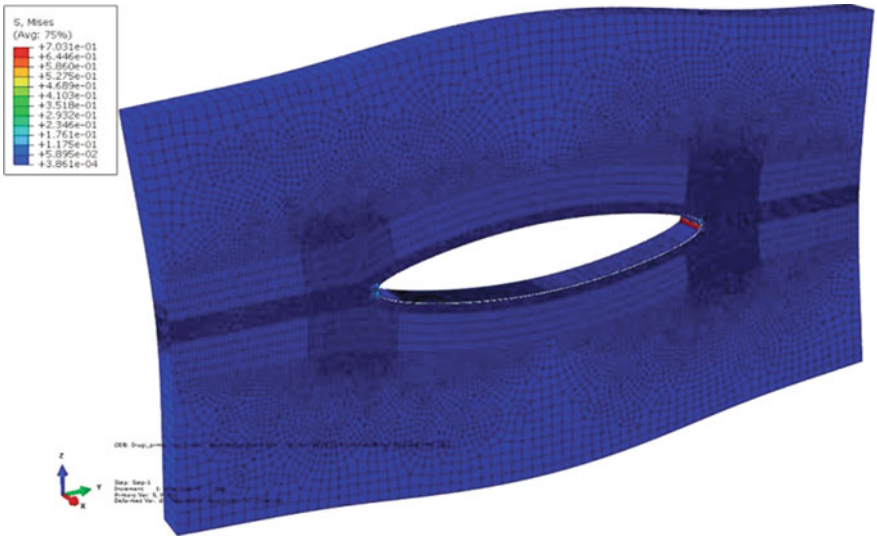

Fig. 5 Stress state (von Mises) of the plate after crack opening displacement (hexahedral elements)

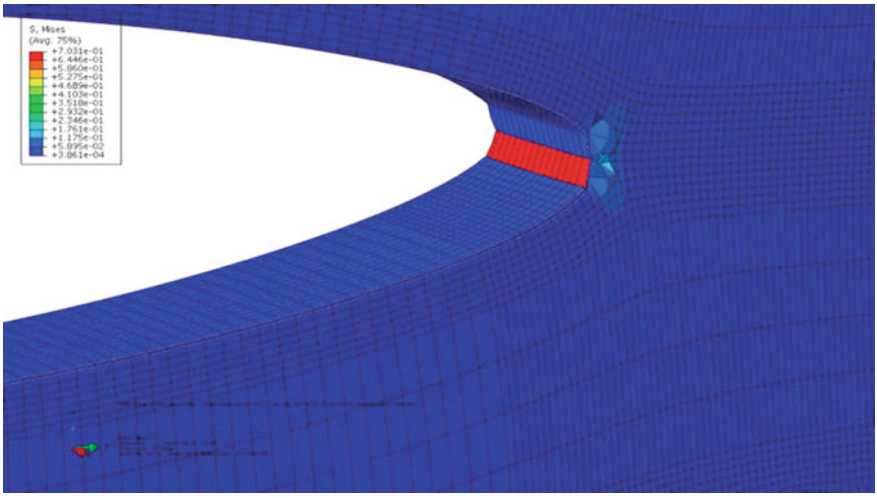

Fig. 6 Stress state (von Mises) of the plate after crack opening displacement (hexahedral elements—magnified presentation)

f(0.5, 0.5) $\approx$ *1.9*, so that theoretical value of K_I is: $\mathbf{K_I^{(teor.)} = 261.08\ KPa\ mm^{0.5} = 0.26108\ MPa\ mm^{0.5}}$

The values of K_I obtained from the 2D analysis ranged from 239.08 KPa $mm^{0.5}$ to as much as 405.99 KPa $mm^{0.5}$, and were obtained for different size of the

integration domain (relative to the length of the crack) and using different methods (classical FEM and XFEM were used) [5]. The XFEM gave far better predictions, since the average deviations from the theoretical value (for different sizes of the integration domain) amounted to only 1%. The average value of K_I, obtained after the crack opening displacement on the 3D model with hexahedral elements (Figs. 5 and 6), was 288.3 KPa $mm^{0.5}$, which is about 10% above the theoretical value and the values from [3]. However, this is the mean value obtained based on 64 stress intensity factors calculated at the same number of points on the front of the 3D crack, while the theoretical value and the value from the 2D analysis using FEM were calculated at only one point of the crack tip. As for the plate with tetrahedral elements, a slightly lower value of K_I (281.1 KPa $mm^{0.5}$) was obtained.

Figures 7 and 8 show the values of von Mises stress around the crack on the tetrahedral mesh after the first step. The maximum stress (1.032 MPa) is slightly higher than that of the plate with hexahedral elements.

In the available literature, however, the values of the stress intensity factor obtained by applying the XFEM to further crack propagation after the "opening" of the initial damage 254 mm-long cannot be found. In the NASGRO base of standard samples, there is an example of a plate with a crack in the middle, but the values of the stress intensity factor obtained in the NASGRO v4 software cannot be used to verify the solutions obtained using XFEM in Abaqus, because the NASGRO uses a plate of infinite length for a calculation.

Plate dimensions significantly affect the accuracy of the results obtained using the FEM so that, in order to verify the results, the values obtained for the 2D plate model calculated in the FRANC2D/L software had to be used here. In Figs. 9 and 10, the

Fig. 7 Stress state (von Mises) of the plate after crack opening displacement (tetrahedral elements)

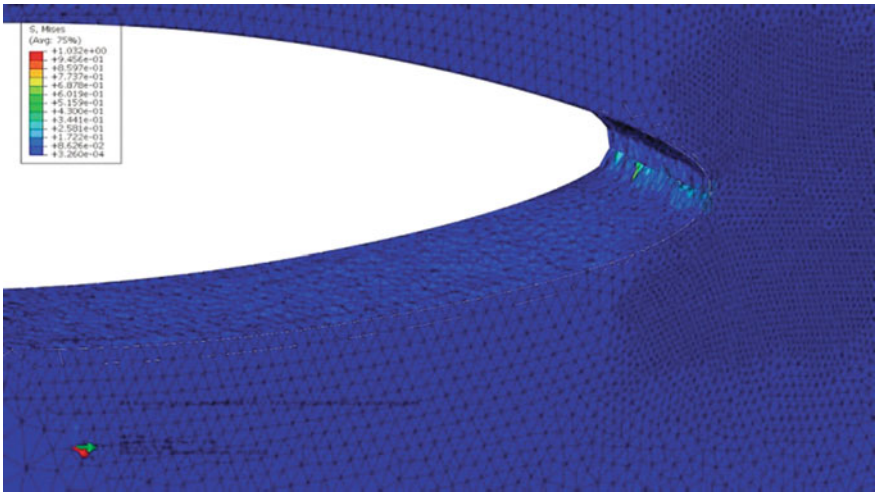

Fig. 8 Stress state (von Mises) of the plate after crack opening displacement (tetrahedral elements —magnified presentation)

Fig. 9 Stress state (von Mises) of a plate after 18 steps of crack propagation (hexahedral elements)

stress state of the plates with hexahedral and tetrahedral elements after 18 crack propagation steps is shown, while Fig. 11 shows the appearance of the mesh of the central-crack plate generated in the FRANC2D/L software.

The model in FRANC2D/L was loaded with the same tensile stress at the ends of the plate as well as the model in Abaqus, and the same boundary conditions and

Fig. 10 Stress state (von Mises) of a plate after 18 steps of crack propagation (tetrahedral elements)

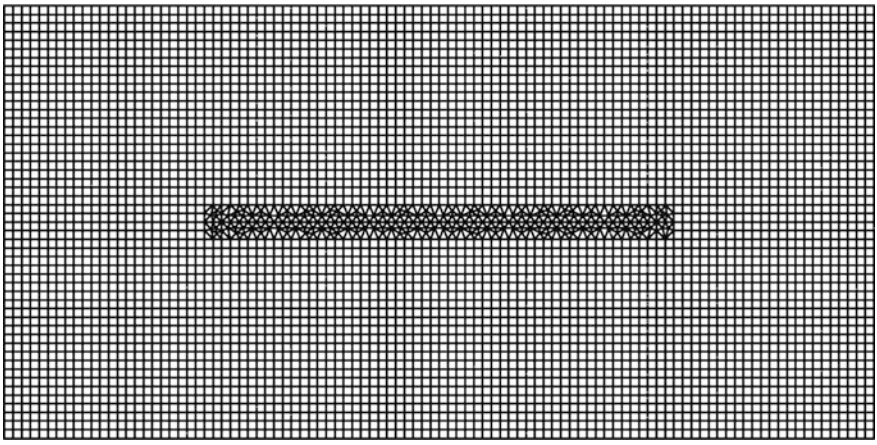

Fig. 11 The appearance of the mesh of elements of the central-crack 508 × 254 mm plate in the FRANC2D/L software

material characteristics were applied (plate thickness is one of them), too. The final appearance of the deformed mesh of elements in Fig. 12 confirmed that all the crack-propagation parameters were well defined, since the mesh is very similar to the deformed 3D meshes shown in Figs. 9 and 10. The crack shape shown in Fig. 12 was obtained after a 20 propagation step (crack opening displacement +19

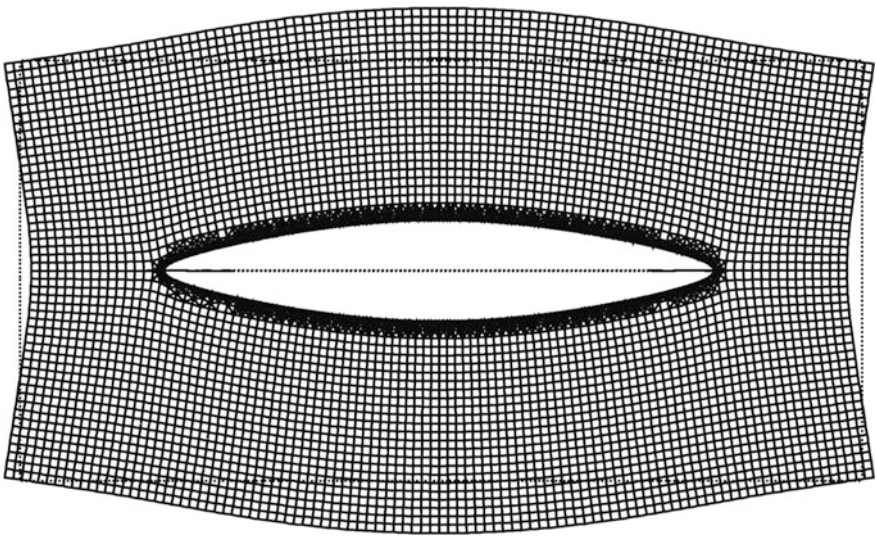

Fig. 12 The appearance of the deformed mesh of elements in the FRANC2D/L software after 20 steps of crack propagation

propagations), so that the appearance of the plate is slightly different than in Figs. 9 and 10, because in the 3D simulations 18 steps of propagation of a maximum value of 2.5 mm were carried out in both crack tips. The final crack length, therefore, was 339 mm for the 3D model, and 349 mm for the 2D. In both simulations (2D and 3D), the option for free crack propagation was used, that is, they were not "forced" to move in the plane. However, in all three cases, cracks propagated exclusively in the horizontal plane.

Table 1 gives the values of the stress intensity factor obtained by simulation of crack propagation on the plate with hexahedral elements, while the values given in Table 2 were obtained on the plate with tetrahedral elements.

What can be observed is that **the differences between the minimum and maximum values** and the equivalent stress safety factor of Mode I are **now significantly lower than in the first case**, which confirms the conclusion that the shape and density of the mesh have a significant effect on the accuracy of the results obtained using the extended finite element method.

In the model of the central-crack plate, it is easier to make a quality mesh of elements since it has no hole that is the source of the stress concentration and around which the mesh must be carefully generated to prevent the occurrence of unrealistically high or low stress values.

The values in Table 1 show that on the mesh with hexahedrons the number of the front points in which the values of K_{ekv} and K_I were calculated was constant almost all the time and was 64 (in a few steps it was somewhat larger, 66 and 68), **and that calculated mean values of the equivalent stress intensity factor and stress intensity factor of Mode I in all steps were almost identical**. This shows

Table 1 The value of the equivalent stress intensity factor and stress intensity factor Mode I in the case of the model with hexahedral elements

			Hexahedral elements					
			The value of the equivalent stress intensity factor, K_{ekv} (MPamm$^{0.5}$)			Stress intensity factor Mode I, K_I (MPamm$^{0.5}$)		
Step	Length of the crack (mm)	Number of front points	Max	Min	Mean values	Max	Min	Mean values
1	254	64	0.2926	0.2823	0.2884	0.2923	0.2822	0.2883
2	259	64	0.3015	0.2944	0.2981	0.3012	0.2942	0.2978
3	264	64	0.3076	0.3056	0.3069	0.3073	0.3055	0.3067
4	269	64	0.3177	0.3143	0.3159	0.3174	0.3142	0.3156
5	274	64	0.3265	0.3238	0.3252	0.3264	0.3236	0.3249
6	279	64	0.3364	0.3332	0.3346	0.3361	0.3332	0.3343
7	284	64	0.3471	0.3427	0.3448	0.3469	0.3427	0.3445
8	289	64	0.3562	0.3534	0.3657	0.3559	0.3533	0.3542
9	294	64	0.3684	0.3632	0.3755	0.3681	0.3631	0.3654
10	299	64	0.3769	0.3739	0.3879	0.3766	0.3735	0.3753
11	304	64	0.3915	0.3848	0.3879	0.3913	0.3847	0.3876
12	309	64	0.4000	0.3956	0.3982	0.3997	0.3952	0.3978
13	314	64	0.4151	0.4082	0.4114	0.4148	0.4080	0.4111
14	319	66	0.4241	0.4196	0.4224	0.4238	0.4194	0.4221
15	324	64	0.4390	0.4332	0.4363	0.4386	0.4330	0.4360
16	329	66	0.4499	0.4472	0.4482	0.4496	0.4469	0.4479
17	334	66	0.4661	0.4596	0.4629	0.4656	0.4594	0.4625
18	339	68	0.5121	0.5048	0.5087	0.5118	0.5046	0.5084

that the values of the stress intensity factors of the Modes II and III were either negligibly small or negative, that is, that these modes do not occur at all during the crack propagation. And indeed, by inspecting the files in which Abaqus kept all calculated values during the propagation step, enough arguments were found to confirm the previous conclusion.

Through the analysis of the values presented in Table 2 (case of the plate with tetrahedral elements) one can come to the same conclusion as in the case of the plate with hexahedral elements: **the difference between the mean values of the equivalent stress intensity factor and the intensity factors of Mode I is almost negligible in all steps**, indicating the absence of Modes II and III during crack propagation. Unlike the hexahedral plate, the number of the front points on the tetrahedral plate steadily increased from step to step, from 254 points (as it was at the beginning) to 339 points (as it was in the last propagation). It is assumed that this is a consequence of the very shape of the tetrahedral element through which the crack propagates, and here we can mention another fact that additionally clarifies the great difference in the number of front points: the number of finite elements on

Table 2 The value of the equivalent stress intensity factor and stress intensity factor of Mode I in the case of the model with tetrahedral elements

			Tetrahedral elements					
			The value of the equivalent stress intensity factor, K_{ekv} (MPa $mm^{0.5}$)			Stress intensity factor Mode I, K_I (MPa $mm^{0.5}$)		
Step	Length of the crack (mm)	Number of front points	Max	Min	Mean values	Max	Min	Mean values
1	254	190	0.2871	0.2711	0.2814	0.2870	0.2707	0.2811
2	259	208	0.2927	0.2844	0.2893	0.2925	0.2838	0.2890
3	264	222	0.3006	0.2946	0.2982	0.3008	0.2938	0.2980
4	269	226	0.3074	0.3045	0.3059	0.3087	0.3039	0.3056
5	274	217	0.3194	0.3110	0.3158	0.3193	0.3100	0.3155
6	279	212	0.3259	0.3215	0.3242	0.3259	0.3210	0.3240
7	284	227	0.3348	0.3291	0.3330	0.3342	0.3255	0.3324
8	289	208	0.3460	0.3382	0.3434	0.3456	0.3276	0.3420
9	294	216	0.3543	0.3500	0.3529	0.3544	0.3364	0.3515
10	299	212	0.3688	0.3596	0.3631	0.3640	0.3525	0.3602
11	304	212	0.3794	0.2701	0.3743	0.3753	0.3649	0.3721
12	309	199	0.3938	0.3814	0.3845	0.3871	0.3810	0.3831
13	314	203	0.4026	0.3934	0.3970	0.3982	0.3906	0.3955
14	319	184	0.4120	0.3960	0.4082	0.4126	0.3908	0.4069
15	324	155	0.4223	0.4136	0.4186	0.4216	0.4066	0.4167
16	329	152	0.4354	0.4246	0.4308	0.4351	0.4232	0.4301
17	334	126	0.4566	0.4453	0.4496	0.4547	0.4405	0.4476
18	339	107	0.5122	0.4951	0.5026	0.5110	0.4953	0.5025

the plate with tetrahedrons is significantly higher than the number of elements on the hexahedral plate—917,880 versus 128,190, which is a ratio of 7:1.

The graph in Fig. 13 shows that the differences in the values of the equivalent stress intensity factors obtained on the plates with these two types of elements are almost negligible, although it is evident that the values obtained on the tetrahedral plate are in all steps lower than those on the hexahedral plate. Taking into consideration the results obtained in the FRANC2D/L software as well, it is possible to draw a new diagram (Fig. 14) which shows that the values of the stress intensity factor obtained by the 2D analysis are slightly lower than the values obtained using the hexahedral and tetrahedral elements.

The value of the stress intensity factor of Mode I after the crack opening displacement obtained in the FRANC2D/L software was 0.2715 $MPamm^{0.5}$, which is close to the theoretical value of 0.26108 $MPamm^{0.5}$ obtained by formula (1). During crack propagation in the FRANC2D/L software, the value of K_I was continuously increasing and—unlike the plates with hexahedral and tetrahedral elements—in the 18th step there was no sudden jump of the value (Fig. 14). The jump

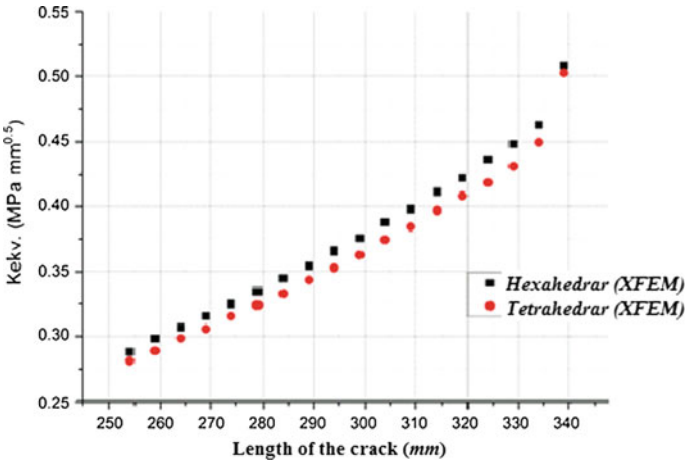

Fig. 13 Graph of variation of the values of equivalent stress intensity factor on the 3D plate with central crack for various types of finite elements

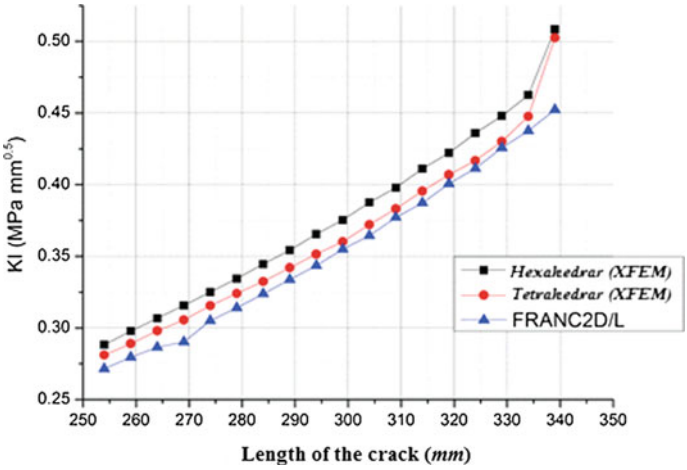

Fig. 14 Graph of variation of the values of stress intensity factor of Mode I on the 3D plate with central crack (hexahedral and tetrahedral elements, Abacus) and 2D plate (FRANC2D/L)

of the value of K_I on the 3D plates is a consequence of the fact that the crack on them has emerged from the area of high density of the mesh, which is another contribution to the thesis that **the quality of the mesh is crucial when the accuracy of the results of simulation is concerned**.

Finally, Table 3 gives a comparative overview of the values of K_I obtained in the FRANC2D/L and Abaqus software on the plate with tetrahedrons, which gave more accurate results than the hexahedron (which is the result of the much larger number

Table 3 Comparative overview of the values of stress intensity factor of Mode I for 3D plate with tetrahedral elements (Abaqus) and 2D plate (FRANC2D/L)

Length of the crack (mm)	FRANC2D/L	Abaqus 3D, tetrahedral elements	Difference (%)
	K_I (MPa $mm^{0.5}$)		
254	0.2715	0.2811	3.54
259	0.2795	0.2890	3.41
264	0.2865	0.2980	4.01
269	0.2902	0.3056	5.29
274	0.3050	0.3155	3.45
279	0.3140	0.3240	3.19
284	0.3238	0.3324	2.65
289	0.3337	0.3420	2.50
294	0.3435	0.3515	2.32
299	0.3549	0.3602	1.50
304	0.3644	0.3721	2.10
309	0.3771	0.3831	1.60
314	0.3873	0.3955	2.12
319	0.4006	0.4069	1.58
324	0.4113	0.4167	1.32
329	0.4257	0.4301	1.04
334	0.4376	0.4476	2.30
339	0.4523	0.5025	11.10

of finite elements generated on the tetrahedral plate, too). As one can see in Table 3, the differences in the K_I values in steps are not large (from 1.04 to 5.29%), with the exception of the last step (11.10%) already explained (cracks emerging from the area of higher density of the elements). The values obtained definitely indicate that 3D simulation—if the generated mesh is a quality mesh—can also provide sufficiently good values of the stress intensity factors, which can then be used in determining the number of cycles that will lead to the crack propagation from the initial length to its final size.

The estimation of the number of cycles can also be obtained within Abaqus which, based on calculated values of K_{ekv} per steps and introduced values of Paris coefficient (n), Paris exponent (C) and stress ratio (R), calculates the number of cycles using a modified Paris law on crack propagation, given by the equation.

$$\frac{da}{dN} = \frac{C(\Delta K)^n}{(1-R)(Kc - Kmax)}. \tag{2}$$

In the case of a central crack on the plate 508 × 254 mm, the value of the exponent n = 2.26 and coefficient C = 7.526 × 10^{-11}, respectively, corresponding

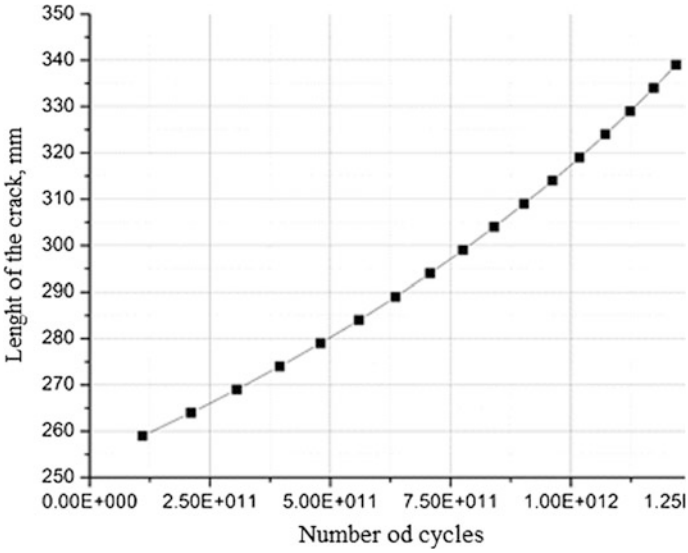

Fig. 15 Graph of variation of the crack length (hexahedral elements, Abaqus) with the number of load cycles

to the steel of HP-9-4-20 190-210 UTS grade were adopted; GTA Weld + SR from NASGRO base. For the ratio of minimum and maximum stress, the value R = −1 was adopted.

The graph in Fig. 15 shows that an extremely large number of cycles (order of magnitude 1×10^{11}) is required to make the crack propagate from the initial length of 254 to 259 mm, while for reaching the total length of 339 mm it is necessary to have more than 1.2 * 1012 cycles. This result is not unexpected, because a very low value of tensile stress (only 0.00689 MPa) was used in the calculation.

It is interesting to note that the NASGRO software for an identical model of plate, only of infinite length, showed the message “crack does not propagate” when attempting to make the crack to propagate, and as a result gave the number of cycles equal to zero. This also confirms that the applied load is very low and that under such a load the crack will propagate by a couple of millimeters only after a very large number of cycles.

However, the actual value of the cycle number can only be obtained by fatigue testing.

Conclusions

Over the years, many numerical techniques such as finite element method (FEM), boundary element method (BEM), meshfree methods and extended finite element method (XFEM) have been developed to simulate the fracture mechanics problems. In XFEM, the conformal meshing is not required, hence, the modelling of moving discontinuities or crack growth is performed with an ease.

Numerical calculation using XFEM, such as that presented in this paper, makes it possible to study complex real problems, including a comprehensive parametric analysis of all influential factors. Detailed three-dimensional elastic-plastic models, which consider the corresponding properties of microstructural heterogeneity of ductile materials, as well as various structural solutions of the seam geometry and various forms of cracks, provide the possibility of—for instance—effective testing of heterogeneity of the welded joint, the strain and stress state in critical areas, singularity effects and the determination of the parameters of elasto-plastic mechanics.

The main advantage of XFEM lies in possibility of SIFs values evaluation on complex cracked geometry but—at the same time—XFEM results are mesh sensitive and depend on the mesh density in the fracture process region. Mesh size must be determined carefully to ensure the computational efficiency and accuracy; therefore, experimental verification of FE model is still necessary, particularly when geometry is result of completely innovative design.

Acknowledgements This work is a contribution to the Ministry of Education and Science of the Republic of Serbia funded Project TR 35011.

References

1. Sedmak, A., Primena mehanike loma na integritet konstrukcija, Mašinski fakultet, 2003, ISBN 86-7083-473-1.
2. http://www.3ds.com/produsts/catia/.
3. Jovicic G., Zivkovic M., Vulovic S., Budgetary fracture and fatigue mechanics, Faculty of Mechanical Engineering, Kragujevac, 2011.
4. Ćulafić V. B., Introduction to fracture mechanics, Podgorica, 1999.
5. Grbović A., Research of the fatigue of structural elements built from super alloys, doctoral dissertation, Belgrade, 2012.